NORTHWESTERN UNIVERSITY

Synthesis of Hierarchically Porous UiO-66 MOF Materials and Their Applications in Catalysis and Water Purification

A DISSERTATION

SUBMITTED TO THE GRADUATE SCHOOL

IN PARTIAL FULFILLMENT OF THE REQUIREMENTS

for the degree

DOCTOR OF PHILOSOPHY

Field of Chemistry

By

Furui Zhang

EVANSTON, ILLINOIS

June 2021

© Copyright by Furui Zhang 2021

All Rights Reserved

ABSTRACT

Polymer-Assisted Synthesis of Hierarchically Porous UiO-66 MOF Materials and Their Applications in Catalysis and Water Purification

Furui Zhang

In the first two decades of the 21st century, metal organic frameworks (MOFs) have attracted much attention in both fundamental-research and-industrial application areas. Derived from a vast library of both inorganic metal nodes and organic linker bridges, MOFs are crystalline materials whose structures and chemical environments can both be tuned in a facile manner. The molecular nature of the building blocks normally engender MOFs with small micropores (< 2 nm) and very high surface areas, but they also limit the diffusivity of guest molecules inside its porous matrix and restrict the entrance of species larger than the aperture size. This could greatly slow down their performance in applications that requires fast molecular transport, such as sorption and catalysis. Designing and synthesizing MOF materials with both micropores (< 2 nm) and large mesopores (2-50 nm) or even macropores (>50 nm), namely hierarchically porous MOF materials, can overcome these limitations, achieve efficient mass transport, and enhanced performances, thus broaden applications of the MOF materials. To implement this approach, this thesis focuses on the development of meso-/microporous and macro-/microporous MOF-based materials and corroborate their applications in catalysis and water purifications.

Specifically, a class of removable block-copolymer templates were used to engender mesopores into a Zr-based MOF during its growth, seeded by pre-synthesized MOF nanoparticles. Such a seed-mediated, template-assisted growth could be iteratively repeated to increase the

proportion of mesopore in the resulted materials. With a thrice-grown material, significant enhancements in adsorption capacity and catalytic activity were observed, comparing to its micropore-only counterpart. Further studies of the templating effect by Pluronic polymers led us to a new 2D Zr-based MOF structure, proposed to arise from the coordination hindrance brought by the polymers on the metal nodes during MOF growth.

A commercially available water-purification polymer membrane was then combined with the seeded strategy to grow microporous Zr-based MOFs inside its macropores, resulting in a macro-/microporous membrane material, which were shown to be highly efficient and selective in removing phosphate from groundwater with the presence of other anions. A unique electro-assisted technique was additionally applied on this composite membrane to further improve the adsorption and desorption kinetics. This strategy, when combined with the template-assisted strategy described above can form a general approach for fabricating the next generation of hierarchically porous MOF materials.

ACKNOWLEDGEMENTS

I express my sincere gratitude to Prof. SonBinh T. Nguyen, my graduate advisor, for his mentorship throughout my graduate career at Northwestern. In the past four years, we have had over 200 meetings on research & teaching and hundreds hours of one-to-one writings. His dedication in time and effort guided me to become a critical-thinking scientist, a team-oriented communicator, and a wholehearted project leader. The 4-year plan that we blueprinted together during my 1st year helped me significantly in framing this thesis work. Beyond scientific knowledge, his extraordinary advising equipped me with invaluable skills in efficient communication, technical writing, and project presentation. Outside of research, I am very grateful for his constant support to my family and career decisions. Of course, many thanks to him for his sharing of coffee mocha in many afternoons to keep me alert when writing this thesis. I would like to also extend my gratitude to Prof. Omar Farha and my committee members, Profs. Joseph T. Hupp, Mercouri Kanatzidis, and Nathan C. Gianneschi for their insights on my projects and research proposals along my Ph.D. journey.

This thesis could not have been successfully completed without the help from my brilliant collaborators. First, I want to acknowledge Prof. Chia-Kuang (Frank) Tsung and his team–Prof. Lien-Yang Chou, Prof. Xiaoyuan Liu, Yang Li, and Mr. Wei-Shang Lo–at Boston College. Frank was also my graduate advisor at Boston College who was always optimistic, cheerful, and enthusiastic to research and life. Part of this thesis (chapter 2) is dedicated to his memory, as the core-shell material design was partially inspired by some of his previous works. Second, I want to thank Dr. Xiaobing Hu, Dr. Eric W. Roth, and Dr. Christos D. Malliakas for the electron-microscopic and X-ray diffraction characterizations of the materials. Third, I want to acknowledge Prof. Oded Nir and Dr. Sanhita Chaudhury for their collaboration in membrane project (chapter

4). Last, I want to thank Prof. Neil Schweitzer for his teaching of the ISEN 490 course (on material synthesis & characterization for heterogeneous catalysts) and his help with the reactors at the REACT facility. Many thanks to my lab members, especially Dr. Cornelius Audu, Dr. Lily Mao, Dr. Bong Jin (Bill) Hong, Dr. Gao-Fong Chang, Ananya Agrawal, Matthew Du, Jean Chang, Zhizhi Kong, Edward Y. Zhang, Tori Seto, and Max Sigal, for their kind help and support throughout my graduate career. Special thanks go to Dr. Rungmai Limvorapitux, Dr. Yonghwi Kim, and Mengtan Liu for their patient training in MOF syntheses and catalysis when I first started at NU.

I am very lucky to have family members–Elise Zhang, Chunlan Fu, Hongliang Zhang, Yinjuan Qin, and my wife Dr. Weizi Yuan in particular–who always believe in me and being supportive all the time. Weizi was also a graduate student at NU and thus she could not only share the joy of achievement but also sympathize the frustration with me along this Ph.D. journey. I am also very grateful to have our lovely daughter, Elise, in 2018, making my life in Evanston even more colorful. During the past 4 years, I could not imagine myself without many good companions outside my research lab. Among those, I would like to especially thank Dr. Yao Du, Xu Zhang, Dr. Ran Li, Dr. Lin Sun, Songting Cai, and Dr. Yanming Zhang. They made my weekends and holidays full of laughters and unforgettable memories. I am also very thankful that Zuohao brought me into a climbing world in 2018, which made bouldering as my favorite exercise in Chicago.

To close this thesis, I really treasure my experience at Northwestern University as a Ph.D. student. I hope to apply the research methodology and communication skills I gained throughout my academic career to my future works and life. I would like to always remember that “The fate of our times is characterized by rationalization and intellectualization and, above all, by the disenchantment of the world.” (Max Weber).

TABLE OF CONTENTS

ABSTRACT 3

ACKNOWLEDGEMENTS 5

TABLE OF CONTENTS 7

LIST OF TABLES 9

LIST OF FIGURES 10

LIST OF SCHEMES 22

Chapter 1 Introduction to the designs & applications of hierarchically porous UiO-66 materials 23

1.1 MOFs as a new class of porous materials and the importance of hierarchical porosity in MOFs 24

1.2 The microporous UiO-66 MOF 26

1.3 Self-assembled polymer templates to introduce mesopores into UiO-66 materials 27

1.4 Macroporous polymer membranes as host for microporous UiO-66 materials in water purification 30

1.5 Thesis overview 31

Chapter 2 Template-assisted, seed-mediated synthesis of hierarchically mesoporous core-shell UiO-66: enhancing adsorption capacity and catalytic activity through iterative growth 35

2.1 Introduction 36

2.2 Background and motivation 37

2.3 Combining seed-mediation and template-assistance to build core-shell UiO-66@HM-UiO-66 materials 39

2.4 Employing water and Pluronic F-127 for the iterative overgrowth of hierarchically porous MOF 40

2.5 UiO-66 NP seeds: synthesis and interparticle porosity 42

2.6 UiO-66@HM-UiO-66-F_4: overgrowth of a hierarchically porous UiO-66-F_4 shell on UiO-66 NP seeds. 43

2.7 Iterative overgrowth of the HM-UiO-66-F_4 shell 48

2.8 Extension to other UiO-66-X (X = $(COOH)_2$, $(OH)_2$, and NH_2) shells 50

2.9 Increased dye-uptake capacity with HM-UiO-66: the importance of hierarchical porosity in solution adsorption 51

2.10 UiO-66-catalyzed sulfide oxidation 54

2.11 Conclusion 56

2.12 Experimental and supplementary data 57

Chapter 3 Bottom-up synthesis of a 2D cpp UiO-66 structure by coordination hindrance on Zr_6 clusters 101

3.1 Introduction 102

3.2 Background and motivation 103

3.3 Pluronic-induced formation of the 2D phase 105

3.4 AcOH-induced formation of the 2D cpp UiO-66-F_4 material 109
3.5 Structural characterizations of the 2D cpp UiO-66-F_4 materials 111
3.6 Grow the 2D cpp UiO-66-F_4 on PEEK membrane surface driven by linker deficiency 113
3.7 Conclusion 115
3.8 Experimental and supplementary data 116

Chapter 4 UiO-66-embeded, macroporous-membranes-enabled, electro-assisted sorption for efficient phosphate remediation 137

4.1 Introduction 138
4.2 Background and motivation 138
4.3 Seed-mediated, iterative growth of UiO-66 in PEEK membranes 140
4.4 Selective removal of P^V from solutions of common groundwater anions 142
4.5 Improving P^V uptake by increasing UiO-66 loading in PEEK membranes 145
4.6 Electro-assisted sorption in the synthesized composite membranes 146
4.7 Selective removal of P^V and As^V from simulated groundwater 154
4.8 Conclusion 157
4.9 Experimental and supplementary data 158

Chapter 5 Epilogue 190

5.1 General conclusions from this thesis work 191
5.2 Design UiO-66 membrane materials containing micro-, meso-, and macropores for practical utilities 192
5.3 Extend the synthetic strategies to other Zr-based MOF materials 193
5.4 Last remarks 195

Appendix A 196

References and notes 197

CURRICULUM VITAE 211

LIST OF TABLES

Table 2.1 Molecular formulas of UiO-66s as determined by NMR and ICP-OES quantitative analyses. 73

Table 2.2 N_2 physisorption data of the UiO-66 materials (surface area unit: m^2/g). 89

Table 2.3 The amount of catalysts used in each reaction and the corresponding reaction rate. 98

Table 3.1 Molecular formula of ideal **fcu** UiO-66 and 2D **cpp** UiO-66 materials. 129

Table 3.2 The peak position in PXRD and d-spacing of (100) planes for as-synthesized 2D **cpp** UiO-66-$F_4|_{AcOH}$, activated 2D **cpp** UiO-66-$F_4|_{AcOH}$, and simulated structures. 135

Table 4.1 Weights and thicknesses of the UiO-66|PEEK membranes synthesized and used in the present work. 166

Table 4.2 Data for plotting Figure 4.4, obtained from nine membrane samples. 172

Table 4.3 Physical parameters during electro-assisted sorption experiments. 177

Table 4.4 Anion concentrations in simulated groundwater used for studying adsorption selectivity of UiO-66|PEEK. 180

Table 4.5 Adsorption selectivity ($\alpha_{P^V}^{Cl^-}$) of UiO-66|PEEK membranes for P^V over other anions in simulated groundwater. 180

Table 4.6 The chemical formula of a UiO-66 supernatant powder (batch 3 in Figure 4.24) before and after the hot MeOH soaking (see section 4.9.2 for detailed information of the soaking experiment). 184

Table 4.7 Zr and P compositions in as-synthesized UiO-66 powder, ZrP-1, and ZrP-2 samples. 187

Table 4.8 Solution components in the powder soaking experiments in HCO_3^- solution. 189

Table 4.9 Zr and P compositions in leftover solid after HCO_3^--solution soaking resulted from as-synthesized UiO-66 powder, ZrP-1, and ZrP-2 samples. 189

LIST OF FIGURES

Figure 1.1 A brief timeline listing several porous materials with their discovery times. 24

Figure 1.2 A diagram showing the differences between the hierarchially porous materials (bottom) and the small-pore only porous materials (top) in adsorption (left) and catalytic (right) applications. 25

Figure 1.3 a) Building blocks of UiO-66 MOF (Zr_6(oxo) cluster and the BDC linker), leading to a 12-coordinate mode of the Zr_6 cluster in the "ideal" UiO-66 structure. b) The UiO-66 crystal structure viewed from the <001> direction with two type of pores shown in spheres (octahedral pore with ~11 Å diameter (orange) and tetrahedral pore with a ~9 Å diameter (green)).[17] c) A UiO-66 porous mattrix viewed in a wareframe model, showing its 3D structure and porosity. 26

Figure 1.4 a) Regular assembly/synthesis of MOF materials from metal nodes (grey circles) and organic linkers (blue rods). b) Template-assisted strategy to generate large voids in MOF materials by introducing removable templates (green circles) during the synthesis and washing them away post-synthesis. 29

Figure 1.5 A HM-UiO-66 material synthetic strategy using UiO-66 nanoparticles as seeds and block copolymer micelles as templates, which resulted in materials with enhanced performances in adsorption and catalysis. 32

Figure 1.6 A coordination-hindrance-induced formation of a 2D **cpp** UiO-66 structure, where the hindrance could be resulted from the block copolymers (as templates in chapter 2) and an excess amount of coordination-competing agents. 33

Figure 1.7 A UiO-66-embeded PEEK macroporous membrane where the macropores allow for fast water flow and UiO-66 particles act as phosphate adsorbents. 34

Figure 2.1 (a) Proposed template-assisted, seed-mediated strategy for the iterative synthesis of the UiO-66@HM-UiO-66-F_4 material. The schematic shown here is an artistic rendition representing the core-shell design and hierarchical porosity of the materials, based on Figures 2.1e-f, which shows spherical dimple-laden particles; the inset of Figure 2.1e, which shows a single spherical dimple-laden particle; and Figure 2.4d, which shows the core-shell structure. (b) SEM image of the UiO-66 NP seeds. (c) and (d) Cryo-TEM images of an aqueous mixture of 2.9 wt % F-127 and 0.1 wt % UiO-66 NP seeds. (e) SEM image of UiO-66@HM-UiO-66-F_4 after one growth cycle. The lower inset is a zoomed-in image of a single raspberry-shaped cluster, clearly shows dimples that are consistent with the size of the F-127 micelles, supporting the surface-templating notion shown in panels c-d. (f) and (g) TEM images of UiO-66@HM-UiO-66-F_4 after one growth cycle. As UiO-66 is one of the most chemically, thermally, and mechanically stable MOFs,[15] with bulk modulus of 17 GPa[81] and a calculated minimal sheer modulus of 13.7 GPa,[82] we do not expect that the core will be damaged during the synthesis of the mesoporous structure during the growth. As a point of reference, UiO-66 particles have been used as seeds to overgrow ZIF-8 shells and were found unchanged after the growth.[83] 40

Figure 2.2 PXRD profiles of the simulated UiO-66 (red column), UiO-66 NP seeds (black), UiO-66@HM-UiO-66-F_4 (blue), and the [Zr+BDC-F_4]* non-porous phase (burgundy). 43

Figure 2.3 The N_2 physisorption isotherms of UiO-66 NPs (black square), UiO-66@HM-UiO-66-F_4 with ~2 wt % of encapsulated F-127 (blue triangle), and purified UiO-66@HM-UiO-66-F_4 (i.e., no encapsulated F-127, green diamond). Solid symbols represent the adsorption branch and hollow symbols represent the desorption branch. Inset: DFT PSDF profiles obtained from the isotherms. 44

Figure 2.4 (a) High-angle annular dark field (HAADF) image of a sample of UiO-66@HM-UiO-66(Hf)-F_4. (b-c) EDS elemental maps–imaged by Zr and Hf, respectively–of the same sample. (d) Composite Zr (blue) and Hf (yellow) EDS maps of the same sample, made by overlaid panels b and c, showing a core-shell structure. 48

Figure 2.5 SEM images showing a continuous increment of HM-UiO-66-F_4 shell thickness on top of UiO-66 NP seeds in the iterative growth process. 49

Figure 2.6 a) Adsorption-time profile of the anionic dye DB 86 into UiO-66 NPs (orange diamond), UiO-66-F_4 (green star), UiO-66@HM-UiO-66-F_4 (blue triangle), UiO-66@HM|$_{2nd}$-UiO-66-F_4 (blue circle), and UiO-66@HM|$_{3rd}$-UiO-66-F_4 (blue square). The dash lines are provided only for visual guidance. b) Bar graph of the DB 86-uptake amounts of the corresponding five samples at 48 h; In the latter three, the uptake amounts attributed to a [UiO-66 + UiO-66-F_4] physical mixture at the same mass and composition is represented as the green-orange portion at the bottom of each bar while the enhancements resulted from the HM structure are shown as the blue-grid-pattern portions of the bars. 53

Figure 2.7 (a) Conversion-vs-time profiles of the sulfide oxidation catalyzed by UiO-66@HM|$_{3rd}$-UiO-66-F_4 (blue inverted triangle), UiO-66|UiO-66-F_4 (magenta triangle), UiO-66 NPs (orange diamond), and UiO-66-F_4 (green circle), along with a background reaction without catalyst (black square). (b) Conversion-vs-time profiles (up to 11 % conversion) and the linear fitting results (see Table 2.3 for the rate data). Reaction conditions: rt, methyl phenyl sulfide (20 mM), aqueous H_2O_2 (20 mM), Zr_6 cluster (0.01 equiv), and CH_3CN (10 mL) as solvent. To demonstrate the stability of UiO-66@HM|$_{3rd}$-UiO-66-F_4, we have recycled it 3 times in the sulfide-oxidation reaction and showed that its crystallinity and particle size/morphology were preserved (Figures 2.38 and 2.39). 55

Figure 2.8 ^{1}H NMR spectra of digested UiO-66@HM-UiO-66-F_4 samples after MeOH washing (red) and after 1 (green), 2 (blue), and 3 days (purple) of Soxhlet extraction. The approximate F-127 amount was calculated by integrating the methyl signal from the PPO segment (~1.02-1.05 ppm)[122] against a maleic acid internal standard. The drop in acetic acid amount indicates that the Soxhlet extraction also helped to remove any residual acetic acid that were not rinsed out by simple MeOH washing. 66

Figure 2.9 NMR (^{1}H and ^{19}F) calibration curves for BDC (left), AcOH (middle), and BDC-F_4 (right) against the internal standards (MA for ^{1}H; TFA for ^{19}F). 71

Figure 2.10 ^{1}H NMR spectrum of the digested UiO-66@HM-UiO-66-F_4 with MA as the internal standard. 71

Figure 2.11 ^{19}F NMR spectrum of the digested UiO-66@HM-UiO-66-F_4 with TFA as the internal standard. 72

Figure 2.12 (Top) SEM image of the UiO-66 NPs batch 1 (left). The corresponding SEM-derived particle-size-distribution profile for the UiO-66 NPs batch 1 (μ = 48.2 nm; σ = 10.6 nm) (right). (Bottom) SEM image of the UiO-66 NPs batch 2 (left). The corresponding SEM-derived particle-size-distribution profile for the UiO-66 NPs batch 2 (μ = 80.1 nm; σ = 15.0 nm) (right). 74

Figure 2.13 CyroTEM images of the structures observed in a [2.9 wt % F-127 + 0.1 wt % UiO-66 NP seeds]$_{aq}$ mixture. 74

Figure 2.14 DLS intensity-based distribution profiles of aqueous dispersions of: 2.9 wt % F-127 (top left), 0.1 wt % UiO-66 NPs (top right), and [2.9 wt % F-127 + 0.1 wt % UiO-66 NPs] (bottom). 75

Figure 2.15 (Top) SEM images, TEM image, and corresponding SAED result of UiO-66@HM-UiO-66-F_4. (Middle) SEM images of UiO-66@HM|$_{2nd}$-UiO-66-F_4. (Bottom) SEM images of UiO-66@HM|$_{3rd}$-UiO-66-F_4. In an attempt to show that the HM-MOF shell does possess good crystallinity, we have tried to obtain an SAED pattern for the UiO-66@HM-UiO-66-F_4 sample using TEM. Unfortunately, we did not see convincing SAED data (i.e., clear diffraction spots, see the right panel in the top row) for this sample. This is not suprising in retrospect given the high beam voltage (200 kV) of our equipment and the small size (~50 nm) of our seed nanoparticles. We note that Zhu et al.[124] was only able to obtain good SAED pattern from a large (200 nm) UiO-66 microcrystal under a nano beam diffraction mode with low (120 kV) voltage and a very low electron dosage level; even then the crystal was still damaged during the alignment. As a verification of our instrument limitation, we also attempted to obtain the SAED pattern for the starting UiO-66 seeds (~50 nm in size) and a larger-size crystal (~100-200 nm), both of which also did not show any obvious diffraction pattern (Kikuchi lines were not seen or vanished very quickly). Nevertheless, we are confident that our HM-MOF materials possess good crystallinity based on the BET surface area that for our HM-UiO-66-F_4 material. It matches closely to that predicted for a physical mixture of crystalline [66 wt % UiO-66 + 33 wt % UiO-66-F_4] MOFs at the same mass proportion. See Table 2.2 for the comparative data. 76

Figure 2.16 SEM images of the [Zr+BDC-F_4]* non-porous phase. 77

Figure 2.17 SEM images of UiO-66|UiO-66-F_4. 77

Figure 2.18 SEM images of UiO-66-F_4. 77

Figure 2.19 N_2 physisorption isotherm of the [Zr+BDC-F_4]* non-porous phase. Close symbols, adsorption; open symbols, desorption. 78

Figure 2.20 (a) PXRD profiles of the UiO-66@HM-UiO-66-F_4 overgrowth materials using different ratio of seeds to a 1:1 mixture of precursor solutions C and D (see Section 2.12.2): 0.10 (purple), 0.25 (green), 0.50 (blue), and 1.0 wt % (black). (b-d) PXRD profiles (b), N_2 physisorption isotherms (c), and DFT PSDF profiles (d) of the [Zr+BDC-F_4]*, [Zr+BDC-$(OH)_2$]*, [Zr+BDC-$(COOH)_2$]*, and [Zr+BDC-NH_2]* phases grown in the absence of UiO-66 NP seeds. The data shown in panels b-d clearly illustrate how the pore properties of these phases are affected by the solubility of the added linkers in water. Without the UiO-66 NP seeds to direct the growth, non-porous product was often obtained when the added linkers are soluble in water (i.e., forming clear solution in 50 mM concentration, such a BDC-F_4 and BDC-$(COOH)_2$, see Figure 2.36c). In contrast, crystalline UiO-66 materials can be formed when the organic linker have low solubility in water (as in the case of BDC-$(OH)_2$ and BDC-NH_2, see Figure 2.36c). Interestingly, only the phase made from BDC-$(OH)_2$ exhibits template-induced mesopores (~7 nm) that match the size of the F-127 micelle, probably due to the strong H-bonding interaction between the linker and the Pluronic backbone. To the extreme, a similar non-seed-mediated growth with the BDC linker did not form any solid product after 24 h reaction, attributable to the low solubility of the added linker. 79

Figure 2.21 PXRD profiles of simulated UiO-66, UiO-66@HM-UiO-66-F_4, UiO-66@HM|$_{2nd}$-UiO-66-F_4, and UiO-66@HM|$_{3rd}$-UiO-66-F_4. The d_{xrd} values on the right hand side of each experimental profile were calculated using Scherrer's equation. 80

Figure 2.22 (a) TGA profiles of UiO-66@HM-UiO-66-F_4, UiO-66 NP seeds batch 1, and UiO-66-F_4. (We note that the profiles for our UiO-66 seeds and UiO-66-F_4 materials are comparable to the published data[99] for aqueously synthesized UiO-66 and UiO-66-F_4 samples (see panel c).) The two major mass-loss stages of UiO-66@HM-UiO-66-F_4 (~320 ºC and 480 ºC) match with those of the UiO-66-F_4 and UiO-66 materials respectively, indicating the presence of both components in the core-shell materials. (b) The corresponding GCMS(EI)-temperature profiles on m/z of 44 (CO_2), 78 (C_6H_6), and 150 ($C_6H_2F_4$) collected during the TGA analysis of UiO-66@HM-UiO-66-F_4 (red curve in panel a). They are assigned as fragments generated by decarboxylation reaction under high temperature and Ar atmosphere (CO_2, benzene, and 1,2,4,5-tetrafluorobenzene). (c) TGA profile of UiO-66@HM-UiO-66-F_4 and reported[99] TGA profiles of aqueously synthesized UiO-66 and UiO-66-F_4 materials. Data for these last two materials were digitized by us from the published work.[99] A gradual mass loss before 300 ºC was observed in the TGA profiles of all three materials, which could be resulted from the decomposition of defective regions in aqueously synthesized UiO-66 materials. 81

Figure 2.23 (Top) N_2 physisorption isotherms (top left) and DFT PSDF profiles (top right) of the UiO-66 NP seeds (black square), UiO-66@HM-UiO-66-F_4 (red circle), and UiO-66|UiO-66-F_4 (olive diamond). Close symbols, adsorption; open symbols, desorption. These data clearly showed that UiO-66@HM-UiO-66-F_4 is very different from the other two samples. (Bottom) N_2 physisorption isotherms (bottom left) and BJH PSDF profiles (bottom right) of the as-synthesized UiO-66 NP seeds (black square), the P-U-0.2 materials reported by Zhang et al.[53](blue circle), and the UiO-66-62 sample reported by Niu et al.[52] (burgundy star). Data for the P-U-0.2 material was provided by Dr. Xiaodong Zhang while data for the UiO-66-62 material was digitized by us from the published work.[52] Thus, the number of data points shown for the latter sample in the bottom panels do not reflect the actually number of collected datapoints. Even with these limitations, these data also show that our seed material is quite similar to the other two materials, which have interparticle porosity. For ease of comparison to the data reported by Zhang et al.,[53] the PSDFs profiles shown here for our two materials were produced using the desorption branch of the isotherms. We note, however, that this is not a recommended practice for hierarchically porous materials such as our UiO-66@HM-UiO-66 for which the adsorption branches of the isotherms should be used to obtain PSDFs to take into account the cavitation desorption mechanism when H4-type hysteresis loop or small pore neck size (< 5-6 nm) was observed.[12] (Disclaimer: We do not know from which branch was the PSDF profile reported by Niu et al.[52] being derived. In addition, the PSDF plot was limited to < 40 nm because the reported PSDF profile for UiO-66-62 was only shown to 40 nm pore width.) 82

Figure 2.24 Plot of mass increase (left) and the change in BDC-F_4 content (right: red circle = experimental; black cube = calculated theoretical value; see explanation below) versus the overgrowth rounds. The absolute amounts of BDC-F_4 and BDC were determined by quantitative ^{19}F and ^{1}H NMR spectroscopies, respectively (see Section 2.12.3 and Table 2.1). The error bars in the left plot were the standard deviations from 3 experimental tries. The data in the right plot were based on a single run. The theoretical BDC-F_4/(BDC-F_4+BDC) ratios were calculated based on mass increases and formulas of defect-free UiO-66 ($Zr_6O_4(OH)_4(C_8H_4O_4)_6$) and UiO-66-$F_4$ ($Zr_6O_4(OH)_4(C_8F_4O_4)_6$), assuming that the mass increases were from newly formed UiO-66-F_4. The experimental results are consistently higher than the theoretical ones because linker exchange may happen during the overgrowth process and not all of the original UiO-66 NP seeds were recovered during the work-up stage (especially during centrifugation and washing). 83

Figure 2.25 N_2 physisorption isotherms (top), BJH PSDFs (middle), and DFT PSDFs (bottom) of: UiO-66@HM-UiO-66-F_4 (black square), UiO-66@HM|$_{2nd}$-UiO-66-F_4 (red circle), and UiO-66@HM|$_{3rd}$-UiO-66-F_4 (blue triangle). Close symbols, adsorption; open symbols, desorption. 84

Figure 2.26 Plot of mass increase (top), Hf-content percentage change (bottom left), and BDC-F_4 content percentage change (bottom right) (red circle: experimental; black cube: calculated theoretical value: see explanation below) versus the overgrowth rounds. The absolute amounts of BDC-F_4 and BDC were determined by quantitative ^{19}F and ^{1}H NMR spectroscopies, respectively (see Section 2.12.3 and Table 2.12.1), while the absolute amounts of Hf and Zr were determined using ICP-OES (see Section 2.12.3 for detailed procedure). The theoretical BDC-F_4/(BDC-F_4 + BDC) and Hf/(Hf + Zr) ratios were calculated based on mass increases and formulas of defect-free UiO-66 ($Zr_6O_4(OH)_4(C_8H_4O_4)_6$) and UiO-66-$F_4$ ($Zr_6O_4(OH)_4(C_8F_4O_4)_6$), assuming that the mass increases were from newly formed UiO-66-F_4. The experimental linker ratios are consistently higher than the theoretical ones because linker exchange may happen during the overgrowth and not all of the original UiO-66 NP seeds were recovered during the work-up (especially during centrifugation and washing). A similar trend was observed for the Hf content, which we attributed to node exchange.[125-127] While we could not completely exclude the formation of hafnium oxide as impurities during the overgrowth,[123] we did not observe the hafnium oxide diffraction peak in the PXRD profiles. 85

Figure 2.27 PXRD profiles of simulated UiO-66, UiO-66@HM-UiO-66(Hf)-F_4, UiO-66@HM|$_{2nd}$-UiO-66(Hf)-F_4, and UiO-66@HM|$_{3rd}$-UiO-66(Hf)-F_4. 86

Figure 2.28 SEM images of UiO-66@HM|$_{3rd}$-UiO-66(Hf)-F_4. 86

Figure 2.29 (a) High-angle annular dark field (HAADF) image of a sample of UiO-66@HM|$_{3rd}$-UiO-66(Hf)-F_4 and (b-d) the EDS elemental maps–imaged by Zr, Hf, and F, respectively–of the same sample. (e) HAADF image of a sample of UiO-66@HM-UiO-66(Hf)-F_4 (also shown in Figure 2.4a in Section 2.6) and (f) the corresponding F EDS elemental map of this same UiO-66@HM-UiO-66(Hf)-F_4 sample. As discussed in Section 2.6, the F signals appear throughout the particle rather than concentrated mostly on the surface, suggesting that linker exchange has occurred during the formation of UiO-66@HM-UiO-66(Hf)-F_4. The apparent higher density of the F signals at the center of the particles shown in d and f are consequence of the particles being "thicker" in the center. 87

Figure 2.30 N_2 physisorption isotherms (top), BJH PSDFs (middle), and DFT PSDFs (bottom) of: UiO-66@HM-UiO-66(Hf)-F_4 (blue triangle), UiO-66@HM|$_{2nd}$-UiO-66(Hf)-F_4 (olive diamond), and UiO-66@HM|$_{3rd}$-UiO-66(Hf)-F_4 (wine star). Close symbols, adsorption; open symbols, desorption 88

Figure 2.31 UV-vis calibration curve for DB 86 at $\lambda = 622$ nm. 90

Figure 2.32 UV-vis spectra of the diluted supernatant obtained from the uptake of DB 86 by UiO-66 NPs, UiO-66-F_4, UiO-66@HM-UiO-66-F_4, UiO-66@HM|$_{2nd}$-UiO-66-F_4, and UiO-66@HM|$_{3rd}$-UiO-66-F_4. For each data point, the supernatant was diluted 10 times to obtain a solution with an absorbance close to or less than 1. Three UV-vis measurements were obtained for each sample to ensure that the measurents are consistent. 92

Figure 2.33 Bar graph of the DB 86 uptake-capacity per node by our UiO-66 materials, calculated based on the uptake data shown in Figure 2.6 in Section 2.9. The amount of $Zr_6O_4(OH)_4$ nodes in each material is calculated based on the amount of material used (1 mg) in the uptake experiment and the corresponding chemical formulas in Table 2.1. 93

Figure 3.34 SEM images of UiO-66@HM|$_{3rd}$-UiO-66-$(OH)_2$ (1st row), UiO-66@HM|$_{3rd}$-UiO-66-$(COOH)_2$ (2nd row), UiO-66@IP|$_{3rd}$-UiO-66-NH_2 (3rd row), and UiO-66@IP|$_{3rd}$-UiO-66 (4th row). 94

Figure 2.35 PXRD profiles of simulated UiO-66, UiO-66@HM|$_{3rd}$-UiO-66-$(OH)_2$, UiO-66@HM|$_{3rd}$-UiO-66-$(COOH)_2$, UiO-66@IP|$_{3rd}$-UiO-66-NH_2, and UiO-66@IP|$_{3rd}$-UiO-66. 95

Figure 2.36 (a) N_2 physisorption isotherms and (b) DFT PSDF profiles of: UiO-66 NP seeds batch 2 (black squre), UiO-66@IP|$_{3rd}$-UiO-66-NH_2 (orange pentagon), UiO-66@IP|$_{3rd}$-UiO-66 (burgundy star), UiO-66@HM|$_{3rd}$-UiO-66-$(OH)_2$ (blue triangle), UiO-66@HM|$_{3rd}$-UiO-66-$(COOH)_2$ (green diamond), and UiO-66@HM|$_{3rd}$-UiO-66-F_4 (red circle). Close symbols, adsorption; open symbols, desorption. For comparison, the data are placed into two groups: one for the materials with hierarchical mesoporosity (HM) where the added linkers are more water-soluble and one for the materials with interparticle porosity (IP) where the added linkers are less water-soluble; data for the UiO-66 NP seeds was included in each group for comparison. As shown in panels a and b, the UiO-66 NP seeds have pore properties that are quite similar to those for the materials with interparticle porosity (IP). Interestingly, the N_2-physisorption isotherm for UiO-66@IP|$_{3rd}$-UiO-66-NH_2 is similar in shape to that of the UiO-66 NP seed while that for UiO-66@IP|$_{3rd}$-UiO-66 still features a type-Ia/II adsorption branch, consistent with the latter having a slightly higher proportion of mesopores. c) Photograph of 2-50 mM aqueous solutions of BDC-X (X = F_4, $(COOH)_2$, $(OH)_2$, and NH_2) linkers, showing a solubility trend as BDC-$(COOH)_2$ ~ BDC-F_4 > BDC-$(OH)_2$ > BDC-NH_2, which is consistent with the repoted relative solubilities of BDC linkers in water[128]. Correspondingly, the mass gain after 3-round overgrowth with the four linkers follows a roughly similar trend: BDC-$(COOH)_2$ (79 wt %)^a > BDC-F_4 (60 wt %)^c ~ BDC-$(OH)_2$ (61 wt %)^a >BDC-NH_2 (54 wt %)^b > BDC (~ 0 wt %)^a. (^{a}Result obtained from one trial. ^{b}Result obtained based on average of two trials. ^{c}Result obtained based on average of three trials.) 96

Figure 2.37 Time-dependent DB 86-uptake profiles for our UiO-66@HM|$_{3rd}$-UiO-66-F_4 and a reported mesoporous H-UiO-66(Zr) sample made with metal-organic assembly template by Huang et al.[20] Data for the latter materials were digitized by us from the published work. While not directly comparable (our dye-uptake experiments were carried out with 1 mg of MOF and 1 mL of a 500 µM dye solution while that by Huang et al.[20] was carried out with 10 mg of MOF and 20 mL of a 640 µM dye solution), the kinetic profiles of the two materials are quite similar. 97

Figure 2.38 a) Conversion vs. time profiles of the sulfide oxidation catalyzed by (recycled) UiO-66@HM|$_{3rd}$-UiO-66-F_4. The error bars of the 1st round of catalysis were obtained from the average of three trials. The error bars of the 2nd round was obtained from the average of two trials. There is no error bar for the 3rd round due to the experimental design, where only one vial remained. These catalysis data were generated using the same batch of UiO-66@HM|$_{3rd}$-UiO-66-F_4 catalyst that was used for Figure 2.7 in Section 2.10 but was subsequently stored at rt on the benchtop for more than 1 year. b) PXRD profiles of simulated UiO-66 (red), UiO-66@HM|3_{rd}-UiO-66-F_4 catalyst after a long storage period (> 1 yr) and before the catalysis (black); and after 1 cycle (blue), 2 cycles (green), and 3 cycles (burgundy) of catalysis. 99

Figure 2.39 TEM images of UiO-66@HM|3_{rd}-UiO-66-F_4 catalyst after a long storage period (>1 yr) and before the catalysis (top row); and after 1 cycle (2nd row), 2 cycles (3rd row), and 3 cycles (bottom row) of the catalysis. 100

Figure 3.1 a) PXRD profiles of the 2D **cpp** UiO-66|$_{Plu}$ with the 2θ labelled. The inset table lists the d spacing calculated from the experimental 2θ, ideal **fcu** UiO-66 (orange text) and the derived tetragonal 2D **cpp** UiO-66 structure (blue text) with the (*hkl*) plane as subscript. b) Structures of **fcu** UiO-66 and 2D **cpp** UiO-66 viewing from the <010> and <001> direction (unit cells are circled in dashed squares in the images on the bottom). c) A proposed interaction manner between the Pluronic polymers and the 2D-UiO-66-F_4 structure during its growth. 106

Figure 3.2 a) PXRD profiles of simulated **fcu** UiO-66 (black), products resulted from 2D **cpp** UiO-66-F_4 synthesis with a AcOH : BDC-F_4 ratio of 44.4 (grey), 88.9 (light green), 177.8 (green), and 355.2 (dark green), and the simulated 2D **cpp** UiO-66-F_4 (blue). b) SEM images of the product synthesized with a AcOH : BDC-F_4 ratio of 355.2. c) A cartoon showing the proposed 4-coordinate Zr_6 cluster formed with acetic acid modulators. 109

Figure 3.3 a) TEM of a ground 2D **cpp** UiO-66-F_4|$_{AcOH}$ material. b) HRTEM of the area in red box circled in panel a, showing clear crystalline fringes. c) The electron diffraction pattern collected from the corresponding area in panel b. 111

Figure 3.4 a) A PEEK membrane that allows for a slow diffusion of the BDC-F_4 linker to the other side with Zr precurors, which enables the growth of the 2D **cpp** UiO-66-F_4 on the Zr-side surface of the membrane. b) A SEM image (top view) of the Zr-side surface of the 2D **cpp** UiO-66-$F_4|_{Mem}$ product. c) PXRD profiles of simulated **fcu** UiO-66 structure (black), simulated 2D **cpp** UiO-66 structure (cyan), and the 2D **cpp** UiO-66-$F_4|_{Mem}$ (purple). 113

Figure 3.5 Four possible 2D networks could be formed by BDC-F_4 linkers and Zr clusters (Zr_6 or Zr_{12}). 119

Figure 3.6 Top: The 4-$c_{(1)}$ Zr_6 clusters and its equivalent reticular building block (top). Bottom: A matching between the **cpp** topology[154] and the 2D structure formed by the 4-$c_{(1)}$ Zr_6 clusters (unit cells are circed by black dash lines). 120

Figure 3.7 a) A 3D-model cartoon showing the two-conpartment cell setup with the PEEK microfiltration membrane clampped in between. The solution components for the 2D **cpp** UiO-66-$F_4|_{Mem}$ synthesis on each side was noted with the arrow. b) The photograph of the two conpartment cell with PEEK membrane, rubber cap, and the joint clamp (the setup was vertical for the ease of taking photo and it was put horizontally flat in a container inside the oven during the reaction (beaker or petri dish)). The upper chamber was filled with water and the bottom chamber was empty (air). The PEEK membrane was clamped in between, which hold the water well overnight without obvious permeation. 124

Figure 3.8 NMR (^1H and ^{19}F) calibration curves for AcOH (left), and BDC-F_4 (right) against the internal standards (MA for ^1H; TFA for ^{19}F). 127

Figure 3.9 ^1H NMR spectrum of the digested 2D **cpp** UiO-66-$F_4|_{Plu}$ (bottom) and 2D **cpp** UiO-66-$F_4|_{AcOH}$ (top) with MA as the internal standard. 127

Figure 3.10 ^{19}F NMR spectrum of the digested digested 2D **cpp** UiO-66-$F_4|_{Plu}$ (bottom)and 2D **cpp** UiO-66-$F_4|_{AcOH}$ (top) with TFA as the internal standard. 128

Figure 3.11 a) PXRD profiles of simulated **fcu** UiO-66 structure (black), simulated 2D **cpp** UiO-66 structure (cyan), UiO-66-F_4 synthesized without Pluronic F-127 (grey), the unknown material reported in chapter 2 (blue), and the 2D **cpp** UiO-66-$F_4|_{Plu}$ (green). b) Zr_6 clusters with three coordination modes that can from 2D networks, along with a table listing the (010) diffraction signals resulted from the possible 2D networks. [a]The diffraction signals of (010) planes resulted from 2D networks constructed by the corresponding Zr_6 clusters (4-$c_{(1)}$, 4-$c_{(2)}$, or 6-c), which were calculated based on Cu K_α source (wavelength 1.5406 Å). 130

Figure 3.12 SEM images (left) and TEM images (middle and right) of the 2D **cpp** UiO-66-$F_4|_{Plu}$ particles and with a "coffee bean" morphology. 130

Figure 3.13 a) PXRD profiles of the simulated **hns** UiO-66 (red), **hns** UiO-66 (violet), and 2D **cpp** UiO-66-$F_4|_{Plu}$ (black). The first two were plotted on raw data requested from Firth et al., which were reported previously.[145] b) Left: A polygon demonstration of the 12-coordinate Zr_{12} cluster (top) and the corresponding hns network formed using it as building blocks; Right: Crystalline structure of the hns-UiO-66 viewing from <100> (top) or <001> (bottom). 131

Figure 3.14 a) PXRD profiles of five 2D **cpp** UiO-66-$F_4|_{Plu}$ materials synthesized in a series (on the same day) with different Pluronic: L-31 (black), P-123 (blue), F-68 (green), F-108 (purple), and F-127 (orange). b) Plot of relative PXRD peak integration ratio between 2D **cpp** UiO-66-$F_4|_{Plu}$ (~6.05º 2θ, 100) and **fcu** UiO-66 (~7.30º 2θ, (111)) and the PPO molar mass % in the Pluronic during the synthesis of the 2D **cpp** UiO-66-$F_4|_{Plu}$ material. It shows a positive trend between the PPO molar mass% in the Pluronic and the relative 2D **cpp** UiO-F_4 diffraction intensity, which implies that the hydrophobic chain proportion of the Pluronic facilitates the formation of this 2D-UiO-66-F_4 material during the synthesis. 131

Figure 3.15 SEM images of the products resulted from the 2D **cpp** UiO-66-$F_4|_{AcOH}$ syntheses with different amout of AcOH modulators (see Section 3.8.3 for the detailed protocol). The ratio of BDC-F_4 to AcOH was gradually increased from top to bottom: 1:44.4 (a, b), 1:88.9 (c, d), 1:177.8 (e, f), and 1:355.2 (g, h). A gradual transformation on the particle morphology from cubes to rods with stacking layers was observed, which is consistent with the gradual formtion of the 2D **cpp** UiO-66-F_4 material as the amount of AcOH increases. 132

Figure 3.16 PXRD patterns of the 2D **cpp** UiO-66-$F_4|_{AcOH}$ as-synthesized (green) and ground in mortar for 1 min (blue). 133

Figure 3.17 $Zr_{(6\ or\ 12)}$ clusters with specific coordination mode (top), the corresponding structure viewing from <001> direction (middle), and the simulated SAED pattern under a <001> zone axis. 133

Figure 3.18 Simulated structures without distortion (left), with a tilt angle at ~11˚ (middle) and at 28.2˚ (right). The structure with a 10.8˚ distortion matches gives a lattice parameter with that of our as-synthesized material, while the one with a 28.2˚ distortion alignes well with that of the 150 ˚C activated sample. 134

Figure 3.19. From bottom to top: PXRD patterns of simulated 2D **cpp** UiO-66-F_4 structure without distortion, simulated 2D **cpp** UiO-66-F_4 structure with 10.8˚ distortion , as-synthesized 2D **cpp** UiO-66-$F_4|_{AcOH}$, 2D **cpp** UiO-66-$F_4|_{AcOH}$ samples that were activated at 120 °C and 150 °C, and simulated 2D **cpp** UiO-66-F_4 structure with 28.2˚ distortion. 134

Figure 3.20 SEM images of the product collected from the Zr-side solution in the 2D **cpp** UiO-66-$F_4|_{Mem}$ synthesis. 135

Figure 3.21 Left: Cross-section SEM images of the 2D-UiO-66-$F_4|_{mem}$ membrane with the BDC-F_4 side facing up and the Zr side facing down. Right: A zoom-in SEM image corresponding to the area circled in white dash box in the left panel. 135

Figure 3.22 PXRD profiles of simulated **fcu** UiO-66 (grey), simulated 2D **cpp** UiO-66 (green), powder product collected from Zr side supernatant after the synthesis of 2D **cpp** UiO-66-$F_4|_{Mem}$ (blue), and a strip sample cut from the 2D **cpp** UiO-66-$F_4|_{Mem}$ (violet). A slight shifting toward high-angle region observed for the 2D **cpp** UiO-66-$F_4|_{Mem}$ strip sample could be resulted from the particle activation after MeOH soaking and overnight drying in an 80 ˚C oven. Please see the Section 3.5 for discussions on how activation could affect the lattice parameter and diffraction profile of the materials. 136

Figure 3.23 a) PXRD profiles collected from a diffractometer (Cu K_α, 1.5406 Å) with the 2D **cpp** UiO-66-$F_4|_{Mem}$ material piece and the crust powder on its surface: the diffraction pattern acquired on an area without crust (black), with obvious crust (blue), and the crust powder scraped from the membrane surface (orange). The green shaded area is corresponding to the 1st prominent diffraction signal (010) from the 2D **cpp** UiO-66-F_4 material, while the organe shaded area highlights the 1st prominent diffraction from the **fcu** UiO-66-F_4 material. b, c) Photographs obtained under an optical microscope in the diffractometer on the corresponding exposure area with and without the crust for the data collection in panel a) (the approximate exposure areas in the experiment are highlighted in semi-transparent squares). 136

Figure 4.1 a) Scheme showing the electro-assisted sorption process by using a P^V-selective-sorbent porous membrane. b) A scheme showing the UiO-66|PEEK membrane design allowing water to flow across where P^V can be selectively adsorbed by UiO-66. 140

Figure 4.2 a) Schematic of the iterative, seed-mediated growth of UiO-66 nanocrystals inside a porous PEEK membrane. The PEEK membrane is first soaked in a solution of preformed [$Zr_6(\mu^3\text{-}O)_4(\mu^3\text{-}OH)_4(OAc)_{12}$] clusters,[207] and then immersed in a UiO-66 precursor solution (containing BzOH modulator, BDC linker, and $ZrCl_4$) at 120 °C. b-d) SEM images of the surface portions (as denoted by the box in the insets) of the cross-sections of a UiO-66|PEEK membrane that has been subjected to two cycles of growth. The white arrows indicate the areas that correspond to the surface layer/crust. e-g) SEM images of the inner-membrane portions (as denoted by the box in the insets) of the cross-sections of a UiO-66|PEEK membrane that has been subjected to two cycles of growth. h) PXRD pattern of a typical UiO-66|PEEK membrane after one cycle of growth (green trace) in comparison to that of the amorphous PEEK background (black trace), and that for the simulated defect-free UiO-66 (gray bars). i) A plot of the MOF loadings for another UiO-66|PEEK membrane after three successive growth cycles. The line is included only as a visual guide. 142

Figure 4.3 The removal rate (in %) of different anions ($P^V/Cl^-/NO_3^-/SO_4^{2-}$) in UiO-66|PEEK membranes from (a) a solution containing P^V (0.01 mM) + Cl^- (2.4 mM) and (b) a solution containing P^V (0.01 mM) + Cl^- (2.4 mM) + NO_3^- (0.2 mM) and SO_4^{2-} (0.1 mM). The selectivity of P^V over different anions (α_{PV}^{X}) at different time of solution exposure (marked by the dotted line) are also shown here. Experimental condition for panel a: solution volume = 10 mL, membrane area = 1 cm^2, MOF loading = 26 wt %; experimental conditions for panel b: solution volume = 85 mL, membrane area = 9.1 cm^2, MOF loading = 35 wt %; the % removal of P^V is with respect to the P^V amount present in the initial solution; no external potential applied. The membranes were subjected to pre-wetting treatment (Section 4.9.2) before the adsorption. 144

Figure 4.4 The variation of P^V removal amount as a function of initial MOF weight (black points) and Zr intensity (as obtained from XRF measurement, blue points) in the UiO-66|PEEK membranes. The straight lines are the fitted data to the solid experimental points. See Section 4.9.3 for the XRF measurement protocol; See Section 4.9.4 for detailed protocol for the P^V removal experiments. 146

Figure 4.5 Electro-assisted adsorption kinetics of P^V in a 26wt%-UiO-66|PEEK membrane from a solution containing P^V (0.01 mM) + Cl^- (2.4 mM), where the membrane was exposed to three fresh feed solutions, each cycle continuing for 50 minutes. Experimental conditions: feed solution volume = 40 mL, receiver solution contained 40 mL water spiked with H_2SO_4, so that the initial pH became 4.2 ± 0.1, membrane area = 4.16 cm^2, external potential applied = 5 V, experimental setup is similar to that described in Figure 4.14a. The membrane was subjected to pre-wetting treatment (Section 4.9.4) before the electro-assisted adsorption. The measured $\alpha_{PV}^{Cl^-}$ at the end 1st, 2nd, and 3rd cycle was ~11, 4.2, and 3.5 respectively. 147

Figure 4.6 (a) Voltage-dependent adsorption and kinetics of P^V to UiO-66|PEEK membrane having ~16 wt % MOF loading and (b) electro-assisted adsorption kinetics of P^V to UiO-66|PEEK membranes differing in initial MOF loading (wt %, calculated with respect to the final composite weight). Two separate freshly synthesized composite membranes of comparable MOF loading (approximate 16 wt %) and thickness were used for the two different voltages in panel a. Experimental setup is as per Figure 4.14a: membrane (active surface area of membrane – 4.16 cm^2) was clamped between a two-compartment cell, with P^V feed solution (40 mL, 0.26 mM) on one side and the receiver solution (40 mL, water spiked with H_2SO_4) on the other (the initial pH was 4.3 ± 0.1). The pH and the current densities are listed in Table 4.3. The membrane was subjected to pre-wetting treatment (Section 4.9.4) before the electro-assisted adsorption. 148

Figure 4.7 pH-dependent electro-assisted (at 5 V) desorption kinetics of P^V from two UiO-66|PEEK membranes (initially started from a 16wt%-UiO-66|PEEK (for pH 10, 11, and 12) and a 15wt%-UiO-66|PEEK(for pH 12.5)). KOH solution (100 mL) of varying pH (10 – 12.5) was used for the desorption. The pre-wetted (see Section 4.9.5) membrane (active surface area – 4.16 cm^2) was exposed (without any external electric field) to 0.26 mM P^V solution (60 mL) for overnight to completely saturate with P^V and then was subjected to an electro-assisted desorption process. Experimental setup is similar to that described in Figure 4.14b. The exact pH and the current densities are in Table 4.3. 150

Figure 4.8 Sorption kinetics of P^V to/from a ZrP|PEEK (initially a 34wt%-UiO-66|PEEK) membrane when applied for three consecutive cycles of electro-assisted adsorption at 5 V for 5 h (solid symbols) and electro-assisted desorption at 5 V (pH = 12) for 3 h (empty symbols), indicating the stability/reusability of the membrane. Experimental setup is as per Figure 4.14 (membrane active surface area = 4.16 cm^2). For the electro-assisted adsorption experiment, the feed solution (40 mL) contained exclusively P^V (0.26 mM) and the receiver solution (40 mL) contained water spiked with H_2SO_4, so that the initial pH became 4.3 ± 0.1. The electro-assisted desorption was done using KOH (100 mL, pH = 12). The membrane was subjected to pre-wetting treatment (Section 4.9.4) before the 1st cycle electro-assisted adsorption. At the end of the 1st electro-assisted adsorption stage, the membrane was saturated with P^V by immersing in phosphate solution (0.26 mM, 60 mL) for overnight (without any external electric field). For the next two cycles, it was only electro-assisted adsorption for 300 min, followed by electro-assisted desorption for 150 min, i.e., there was no additional P^V saturation step involved. Here, before the onset of 1st desorption cycle, the P^V removal amount of the membrane is directly from Figure 4.4. This is based on the assumption that the P^V uptake should be the same under (i) overnight soaking (static condition) in 0.26 mM P^V and (2) electro-assisted sorption from 0.26 mM P^V for 300 min, followed by overnight soaking (static condition) in the same solution. 153

Figure 4.9 Adsorption selectivities of P^V over other anions (α_{pv}^{X}, *Eq.* 4.1), in ZrP|PEEK membranes differing in initial MOF loading. The performance of the 10 wt % membrane was an outlier than the rest possibly due to the instantaneous accessibility of the competing anions (especially Cl^- and HCO_3^-, which are abundant) to the MOF sorption sites because of low initial UiO-66 loading. For the measurement (see Section 4.9.7 for details), a UiO-66|PEEK pre-wetted membrane (~ 1 cm^2) stirred in simulated groundwater (30 mL, pH = 6.7, composition in Table 4.4) for 24 h, without any external electric field. 156

Figure 4.10 SEM images of cross sections of the UiO-66|PEEK membrane samples used in the present work (Table 4.1). Membrane thicknesses were measured using ImageJ at multiple sites spanning ~100 µm of the cross section. The scale bars in the images are 10 µm. 168

Figure 4.11 A linear relationship between the weight of UiO-66 in the membrane samples and the Zr $K_{\alpha 1}$ peak integration measured with XRF. The green line is obtained from linear regression with a zero intercept. To obtain a good correlation of Zr $K_{\alpha 1}$ signal and MOF loading amount, 17 other membranes were synthesized by the same method (in additional to the 11 membranes in Table 4.1) and used in this XRF experiment. 169

Figure 4.12 PXRD profiles of the UiO-66|PEEK membrane samples (Table 4.1, entry 1-9) prior to soaking in 0.16 mM P^V solution (Section 4.5). 169

Figure 4.13 SEM images of cross sections of four UiO-66|PEEK membrane samples (10wt%-, 16wt%-, 17wt%-, 14wt%-, and 14wt%-UiO-66|PEEK, entries 2, 3, 6, 7, and 9 in Table 4.1) before (a-e) and after (h-j) soaking in 0.16 mM P^V solution (Section 4.5). 173

Figure 4.14 Schematic of electro-assisted (a) adsorption and (b) desorption to/from UiO-66|PEEK. 175

Figure 4.15 The time-dependent current densities during electro-assisted (at 5 V) adsorption of P^V in UiO-66|PEEK membranes with different UiO-66 loading. The measured current was normalized per unit area (4.16 cm^2) of the membrane. The experimental set up is shown in Figure 4.14a. In the electro-assisted adsorption, the a 0.26 mM P^V solution (40 mL) was used as feed and deionized water spiked with H_2SO_4 (40 mL, pH = 4.3 ± 0.1) was used as receiver. 175

Figure 4.16 a) PXRD profiles of the 16wt%-UiO-66|PEEK membrane sample (Table 4.1, entry 3) before (black) and after (blue) soaking in 0.16 mM P^V solution (Section 4.5). b) PXRD profiles of simulated UiO-66 (red), the 16wt%-UiO-66|PEEK membrane after pH 12 desorption (black), and the 15wt%-UiO-66|PEEK membrane after pH 12.5 desorption (blue). 176

Figure 4.17 SEM images of cross section of 16wt%-UiO-66|PEEK (left panels) and 15wt%-UiO-66|PEEK (right panels) as-synthesized (top) and after regeneration under pH 12 or 12.5 (bottom). 176

Figure 4.18 Top view SEM images of four membranes before P^V uptake (top panel), after P^V uptake for 24 h (middle panel), and after electro-assisted desorption at pH 12 (bottom panel). From left to right, the membranes are corresponding to entry 3, 6, 7, and 9 in Table 4.1. 178

Figure 4.19 Cross-section view SEM images of four membranes samples before P^V uptake (top panel), after P^V uptake for 24 h (middle panel), and after electro-assisted desorption at pH 12 (bottom panel). 178

Figure 4.20 SEM images of cross sections of 34wt%-UiO-66|PEEK membrane samples (a) before P^V uptake and (b) after three consecutive cycles of electro-assisted adsorption and desorption. (c) The size distributions of UiO-66 particles observed inside the membrane in the cross section, before (green) and after (blue) three cycles of electro-assisted P^V adsorption and desorption. 179

Figure 4.21 a) PXRD profiles of 26wt%- and 35wt%-UiO-66|PEEK membranes before and after soaking in P^V-containing mixed anionic solutions (Section 4.5). The 26wt%-UiO-66|PEEK membrane was soaked in a solution of P^V (0.01 mM) and Cl^- (2.4 mM), while the 35wt%-UiO-66|PEEK membrane was soaked in a solution of P^V (0.01 mM), Cl^- (2.4 mM), NO_3^- (0.2 mM), and SO_4^{2-} (0.1 mM). b) PXRD profiles of membrane strips cut from a 27wt%-UiO-66|PEEK that was subjected to P^V (0.01 mM) and Cl^- (2.4 mM) mixture solution over time (0, 2, 4, 12, and 24 h). 182

Figure 4.22 SEM images of cross sections of 26wt%- and 35wt%-UiO-66|PEEK membranes before (a-d) and after (e-h) soaking in P^V-containing mixed anionic solutions (Section 4.4). The 26wt%-UiO-66|PEEK membrane was soaked in a solution of P^V (0.01 mM) and Cl^- (2.4 mM), while the 35wt%-UiO-66|PEEK membrane was soaked in a solution of P^V (0.01 mM), Cl^- (2.4 mM), NO_3^- (0.2 mM), and SO_4^{2-} (0.1 mM). The scale bars in the images are 2 μm. 182

Figure 4.23 The zeta potential of a 12wt%-UiO-66|PEEK membrane and an unmodified PEEK membrane in 1 mM KCl as a function of solution pH. The errors on zeta potential data are directly obtained from the analyzing instrument. 183

Figure 4.24 (a) PXRD profiles and (b) SEM images of UiO-66 powder materials obtained from the supernatant of four UiO-66|PEEK membrane syntheses. 184

Figure 4.25 PXRD profiles of simulated UiO-66, UiO-66 powder after soaking in P^V solution, and 16wt%-UiO-66|PEEK membrane sample after soaking in P^V (see Section 4.9.4 for experimental details). In both soaking experiments, the P^V dosage was similar (0.16 mM, P^V/Zr_6 node ratio ~25, and soaking time 24 h). The loss in crystallinity after P^V soaking was greater for UiO-66|PEEK. As the loss in crystallinity is due to reactions between Zr component of UiO-66 and P^V species in the solution, the UiO-66 in powder form was less accessible to P^V species than UiO-66 supported on/inside the PEEK membrane. 185

Figure 4.26 PXRD profiles of UiO-66 powder material before soaking and after soaking: ZrP-1 (solid from soaking experiment #1), UiO-66-leftover (solid from soaking experiment #2), and ZrP-2 (solid from soaking experiment #3). For soaking experiments #1 and #3, there was no obvious diffraction peak in the PXRD profile, indicating that the products ZrP-1 and ZrP-2 were amorphous. For the solid obtained from soaking experiment #2, UiO-66 diffraction signals with peak broadening were observed, indicating a decrease in crystalline domain size, indicating partial corrosion of the UiO-66 crystals, and thus the solid was labeled as UiO-66-leftover. 187

Figure 4.27 The ^{1}H NMR spectra of digested ZrP-1 (blue), UiO-66-leftover (green), and ZrP-2 (red). The products ZrP-1 and ZrP-2 retain almost none of the BDC linkers from the UiO-66 precursor. The presence of some leftover BDC linker in UiO-66-leftover is consistent with the remaining UiO-66 diffraction peaks in Figure 4.26. The shift of the MA signal (6.0-6.5 ppm) is due to the addition of Cs_2CO_3 during the digestion of ZrP solids (see Section 4.9.3 for the digestion protocols). 188

Figure 4.28 The ^{1}H NMR spectra of digested as-synthesized UiO-66 sample (blue) and UiO-66|HCO_3^- sample (red). After the HCO_3^- soaking experiment, BzOH and BDC signals were not observed for UiO-66|HCO_3^-, indicating that these organic species were removed during soaking in the HCO_3^- solution. 189

Figure 5.1 a) A proposed HM-UiO-66-incorporated PEEK polymer membrane material. b) A hierarchical porous structure having micro-, meso-, and macropores. 193

Figure 5.2 Three potential Zr-based MOFs that can be used in the template-assisted strategy or grown into PEEK porous membrane to form hierarchically porous materials. 194

Figure A.1 Cross-section SEM images of the PEEK membrane product resulted from the synthesis described above. MOF-808 particles with a octahedral morphology were observed on the PEEK membrane surface (left panel), while there were few particles seen inside the PEEK membrane. This could be resulted from the large particle size of MOF-808 (~1 μm) resulted from the current condition, which was much larger than the PEEK pore size (~100 – 500 nm). In order to grow MOF-808 uniformly inside the PEEK membrane, the growth condition needs to be carefully tunned. For example, modulator/linker ratio could be decreased or the growth temperature could be elavated (<1 h) to accelerate the nucleation rate, which should give MOF-808 particles with smaller sizes. 196

LIST OF SCHEMES

Scheme 2.1 Syntheses of a HM UiO-66-X shell on a UiO-66 core and the resulted potential enhancement in performances in uptake and catalysis. 36

Scheme 2.2 Template-assisted overgrowth of a mesoporous UiO-66-X shell on a UiO-66 core. 38

Scheme 3.1 A coordination hindrance on the Zr_6 clusters could result in a lower coordination number, favoring the growth of a 2D MOF network. 102

Scheme 3.2 Three possible coordination modes of the Zr_6 cluster that can form 2D networks and the 2D structure (**1**) formed by the tetragonal, 4-coordination cluster. 104

Chapter 1

Introduction to the designs & applications of hierarchically porous UiO-66 materials

1.1 MOFs as a new class of porous materials and the importance of hierarchical porosity in MOFs

Porous materials are of great scientific and industrial interests because they have much higher specific surface area (total surface area per unit of mass or volume) than non-porous materials. This allows guest species (molecules, atoms, or ions) smaller than the pore size to diffuse through the matrix and interact with the pore surfaces efficiently throughout the entire materials, which is especially useful in adsorption, catalysis, and energy storage. Currently, a lot of these materials are broadly used, from household daily usage (e.g., cellulose sponge and activated charcoal) to industrial production (e.g., zeolites and mesoporous silica) (Figure 1.1). Distinct from these are metal organic frameworks (MOFs), porous crystalline materials composed of inorganic metal nodes and organic linkers with a long-range order. While the [organic linker + metal] composition endow them with chemical functionalities from both building blocks, their crystalline nature allows for a structural design at the molecular level by the choice of the two and how they are connected. These characteristics attract great attention to MOFs as potential next-generation porous materials since their discovery at the late 90's.[1-3] Up to now, more than 90,000 MOFs have been synthesized, many of which have been demonstrated as promising candidates in adsorption,[4] separation,[5] catalysis,[6, 7] and photovoltaics[8].

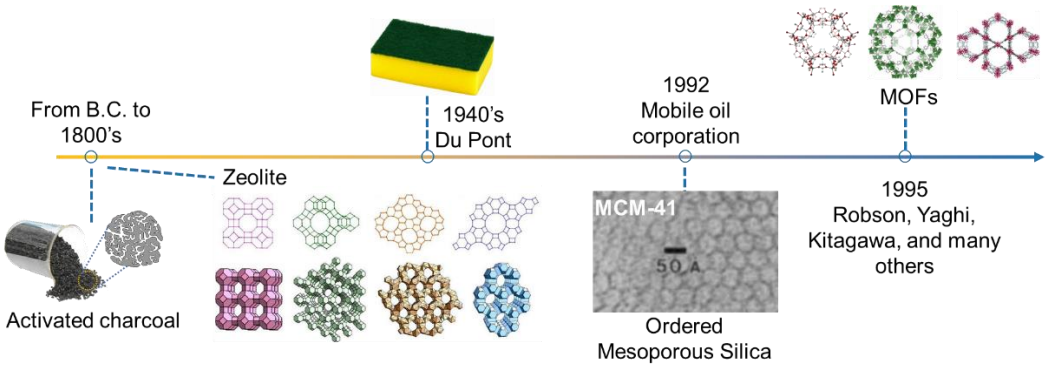

Figure 1.1 A brief timeline listing several porous materials with their discovery times.

According to the IUPAC, the pore in porous materials can be classified into three categories: micropore (< 2nm), mesopore (2 to 50 nm), and macropore (> 50 nm).[9] Stemming from the sub nanometer sizes of the building blocks (metal nodes and organic linkers), the pore sizes of the majority of MOFs are in the micropore range (< 2 nm).[10] While small pore size could lead to high specific surface area (per volume), it also lowers the efficiency of molecular transport inside the porous structure and restrict the entrance of guest species that are larger than the aperture/window size. Both could greatly limit their applications in adsorption and catalysis (Figure 1.2).[11-13] Thus, designing MOF-based materials with both small (micro-) and large (meso-/macro-) pores (i.e., hierarchically porous structures) can overcome these limitations and thus enhance performances (Figure 1.2).

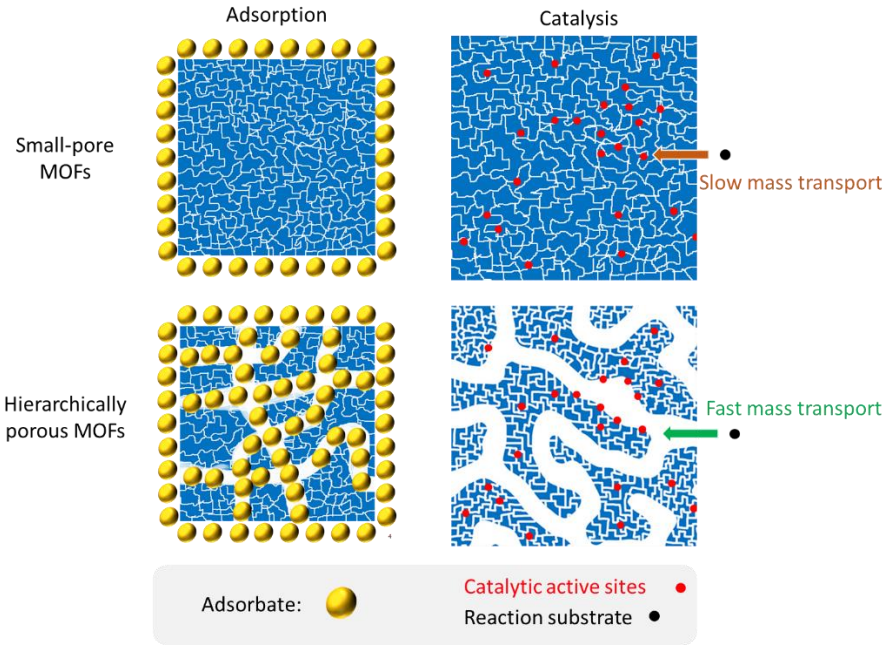

Figure 1.2 A diagram showing the differences between the hierarchially porous materials (bottom) and the small-pore-only porous materials (top) in adsorption (left) and catalytic (right) applications.

1.2 The microporous UiO-66 MOF

In the massive library of currently available MOF materials, Zr-based MOFs are a subclass of materials comprised Zr^{IV}-based cluster nodes and organic linkers, mostly Zr^{IV} carboxylates. Derived from the strong affinity between the Zr^{IV} clusters and carboxylate O atoms, these materials have outstanding thermal and chemical stabilities, which enable them to be used in many industrial and environmental applications.[14] As one of the most stable Zr-based MOF materials, UiO-66 (UiO stands for the University of Oslo) is composed of $Zr_6(\mu_3\text{-}O)_4(\mu_3\text{-}OH)_4$ clusters, each coordinated with 12 terephthalic acid (BDC) linkers (chemical formula: $Zr_6(\mu_3\text{-}O)_4(\mu_3\text{-}OH)_4(C_6H_4(COO)_2)_6$, Figure 1.3).[15] Such a high coordination number on the Zr_6 clusters not only gives the MOF its great stability, but also allows for the presence of structural defects (missing linkers/clusters), which engenders stable materials with highly active (open coordination) sites on the Zr_6 clusters.[14, 16]

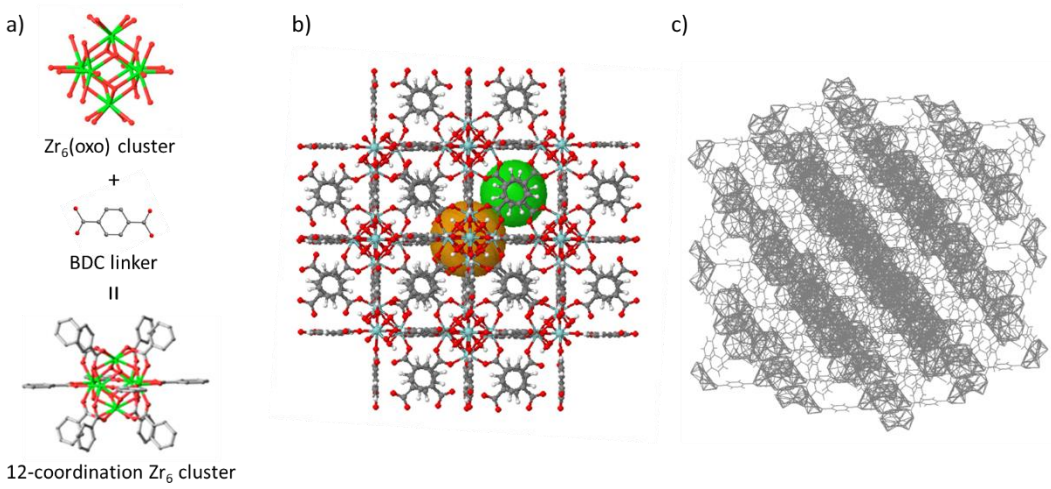

Figure 1.3 a) Building blocks of UiO-66 MOF (Zr_6(oxo) cluster and the BDC linker), leading to a 12-coordinate mode of the Zr_6 cluster in the "ideal" UiO-66 structure. b) The UiO-66 crystal structure viewed from the <001> direction with two type of pores shown in spheres (octahedral pore with ~11 Å diameter (orange) and tetrahedral pore with a ~9 Å diameter (green)).[17] c) A UiO-66 porous mattrix viewed in a wareframe model, showing its 3D structure and porosity.

The Nguyen group had previously synthesized UiO-66 materials with increasing number of missing-linker sites (as active open sites for sorption & catalysis) and thus enhanced their performances in arsenate capture[18] and catalytic sulfide oxidation reactions.[19] However, it was observed that the accessibility of the active open sites for arsenate removal was limited by the small aperture (~6 Å) of the UiO-66 MOF, which could be partially mitigated by using an analogue UiO-67 possessing a longer linker (biphenyl-4,4'-dicarboxylate) and thus a slightly larger aperture (~11.5 Å).[18] However, in sulfide oxidation, when the number of active open sites was elevated by ~5× in the catalytic sulfide oxidation, only ~2× increment on the reaction rate was observed.[19] This was proposed to result from the lack of substrate accessibility to active sites (around the Zr_6 clusters) inside the MOF crystals, given the small UiO-66 apertures. Sorption applications using UiO-66 materials are also greatly restricted when the sorbates are much larger than the intrinsic pore sizes (i.e. > 9 Å).[20, 21] Motivated by these previous studies, this thesis focuses on developing strategies to incorporate mesopores into UiO-66 materials and corroborate the performance enhancement that can be brought about by the resulting hierarchically meso-/microporous structures. In addition, it also explores the possibility of combining UiO-66 materials with macroporous membranes to make materials with macro-/microporosity.

1.3 Self-assembled polymer templates to introduce mesopores into UiO-66 materials

There are three generally routes to build MOFs with two different types of pores of different dimensions (commonly [micropore + mesopore] or [micropore + macropore]): 1) *de novo* construct of structures with large pores by elongating the organic linkers,[10] 2) introduce labile linkers during the synthesis and create large defect/voids by post-synthesis deletion,[22] and 3) add removable templates during the synthesis to template the formation of pores with particular sizes

through self-assembly and remove them by post-synthesis workup (washing/etching away the templates)[23]. While this thesis focuses on the third route, the application of first two strategies on UiO MOFs are also briefly reviewed in this section.

Many of the organic linkers in a class of MOF can be systematically elongated by adding additional rigid groups, such as alkyl or phenyl, to engender MOF products with similar structures but with successively larger pores.[24] A classic example of this strategy was shown by Eddaoudi et al. for IRMOFs, which are composed of $[Zn_4O]^{6+}$ clusters and BDC-type linkers. They have demonstrated that the aperture sizes of IRMOFs can be systematically tuned from 3.8 to 19.1 Å by chemically lengthening the rigid linkers between clusters (for example, by increasing the number of phenyl rings of the linker).[25] Using the same linker extension strategy, aperture sizes of the UiO family materials can also be enlarged from 6 Å to 8 and 10 Å by using linkers with two or three phenyl rings (resulting in UiO-67 and UiO-68, respectively).[15] However, interpenetrated network (UiO-69)[26] formed when the linker length was further increased to ~19 Å (with four phenyl rings in a line in one linker). To form this UiO-69 material without interpenetration, *de novo* synthesis was not successful; rather a post-synthesis route starting from UiO-68 must be used, where the short linkers are slowly and stepwisely replaced by slightly longer ones to gradually extend the pore width.[27]

Without changing the length of the BDC linker, a large fraction of the building blocks in UiO-66 crystals can be removed by defect engineering to create mesopores.[22] Bueken et al. have found that UiO-66 synthesized with mixture of BDC and 2-aminoterephthalic acid (BDC-NH_2) linkers tend to form nanosized domain comprising only one type of linker. Taking advantage of the weaker bonding between BDC-NH_2 and Zr_6 cluster comparing to that of BDC, nanosized voids can be generated by appropriate heating treatment.[28, 29] Ozone-cleavable linkers are also used in

the synthesis of UiO-67, followed by ozone treatments to introduce mesopores (2-5 nm) into the final structure.[30]

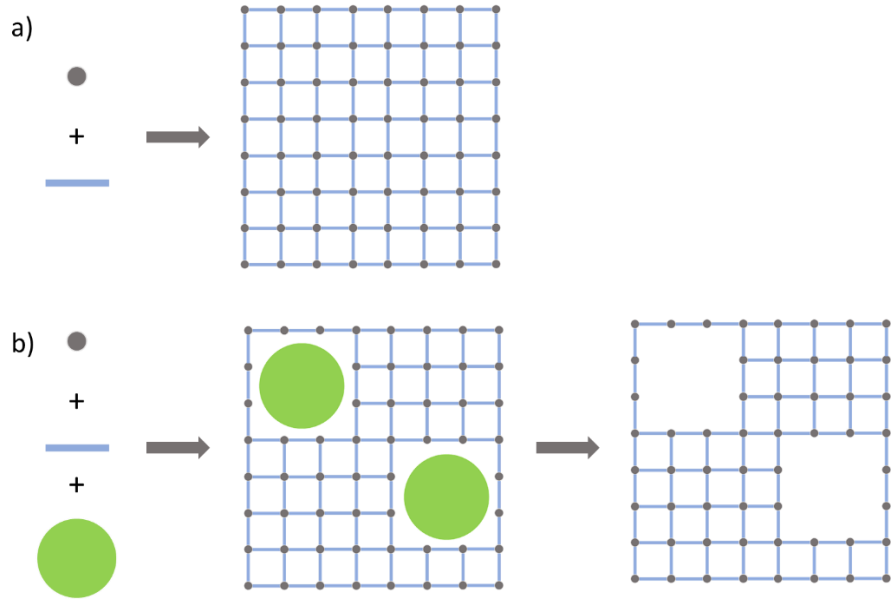

Figure 1.4 a) Regular assembly/synthesis of MOF materials from metal nodes (grey circles) and organic linkers (blue rods). b) Template-assisted strategy to generate large voids in MOF materials by introducing removable templates (green circles) during the synthesis and washing them away post-synthesis.

Not surprisingly, the aforementioned two strategies require careful design and selection of linkers (either elongated linker in the 1st case or labile linker in the 2nd case) to introduce large pores into MOF materials. Nevertheless, the pore sizes in the materials synthesized by both methods are still limited (< 5 nm). To incorporate large mesopores into UiO-66 materials without changing the chemical structure of linkers, removable templates have been added during the synthesis and engender pores with the corresponding sizes by post-synthesis workup (washing/etching away the templates) (Figure 1.4).[23] This template-assisted strategy has been applied to synthesize other porous materials, such as the MCM-41 mesoporous silica at early 90s.[31] In 2008, Qiu et al implemented the same strategy in the synthesis of HKUST-1 MOF (comprising dimeric Cu clusters and trimesic acid linkers) and introduced 30 nm mesopore into the materials.[32]

In UiO-66 materials, metal clusters[20] and long-chain fatty acids[21] have been used to template mesopores up to 30 nm. With these initial studies implying the great potential of this template-assisted strategy in introducing mesopores into UiO-66 MOFs, we focused on synthesizing hierarchically mesoporous UiO-66 materials with controllable mesoscale porosity by using a class of block-copolymer as templates as described in chapter 2 and 3 of this thesis; we also studied how the polymer template interacts with UiO-66 building blocks to afford the hierarchical meso/microporous structure of the final materials.

1.4 Macroporous polymer membranes as host for microporous UiO-66 materials in water purification

Given their great excellent chemical stability, UiO MOF materials have attracted much attention in environmental applications, especially in water purifications.[33] Their micropores and node chemistry allows for the high-capacity adsorption of environmental contaminants such as phosphate,[34, 35] arsenate,[18, 36], selenium,[37] uranium,[38] and mercury.[39] However, macropores must be closely integrated into the MOF for efficient water infiltration and mass transport.[40, 41] Although the aforementioned template-assisted strategy can efficiently introduce mesopores (2-50 nm) into UiO-66, a bottom-up synthesis of large UiO-66 crystal with such integrated macropores is still very challenging. Thus, growing UiO-66 particles onto/inside a macroporous material (substrate) is a simpler strategy for achieving this desirable [micropore + macropore] combination. By doing so, and taking advantage of the macroscopic nature of the substrate (e.g., a monolith or a membrane), the regeneration/recycling of the UiO-66 will be much easier than that for the powder form where centrifugation or filtration is needed to recover the materials after usage. As an example, Liu et al. have grown a UiO-66 layer on the outer surface of a hollow alumina fiber and

used the resulting composite in water desalination where the structure and morphology of the membrane remained unchanged after the test.[42] Under the same vein, UiO-66 materials have been grown on top of porous cellulose,[43] polyethersulfone,[37] and polysulfone[44] membranes and used for efficient salt rejection[44] or decontamination.[37] Based on these previous works, we further envision a UiO-66-in-membrane material with UiO-66 particles uniformly distributed inside the porous structure, which thus results in hierarchically macro- and micro-porous hybrid materials. This should allow for efficient water flow around each microporous UiO-66 particle when used as adsorbents for contaminants in water, greatly increasing the overall kinetics adsorption capacity. Thus, in chapter 4 of this thesis, we explored the possibility of uniformly embedding a high loading of UiO-66 particles into commercially available macroporous, water-filtration membranes and utilizing the resulting composite for phosphate removal from groundwater.

1.5 Thesis overview

The works in this thesis focus on the design of hierarchically porous UiO-66 MOF materials and explore their applications in catalysis and water purifications. As decribed thus far, chapter 2 reported a seed-mediated, template-assisted synthesis that can be used to iteratively grow hierarchically mesoporous (HM) UiO-66 materials in water (Figure 1.5). By this method, HM-UiO-66 shell materials can be iteratively grown on top of UiO-66 nanoparticle seeds, where the proportion of mesopores can be tuned by the number of growth cycles. When being used in the removal of a large anionic dye from water, our thrice-grown (i.e., after three growth cycles) HM material exhibited ~320% enhancement in per-mass uptake capacity than the corresponding micropore-only UiO-66 materials. Similar enhancements were also observed in a catalytic sulfide oxidation reaction by using the HM-UiO-66 materials. Interestingly, the growth of HM-UiO-66

materials was induced by pre-synthesized UiO-66 nanoparticles as seeds (light-green cube in Figure 1.5), without which an unknown phase with low porosity can be obtained; prompted us to further study how the block copolymer affects the UiO-66 growth process (chapter 3).

Figure 1.5 A HM-UiO-66 material synthetic strategy using UiO-66 nanoparticles as seeds and block copolymer micelles as templates, which resulted in materials with enhanced performances in adsorption and catalysis.

In chapter 3, we resolved the structure of the unknown phase observed in chapter 2 and studyied its formation mechanism. It was determined that this phase is a 2D **cpp** UiO-66 structure with 4-linker-coordination Zr_6 clusters rather than the 12-linker-coordination version in UiO-66. The formation of this phase could be resulted from a hindrance on linker-node coordination brought about by "polymer barricades" near the clusters during the growth (Figure 1.6). Such a coordination-hindrance hypothesis was further supported by the observation that the same 2D structure also formed in the presence of an excess amount of acetic acid modulators, which compete against linker binding, or with a deficiency of linker in the synthetic media. Either of these two conditions would restrict coordination of the linker to the node to form UiO-66. The studies in this chapter not only suggest a strong affinity between the polymer template and the UiO-66 components that could prevent MOF formation in all three dimensions, but also highlight

the importance of seeding in the template-assisted strategy described in chapter 2, where the 3D MOF is the desired product.

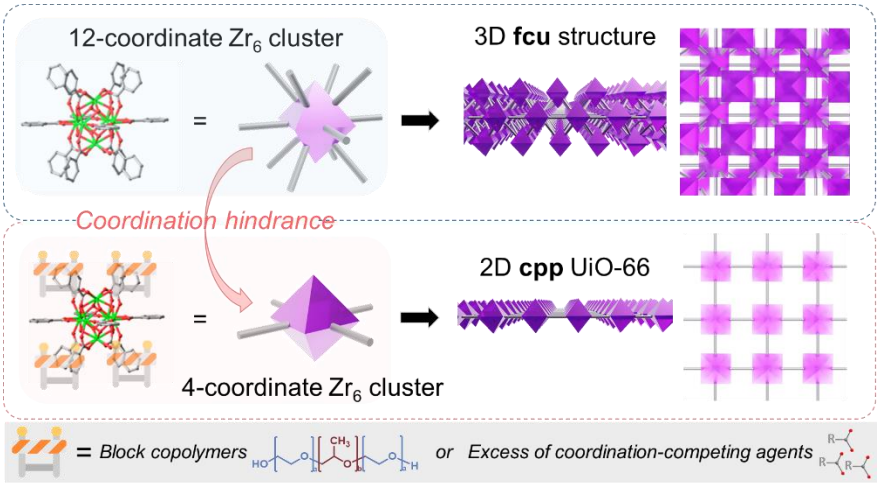

Figure 1.6 A coordination-hindrance-induced formation of a 2D **cpp** UiO-66 structure, where the hindrance could be resulted from the block copolymers (as templates in chapter 2) and an excess amount of coordination-competing agents.

In chapter 4, we reported a strategy for uniformly growing a high density of UiO-66 nanoparticle adsorbents into a macroporous polymer membrane (polyether ether ketone, PEEK; Figure 1.7), where the UiO-66 loading can be tuned by iterative growth cycles. The UiO-66-embeded macroporous membranes was shown to be highly efficient and selective in removing phosphate contaminants from water even in the presence of excess amounts of other anions. We further implemented a unique electro-assisted technique where ion transport can be accelerated by a small (5 V) external electric field to further enhance both the adsorption and desorption kinetics. The chemical transformation of UiO-66 materials into a more-stable zirconium-phosphate phase under high-dosage phosphate exposure was also explored, suggesting a possibility of using UiO-66 as precursor to engender stable Zr-based composite materials for practical groundwater treatments.

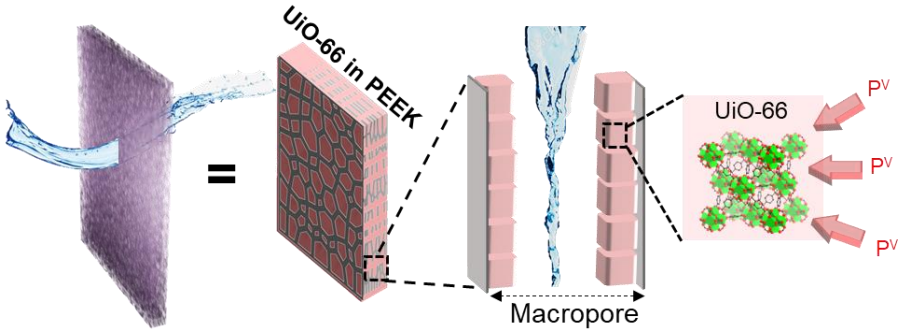

Figure 1.7 A UiO-66-embeded PEEK macroporous membrane where the macropores allow for fast water transport and UiO-66 particles act as phosphate adsorbents.

In chapter 5, we summarized the designs and outcomes of our strategies for generating the hierarchically porous UiO-66 materials described in this thesis. In addition, we provide an outlook for the possibility of extending these strategies onto other MOF materials and how future generations of hierarchically porous MOF composite materials can be designed.

Chapter 2

Template-assisted, seed-mediated synthesis of hierarchically mesoporous core-shell UiO-66: enhancing adsorption capacity and catalytic activity through iterative growth

Portions of this chapter appeared in the following manuscript: Zhang, F.; Hu, X.; Eric, W. R.; Kim, Yonghwi; Nguyen, S. T., *Chem. Mater.* **2020**, *32*, 4292-4302.

This chapter is dedicated to the memory of Professor Chia-Kuang (Frank) Tsung, whose works on core-shell MOF materials partially inspire the ideas in this chapter.

2.1 Introduction

As discussed in chapter 1, utilizing the interaction between polymer micelles with the surface of Zr-based MOFs can lead to the formation of MOF materials with hierarchically mesoporous (HM) structures, resulted from the templating effects from the micelles. In this chapter, we described a template-assisted, seed-mediated strategy for synthesizing such a hierarchically porous UiO-66 materials and demonstrate its advantages in adsorption and catalysis applications (Scheme 2.1). First, we demonstrated that a HM-UiO-66-F_4 shell with ~8 nm mesopores can be iteratively grown on top of UiO-66 nanoparticle (NP) seeds over several cycles templated by Pluronic F-127 micelles. Second, the UiO-66 NP seeds serve an important role in directing the continuous growth of the HM-UiO-66-F_4 shell, as only a non-porous phase was obtained in their absence. Third, this method can be extended to produce other UiO-66-X (X = $(OH)_2$, $(COOH)_2$, etc.) shells, demonstrating its generality for the UiO-66 family of MOF.

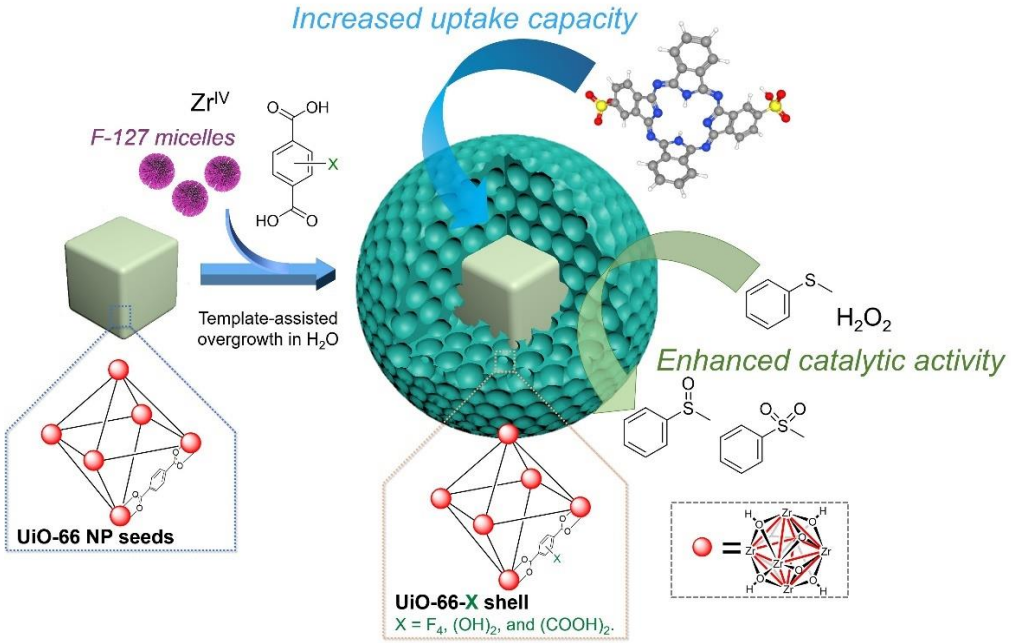

Scheme 2.1 Syntheses of a HM UiO-66-X shell on a UiO-66 core and the resulted potential enhancement in performances in uptake and catalysis.

2.2 Background and motivation

In porous materials, the presence of a hierarchical structure with interconnected pores of different sizes (micro, meso, and macro) has been deemed to be crucial for applications that require facile mass transport, such as absorption, energy storage, and catalysis.[12, 23, 45, 46] Thus, it is not surprising that the inclusion of hierarchical porosity[10, 20, 47-50] has recently emerged as an important research direction for metal-organic frameworks (MOFs). While MOF has been one of the most exciting materials being explored over the last two decades,[1, 3, 5, 6, 51] a majority of the MOFs that were produced have been microporous materials with pores that are smaller than 2 nm, which can limit their performance in many applications. For example, UiO-66, a stable and well-known Zr-based MOF with many uses in catalysis and molecule adsorption,[7] has had its performance being limited by its small aperture (~6 Å),[15] resulting in most of the active sites being limited to the surface of the MOF microcrystals.[18, 19] While UiO-66 samples with large external surface areas (up to 40% of the total surface area) have been reported,[52, 53] these larger pores are based on interparticle porosity (IP), some of which may not persist for solution-phase applications. Given our long-time interests in employing UiO-66-type MOFs for capture[18] and catalysis,[19, 54-56] we were interested in the possibility of incorporating persistent mesopores (i.e., in the 2-50 nm range) into this material to increase its overall storage/capture capacities[57-59] and catalytic activities. We were intrigued by recent works that formed UiO-66 around templates such as long chain fatty acids[21] and metal-organic assembly,[20] but wonder if the proportion of mesopores on a MOF particle can be progressively increased beyond the initial synthesis through an iterative growth strategy that add mesoporous shells onto a seed in an onion-layer fashion.

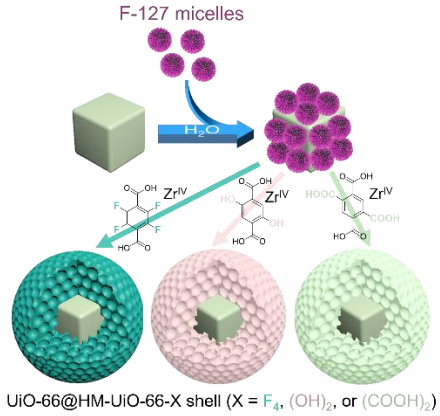

Scheme 2.2 Template-assisted overgrowth of a mesoporous UiO-66-X shell on a UiO-66 core.

In this chapter, we present a template-assisted, seed-mediated synthesis of a hierarchically mesoporous UiO-66 (HM-UiO-66) material using Pluronic F-127 as the template and UiO-66 nanoparticles (NPs) as the seeds (Scheme 2.2). With this strategy, pores ~ 8 nm in size are easily introduced into a UiO-66-X (X = F_4, $(OH)_2$, and $(COOH)_2$) hierarchically porous shell that can be grown iteratively on the top of UiO-66 NP seeds in water. The presence of the NP seeds is critical during the growth of the mesoporous UiO-66 shell as non-porous phases can arise in its absence. This core-shell strategy can be extended to iteratively grow additional layers of the HM-UiO-66-X shells on top of the same UiO-66 NP cores, allowing for large increases in mesoporosity and thus large enhancements in storage capacities and catalytic activities. For example, when a thrice-overgrown HM-UiO-66-F_4 material is used to adsorb the large anionic dye molecule DB 86, large improvements in per-mass uptake capacity was observed in comparison to both the parent UiO-66 seed (320% increase) and the corresponding [UiO-66 + UiO-66-F_4] physical mixture (150% increase). Consistent with these increases, the MOF nodes of this materials are more easily accessible to substrates, resulting in a faster (~3.6 times) rate in the sulfide-oxidation reaction than the micropore-only UiO-66 NP seeds. Together, these results suggest that this template-assisted,

seed-mediated growth of mesoporous shells should be extendable to iteratively enhance the performance of microporous MOFs.

2.3 Combining seed-mediation and template-assistance to build core-shell UiO-66@HM-UiO-66 materials

Among the strategies that have been applied to the synthesis of HM MOFs,[24, 47, 60] templating with surfactants,[23, 61, 62] has the potential to be the most general as it can be applied to a broad range of MOFs simply by combining a mesopore-forming template with the inorganic precursors and the organic linkers under a known MOF synthesis condition. In this manner, hierarchically porous HKUST-1,[32, 63-71] MOF-5,[72] MIL-101,[73, 74] MIL-125,[50] ZIF-8,[75, 76] MIL-53(Al),[77-79] and UiO-66[21, 53] have been achieved. However, undesirable impurities[53, 65, 78] and small crystalline domains[73] often accompanied such template introduction, requiring extra efforts to fine tune synthetic condition or to purify and isolate desired products.

Recent examples in the use of crystalline seeds to grow phase-pure PCN MOFs,[80] have prompted us to explore this strategy to induce the growth of mesopore-containing crystalline MOF overlayers (with different linker/node components) around UiO-66 nanoparticle seeds (Scheme 2.1 and Figure 2.1a) that have been coated with micellar surfactants. The presence of the seeds should allow for the MOF shell to bypass the nucleation stage, grow around the micelles with good crystallinity, and exclude the formation of any unexpected phases. We were further intrigued by the possibility that iterative growth can be applied to such a process (i.e., using the materials obtained after one cycle of growth as the seeds for the next overlayer) to successively increase the overall persistent mesoporosity and compositional diversity. As will be discussed below, combining seed mediation and iterative growth has allowed us to eliminate non-porous side

products in the growth of the HM-UiO-66 shell, grow shells that have different compositions from the core, iteratively increase the thickness of the HM shell, and thus enhance the overall performance in uptake and catalysis.

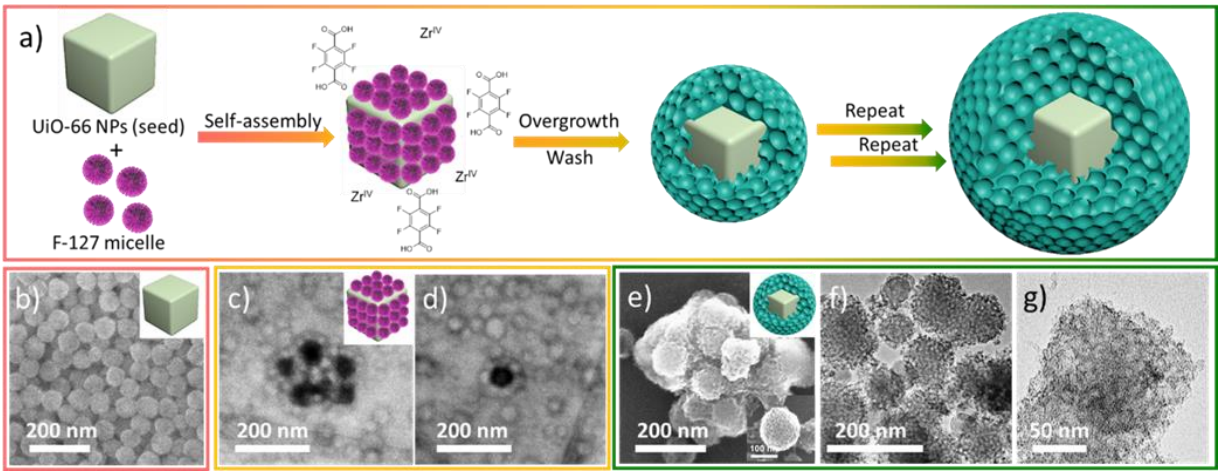

Figure 2.1 (a) Proposed template-assisted, seed-mediated strategy for the iterative synthesis of the UiO-66@HM-UiO-66-F_4 material. The schematic shown here is an artistic rendition representing the core-shell design and hierarchical porosity of the materials, based on Figures 2.1e-f, which shows spherical dimple-laden particles; the inset of Figure 2.1e, which shows a single spherical dimple-laden particle; and Figure 2.4d, which shows the core-shell structure. (b) SEM image of the UiO-66 NP seeds. (c) and (d) Cryo-TEM images of an aqueous mixture of 2.9 wt % F-127 and 0.1 wt % UiO-66 NP seeds. (e) SEM image of UiO-66@HM-UiO-66-F_4 after one growth cycle. The lower inset is a zoomed-in image of a single raspberry-shaped cluster, clearly shows dimples that are consistent with the size of the F-127 micelles, supporting the surface-templating notion shown in panels c-d. (f) and (g) TEM images of UiO-66@HM-UiO-66-F_4 after one growth cycle. As UiO-66 is one of the most chemically, thermally, and mechanically stable MOFs,[15] with bulk modulus of 17 GPa[81] and a calculated minimal sheer modulus of 13.7 GPa,[82] we do not expect that the core will be damaged during the synthesis of the mesoporous structure during the growth. As a point of reference, UiO-66 particles have been used as seeds to overgrow ZIF-8 shells and were found unchanged after the growth.[83]

2.4 Employing water and Pluronic F-127 for the iterative overgrowth of hierarchically porous MOF

For surfactant-templated MOF syntheses to be successful in organic solvents, the surfactant concentration required to form micellar structures oftentimes must be increased significantly (e.g.,

10-30 times higher than that in water),[84-86] to achieve the desired templating effect.[32, 65, 77-79, 87] Indeed, when the amphiphilic surfactant Pluronic F-127 is used in small amounts in the DMF-based synthesis of UiO-66, only microporous materials are obtained.[88] When the concentration of the surfactant is increased to the point that micelles can form in organic solvents,[84-86] more organic residues can be left in the final MOF product, making purification difficult. In this sense, using water, in which many surfactants will form self-assembled micellar structures at low concentrations, can simplify product isolation in our soft template-assisted synthesis strategy.

We thus select Pluronic F-127, a tri-block copolymer that readily forms micelles in water, as the soft template in our HM-UiO-66 synthesis because it has been proposed to interact strongly enough with the Zr-based nodes of UiO-66 to alter the morphology of the resulted MOF material.[88] In addition, F-127 has been used to synthesize mesoporous zirconia nanocomposite,[89] presumably due to its strong complexations with ZrO_x species. Following these precedents, we hypothesize that if F-127 micelles can complex to a large proportion of the exposed, unsaturated coordination sites on the surface of UiO-66 NP seeds, subsequent MOF shells can be induced to grow from the seed around these mesopore-templating micelles (Figure 2.1a). The F-127 micelles can then be induced to disassemble simply by lowering the temperature,[90] and be removed from the particles through post-synthesis rinsing at ambient conditions, leaving behind the desired mesopores as persistent features. The UiO-66@HM-UiO-66 product thus obtained (Figure 2.1a, right structure) will have a microporous UiO-66 seed core surrounded by a hierarchically meso-and-microporous UiO-66 shell.

Notably, when the UiO-66@HM-UiO-66 product is re-exposed to F-127 under the MOF growth conditions, its surface should again interact with the F-127 micelles, enabling the growth

of additional MOF shells with meso-pores of the same size. Such a process can be carried out iteratively in a manner that allows for the incorporation of different [node + linker] compositions and with uniformly dispersed micro/meso-pores in each successive shell. The core-shell morphology is continuously maintained during such cycling, creating an onion-layer structure with tunable chemical diversity that is distinctive from those obtained in one-pot syntheses in the presence of long chain fatty acids[21] and metal-organic assembly.[20]

2.5 UiO-66 NP seeds: synthesis and interparticle porosity

Using a stepwise protocol derived from previous literature[91] (see Section 2.12.2), we synthesized cubic UiO-66 NPs ~50-80 nm in size (Figure 2.1b; see also Figure 2.12). The PXRD profile of this material matches the simulated profile for UiO-66 (fcu) (Figure 2.2, cf black and red profiles), confirming a crystalline phase. It exhibits a type-I_a/IV_a N_2-adsorption/desorption isotherm (BET surface area = 1285 cm^2/g) with a large H1 hysteresis loop (Figure 2.3, black square; see also Figure 2.23 for the pore-size-distribution function (PSDF)), indicating that the microporous UiO-66 NPs were likely to have agglomerated together in the solid state,[92-94] creating interparticle porosity as suggested by SEM imaging (Figure 2.12). This agglomeration and the presence of the large H1 hysteresis loop translate into a large fraction of pore volume in the 20-100 nm region of the PSDF (Figure 2.23) and external surface area (S_{ext} = 164 m^2/g). Curiously, the latter value is comparable to those obtained for UiO-66 materials obtained from DMF synthesis in the presence of Pluronic P-123 (S_{ext} = 90-180 m^2/g)[53] or some water (S_{ext} = 40-350 m^2/g)[52] both of which having pores in the same 20-60 nm range as measured by N_2 adsorption (Figure 2.23). As will be discussed later, the interparticle porosity in our UiO-66 seed will allow it to serve as the baseline comparison for our HM-UiO-66 materials in dye-uptake experiments.

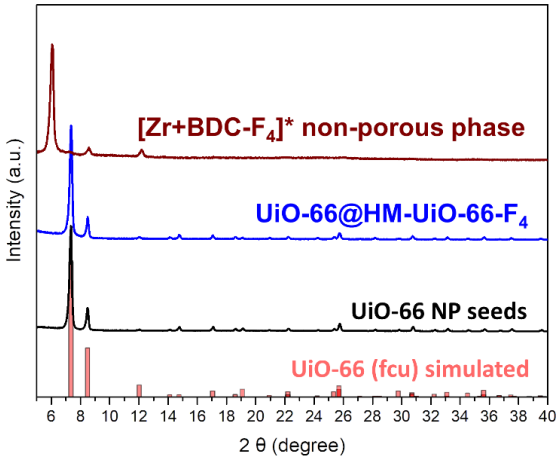

Figure 2.2 PXRD profiles of the simulated UiO-66 (red column), UiO-66 NP seeds (black), UiO-66@HM-UiO-66-F_4 (blue), and the [Zr+BDC-F_4]* non-porous phase (burgundy).

2.6 UiO-66@HM-UiO-66-F_4: overgrowth of a hierarchically porous UiO-66-F_4 shell on UiO-66 NP seeds.

As expected, cryo-TEM imaging of a frozen aqueous mixture of UiO-66 NPs and F-127 micelles suggests associations between these two components. As shown in Figure 2.1c-d and Figure 2.13, UiO-66 NPs appear as dark spheres surrounded by several lighter-shaded F-127 micelles, supporting our templates-around-the-seed hypothesis. Dynamic light scattering (DLS) analysis of the same mixture is also consistent with the presence of aggregates that are much larger than either of the components (R_H ~360 nm; see Figure 2.14). By surrounding the UiO-66 particles, the F-127 micelles can presumably introduce mesopores to the desired HM-UiO-66 shell in the subsequent overgrowth step (Figure 2.1a), when extra precursors (Zr^{IV} precursors and terephthalic acid-type linkers) are added.

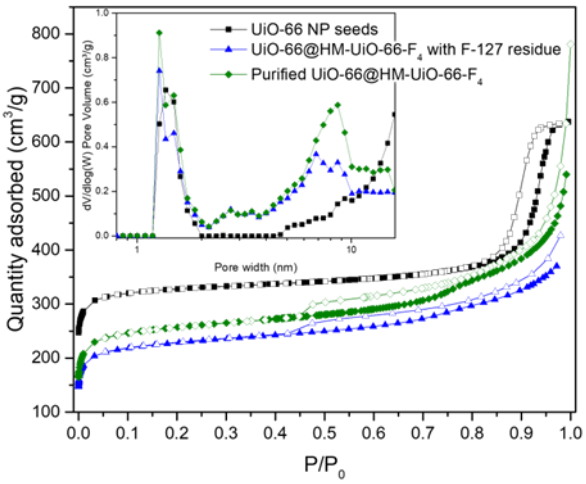

Figure 2.3 The N_2 physisorption isotherms of UiO-66 NPs (black square), UiO-66@HM-UiO-66-F_4 with ~2 wt % of encapsulated F-127 (blue triangle), and purified UiO-66@HM-UiO-66-F_4 (i.e., no encapsulated F-127, green diamond). Solid symbols represent the adsorption branch and hollow symbols represent the desorption branch. Inset: DFT PSDF profiles obtained from the isotherms.

BDC-F_4 was initially chosen as the organic linker for the overgrowth step in our proposed synthesis (Figure 2.1a) given its better solubility (>30 mg/mL)[95, 96] in water comparing to that of terephthalic acid (BDC, ~2 × 10-5 mg/mL),[97] which would be advantageous in aqueous media. Indeed, combining $ZrCl_4$, BDC-F_4, and acetic acid modulator together with a UiO-66 seed/F-127 aqueous suspension under vigorous stirring at 90 ºC resulted in a milky suspension that signals the presence of large particles. Working up this reaction mixture afforded a white powder with ~50% mass increase (see Section 2.12.2 and Figure 2.24).[98] The PXRD data (Figure 2.2, blue pattern) of this [Zr^{IV}/BDC-F_4]-overgrown product, henceforth referred to as UiO-66@HM-UiO-66-F_4, is consistent with UiO-66-based materials being the only crystalline component present.

Thermogravimetric analysis (TGA) of UiO-66@HM-UiO-66-F_4 under argon atmosphere shows two separate mass-loss stages at 320 and 480 ºC, consistent with reported TGA data for UiO-66-F_4 and UiO-66, respectively (Figure 2.22).[99] Mass spectrometric analysis of the volatiles generated during the TGA clearly shows the decarboxylated fragments from both BDC-F_4 and

BDC (Figure 2.22). Quantitative NMR (^{1}H and ^{19}F) and ICP-OES analyses of the digested product yielded a linker-to-node (L/N) ratio of ~4.6 and a BDC-F_4 linker content of ~45% (Figure 2.24 and Table 2.1).

SEM and TEM images (Figure 2.1e-g; see also Figure 2.15) of the UiO-66@HM-UiO-66-F_4 material shows large clusters of raspberry-shaped particles with "dimples" on the surface that are quite distinct from the clean-edged, cubic shape of the seeds. The dimples (~ 10 nm in size; lower inset in Figure 2.1e) are comparable in size to the F-127 micelles, supporting their templating effect when being considered alongside the cryo-TEM image of the [F-127 + UiO-66 NP seeds] mixture (Figure 2.1c-d). The N_2-adsorption isotherm (Figure 2.3) of this UiO-66@HM-UiO-66-F_4 material has a vertical rise at low partial pressures ($P/P_0 < 0.01$) that is representative of the uniform microporous character of UiO-66. However, the overall profile can be classified as comprising a type-I_a/II adsorption branch and a H4 hysteresis loop,[100] similar to those observed for mesoporous zeolites[101] and HKUST-1.[102] This type of isotherm has been suggested to indicate a porous structure having cage-like/slit-shape mesopores surrounding by microporous "walls", which lead to cavitation-desorption behaviour rather than pore-blocking.[12] Such a structure is consistent with the hierarchical shell morphology obtained when the microporous UiO-66 grows around the mesopores-templating F-127 micelles.

The BET surface area of the UiO-66@HM-UiO-66-F_4 material (950 m^2/g) is intermediate between those of UiO-66 (1100-1525 m^2/g)[99, 103] and UiO-66-F_4 (830-890 m^2/g),[99,104] not inconsistent with it being a hybrid material with both types of linkers. Its DFT PSDF shows an 8 nm mesopore that matches well with the size of F-127 micelles.[105] This is in contrast to the PSDF for the UiO-66 NP seeds, which shows a broad interparticle-pore peak (20-60 nm, straddling the meso-/macro-pore range) well-known to arise from the agglomeration of particles with regular

shapes (Figure 2.23).[106,107] As mentioned above, such a peak would have arisen from the N_2-adsorption data in the region that contains the H1 hysteresis loop (Figure 2.3, black square). Similar N_2 physisorption data have been observed for UiO-66 materials obtained from DMF synthesis in the presence of Pluronic P-123 [53] or an appropriate amount of water.[52] Like our UiO-66 NP seeds, these materials possess mostly interparticle porosity (IP) that is quite different from the hierarchically mesoporous (HM) shell in our UiO-66@HM-UiO-66-F_4 material (Figure 2.23 and the discussion in its caption).

To support the notion that the 8 nm peak in the PSDF of UiO-66@HM-UiO-66-F_4 arose from the growth of the mesoporous UiO-66-F_4 shell around F-127 micelles, we compare the N_2-physisorption data for an as-synthesized sample, which still contains ~2 wt % F-127 after a quick MeOH rinse, vs that of a purified sample, where this residual F-127 was completely removed via Soxhlet extraction (Figure 2.8). The latter has an increased BET surface area (950 m^2/g, Figure 2.3) as well as a larger pore-volume contribution from the peak at 6-10 nm in the PSDF profile (Figure 2.3, green). Additionally, a control experiment, grown in the absence of F-127, afforded a UiO-66|UiO-66-F_4 material with no mesopore at 8 nm (see Figure 2.17 for SEM images and Figure 2.23 for N_2-physisorption data).

Based on the aforementioned TGA, PXRD, and N_2-physisorption data, as well as the assumption of seed-mediated overgrowth, it is reasonable to conclude that our strategy indeed affords an HM-UiO-66-F_4 shell over-grown on top of UiO-66 NP cores. The important role of the seed in "directing" the overgrown layer to be UiO-66-type is reinforced by a control experiment where F-127, $ZrCl_4$, BDC-F_4, and acetic acid modulator were combined under the same conditions as our overgrowth experiment but in the absence of the UiO-66 NP seeds. This synthesis resulted only in the formation of a [Zr+BDC-F_4]* non-porous phase (Figure 2.19) that has a completely

different PXRD pattern from that of UiO-66 (Figure 2.2, cf the burgundy and black profiles). Indeed, more of this non-porous phase was observed when the concentration of NP seeds was decreased from that of the optimized UiO-66@HM-UiO-66-F_4 synthesis (Figure 2.20). Together, these observations emphasize that a contiguous growth around the UiO-66 NP seed is critical for the formation of the crystalline (fcu) HM-UiO-66-F_4 shell. Thus, we proposed the aforementioned UiO-66@HM-UiO-66-F_4 notation for our material, which indicates a UiO-66 NP seed at the core and a layer of HM-UiO-66-F_4 as the shell.

To better differentiate the newly formed HM-UiO-66-F_4 shell and the original UiO-66(Zr) seed core in the final product, we also grew a UiO-66(Hf)-F_4 shell around UiO-66(Zr) NP seeds. Using $HfCl_4$ as the inorganic precursor in place of $ZrCl_4$ in our templated synthesis afforded the corresponding UiO-66@HM-UiO-66(Hf)-F_4 material in good yields (see Section 2.12.2). The PXRD (Figure 2.27), EM imaging (Figure 2.4a; see also Figure 2.28), and porosity (Figure 2.30) data for this material are similar to those of UiO-66@HM-UiO-66-F_4. This observation stands in contrast that of a recent report when unexpected impurities were obtained when $HfCl_4$ and BDC-F_4 were combined under similar aqueous solvothermal conditions,[108] further supporting the important role played by the seed. Consistent with a core-shell structure, STEM-EDS mapping of a particle of this material reveals a Zr-rich core surrounded by an Hf-rich shell (Figure 2.4b-d). Interestingly, the F signals appear throughout the particle rather than concentrated on the surface (see also Figure 2.29f), suggesting that some linker exchange has also occurred during the formation of UiO-66@HM-UiO-66(Hf)-F_4. This is supported by a higher BDC-F_4 linker ratio than theoretically predicted for a simple over-growth process (Figure 2.24 and Figure 2.26; see additional discussion below).

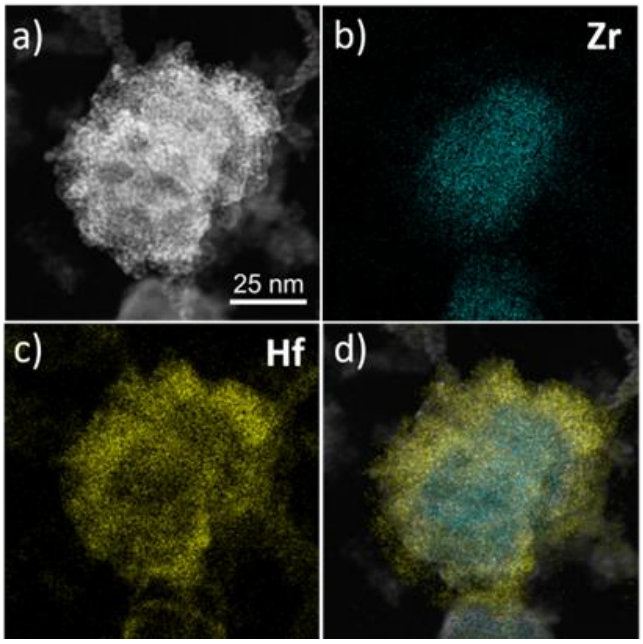

Figure 2.4 (a) High-angle annular dark field (HAADF) image of a sample of UiO-66@HM-UiO-66(Hf)-F_4. (b-c) EDS elemental maps–imaged by Zr and Hf, respectively–of the same sample. (d) Composite Zr (blue) and Hf (yellow) EDS maps of the same sample, made by overlaid panels b and c, showing a core-shell structure.

2.7 Iterative overgrowth of the HM-UiO-66-F_4 shell

Notably, the MOF overgrowth process can be carried out iteratively in the presence of the F-127 template to in-crease the proportion of the HM-UiO-66-F_4 shell. As mentioned above for UiO-66@HM-UiO-66-F_4, which we will refer to as the material obtained after the 1st-round of overgrowth, a mass increase of ~50% (Figure 2.24) was observed. Using this material as seeds in our overgrowth scheme should lead to additional increases in mass as well as the BDC-F_4 content. This is indeed the case: subjecting UiO-66@HM-UiO-66-F_4 to two additional overgrowth cycles led to UiO-66@HM$|_{2nd}$-UiO-66-F_4 and UiO-66@HM$|_{3rd}$-UiO-66-F_4, respectively, with a linear mass-gain trend (Figure 2.24) and increased proportion of the external surface areas (Table 2.2). SEM imaging (Figure 2.5; see also Figure 2.15) also shows a successive increase in particle size, consistent with the additional growth after each cycle. Comparing to the predicted values (Figure 2.24), the experimental BDC-F_4 contents are always slightly higher, which can be explained by

some exchange of the linkers[109, 110] during the overgrowth step. The XRD patterns (Figure 2.27) and the N_2-physisorption data (Figure 2.23 and Table 2.2) of these materials are similar to those of the UiO-66@HM-UiO-66-F_4 1st-round-overgrowth material, suggesting that the crystalline HM-UiO-66-F_4 phase can be consistently maintained over the repeated overgrowth cycles and that the formation of the [Zr+BDC-F_4]* non-porous phase can be excluded.

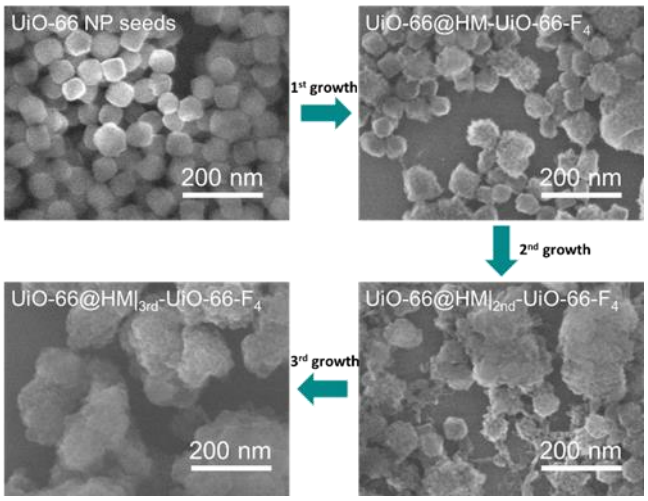

Figure 2.5 SEM images showing a continuous increment of HM-UiO-66-F_4 shell thickness on top of UiO-66 NP seeds in the iterative growth process.

The iterative growth with $HfCl_4$ as the inorganic precursor also resulted in materials with increased BDC-F_4 and Hf contents (Figure 2.26). STEM-EDS mapping (Figure 2.29) of these materials also showed Hf-rich shells surrounding Zr-rich cores, consistent with the core-shell structure being maintained during the iterative overgrowth process. Their PXRD profiles (Figure 2.27), SEM images (Figure 2.28), and N_2-physisorption data (Figure 2.30) are similar to the Zr analogs described above, suggesting that our iterative strategy is generally compatible with group IV inorganic precursors.

2.8 Extension to other UiO-66-X (X = $(COOH)_2$, $(OH)_2$, and NH_2) shells

BDC-$(COOH)_2$, BDC-$(OH)_2$, BDC-NH_2, and BDC linkers were also successfully used in three successively overgrowth cycles to give UiO-66@HM|$_{3rd}$-UiO-66-$(COOH)_2$, UiO-66@HM|$_{3rd}$-UiO-66-$(OH)_2$, UiO-66@IP|$_{3rd}$-UiO-66-NH_2, and UiO-66@IP|$_{3rd}$-UiO-66, (IP = interparticle porosity) respectively. These materials have particles that are larger in size than that the seeds and possess similar raspberry-like morphologies (Figure 2.34) and PXRD profiles (Figure 2.35) as the UiO-66@HM|$_{3rd}$-UiO-66-F_4 analogue, suggesting that the surface-templating effects of the F-127 micelles can indeed be easily extended to other terephthalic-acid-based linkers. However, their PSDF profiles (Figure 2.36) diverge into two classes: hierarchically mesoporous for UiO-66@HM|$_{3rd}$-UiO-66-X and interparticle porous for UiO-66@IP|$_{3rd}$-UiO-66-X materials. The first class, with BDC-F_4, BDC-$(COOH)_2$, and BDC-$(OH)_2$ linkers in the shell possessing a significant amount of mesopores in the 2-20 nm region (i.e., matching the size of the F-127 micelles). In contrast, the second group with the less-soluble linkers (BDC-NH_2 and BDC) showed a much larger proportion of interparticle-derived pores (20-100 nm). These peaks are in the same region as those for the UiO-66 NP seeds (Figure 2.36) but are either at higher intensity (UiO-66@IP|$_{3rd}$-UiO-66) or shifted to the large size (UiO-66@IP|$_{3rd}$-UiO-66-NH_2). These features are consistent with the more-pronounced H1 hysteresis loops in their N_2-physisorption isotherms (Figure 2.36) in comparison to the UiO-66 NP seeds and are different from those for the UiO-66@HM|$_{3rd}$-UiO-66-X materials where an H4-type hysteresis loop is featured prominently.

Interestingly, the average mass gains of these materials (Figure 2.36c) follow the BDC-F_4 ~ BDC-$(COOH)_2$ > BDC-$(OH)_2$ > BDC-NH_2 >> BDC (no mass gain) trend, consistent with their observed relative solubilities in water (Figure 2.36c). This is not surprising as the growth of the HM shells around the seed should proceed easier with the more-water-soluble linkers being more

available for MOF growth in water. In connection with the porosity classification above, it appears that the more-soluble linkers will afford materials with a hierarchical mesoporous shell structure and those that are less soluble will afford materials with interparticle porosity. As shells with functional linkers that are distinct from the initial seed can be iteratively added, core-shell materials with different porosity types can be easily achieved by ligand selection based on solubilities. This in turn will extend the range of functionalities and porous structures available through our template-assisted strategy.

2.9 Increased dye-uptake capacity with HM-UiO-66: the importance of hierarchical porosity in solution adsorption

With easily accessible mesopores (~8 nm) in the framework, the HM-UiO-66 materials have much higher uptake of adsorbates than the UiO-66 NP seeds and UiO-66-F_4 control. As shown in Figure 2.6a (see also Figure 2.32), the end-point (i.e., at 48 h) uptake of the anionic dye Direct Blue 86 (DB 86) by UiO-66@HM|$_{3rd}$-UiO-66-F_4 reaches an impressive adsorption, which corresponds to a ~0.57 dye/node ratio.[111] This is ~320% more than the observed capacity and dye/node ratio for the UiO-66 seed (81 mg/g, ~0.17 dye/node) and 150% better than that for a [UiO-66 + UiO-66-F_4] physical mixture at the same mass proportion (Figure 2.6). This is notable as all three MOF materials have similar external surface areas (Table 2.2) but the pores in the 20-100 nm region in the PSDF of the UiO-66 NP seeds were derived mainly from interparticle porosity that do not persist in solution and UiO-66-F_4 does not have any mesopores. Together these data clearly show that the hierarchical mesopores in the shell play an important role in increasing the accessibility of the dye-binding sites on the MOF, even though UiO-66-F_4 does have

a higher intrinsic dye-uptake capacity (UiO-66-F_4 uptake = 129 mg/g, ~0.32 dye/node; see Figure 2.33) compared to UiO-66, presumably due to its higher hydrophobicity.[108, 112, 113]

The aforementioned solution-based dye-uptake experiments bring out a stark contrast between hierarchical and interparticle porosities in our series of materials. While the UiO-66 NP seeds possess a higher proportion of pore volume in the 10-100 nm region of the PSDF (see Figure 2.23 top right panel) than the UiO-66@HM|$_{3rd}$-UiO-66-F_4 material, it was the latter that has a much-higher dye-uptake capacity. The explanation is simple: the pore volume in the former sample represents interparticle porosity measured using gas adsorption and are not preserved when the NPs are dispersed in a liquid media, leading to lower uptake capacity because DB 86 can only access the surface sites on each NP. In contrast, the mesoporosity in UiO-66@HM|$_{3rd}$-UiO-66-F_4 material was derived from the F-127-micelle template on the shell of the NP and are preserved during the dispersion, allowing for the large DB 86 adsorbate to access many of the binding sites within the particle.

The combination of core-shell morphology and iterative overgrowth strategy easily allows for a systematic and continuous improvement in dye-adsorption capacity. After the first round of overgrowth, the UiO-66@HM-UiO-66-F_4 material already exhibits an experimental uptake that is 40% more than predicted for a [UiO-66 + UiO-66-F_4] physical mixture at the same mass and composition (Figure 2.6b). As the proportion of the HM-UiO-66-F_4 shell in our materials is increased with the number of overgrowth cycle, the dye-uptake capacity (Figure 2.6a), the dye/node ratio (Figure 2.33), and the uptake enhancement brought by HM structure (Figure 2.6b) continues to increase at an accelerated pace, reaching an impressive 150% increase for UiO-66@HM|$_{3rd}$-UiO-66-F_4 comparing to that expected for the corresponding physical mixtures (Figure 2.6b). Together these data clearly highlight the advantage of iteratively introducing

persistent mesopores into UiO-66 materials: They allow the large DB 86 adsorbate (4 × 12 × 14 Å,[20] larger than the UiO-66 aperture (~6 Å)[15]) to access more of the binding sites in the MOF, thus increasing the capacity in capture-and-storage applications.

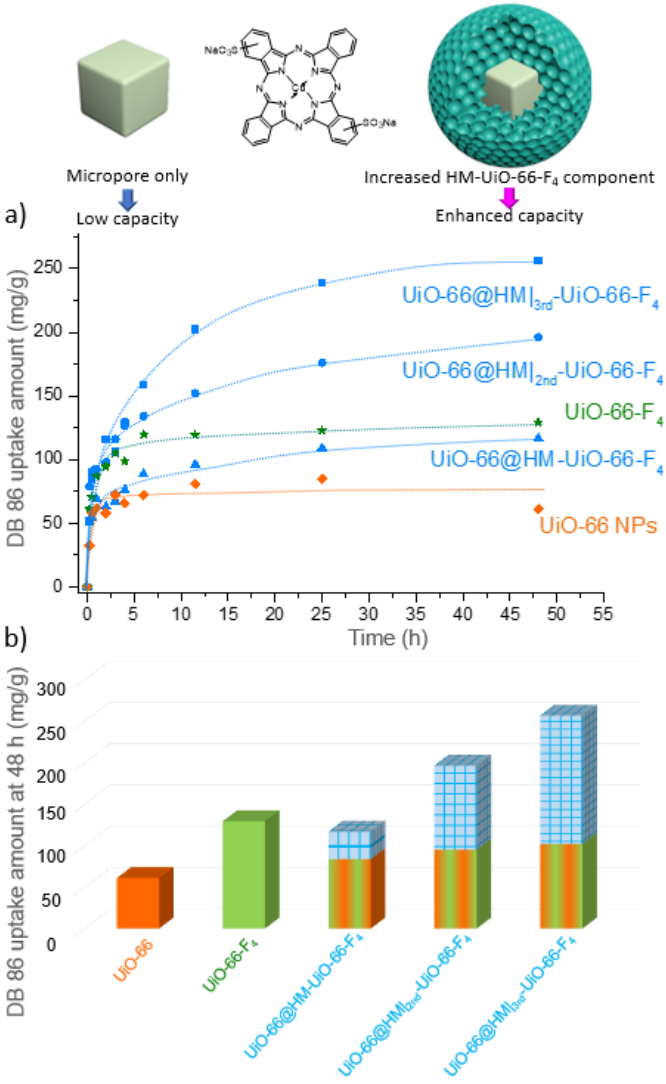

Figure 2.6 a) Adsorption-time profile of the anionic dye DB 86 into UiO-66 NPs (orange diamond), UiO-66-F_4 (green star), UiO-66@HM-UiO-66-F_4 (blue triangle), UiO-66@HM|$_{2nd}$-UiO-66-F_4 (blue circle), and UiO-66@HM|$_{3rd}$-UiO-66-F_4 (blue square). The dash lines are provided only for visual guidance. b) Bar graph of the DB 86-uptake amounts of the corresponding five samples at 48 h; In the latter three, the uptake amounts attributed to a [UiO-66 + UiO-66-F_4] physical mixture at the same mass and composition is represented as the green-orange portion at the bottom of each bar while the enhancements resulted from the HM structure are shown as the blue-grid-pattern portions of the bars.

2.10 UiO-66-catalyzed sulfide oxidation

The interconnectivity of the mesopores and micropores in our HM-UiO-66-F_4 materials can also be highly advantageous in catalytic applications. Indeed, hierarchically porous materials containing a mixture of interconnected micropores and larger pores have been shown to induce higher reaction rates in catalysis comparing to their microporous counterparts[24, 48, 114-116] as reagents can better access the active sites. To this end, we employed UiO-66@HM|$_{3rd}$-UiO-66-F_4 as the catalyst in the oxidation of thioanisole with H_2O_2 as the oxidant (reaction 1, Figure 2.7), which has been shown to be catalyzed by open sites at the Zr_6-cluster nodes of UiO-66.[19, 117] As controls, we also examined the activity of UiO-66 NPs, UiO-66-F_4, and UiO-66|UiO-66-F_4 (the material without adding F-127 during the overgrowth to calibrate for any difference in node chemistry between the first two materials; see Table 2.3).

As expected, UiO-66@HM|$_{3rd}$-UiO-66-F_4 exhibits the best activity in sulfide oxidation (Figure 2.7a) with an initial reaction rate that is ~3.6-fold that observed for the UiO-66 NP seeds (Figure 2.7b and Table 2.3, cf first vs last entries) and 2.5-fold that observed for a BzOH-UiO-66 sample with similar particle size.[19] In contrast, the non-mesoporous UiO-66|UiO-66-F_4 material shows a reaction rate that is only ~1.3-fold that of the UiO-66 NP seeds, (Table 2.3, cf first vs third entries). These comparisons indicate that the enhanced mesoporosity of the UiO-66@HM|$_{3rd}$-UiO-66-F_4 material can play an important role in enhancing the catalytic activity of UiO-66 by facilitating the transport of reagents to and from the active sites throughout the materials instead of just the sites on the surface of the MOF nanparticles.[19]

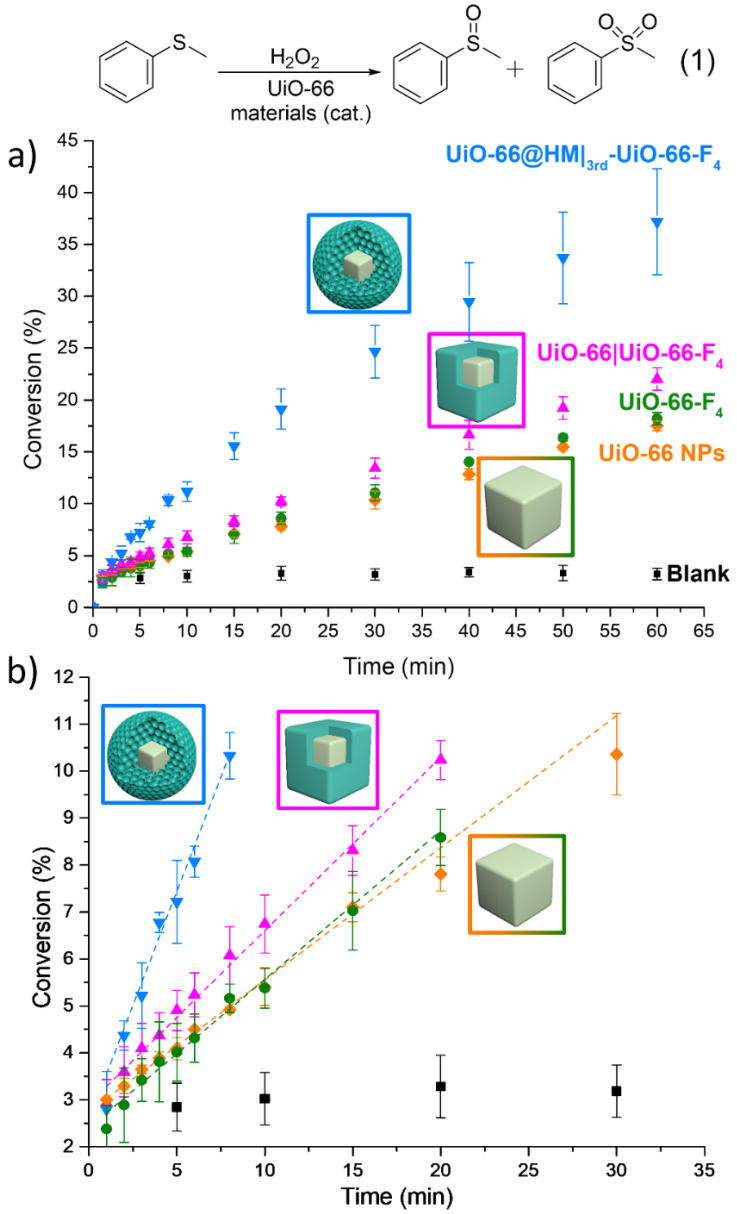

Figure 2.7 (a) Conversion-vs-time profiles of the sulfide oxidation catalyzed by UiO-66@HM|$_{3rd}$-UiO-66-F$_4$ (blue inverted triangle), UiO-66|UiO-66-F$_4$ (magenta triangle), UiO-66 NPs (orange diamond), and UiO-66-F$_4$ (green circle), along with a background reaction without catalyst (black square). (b) Conversion-vs-time profiles (up to 11 % conversion) and the linear fitting results (see Table 2.3 for the rate data). Reaction conditions: rt, methyl phenyl sulfide (20 mM), aqueous H_2O_2 (20 mM), Zr_6 cluster (0.01 equiv), and CH_3CN (10 mL) as solvent. To demonstrate the stability of UiO-66@HM|$_{3rd}$-UiO-66-F$_4$, we have recycled it 3 times in the sulfide-oxidation reaction and showed that its crystallinity and particle size/morphology were preserved (Figures 2.38 and 2.39).

2.11 Conclusion

In summary, we have demonstrated the successful incorporation of ~8 nm mesopores into the small-apertured UiO-66 MOF, creating a hierarchically mesoporous UiO-66 material with excellent enhancements in storage capacities and catalytic activities. Using a F-127 template-assisted strategy that enables the growth of a UiO-66-X (X = F_4, $(OH)_2$, and $(COOH)_2$) shell on top of UiO-66 NP seeds, we can facilitate the continuous formation of a crystalline phase (fcu) in the shell rather than an undesired non-porous side product. Depending on the solubility of the added linkers, either hierarchical or interparticle porosity can be engendered into the core-shell materials. Notably, additional shells can be iteratively grown over the "seed" in an onion-layer fashion, allowing for the addition of chemical diversity as well as leading to increased proportions of the HM-UiO-66 component. After three cycles of growth, the resulting UiO-66@HM|$_{3rd}$-UiO-66-F_4 material exhibits uptake capacity for the large anionic dye DB 86 that is 320% better than the parent microporous UiO-66 seeds, and 150% better than that for a [UiO-66 + UiO-66-F_4] physical mixture at the same mass proportion. Moreover, the co-existing micro- and meso-porosities in UiO-66@HM|$_{3rd}$-UiO-66-F_4 enables it to catalyze the oxidation of thioanisole at an enhanced rate compared to the microporous UiO-66 seeds, attributable to increased surface active sites and enhanced diffusion efficiency. Such an iterative, template-assisted, seed-mediated synthesis strategy should be extendable to endow other microporous MOFs with mesopores, thus enhancing their performance.

2.12 Experimental and supplementary data

2.12.1 Materials and methods

Unless otherwise stated, all reagents were used as received. Zirconium chloride ($ZrCl_4$) was purchased from Strem Chemicals, Inc. (Newburyport, MA, USA). Hydrogen peroxide (H_2O_2, 30 wt % in water), naphthalene, acetic acid (AcOH), 1,4-benzene dicarboxylic acid (BDC), tetrafluoro terephthalic acid (BDC-F_4), Pluronic® F-127, methanesulfonic acid, methyl phenyl sulfide, methyl phenyl sulfoxide, methyl phenyl sulfone, maleic acid, pyromellitic acid (BDC-$(COOH)_2$), 2-amino terephthalic acid (BDC-NH_2), and zirconium ICP standards were purchased from Sigma-Aldrich Co., LLC. (St. Louis, MO, USA) and used as received. Direct Blue 86 (DB 86), 2,5-dihydroxyterephthalic acid (BDC-$(OH)_2$) was purchased from TCI America (Portland, OR, USA) and used as received. Deuterated dimethylsulfoxide (DMSO-d_6, 99%) was purchased from Cambridge Isotope Laboratories, Inc. (Tewksbury, MA, USA). Ultrapure deionized (DI) water (18.2 MΩ•cm resistivity) was obtained from a Millipore Milli-Q Biocel A10 instrument (Millipore Inc., Billerica, MA, USA). Solvents were purchased from either Sigma-Aldrich Co., LLC. (St. Louis, MO, USA) or Fisher Scientific, Inc. (Pittsburg, PA, USA) and used as received.

Powder X-ray diffraction (PXRD) patterns were collected on a STOE's STADI-MP powder diffractometer (STOE & Cie. Ltd, Darmstadt, Germany) equipped with an asymmetric curved Germanium monochromator (Cu $K_{\alpha 1}$ radiation, λ = 1.54056 Å), a one-dimensional silicon strip detector (MYTHEN2 1K from Dectris AG, Baden, Switzerland), and a line-focused Cu X-ray tube operated at 40 kV and 40 mA. The as-received powder was sandwiched between two acetate foils (polymer substrate with neither Bragg reflections nor broad peaks above 10 degrees) and measured in transmission geometry in a rotating holder. Prior to the measurement, the instrument was

calibrated against a NIST Silicon standard (640d). Measurements were made over the range 5° < 2θ < 60° in 6° steps of the detector and an exposure time of 20 s per step.

N_2 adsorption and desorption isotherms were measured on a Micromeritics Tristar II 3020 (Micromeritics Instrument Corporation, Norcross, GA, USA) at 77 K. Before each run, samples were activated in a National Appliance Laboratory Bench Vacuum Oven-model M5831 (National Appliance Co., Portland, OR, USA) that was connected to house vacuum (20 in Hg), and then at 120 °C for 24 h on a Micrometrics VacPrep 061 (Micromeritics Instrument Corporation, Norcross, GA, USA) sample-degas station. About 40-100 mg of sample was used in each measurement and the BET area was calculated in the region P/P_0 = 0.005-0.01, which is selected to satisfy the first consistency criterion for materials containing micropores, as recommended by Walton and Snurr.[118] The pore-size-distribution functions (PSDFs) of the MOFs were calculated from the adsorption-desorption isotherms by density functional theory (DFT) using the carbon slit-pore N_2-DFT model in the range of $5.0 \times 10^{-5} < P/P_0 < 0.95$. For comparison, PSDFs calculated from the BJH model (on the adsorption branch) were also included in the Section 2.12. The micropore surface area and external surface area were calculated using conventional t-plot methods[119] from N_2-adsorption data. The values were selected over the t range of 3.5-5.0 Å by fitting the data to the Harkins-and-Jura thickness equation that affords a physically sensible micropore volume while maintaining a correlation coefficient that is closest to 1. This is the process we used in a recent publication on hierarchical porous organic polymers[120] and is recommended by the Micromeritics Instrument Corporation. [121]

Scanning electron microscopy (SEM) images were obtained at Northwestern University's EPIC/NUANCE facility on an SU8030 FE-SEM microscope (Hitachi High Technologies America, Inc., Dallas, TX, USA) with an acceleration voltage of 10-15 kV. Size measurements

were obtained from sample populations of >100 particles, which were used to construct the standard normal distribution plots (mean ± 3 standard deviation units) and the histograms.

Transmission electron microscopy (TEM) images were obtained at Northwestern University's EPIC/NUANCE facility on either a Hitachi 8100 (Hitachi High Technologies America, Inc., Dallas, TX, USA) or a JEOL 2100F (JEOL USA, Inc., Peabody, MA, USA) microscope with an acceleration voltage of 200 kV. TEM copper grids coated with formvar/carbon film were used (300 mesh, Ted Pella Inc. Redding, CA, USA, product # 01753-F).

The energy-dispersive spectral (EDS) data and high-angle annular dark field (HAADF) images were collected using ARM 200CF transmission electron microscope (JEOL USA, Inc., Peabody, MA, USA). The microscope is equipped with a probe corrector and a dual-solid silicon drift (SSD) detector and is operated at 200 kV. The total area for the detector is 200 mm^2 and the solid angle for EDS collection is estimated as 1.7 sr.

For cryo-TEM measurement, 200 mesh Cu grids with a lacey carbon membrane (EMS Cat. # LC200-CU) were placed in a Pelco easiGlow glow discharger (Ted Pella Inc., Redding, CA, USA) and an atmosphere plasma was introduced on the surface of the grids for 30 seconds with a current of 15 mA. This treatment creates a negative charge on the carbon membrane, allowing for liquid samples to spread evenly over of the grid. An aliquot (4 µL) of sample were pipetted onto the grid and blotted for 5 seconds with a blot offset of +0.5 mm, followed by immediate plunging into liquid ethane within a FEI Vitrobot Mark III (Thermo Fisher Scientific, Waltham, MA, USA) plunge-freezing instrument. Grids were then transferred to liquid nitrogen for storage. The plunge-frozen grids were kept vitreous at –172 ºC in a Gatan Cryo Transfer Holder model 626.6 (Gatan Inc., Pleasanton, CA, USA) while viewing in a JEOL JEM1230 LaB6 emission TEM

(JEOL USA, Inc., Peabody, MA, USA) at 120 kV. Image data was collected by a Gatan Orius SC1000 CCD camera Model 831 (Gatan Inc., Pleasanton, CA, USA).

Gas chromatography was carried out on an Agilent Technologies 6890N Network GC system (Agilent Technologies, Inc., Santa Clara, CA, USA) equipped with an FID detector. An ZB-624 capillary column (30 m × 320 μm × 1.80 μm film thickness) was used to analyze the substrates. Analysis parameters were as follows: initial temperature = 50 °C, initial time = 2 minutes, ramp = 20 °C/min, final temperature = 260 °C, final time = 7.5 minute. Elution times (min) = 10.7 (methyl phenyl sulfide), 11.7 (naphthalene), 13.8 (methyl phenyl sulfoxide), and 14.8 (methyl phenyl sulfone). The amount of oxidation product was calculated based on calibration curves against naphthalene as an internal standard. Response factors: methyl phenyl sulfide = 0.709, methyl phenyl sulfoxide = 0.598, and methyl phenyl sulfone = 0.679.

UV-vis absorption spectra of DB 86 aqueous solutions were recorded on a Varian Cary 300 Bio UV-vis spectrophotometer (Varian, Inc., Palo Alto, CA, USA) using 1.5-3.0 mL disposable plastic cuvette (12.5 × 12.5 × 45 mm, catalog # 7591 50, BrandTech, Wertheim, Germany).

Inductively coupled plasma optical emission spectroscopy (ICP-OES) was conducted on a computer-controlled (QTEGRA software v. 2.2) Thermo iCap 7600 Duo ICP-OES (Thermo Fisher Scientific, Waltham, MA, USA) instrument equipped with a SPRINT valve and a CETAC 520ASX autosampler (Teledyne CETAC, Inc., Omaha, NE, USA).

For obtaining MOF compositions, ^{1}H NMR and ^{19}F NMR spectra were recorded on a Bruker Neo 600 MHz spectrometer (Bruker Biospin Corp., Billerica, MA, USA) equipped with a triple-resonance (HCFN) cold probe w/ Z-gradient and the following manufacturer-reported sensitivities: ^{1}H = 5000, ^{19}F = 7000, and ^{13}C = 800. ^{1}H NMR chemical shifts are referenced in ppm downfield from tetramethylsilane (TMS, δ scale) using the residual solvent resonances as internal standards.

^{19}F NMR chemical shifts are referenced in ppm downfield from trichlorofluoromethane ($CFCl_3$, δ scale). Trifluoroacetic acid (TFA) was used as an internal standard.

A Mettler ToledoTM Micro-Analytical Balance (Mettler-Toledo, LLC., Columbus, OH), located in the IMSERC facility of Northwestern University, was used to weigh samples ≤ 10 mg. To minimize static, samples were weighed into Al sample pans; the weighing apparatus and sample containers were also de-staticized with a Milty Zerostat 3 anti-static gun when necessary.

An IKA-Werke RCT Basic S1 Magnetic Stirrer (IKA Works, Inc., Wilmington, NC, USA) was used to carry out the experiments that requires heating and stirring. The stirring rate was kept at a relatively vigorous rate (~ 800 rpm) to maintain nanoparticle dispersion and favors overgrowth on the seed instead of undesirable self-nucleation. To maintain a consistent temperature throughout the reaction volume, the reaction vial was immersed in a mineral oil bath in a manner that the top of the reaction volume is below the level of the oil bath.

Sonication was carried out in a Branson 2510 Ultrasonic Sonicator (St. Louis, MO, USA).

For the synthesis and catalysis experiments, centrifugation was carried out in an Eppendorf Centrifuge 5804 R, Model AG 22331 (Eppendorf AG, Hamburg, Germany) equipped with an F34-6-38 rotor. All centrifugations were carried out at 25 °C and 8000-11000 rpm (8228-15557 g) for 10-30 minutes. For the uptake, centrifugation was carried out in an Eppendorf Centrifuge 5424 equipped with an F-45-24-11 rotor. The centrifugations were carried out at 25 ºC and 15000 rpm (21130 *g*).

The drying of MOF samples after synthesis was routinely carried out at 120 ºC for 24 h in a National Appliance Laboratory Bench Vacuum Oven-model M5831 (National Appliance Co., Portland, OR, USA) that was connected to house vacuum (20 in Hg).

Volume measurements were carried out using mechanical pipets (professionally calibrated every 3 months) for convenience. However, the volume accuracy does not need to be maintain at the ± 0.005 mL level of accuracy that is intrinsic to these instruments.

2.12.2 Synthesis of materials

UiO-66 Nanoparticles (NPs) batch 1. The UiO-66 NPs were made from a stepwise nucleation and growth procedure.

Stock solution A: This stock solution was prepared by modifying the protocol reported by Taddei et al.[91] In a 125 mL Erlenmeyer flask, ZrCl4 (1.282 g, 5.5 mmol) was dissolved in dimethylformamide (DMF, 61 mL) with the help of sonication (~15 min). Glacial acetic acid (22 mL, 348 mmol) was then added and the resulting mixture was again sonicated (~15 min) to help with homogenization. Depending on the source of reagent, a small amount of materials may remain undissolved (lightly cloudy solution). The resulting solution was stored/aged for 1 day at room temperature and then syringe-filtered through a PTFE membrane filter (Fisherbrand catalog 28145-495, 0.2 μm) to remove any undissolved compounds or precipitate. The clear filtrate is then combined with stock solution B in the MOF NP synthesis.

Stock solution B: In a 125 mL Erlenmeyer flask, terephthalic acid (3.652 g, 22.0 mmol) was dissolved in DMF (83 mL) with the help of sonication (~15 min).

In a typical synthesis, solution A and solution B (1:1 ratio, 80 mL each) were mixed together by swirling in a 500 mL beaker and left under room temperature for 1 day (cover with a watch glass), after which the mixture solution was transferred into a 2 L pyrex bottle (Fisher-brand catalog # 06-414-1E) and diluted with DMF (1.12 L). The bottle was capped, swirled to homogenize the mixture, and then put into a preheated 90 ºC oven during which time the reaction mixture becomes cloudy, indicating the formation of UiO-66 NPs. After 24 h, the bottle was

removed from the oven and cooled down to room temperature. The UiO-66 NPs were collected by successive centrifugation (10000 rpm, 30 min per cycle before decanting and add more reaction mixture) in six 50 mL polypropylene centrifuge tubes (Fisher-brand catalog # 14-959-49A). The final product fractions were then combined into one tube by transferring with DMF (~40 mL total) and centrifuged again. The supernatant DMF was removed by decantation. The remaining suspension was re-dispersed into MeOH (40 mL) by sonication (~15 min) before being subjected to centrifugation (10000 rpm, 30 min) and decantation to wash off any extra reagent. This MeOH-washing procedure was repeated for two more times, after which the product was left to air-dry inside the tube before being transferred into a 20 mL scintillation vial. The vial was then placed into a 120 ºC vacuum oven to further dry. Yield = 0.2-0.4 g (13-26 %).

For series of experiments that need an amount of UiO-66 NP seeds that is larger than can be obtained in a single synthesis, the products of two successive experiments were combined after verification by SEM to have the same particle size distribution. BET data was then obtained for the combined materials as a secondary verification of the quality. The combined materials (~1.2 g) were used for the cryoEM experiment; as seeds for the synthesis of UiO-66@HM-UiO-66-F4, UiO-66@HM|2nd-UiO-66-F4, UiO-66@HM|3rd-UiO-66-F4, and UiO-66|UiO-66-F4 materials; and in the uptake and catalysis experiments.

UiO-66 NPs batch 2. For the syntheses of UiO-66@HM|$_{3rd}$-UiO-66-X (X = $(OH)_2$, $(COOH)_2$, NH_2, and H_4), another batch of material (~600 mg) was synthesized ~four months after batch 1. For analytical data, see Figure 2.12 (SEM and size distribution histogram) and Figure 2.36 (N_2 physisorption isotherm and DFT PSDF).

For the next three syntheses, the following solutions are prepared in advance and used within 2 days:

Solution C. This solution was prepared by dissolving F-127 (600 mg, 48 μmol) with $AcOH_{aq}$ (20 mL of a 1.75 M aqueous solution), followed by dissolving BDC-F_4 (238 mg, 1 mmol) under sonication (~5 min).

Solution D. This solution was prepared by dissolving F-127 (600 mg, 48 μmol) with $AcOH_{aq}$ (20 mL of a 1.75 M aqueous solution), followed by dissolving $ZrCl_4$ (233 mg, 1 mmol) under sonication (~5 min).

UiO-66@HM-UiO-66-F_4. A suspension (10 mL) comprising 25 mM BDC-F_4, 25 mM $ZrCl_4$, 2.9 wt % F-127, 1.75 M AcOH, and 1.0 wt % UiO-66 NPs was heated and stirred to achieve the overgrowth of UiO-66-F_4 on the UiO-66 NP seeds. Specifically, as-synthesized UiO-66 NPs batch 1 (100 mg) were added to an aliquot (5 mL) of stock solution C in an 8 dram vial. The resulting suspension was sonicated for 10 min to ensure homogenization and then combine with an aliquot (5 mL) of stock solution D. A magnetic stir bar was added; the vial was capped and put into a 90 ºC oil bath with stirring on for 24 h, during which time the reaction mixture becomes white and milky. The vial was then removed from the oil bath and left to cool down to room temperature to afford a homogeneous suspension that remains stable for several hours without obvious precipitation, indicating that the mixture is reasonably stable as a colloidal suspension. The reaction mixture was transferred into a 50 mL centrifuge tube and subjected to centrifugation (10000 rpm, 10 min); the supernatant was removed by decantation to remove unreacted reagents and F-127. MeOH (~25 mL) was added to the centrifuge tube and the tube was sonicated (~10 min) to homogenize the mixture. The resulting suspension was subjected to centrifugation (10000 rpm, 10 min) and the supernatant was removed by decantation. This MeOH-washing procedure was repeated twice more, after which the product was left to air-dry inside the tube. The dry product was then subjected to Soxhlet extraction with MeOH to fully remove the F-127 polymer

from the product (~ 3 days under vigorous heating with a 120 ºC oil bath; as analyzed by absence of the polymer signals in the ^{1}H NMR spectrum of a small amount of the digested MOF (Figure 2.8; see Section 2.12.3 for procedure). The product was then collected from the Soxhlet thimble, air-dried, and further dried for 24 h inside a 120 ºC vacuum oven. Yield = 150 ± 7 mg based on average of three experiments, indicating ~50% mass increase from the overgrowth (~57 % yield calculated from the amount of starting materials (Zr (IV) and BDC-F_4) and the ideal formula of UiO-66-F_4 ($Zr_6O_4(OH)_4(C_8F_4O_4)_6$)). This material can be redispersed in water at the 1 mg/mL concentration without visible sign of precipitations.

UiO-66@HM|$_{2nd}$-UiO-66-F_4 and UiO-66@HM|$_{3rd}$-UiO-66-F_4. UiO-66@HM|$_{2nd}$-UiO-66-F_4 was synthesized from UiO-66@HM-UiO-66-F_4 prior to work up. Briefly, after the 24 h overgrowth period of the 1st round of growth, the reaction suspension in the 8 dram vial was cooled down to room temperature, transferred into a 50 mL centrifuge tube, subjected to centrifugation (10000 rpm, 10 min), and then subjected to decantation to afford a white paste on the bottom of the centrifuge tube. This paste was then re-dispersed into an aliquot (5 mL) of solution C under sonication (10 min) to give a milky suspension that was transferred back into the 8 dram vial. An aliquot (5 mL) of solution D was then added into the vial, which was capped and put back to the 90 ºC oil with stirring on for another 24 h.

For UiO-66@HM|$_{3rd}$-UiO-66-F_4, the aforementioned overgrowth procedure was repeated once more from UiO-66@HM|$_{2nd}$-UiO-66-F_4 prior to work up.

Workup. After the overgrowth step, the vial was removed from the oil bath and left to cool down to room temperature. In both cases (2nd and 3rd round of overgrowth), stable white milky suspensions were observed in the vial for several hours without obvious precipitation, indicating that the mixtures are reasonably stable as colloidal suspensions. The reaction mixture was

transferred into a 50 mL centrifuge tube and subjected to centrifugation (10000 rpm, 10 min); the supernatant was removed by decantation to remove unreacted reagents and F-127. MeOH (~25 mL) was added to the centrifuge tube and the tube was sonicated (~10 min) to homogenize the mixture. The resulting suspension was subjected to centrifugation (10000 rpm, 10 min) and the supernatant was removed by decantation. This MeOH-washing procedure was repeated twice more, after which the product was left to air-dry inside the tube. The dry product was then subjected to Soxhlet extraction with MeOH to fully remove the F-127 polymer from the product (~ 3 days under vigorous heating with a 120 ºC oil bath; as confirmed by absence of the polymer signals in the ^{1}H NMR spectrum of a small amount of the digested MOF; see Section 2.12.3 for procedure). The product was then collected from the Soxhlet thimble, air-dried, and further dried for 24 h inside a 120 ºC vacuum oven. Each growth round gives a mass gain ~50 mg, which corresponds to a ~57% yield calculated from the amount of starting materials (Zr(IV) and BDC-F_4) and the ideal formula of UiO-66-F_4 ($Zr_6O_4(OH)_4(C_8F_4O_4)_6$). These materials can be redispersed in water at the 1 mg/mL concentration without visible sign of precipitations.

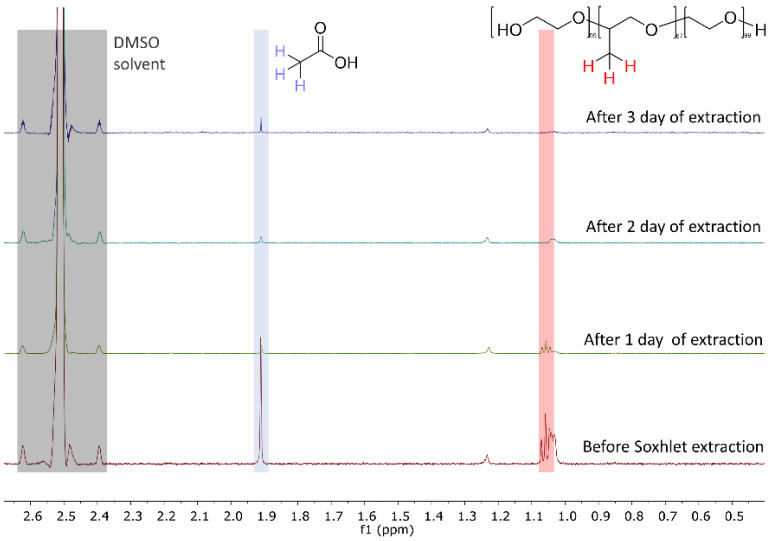

Figure 2.8 ^{1}H NMR spectra of digested UiO-66@HM-UiO-66-F_4 samples after MeOH washing (red) and after 1 (green), 2 (blue), and 3 days (purple) of Soxhlet

extraction. The approximate F-127 amount was calculated by integrating the methyl signal from the PPO segment (~1.02-1.05 ppm)[122] against a maleic acid internal standard. The drop in acetic acid amount indicates that the Soxhlet extraction also helped to remove any residual acetic acid that were not rinsed out by simple MeOH washing.

UiO-66@HM-UiO-66(Hf)-F_4, UiO-66@HM|$_{2nd}$-UiO-66(Hf)-F_4, or UiO-66@HM|$_{3rd}$-UiO-66(Hf)-F_4. These three materials were synthesized and worked up using the same procedures as the Zr counterparts (UiO-66@HM-UiO-66-F_4, UiO-66@HM|$_{2nd}$-UiO-66-F_4, and UiO-66@HM|$_{3rd}$-UiO-66-F_4) except that $HfCl_4$ (320 mg, 1 mmol) was used to prepare solution D instead of $ZrCl_4$.

UiO-66@HM|$_{3rd}$-UiO-66-$(OH)_2$, UiO-66@HM|$_{3rd}$-UiO-66-$(COOH)_2$, UiO-66@IP|$_{3rd}$-UiO-66-NH_2, and UiO-66@IP|$_{3rd}$-UiO-66. These four materials were synthesized and worked up using the same procedures as the UiO-66@HM|$_{3rd}$-UiO-66-F_4 except that BDC-$(OH)_2$ (198 mg, 1 mmol), BDC-$(COOH)_2$ (254 mg, 1 mmol), BDC-NH_2 (181 mg, 1 mmol), and BDC (166 mg, 1 mmol) was used to prepare solution C instead of BDC-F_4. In addition, UiO-66 NPs batch 2 was used as the seeds.

[Zr+BDC-F_4]* non-porous phase. An aliquot (5 mL) of solution C was mixed with an aliquot (5 mL) of solution D in an 8 dram vial equipped with a magnetic stir bar. The vial was capped and put into a 90 ºC oil bath with the stirring on for 24 h, during which time the reaction mixture becomes white and milky. The vial was then removed from the oil bath and left to cool down to room temperature. The reaction mixture was transferred into a 50 mL centrifuge tube and subjected to centrifugation (10000 rpm, 10 min); the supernatant was removed by decantation to remove unreacted reagents and F-127. MeOH (~25 mL) was added to the centrifuge tube and the tube was sonicated (~10 min) to homogenize the mixture. The resulting MeOH suspension was subjected to centrifugation (10000 rpm, 10 min) and the supernatant was removed by decantation.

This MeOH-washing procedure was repeated twice more, after which the product was left to air-dry inside the tube. The dry product was then subjected to Soxhlet extraction with MeOH. The product was then collected from the Soxhlet thimble, air-dried, and further dried for 24 h inside a 120 ºC vacuum oven. Yield = ~30 mg.

[Zr+BDC-$(OH)_2$]*, [Zr+BDC-$(COOH)_2$]*, and [Zr+BDC-NH_2]* phases. These materials were synthesized and worked up using the same procedures as the [Zr+BDC-F_4]* except that BDC-$(OH)_2$ (198 mg, 1 mmol), BDC-$(COOH)_2$ (254 mg, 1 mmol), and BDC-NH_2 (181 mg, 1 mmol) was used to prepare solution C instead of BDC-F_4.

For the next two syntheses, the following solutions are prepared in advance and used within 1 day:

Solution E. This solution was prepared by dissolving BDC-F_4 (238 mg, 1 mmol) with $AcOH_{aq}$ (20 mL of a 1.75 M aqueous solution) under sonication (~5 min).

Solution F. This solution was prepared by dissolving $ZrCl_4$ (233 mg, 1 mmol) with $AcOH_{aq}$ (20 mL of a 1.75 M aqueous solution) under sonication (~5 min).

UiO-66|UiO-66-F_4. As-synthesized UiO-66 NPs batch 1 (100 mg) were dispersed into an aliquot (5 mL) of solution E in an 8 dram vial equipped with a magnetic stir bar. The resulting suspension was sonicated for 10 min to homogenize the mixture and then combined with an aliquot (5 mL) of solution F. The vial was capped and put into a 90 ºC oil bath with stirring on for 24 h, during which time the reaction mixture becomes white and milky. The vial was then removed from the oil bath and left to cool down to room temperature. The reaction mixture was transferred into a 50 mL centrifuge tube and subjected to centrifugation (10000 rpm, 10 min). The supernatant was removed by decantation; the remaining paste was re-dispersed into MeOH (25 mL) by sonication (10 min) before being subjected to centrifugation (10000 rpm, 10 min) and decantation of the supernatant. This MeOH-washing procedure was repeated twice more, after which the product

was left to air-dry inside the tube, transferred into a 20 mL vial, and further dried inside a 120 °C vacuum oven. Yield = ~160 mg.

UiO-66-F_4. This MOF was synthesized based on a reported aqueous synthesis.[99] An aliquot (5 mL) of solution of E was mixed with an aliquot (5 mL) of solution F in an 8 dram vial equipped with a magnetic stir bar. The vial was capped and put into a 90 ºC oil bath with stirring on for 24 h, during which time the reaction mixture becomes white and milky. The vial was then removed from the oil bath and left to cool down to room temperature. The reaction mixture was transferred into a 50 mL centrifuge tube and subjected to centrifugation (10000 rpm, 10 min). The supernatant was removed by decantation; the remaining paste was re-dispersed into MeOH (25 mL) by sonication (10 min) before being subjected to centrifugation (10000 rpm, 10 min) and decantation of the supernatant. This MeOH-washing procedure was repeated twice more, after which the product was left to air-dry inside the tube, transferred into a 20 mL vial, and further dried inside a 120 ºC vacuum oven under. Yield = ~30 mg.

2.12.3 Compositional analyses of the UiO-66s and the unknown phase

Procedure for the quantitative analysis of the Zr/Hf content in UiO-66 materials. Into a 15 mL polypropylene centrifuge tube, conc. HNO_3 (750 μL), HCl (250 μL), and HF (250 μL) were added to a small amount of sample (~1 mg) to be analyzed. The resulting mixture was sonicated until the solution became clear (~2 h) albeit sometimes small white flakes could still be seen on the bottom. After the sonication, DI H_2O (3.750 mL) was added into the tube, which was then capped and placed into a 70 ºC oil bath for 12 h. At the end, the solution was clear and no solid was visible. The resulting solution was then transferred into a 50 mL polypropylene centrifuge tube and diluted with DI water to a final volume of 50 mL. This solution was then analyzed for Zr and

Hf by ICP-OES (λ_{Zr} = 343.823, 327.305, 349.621, and 339.198 nm; λ_{Hf} = 339.980, 232.247, and 277.336 nm) against a calibration curve of standards with known [Zr] or [Hf].

Caution: HF is very toxic and dangerous to handle without proper safety training. PPE must include Silvershield gloves and goggles. Acid digestions and subsequent dilutions should be carried out in a well-ventilated hood.

Procedure for the quantitative analyses of BDC, BDC-F_4, and acetic acid in MOF. The ^{1}H NMR/^{19}F NMR spectra of the digested MOFs can quantitatively reveal the composition of the organic ligands and acetic acid present in each digested sample and the ICP-OES data can yield the weight percentage of Zr and Hf composition in the sample. Thus, the linker to node (L/N) ratio and chemical formula can be determined for the materials. Data is shown in Table 2.1.

BDC (^{1}H NMR). In a 15 mL polypropylene centrifuge tube, HF (10 μL) and DMSO-*d*$_6$ (90 μL) were added to a small sample (~2 mg) of the material to be analyzed. The resulting mixture was sonicated until the solution became clear (~1 h). Then an aliquot (10 μL, corresponding to ~0.2 mg of the sample) of the resulting solution was transferred to a 2 mL polypropylene centrifuge tube along with an aliquot of maleic acid (MA) solution in DMSO-d_6 (12 mM, 50 μL), and fresh DMSO-*d*$_6$ (540 μL). This combined solution was transferred into an NMR tube and then analyzed by ^{1}H NMR spectroscopy with a 90^o pulse using a 50 s delay between scans, which exceed the T1 relaxation time for BDC (3.7 s) and MA (2.8 s). The amount of each substrate was calculated by comparing the integration against a calibration curve of standards with known concentrations (see Figure 2.9 for calibration curve, and Figure 2.10 for NMR spectra).

BDC-F_4 (^{19}F NMR). In a 15 mL polypropylene centrifuge tube, HF (10 μL) and DMSO-*d*$_6$ (90 μL) were added to a small sample (~2 mg) of the material to be analyzed. The resulting mixture was sonicated until the solution became clear (~1 h). Then an aliquot (10 μL, corresponding to

~0.2 mg of the sample) of the resulting solution was transferred to a 2 mL polypropylene centrifuge tube along with an aliquot of 4.0 mM trifluoroacetic acid (TFA) solution in DMSO-d_6 (50 µL), and fresh DMSO-d_6 (540 µL). This combined solution was transferred into an NMR tube and then analyzed by ^{19}F NMR spectroscopy with a 90º pulse using a 5 s delay between scans, which exceed the T1 relaxation time for BDC-F_4 (435 ms), and TFA (107 ms). The amount of each substrate was calculated by comparing the integration against a calibration curve of standards with known concentrations (see Figure 2.9 for calibration curve, and Figure 2.11 for NMR spectra).

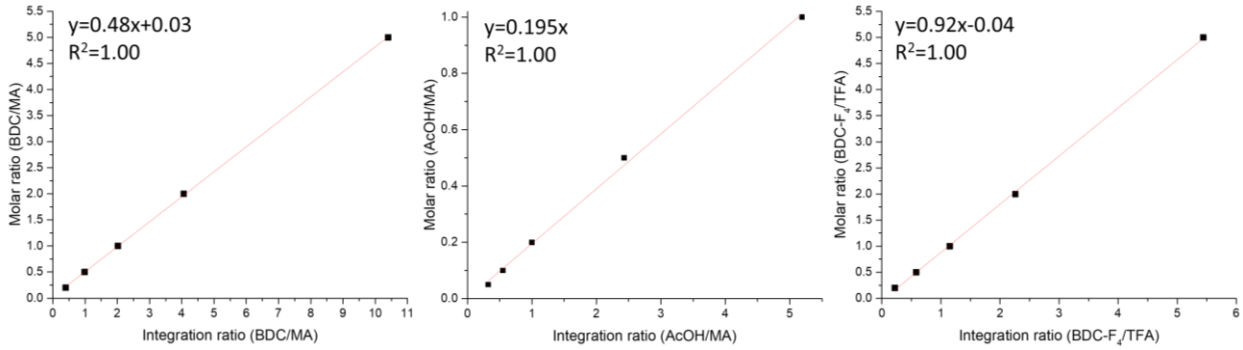

Figure 2.9 NMR (^{1}H and ^{19}F) calibration curves for BDC (left), AcOH (middle), and BDC-F_4 (right) against the internal standards (MA for ^{1}H; TFA for ^{19}F).

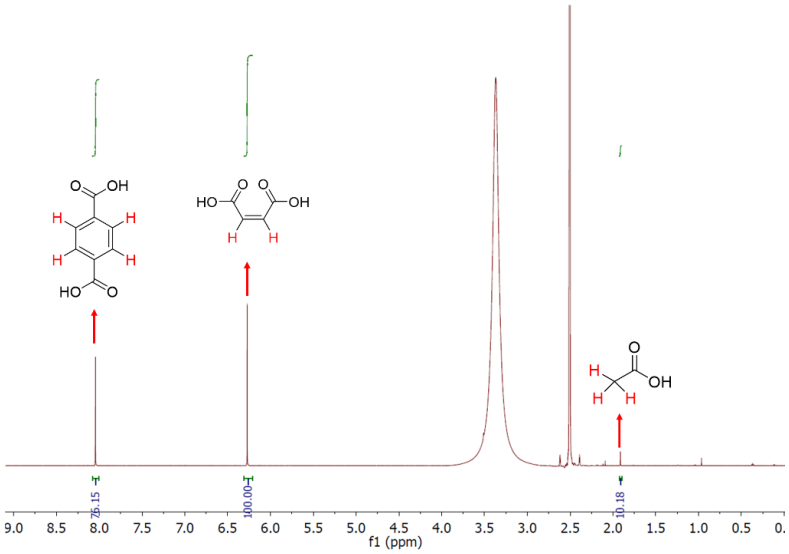

Figure 2.10 ^{1}H NMR spectrum of the digested UiO-66@HM-UiO-66-F_4 with MA as the internal standard.

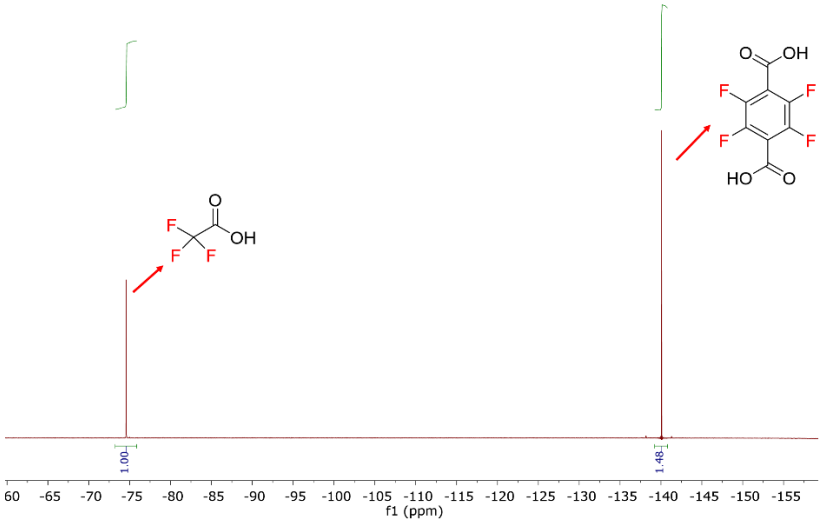

Figure 2.11 ^{19}F NMR spectrum of the digested UiO-66@HM-UiO-66-F_4 with TFA as the internal standard.

Table 2.1 Molecular formulas of UiO-66s as determined by NMR and ICP-OES quantitative analyses.

UiO-66 sample	Zr_6-cluster content (μmol/mg of MOF)	Hf_6-cluster content (μmol/mg of MOF)	BDC content (μmol/mg of MOF)	BDC-F_4 content (μmol/mg of MOF)	Molecular formula[a]
UiO-66 seeds	0.52	-	2.74	-	$Zr_6O_4(OH)_4(BDC)_{5.3}(CH_3COO)_{0.1}(OH)_{1.3}(H_2O)_{1.3}$
UiO-66-F_4	0.49	-	-	2.44	$Zr_6O_4(OH)_4(BDC\text{-}F_4)_{5.0}(CH_3COO)_{0.1}(OH)_{1.9}(H_2O)_{1.9}$
UiO-66|UiO-66-F_4	0.55	-	1.48	1.18	$Zr_6O_4(OH)_4(BDC)_{2.7}(BDC\text{-}F_4)_{2.1}(CH_3COO)_{0.2}(OH)_{2.2}(H_2O)_{2.2}$
UiO-66@HM-UiO-66-F_4	0.56	-	1.48	1.18	$Zr_6O_4(OH)_4(BDC)_{2.6}(BDC\text{-}F_4)_{2.1}(CH_3COO)_{0.1}(OH)_{2.5}(H_2O)_{2.5}$
UiO-66@HM|$_{2nd}$-UiO-66-F_4	0.55	-	1.10	1.47	$Zr_6O_4(OH)_4(BDC)_{2.0}(BDC\text{-}F_4)_{2.7}(CH_3COO)_{0.1}(OH)_{2.5}(H_2O)_{2.5}$
UiO-66@HM|$_{3rd}$-UiO-66-F_4	0.54	-	0.93	1.52	$Zr_6O_4(OH)_4(BDC)_{1.7}(BDC\text{-}F_4)_{2.8}(CH_3COO)_{0.1}(OH)_{2.9}(H_2O)_{2.9}$
UiO-66@HM-UiO-66(Hf)-F_4	0.31	0.32	1.4	1.1	$[Zr_6O_4(OH)_4]_{0.5}[Hf_6O_4(OH)_4]_{0.5}(BDC)_{2.2}(BDC\text{-}F_4)_{1.7}(OH)_{4.2}(H_2O)_{4.2}$[b]
UiO-66@HM|$_{2nd}$-UiO-66(Hf)-F_4	0.24	0.40	0.96	1.2	$[Zr_6O_4(OH)_4]_{0.37}[Hf_6O_4(OH)_4]_{0.63}(BDC)_{1.5}(BDC\text{-}F_4)_{1.9}(OH)_{5.2}(H_2O)_{5.2}$[b]
UiO-66@HM|$_{3rd}$-UiO-66(Hf)-F_4	0.15	0.53	0.88	1.6	$[Zr_6O_4(OH)_4]_{0.23}[Hf_6O_4(OH)_4]_{0.77}(BDC)_{1.3}(BDC\text{-}F_4)_{2.4}(OH)_{4.6}(H_2O)_{4.6}$[b]

[a]The formulas of UiO-66 MOFs are determined from the ^1H and ^{19}F NMR spectra and ICP-OES data of the digested materials. The open sites were assumed to be terminated by μ_1-OH and μ_1-OH_2. [b]The chemical formulas are calculated based on the assumption that all of the Hf contents are from the $Hf_6O_4(OH)_4$ cluster nodes. However, a recent work has shown hafnium oxide can form on the surface of Zr-based UiO-66 during metal-ion exchange.[123] This could explain the derived "defect-rich" chemical formulas of the Hf overgrown materials.

2.12.4 Characterization data for the MOF materials

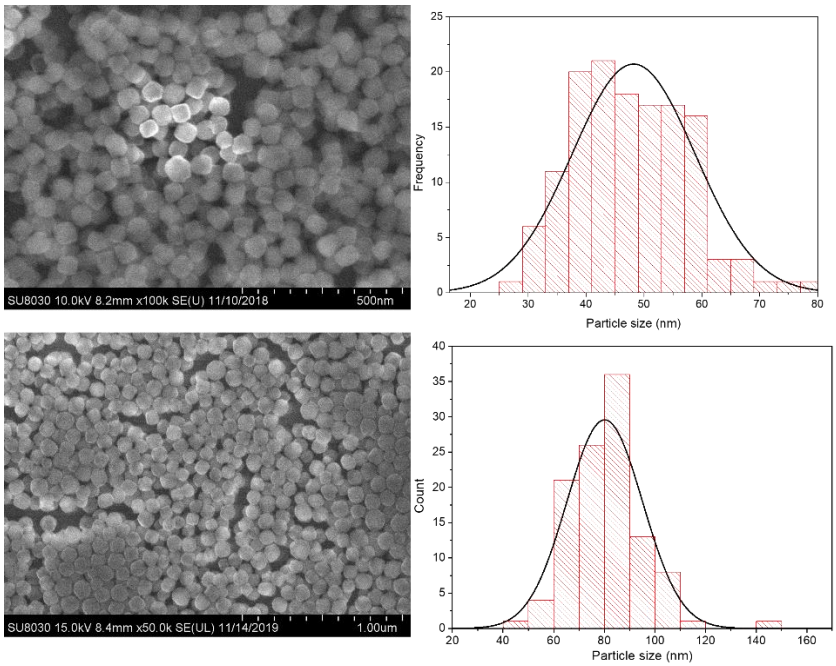

Figure 2.12 (Top) SEM image of the UiO-66 NPs batch 1 (left). The corresponding SEM-derived particle-size-distribution profile for the UiO-66 NPs batch 1 (μ = 48.2 nm; σ = 10.6 nm) (right). (Bottom) SEM image of the UiO-66 NPs batch 2 (left). The corresponding SEM-derived particle-size-distribution profile for the UiO-66 NPs batch 2 (μ = 80.1 nm; σ = 15.0 nm) (right).

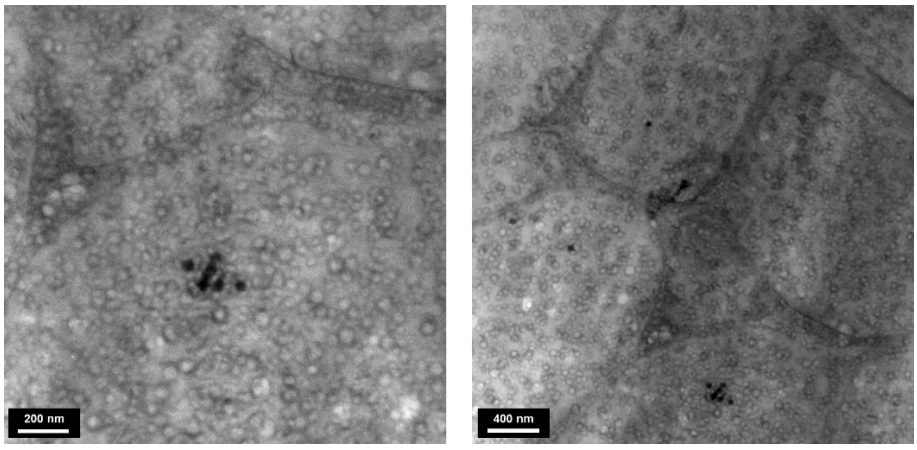

Figure 2.13 CyroTEM images of the structures observed in a [2.9 wt % F-127 + 0.1 wt % UiO-66 NP seeds]$_{aq}$ mixture.

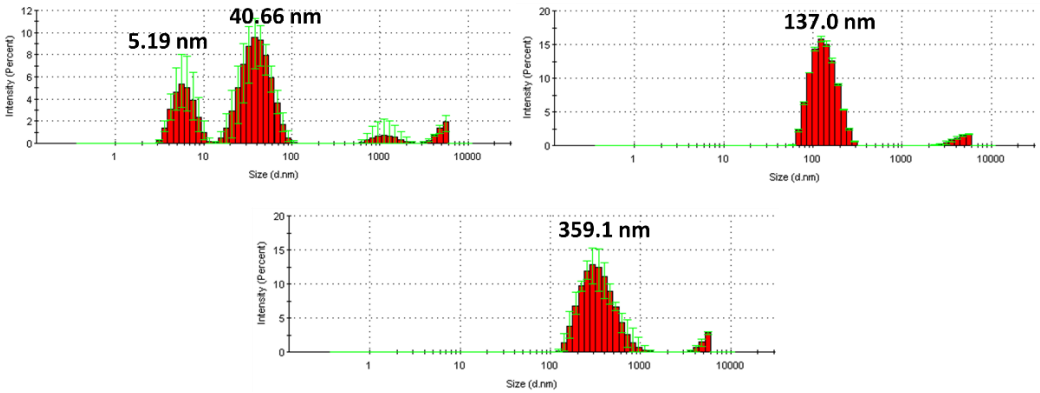

Figure 2.14 DLS intensity-based distribution profiles of aqueous dispersions of: 2.9 wt % F-127 (top left), 0.1 wt % UiO-66 NPs (top right), and [2.9 wt % F-127 + 0.1 wt % UiO-66 NPs] (bottom).

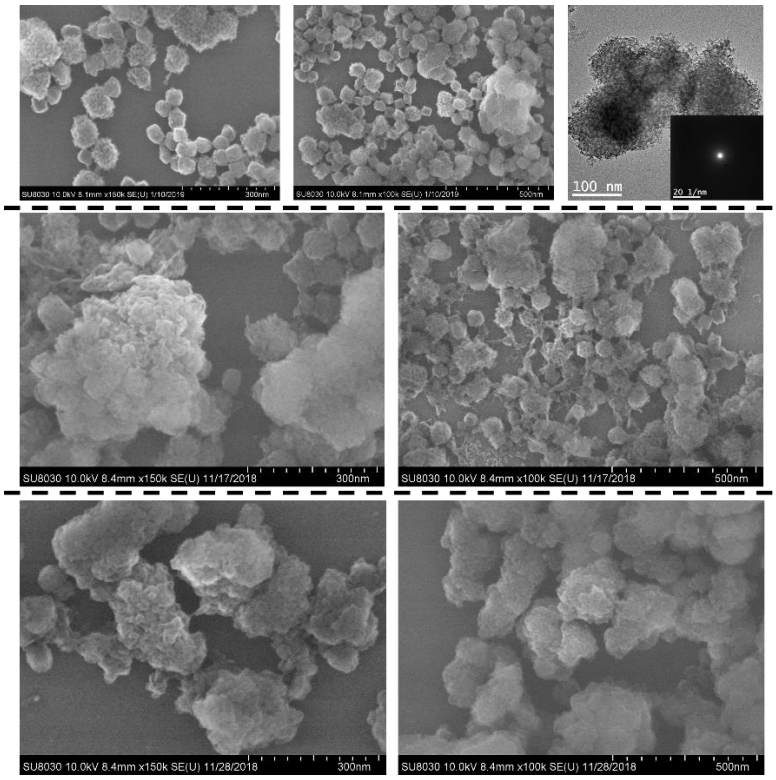

Figure 2.15 (Top) SEM images, TEM image, and corresponding SAED result of UiO-66@HM-UiO-66-F_4. (Middle) SEM images of UiO-66@HM|$_{2nd}$-UiO-66-F_4. (Bottom) SEM images of UiO-66@HM|$_{3rd}$-UiO-66-F_4. In an attempt to show that the HM-MOF shell does possess good crystallinity, we have tried to obtain an SAED pattern for the UiO-66@HM-UiO-66-F_4 sample using TEM. Unfortunately, we did not see convincing SAED data (i.e., clear diffraction spots, see the right panel in the top row) for this sample. This is not suprising in retrospect given the high beam voltage (200 kV) of our equipment and the small size (~50 nm) of our seed nanoparticles. We note that Zhu et al.[124] was only able to obtain good SAED pattern from a large (200 nm) UiO-66 microcrystal under a nano beam diffraction mode with low (120 kV) voltage and a very low electron dosage level; even then the crystal was still damaged during the alignment. As a verification of our instrument limitation, we also attempted to obtain the SAED pattern for the starting UiO-66 seeds (~50 nm in size) and a larger-size crystal (~100-200 nm), both of which also did not show any obvious diffraction pattern (Kikuchi lines were not seen or vanished very quickly). Nevertheless, we are confident that our HM-MOF materials possess good crystallinity based on the BET surface area that for our HM-UiO-66-F_4 material. It matches closely to that predicted for a physical mixture of crystalline [66 wt % UiO-66 + 33 wt % UiO-66-F_4] MOFs at the same mass proportion. See Table 2.2 for the comparative data.

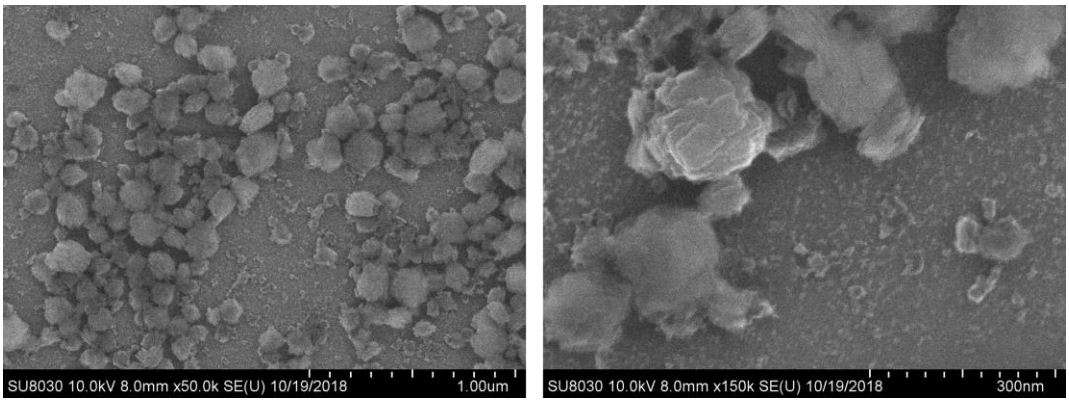

Figure 2.16 SEM images of the [Zr+BDC-F_4]* non-porous phase.

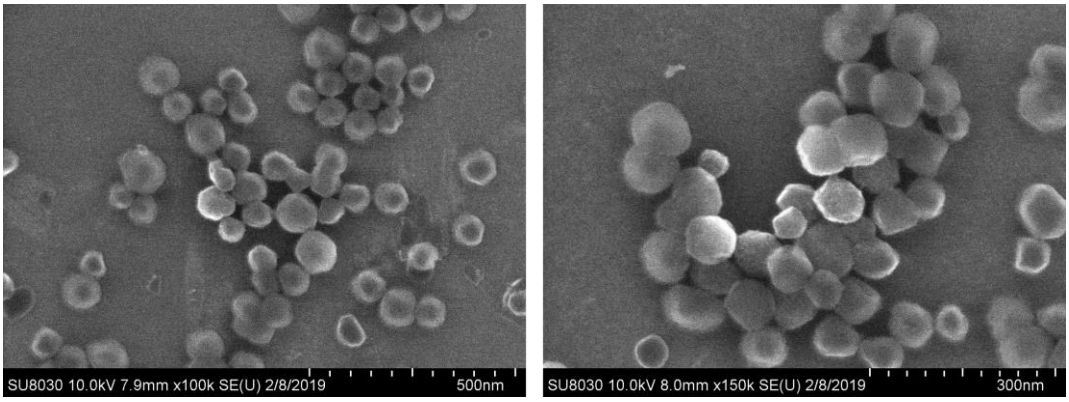

Figure 2.17 SEM images of UiO-66|UiO-66-F_4.

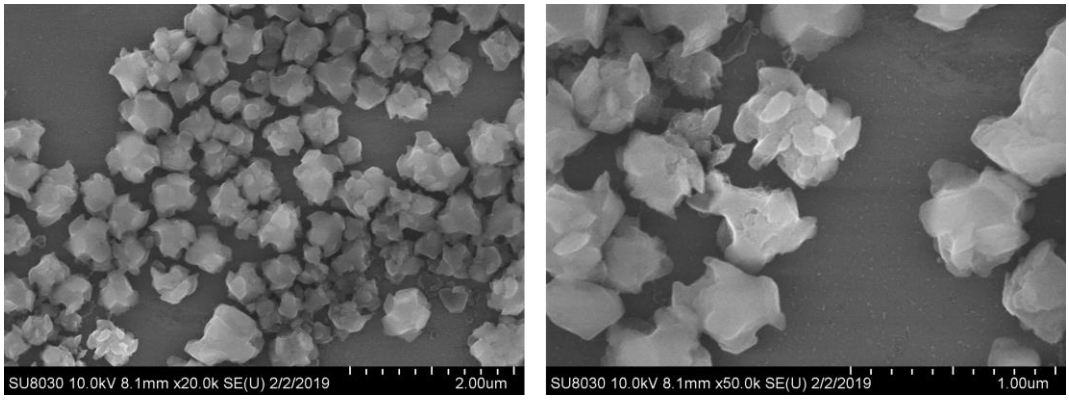

Figure 2.18 SEM images of UiO-66-F_4.

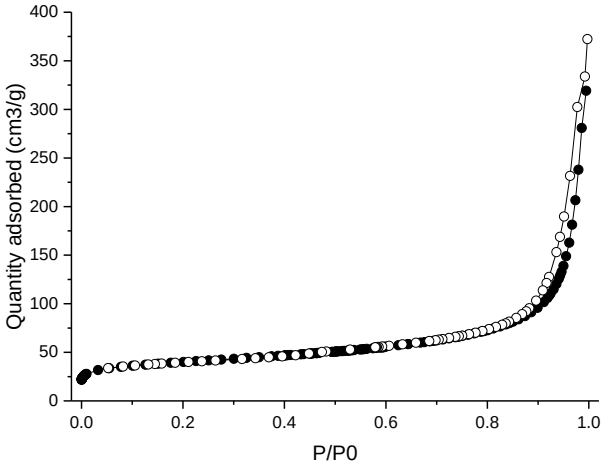

Figure 2.19 N_2 physisorption isotherm of the [Zr+BDC-F_4]* non-porous phase. Close symbols, adsorption; open symbols, desorption.

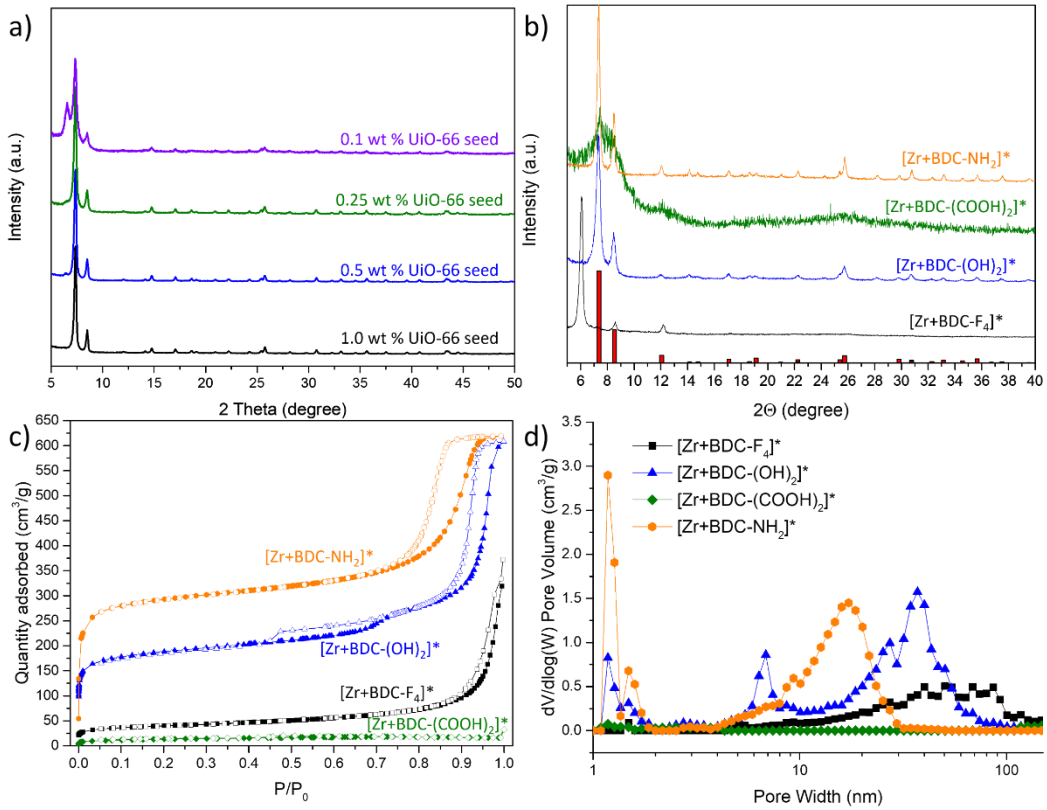

Figure 2.20 (a) PXRD profiles of the UiO-66@HM-UiO-66-F_4 overgrowth materials using different ratio of seeds to a 1:1 mixture of precursor solutions C and D (see Section 2.12.2): 0.10 (purple), 0.25 (green), 0.50 (blue), and 1.0 wt % (black). (b-d) PXRD profiles (b), N_2 physisorption isotherms (c), and DFT PSDF profiles (d) of the [Zr+BDC-F_4]*, [Zr+BDC-$(OH)_2$]*, [Zr+BDC-$(COOH)_2$]*, and [Zr+BDC-NH_2]* phases grown in the absence of UiO-66 NP seeds. The data shown in panels b-d clearly illustrate how the pore properties of these phases are affected by the solubility of the added linkers in water. Without the UiO-66 NP seeds to direct the growth, non-porous product was often obtained when the added linkers are soluble in water (i.e., forming clear solution in 50 mM concentration, such a BDC-F_4 and BDC-$(COOH)_2$, see Figure 2.36c). In contrast, crystalline UiO-66 materials can be formed when the organic linker have low solubility in water (as in the case of BDC-$(OH)_2$ and BDC-NH_2, see Figure 2.36c). Interestingly, only the phase made from BDC-$(OH)_2$ exhibits template-induced mesopores (~7 nm) that match the size of the F-127 micelle, probably due to the strong H-bonding interaction between the linker and the Pluronic backbone. To the extreme, a similar non-seed-mediated growth with the BDC linker did not form any solid product after 24 h reaction, attributable to the low solubility of the added linker.

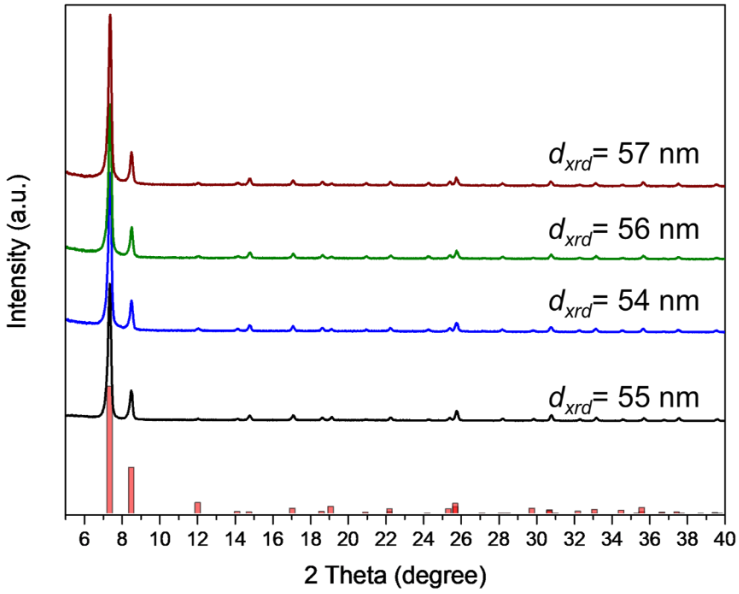

Figure 2.21 PXRD profiles of simulated UiO-66, UiO-66@HM-UiO-66-F_4, UiO-66@HM|$_{2nd}$-UiO-66-F_4, and UiO-66@HM|$_{3rd}$-UiO-66-F_4. The d_{xrd} values on the right hand side of each experimental profile were calculated using Scherrer's equation.

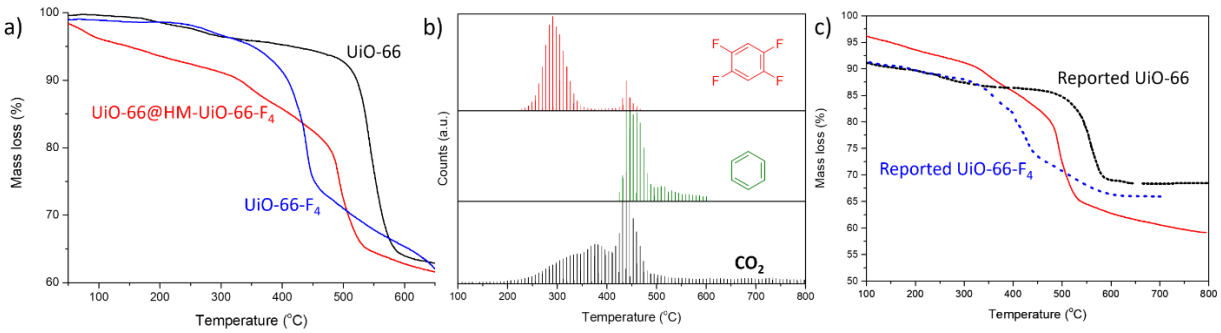

Figure 2.22 (a) TGA profiles of UiO-66@HM-UiO-66-F_4, UiO-66 NP seeds batch 1, and UiO-66-F_4. (We note that the profiles for our UiO-66 seeds and UiO-66-F_4 materials are comparable to the published data[99] for aqueously synthesized UiO-66 and UiO-66-F_4 samples (see panel c).) The two major mass-loss stages of UiO-66@HM-UiO-66-F_4 (~320 ºC and 480 ºC) match with those of the UiO-66-F_4 and UiO-66 materials respectively, indicating the presence of both components in the core-shell materials. (b) The corresponding GCMS(EI)-temperature profiles on m/z of 44 (CO_2), 78 (C_6H_6), and 150 ($C_6H_2F_4$) collected during the TGA analysis of UiO-66@HM-UiO-66-F_4 (red curve in panel a). They are assigned as fragments generated by decarboxylation reaction under high temperature and Ar atmosphere (CO_2, benzene, and 1,2,4,5-tetrafluorobenzene). (c) TGA profile of UiO-66@HM-UiO-66-F_4 and reported[99] TGA profiles of aqueously synthesized UiO-66 and UiO-66-F_4 materials. Data for these last two materials were digitized by us from the published work.[99] A gradual mass loss before 300 ºC was observed in the TGA profiles of all three materials, which could be resulted from the decomposition of defective regions in aqueously synthesized UiO-66 materials.

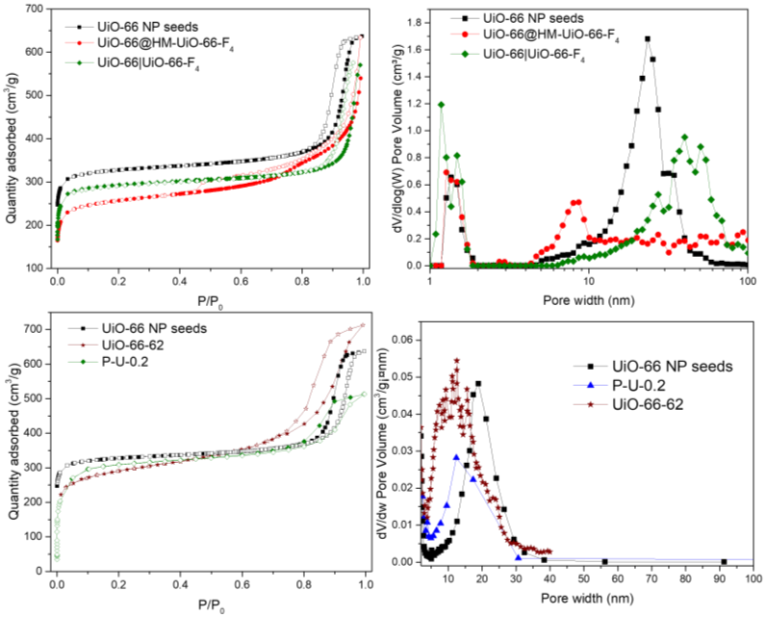

Figure 2.23 (Top) N_2 physisorption isotherms (top left) and DFT PSDF profiles (top right) of the UiO-66 NP seeds (black square), UiO-66@HM-UiO-66-F_4 (red circle), and UiO-66|UiO-66-F_4 (olive diamond). Close symbols, adsorption; open symbols, desorption. These data clearly showed that UiO-66@HM-UiO-66-F_4 is very different from the other two samples. (Bottom) N_2 physisorption isotherms (bottom left) and BJH PSDF profiles (bottom right) of the as-synthesized UiO-66 NP seeds (black square), the P-U-0.2 materials reported by Zhang et al.[53](blue circle), and the UiO-66-62 sample reported by Niu et al.[52] (burgundy star). Data for the P-U-0.2 material was provided by Dr. Xiaodong Zhang while data for the UiO-66-62 material was digitized by us from the published work.[52] Thus, the number of data points shown for the latter sample in the bottom panels do not reflect the actually number of collected datapoints. Even with these limitations, these data also show that our seed material is quite similar to the other two materials, which have interparticle porosity. For ease of comparison to the data reported by Zhang et al.,[53] the PSDFs profiles shown here for our two materials were produced using the desorption branch of the isotherms. We note, however, that this is not a recommended practice for hierarchically porous materials such as our UiO-66@HM-UiO-66 for which the adsorption branches of the isotherms should be used to obtain PSDFs to take into account the cavitation desorption mechanism when H4-type hysteresis loop or small pore neck size (< 5-6 nm) was observed.[12] (Disclaimer: We do not know from which branch was the PSDF profile reported by Niu et al.[52] being derived. In addition, the PSDF plot was limited to < 40 nm because the reported PSDF profile for UiO-66-62 was only shown to 40 nm pore width.)

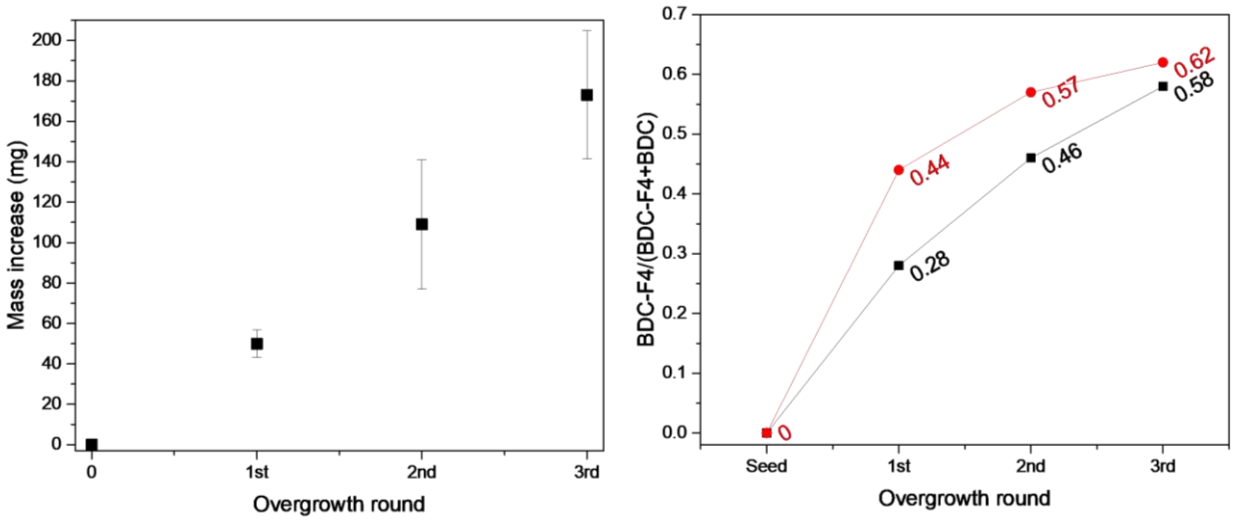

Figure 2.24 Plot of mass increase (left) and the change in BDC-F_4 content (right: red circle = experimental; black cube = calculated theoretical value; see explanation below) versus the overgrowth rounds. The absolute amounts of BDC-F_4 and BDC were determined by quantitative ^{19}F and ^{1}H NMR spectroscopies, respectively (see Section 2.12.3 and Table 2.1). The error bars in the left plot were the standard deviations from 3 experimental tries. The data in the right plot were based on a single run. The theoretical BDC-F_4/(BDC-F_4+BDC) ratios were calculated based on mass increases and formulas of defect-free UiO-66 ($Zr_6O_4(OH)_4(C_8H_4O_4)_6$) and UiO-66-$F_4$ ($Zr_6O_4(OH)_4(C_8F_4O_4)_6$), assuming that the mass increases were from newly formed UiO-66-F_4. The experimental results are consistently higher than the theoretical ones because linker exchange may happen during the overgrowth process and not all of the original UiO-66 NP seeds were recovered during the work-up stage (especially during centrifugation and washing).

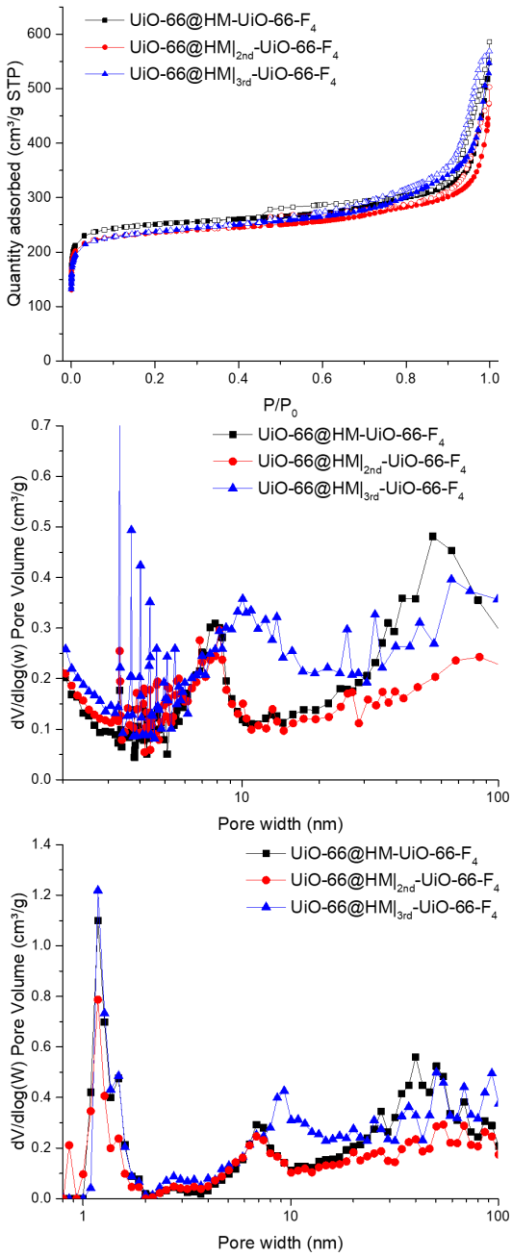

Figure 2.25 N_2 physisorption isotherms (top), BJH PSDFs (middle), and DFT PSDFs (bottom) of: UiO-66@HM-UiO-66-F_4 (black square), UiO-66@HM|$_{2nd}$-UiO-66-F_4 (red circle), and UiO-66@HM|$_{3rd}$-UiO-66-F_4 (blue triangle). Close symbols, adsorption; open symbols, desorption.

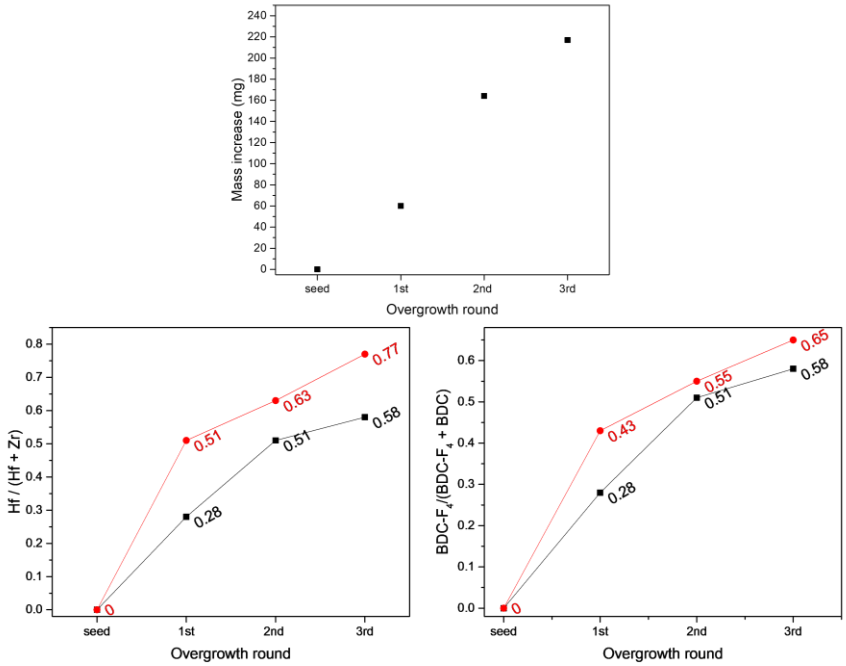

Figure 2.26 Plot of mass increase (top), Hf-content percentage change (bottom left), and BDC-F_4 content percentage change (bottom right) (red circle: experimental; black cube: calculated theoretical value: see explanation below) versus the overgrowth rounds. The absolute amounts of BDC-F_4 and BDC were determined by quantitative ^{19}F and ^{1}H NMR spectroscopies, respectively (see Section 2.12.3 and Table 2.12.1), while the absolute amounts of Hf and Zr were determined using ICP-OES (see Section 2.12.3 for detailed procedure). The theoretical BDC-F_4/(BDC-F_4 + BDC) and Hf/(Hf + Zr) ratios were calculated based on mass increases and formulas of defect-free UiO-66 ($Zr_6O_4(OH)_4(C_8H_4O_4)_6$) and UiO-66-$F_4$ ($Zr_6O_4(OH)_4(C_8F_4O_4)_6$), assuming that the mass increases were from newly formed UiO-66-F_4. The experimental linker ratios are consistently higher than the theoretical ones because linker exchange may happen during the overgrowth and not all of the original UiO-66 NP seeds were recovered during the work-up (especially during centrifugation and washing). A similar trend was observed for the Hf content, which we attributed to node exchange.[125-127] While we could not completely exclude the formation of hafnium oxide as impurities during the overgrowth,[123] we did not observe the hafnium oxide diffraction peak in the PXRD profiles.

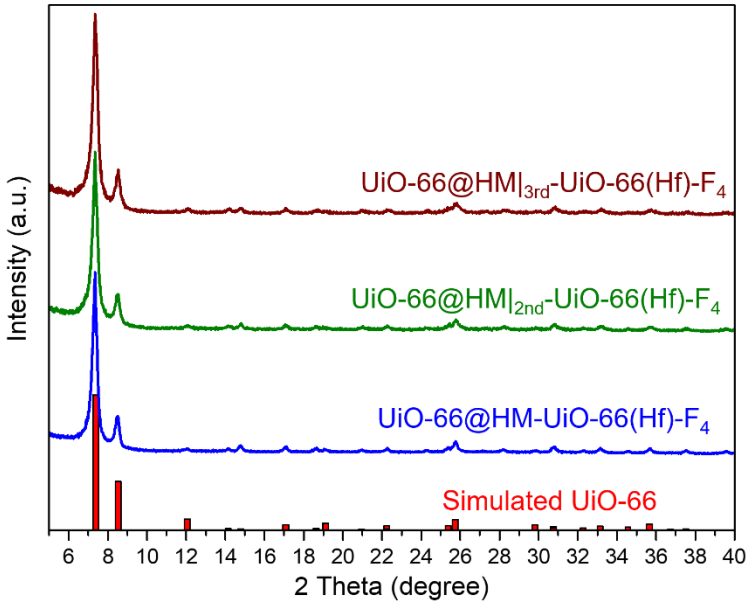

Figure 2.27 PXRD profiles of simulated UiO-66, UiO-66@HM-UiO-66(Hf)-F_4, UiO-66@HM|$_{2nd}$-UiO-66(Hf)-F_4, and UiO-66@HM|$_{3rd}$-UiO-66(Hf)-F_4.

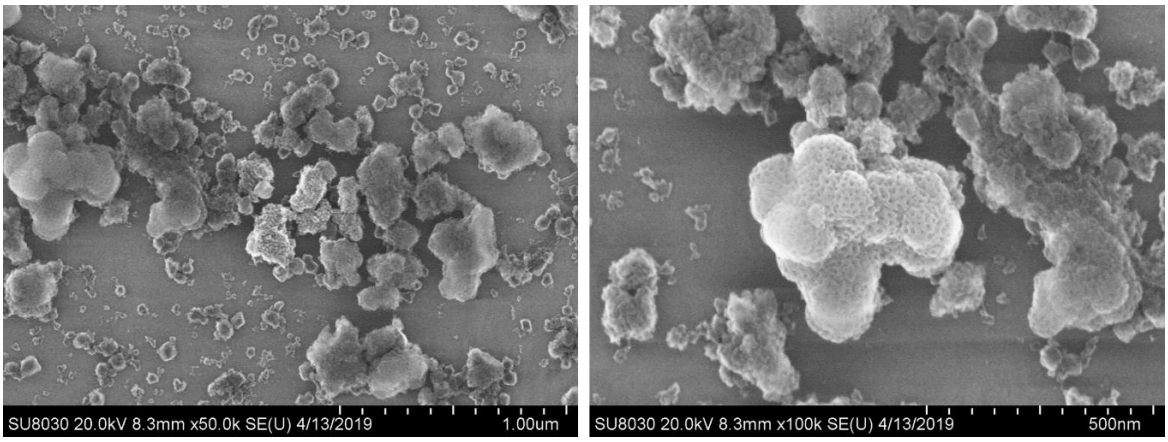

Figure 2.28 SEM images of UiO-66@HM|$_{3rd}$-UiO-66(Hf)-F_4.

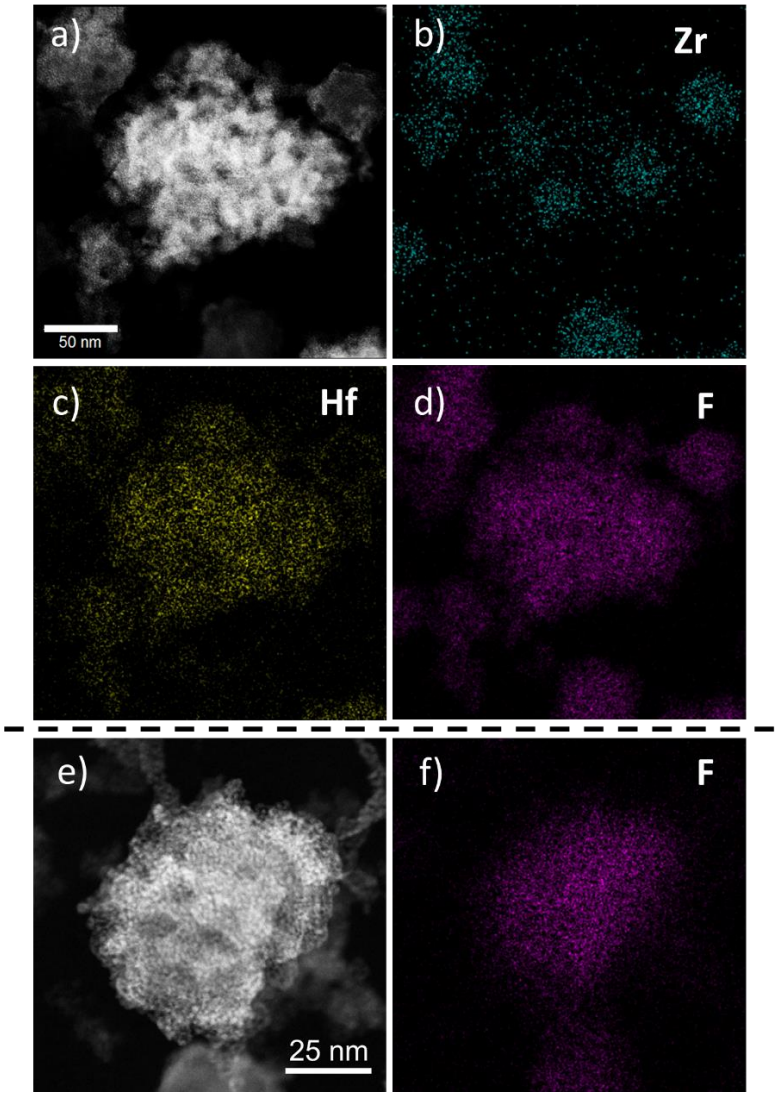

Figure 2.29 (a) High-angle annular dark field (HAADF) image of a sample of UiO-66@HM|$_{3rd}$-UiO-66(Hf)-F_4 and (b-d) the EDS elemental maps–imaged by Zr, Hf, and F, respectively–of the same sample. (e) HAADF image of a sample of UiO-66@HM-UiO-66(Hf)-F_4 (also shown in Figure 2.4a in Section 2.6) and (f) the corresponding F EDS elemental map of this same UiO-66@HM-UiO-66(Hf)-F_4 sample. As discussed in Section 2.6, the F signals appear throughout the particle rather than concentrated mostly on the surface, suggesting that linker exchange has occurred during the formation of UiO-66@HM-UiO-66(Hf)-F_4. The apparent higher density of the F signals at the center of the particles shown in d and f are consequence of the particles being "thicker" in the center.

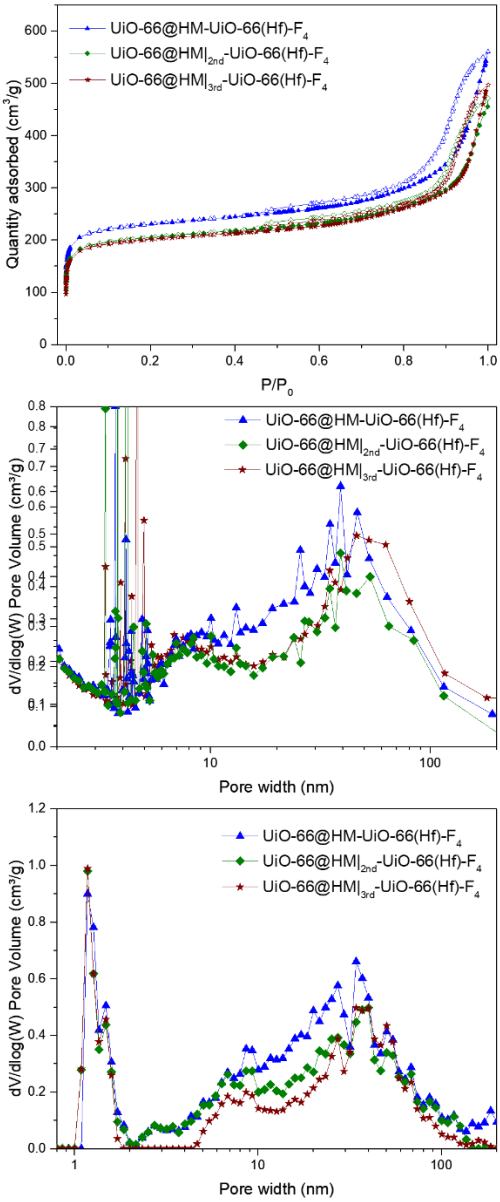

Figure 2.30 N_2 physisorption isotherms (top), BJH PSDFs (middle), and DFT PSDFs (bottom) of: UiO-66@HM-UiO-66(Hf)-F_4 (blue triangle), UiO-66@HM|$_{2nd}$-UiO-66(Hf)-F_4 (olive diamond), and UiO-66@HM|$_{3rd}$-UiO-66(Hf)-F_4 (wine star). Close symbols, adsorption; open symbols, desorption

Table 2.2 N_2 physisorption data of the UiO-66 materials (surface area unit: m^2/g).

UiO-66	$\mathbf{S}_{microporous}$[a]	$\mathbf{S}_{external}$[a]	$\mathbf{S}_{total}$[b]	$(\mathbf{S}_{external}/\mathbf{S}_{total})$[a]	**mesopore size**[e] (nm)
Ideal UiO-66	-	-	1100[c]	-	-
UiO-66 seeds	1121	164	1285	0.13	-
UiO-66-F_4	749	145	894	0.16	-
UiO-66|UiO-66-F_4	955	155	1110	0.14	-
UiO-66@HM-UiO-66-F_4	803	163	966	0.17	8
[66 wt % UiO-66 + 33 wt % UiO-66-F_4]	-	-	1021[d]	-	-
UiO-66@HM$\|_{2nd}$-UiO-66-F_4	746	162	908	0.18	8
UiO-66@HM$\|_{3rd}$-UiO-66-F_4	692	204	895	0.23	9
UiO-66@HM-UiO-66(Hf)-F_4	642	212	855	0.25	9
UiO-66@HM$\|_{2nd}$-UiO-66(Hf)-F_4	575	189	764	0.25	9
UiO-66@HM$\|_{3rd}$-UiO-66(Hf)-F_4	563	183	746	0.25	9

[a]The values were calculated using the t-plot method (see Section 2.12.1 for more parameters and settings for this calculation). [b]The total surface area, S_{total}, was calculated using the BET model. [c]This BET area was obtained from a literature report,[103] calculated by fitting simulated N_2 isotherms. [d]Calculated using the rule of mixture from the specific surface area values of individual components in a physical mixture possessing similar mass proportions as UiO-66@HM-UiO-66-F_4. [e]Only the size of the mesopore resulted from F-127 template effect was listed, as the broad peaks (10-100 nm) in the PSDFs are attributed to interparticle packing that does not contribute to the performance enhancement in solution-uptake experiments (see discussion in Section 2.9).

2.12.5 Procedures for the DB 86-uptake studies

Stock solution of DB 86. DB 86 (78 mg, 0.10 mmol) was dissolved in an aliquot (~5 mL) of DI water and dilute with DI water to 10 mL in a 10 mL volumetric flask to obtain a 10 mM stock solution. Small portions (~0.5-1 mL) of this stock solution were then diluted to appropriate concentrations for calibration and uptake experiments as described below.

UV-vis calibration curve of DB 86. An aliquot (0.5 mL) of the aforementioned stock solution of DB 86 was diluted with DI water to 100 mL in a 100 mL volumetric flask to obtain a 50 µM solution, which was further diluted 2, 5, and 10 times (using a 5 mL calibrated micropipette) to obtain 25, 10, and 5 µM solutions, respectively. The calibration curve (Figure 2.31) was obtained by measuring the absorbance of these four solutions at 622 nm wavelength.

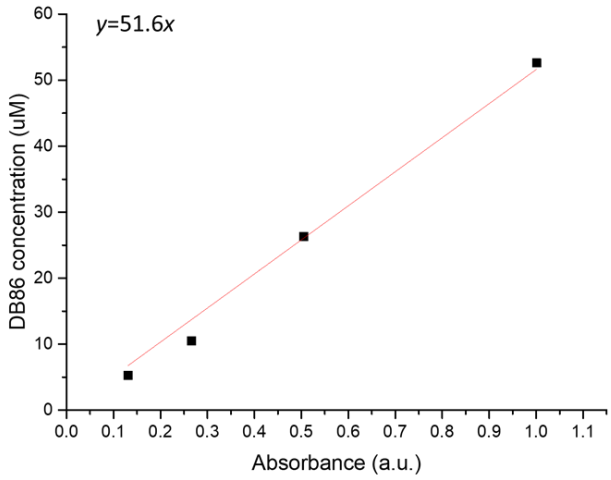

Figure 2.31 UV-vis calibration curve for DB 86 at λ = 622 nm.

The DB 86-uptake experiment. For each uptake experiment, a small portion (2 mL) of the aforementioned stock solution of DB 86 was diluted with DI water to 20 times (using a 5 mL calibrated micropipette) to obtain a solution with a concentration ~500 µM. The exact initial concentration (C_0) of the resulted solution was measured by UV-vis spectroscopy and calculated based on the calibration curve (Figure 2.31). For the uptake experiments, ten portions (1.00 ± 0.05 mg) of each UiO-66 material were weighed into 1 dram vials. Aliquots (1.00 mL) of the just-prepared DB 86 solution (C_0 ~500 µM) was quickly added to each of the vials (within 1 min) and the timing (t_0) commenced when the solution was added to the first vial. The vials were capped and left without disturbing for fixed periods of time (t = 15 and 30 min; 1, 2, 3, 4, 6, 12, 24, and 48 h) prior to analysis.

For analysis, the solution from the corresponding vial was transferred to a 2 mL polypropylene centrifuge tube and subjected to centrifugation (15000 rpm, 5 min). After the centrifugation, the top 100 µL of the supernatant was carefully taken into a calibrated 200 µL micropipette and transferred into a 1.5-3.0 mL cuvette, which was then combined with DI water (900 µL) using a calibrated 1 mL micropipette, with careful mixing by 2-3 cycles of suction/release. The DB 86 absorbance of the solution in the cuvette was then determined by UV-vis spectroscopy and the DB 86 concentration of the supernatant at time t (C_t) can be calculated using the calibration curve. Gradual decreases of the absorbance at 622 nm can observed as a function of time for each material (Figure 2.32), indicating decreases of DB 86 amount in the supernatant. The amount of DB 86 adsorbed in the UiO-66 materials is calculated using *Eq*. 2.1 and the results are shown in Figure 2.6 Section 2.9.

$$DB\ 86\ adsorbed\ in\ MOFs\ after\ time\ t\ (mg/g) = \frac{(C_0 - C_t) \times 1\ mL \times 780.2\ mg/mmol}{1\ mg \div 1000\ mg/g} \qquad (2.1)$$

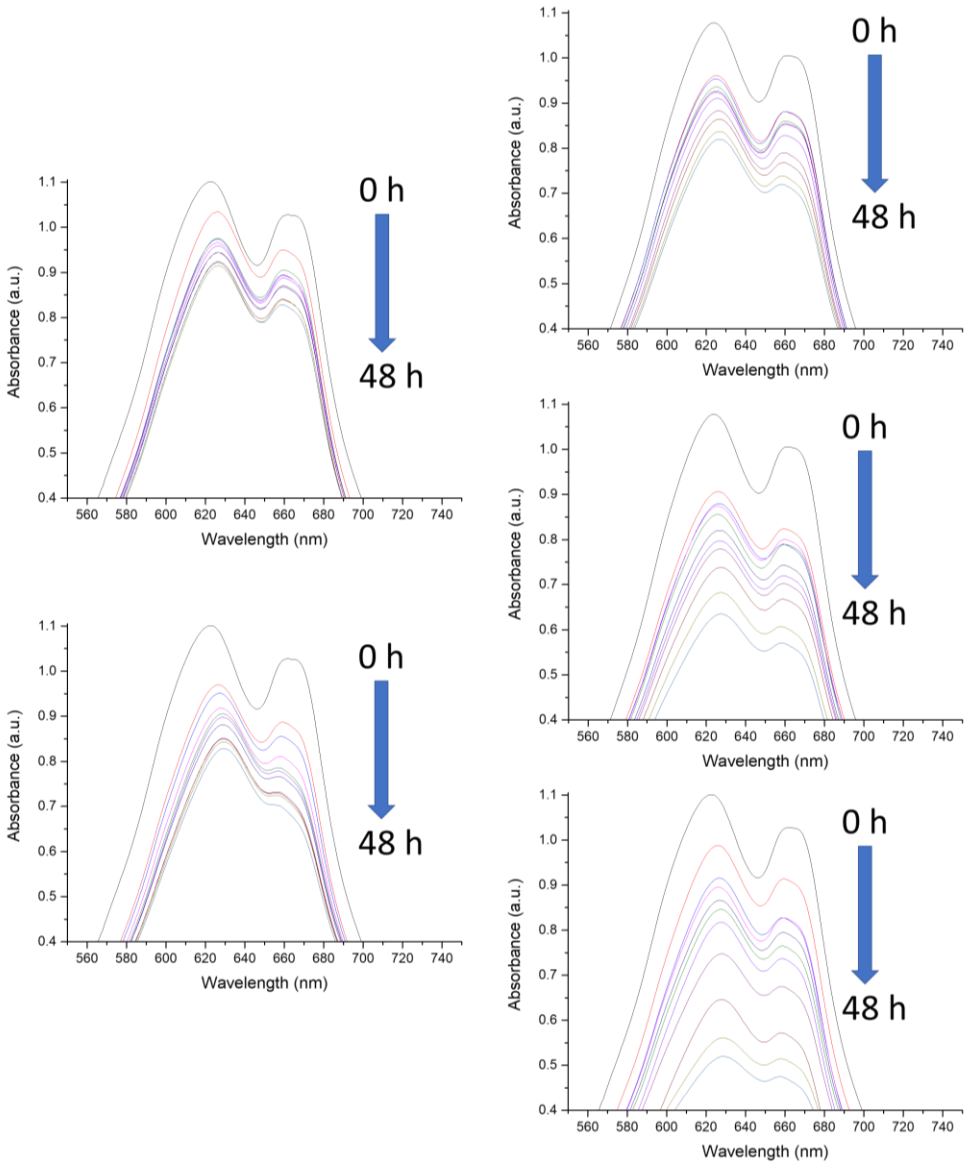

Figure 2.32 UV-vis spectra of the diluted supernatant obtained from the uptake of DB 86 by UiO-66 NPs, UiO-66-F_4, UiO-66@HM-UiO-66-F_4, UiO-66@HM|$_{2nd}$-UiO-66-F_4, and UiO-66@HM|$_{3rd}$-UiO-66-F_4. For each data point, the supernatant was diluted 10 times to obtain a solution with an absorbance close to or less than 1. Three UV-vis measurements were obtained for each sample to ensure that the measurents are consistent.

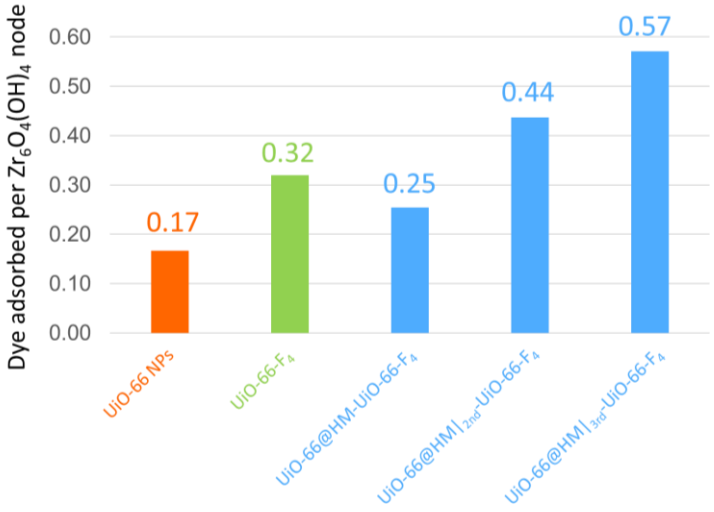

Figure 2.33 Bar graph of the DB 86 uptake-capacity per node by our UiO-66 materials, calculated based on the uptake data shown in Figure 2.6 in Section 2.9. The amount of $Zr_6O_4(OH)_4$ nodes in each material is calculated based on the amount of material used (1 mg) in the uptake experiment and the corresponding chemical formulas in Table 2.1.

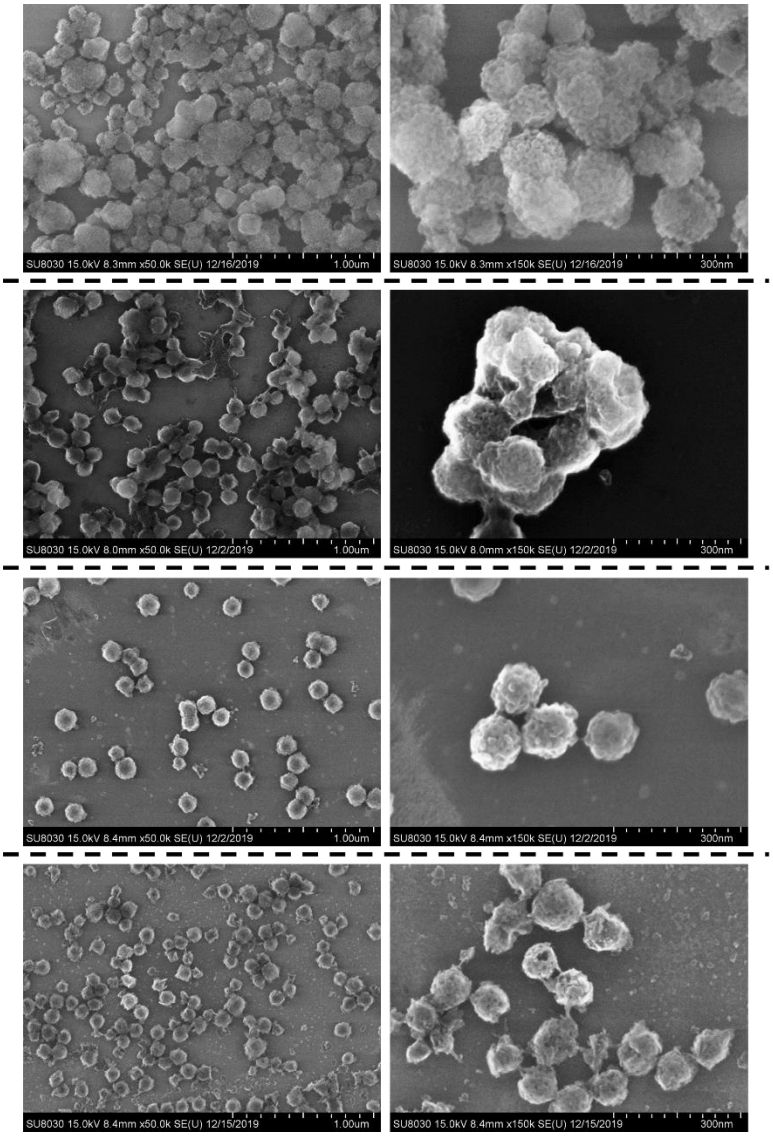

Figure 3.34 SEM images of UiO-66@HM|$_{3rd}$-UiO-66-$(OH)_2$ (1^{st} row), UiO-66@HM|$_{3rd}$-UiO-66-$(COOH)_2$ (2^{nd} row), UiO-66@IP|$_{3rd}$-UiO-66-NH_2 (3^{rd} row), and UiO-66@IP|$_{3rd}$-UiO-66 (4^{th} row).

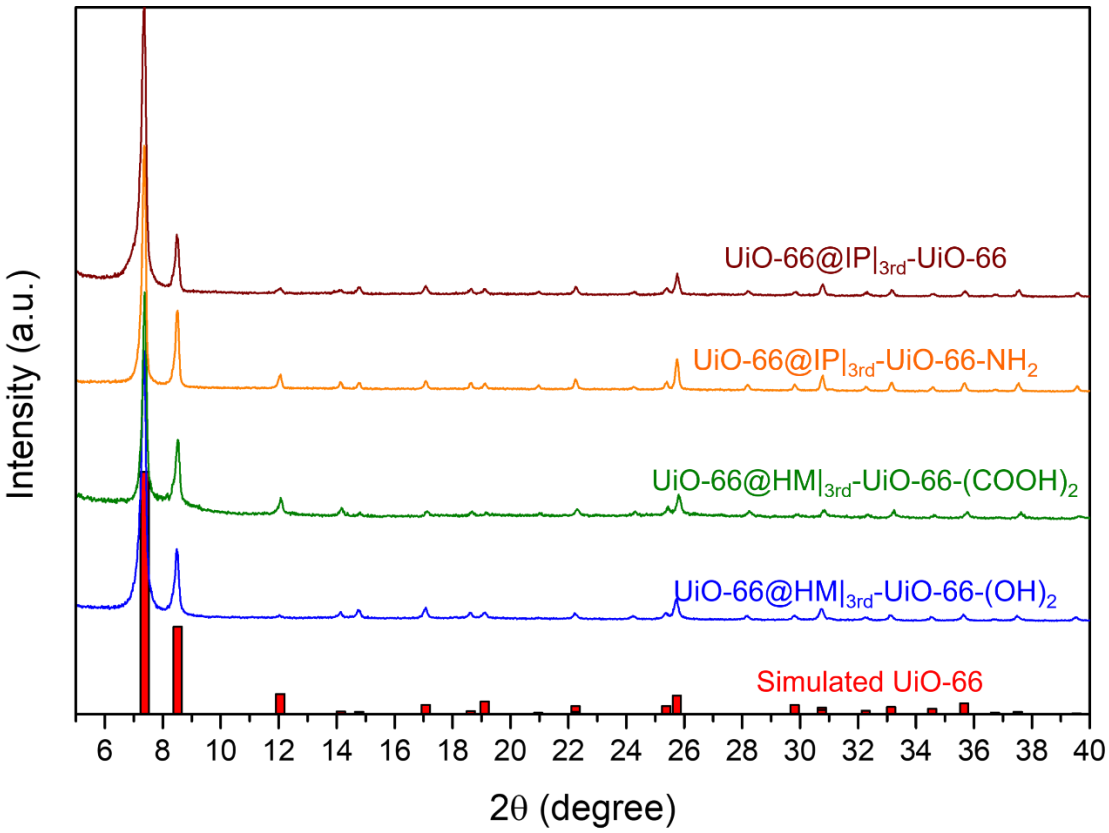

Figure 2.35 PXRD profiles of simulated UiO-66, UiO-66@HM|$_{3rd}$-UiO-66-(OH)$_2$, UiO-66@HM|$_{3rd}$-UiO-66-(COOH)$_2$, UiO-66@IP|$_{3rd}$-UiO-66-NH$_2$, and UiO-66@IP|$_{3rd}$-UiO-66.

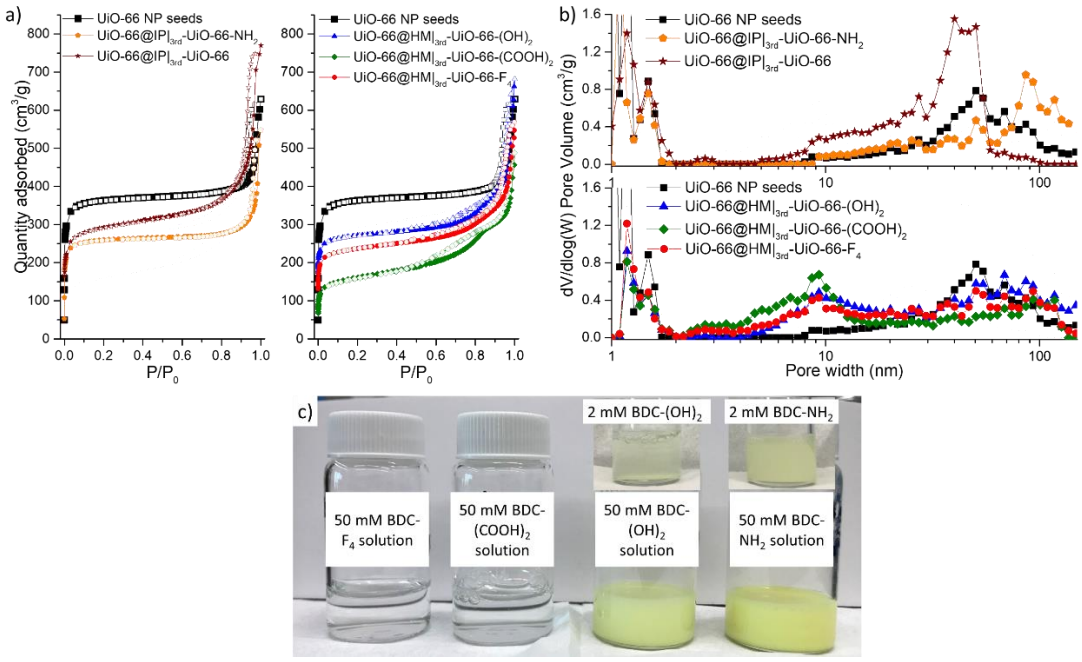

Figure 2.36 (a) N_2 physisorption isotherms and (b) DFT PSDF profiles of: UiO-66 NP seeds batch 2 (black squre), UiO-66@IP|$_{3rd}$-UiO-66-NH_2 (orange pentagon), UiO-66@IP|$_{3rd}$-UiO-66 (burgundy star), UiO-66@HM|$_{3rd}$-UiO-66-$(OH)_2$ (blue triangle), UiO-66@HM|$_{3rd}$-UiO-66-$(COOH)_2$ (green diamond), and UiO-66@HM|$_{3rd}$-UiO-66-F_4 (red circle). Close symbols, adsorption; open symbols, desorption. For comparison, the data are placed into two groups: one for the materials with hierarchical mesoporosity (HM) where the added linkers are more water-soluble and one for the materials with interparticle porosity (IP) where the added linkers are less water-soluble; data for the UiO-66 NP seeds was included in each group for comparison. As shown in panels a and b, the UiO-66 NP seeds have pore properties that are quite similar to those for the materials with interparticle porosity (IP). Interestingly, the N_2-physisorption isotherm for UiO-66@IP|$_{3rd}$-UiO-66-NH_2 is similar in shape to that of the UiO-66 NP seed while that for UiO-66@IP|$_{3rd}$-UiO-66 still features a type-Ia/II adsorption branch, consistent with the latter having a slightly higher proportion of mesopores. c) Photograph of 2-50 mM aqueous solutions of BDC-X (X = F_4, $(COOH)_2$, $(OH)_2$, and NH_2) linkers, showing a solubility trend as BDC-$(COOH)_2$ ~ BDC-F_4 > BDC-$(OH)_2$ > BDC-NH_2, which is consistent with the repoted relative solubilities of BDC linkers in water[128]. Correspondingly, the mass gain after 3-round overgrowth with the four linkers follows a roughly similar trend: BDC-$(COOH)_2$ (79 wt %)^a > BDC-F_4 (60 wt %)^c ~ BDC-$(OH)_2$ (61 wt %)^a >BDC-NH_2 (54 wt %)^b > BDC (~ 0 wt %)^a. (^{a}Result obtained from one trial. ^{b}Result obtained based on average of two trials. ^{c}Result obtained based on average of three trials.)

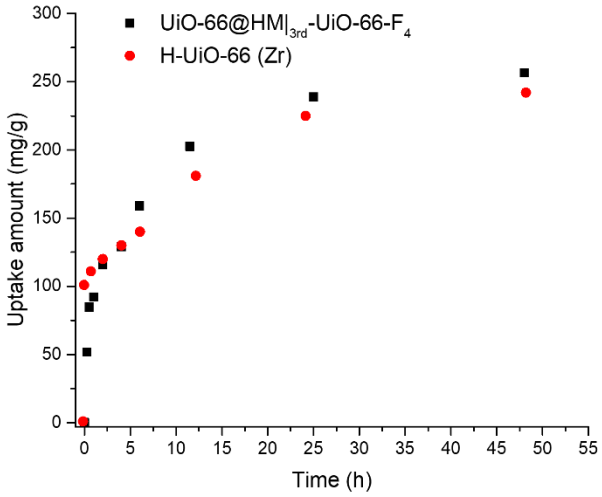

Figure 2.37 Time-dependent DB 86-uptake profiles for our UiO-66@HM|$_{3rd}$-UiO-66-F$_4$ and a reported mesoporous H-UiO-66(Zr) sample made with metal-organic assembly template by Huang et al.[20] Data for the latter materials were digitized by us from the published work. While not directly comparable (our dye-uptake experiments were carried out with 1 mg of MOF and 1 mL of a 500 μM dye solution while that by Huang et al.[20] was carried out with 10 mg of MOF and 20 mL of a 640 μM dye solution), the kinetic profiles of the two materials are quite similar.

2.12.6 Procedures for the catalysis studies

Stock solution of methyl phenyl sulfide. In a 120 mL Erlenmeyer flask equipped with a ground-glass joint, methyl phenyl sulfide (240 μL, 2 mmol) and naphthalene (256 mg, 2 mmol, as an internal standard) were dissolved by sonication (~ 1-2 min) in CH_3CN (100 mL). The flask was stoppered with a ground-glass plug and the solution was stored at room temperature until use.

The oxidation of methyl phenyl sulfide with H_2O_2 in MeCN. Into an 8 dram vial equipped with a magnetic stir bar was added a catalyst sample (0.002 mmol Zr_6 cluster, 0.01 equiv (see Table 2.3)) was weighed. An aliquot of the pre-prepared 20 mM methyl phenyl sulfide stock solution (10 mL, 0.2 mmol) was next added into the vial and the mixture was stirred at room temperature. H_2O_2 (20 μL of a 30 wt % solution in water, 0.2 mmol) was then added and the timing (t_0) was commenced. At specific time intervals (every 1 min during the first 6 min, every 2 min during the

next 4 min, every 5 min during the next 10 min, and then every 10 min during the remaining 40 min), an aliquot (~0.1 mL) of the reaction mixture was removed and filtered through a 0.2 μm PTFE syringe filter (VWR International, North American Catalog # 28145-495) that is attached to a 1 mL disposable syringe. The filter was rinsed with additional CH_3CN (~0.5-0.7 mL) and the combined organics was then analyzed by GC-FID. Data are shown in Figure 2.6 and Table 2.3. The error bars are the standard deviations of three trials.

Table 2.3 The amount of catalysts used in each reaction and the corresponding reaction rate.

UiO-66 material	Number of open site	Amount of material[a] (mg)	10^6 × Reaction rate (M/s)
UiO-66 NP seeds	1.3	3.20	1.04
UiO-66-F_4	1.9	3.85	1.18
UiO-66|UiO-66-F_4	2.2	3.40	1.35
UiO-66@HM$_{|3rd}$-UiO-66-F_4	2.9	3.45	3.77
BzOH-UiO-66[19]	1.0	3.40	1.50

[a]Calculated for a stoichiometry of 100 equiv substrate/$Zr_6O_4(OH)_4$ cluster based on the formulas shown in Table 2.1. A microbalance (see Section 2.12.1 for the instrument) was used to weigh the samples. For the three trials of each sample, the variation of weighing was controlled to be within 0.05 mg.

Catalyst recycling. This experiment was carried out following the procedure described at the beginning of this section and the stoichiometry shown in Table 2.3. Specifically, the same amount of UiO-66@HM$_{|3rd}$-UiO-66-F_4 was added to three 8 dram vials labeled 1, 2, and 3; each of which was then used to catalyze the sulfide oxidation reaction for 1, 2, and 3 cycles, respectively. Kinetic data was collected for each cycle, after which the corresponding catalyst was isolated for TEM and PXRD characterization (data are shown in Figure 2.38b and Figure 2.39) depend on the numerical label of the vial. That is, the catalyst in vial 1 was isolated after 1 cycle; that in vial 2 was isolated after 2 cycles; and that in vial 3 was isolated after 3 cycles of catalytic reaction, respectively.

Each round of the catalytic reaction was carried out using the same protocol described at the beginning of this section. Data is shown in Figure 2.38a.

The isolation and recycling of the catalyst. After 60 min of reaction, the reaction mixture was subjected to centrifugation (10000 rpm, 30 min) and the supernatant was isolated by carefully decanting to leave the catalyst behind. The remaining catalyst was immersed in fresh methanol (~10 mL) for ~5 min before being collected by centrifugation (10000 rpm, 30 min) and decantation. This immersion and centrifugation process was repeated two more times. New aliquots of substrates and oxidant (same stoichiometry as shown at the beginning of this section) were then added to repeat the oxidation of methyl phenyl sulfide. Another cycle of the catalytic oxidation was initiated after adding H_2O_2 (20 μL of a 30 wt % solution in water, 0.2 mmol).

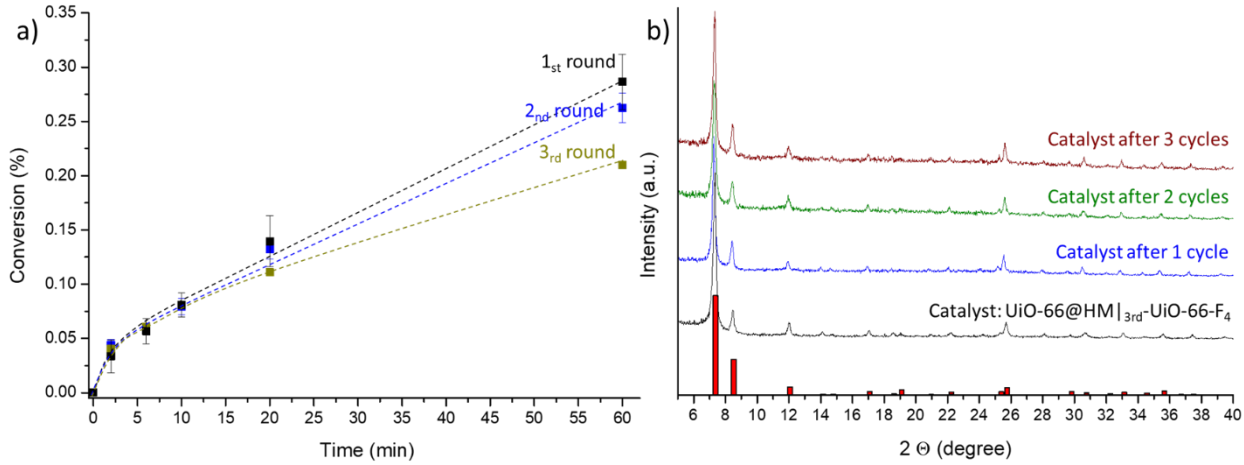

Figure 2.38 a) Conversion vs. time profiles of the sulfide oxidation catalyzed by (recycled) UiO-66@HM|$_{3rd}$-UiO-66-F$_4$. The error bars of the 1st round of catalysis were obtained from the average of three trials. The error bars of the 2nd round was obtained from the average of two trials. There is no error bar for the 3rd round due to the experimental design, where only one vial remained. These catalysis data were generated using the same batch of UiO-66@HM|$_{3rd}$-UiO-66-F$_4$ catalyst that was used for Figure 2.7 in Section 2.10 but was subsequently stored at rt on the benchtop for more than 1 year. b) PXRD profiles of simulated UiO-66 (red), UiO-66@HM|3$_{rd}$-UiO-66-F$_4$ catalyst after a long storage period (> 1 yr) and before the catalysis (black); and after 1 cycle (blue), 2 cycles (green), and 3 cycles (burgundy) of catalysis.

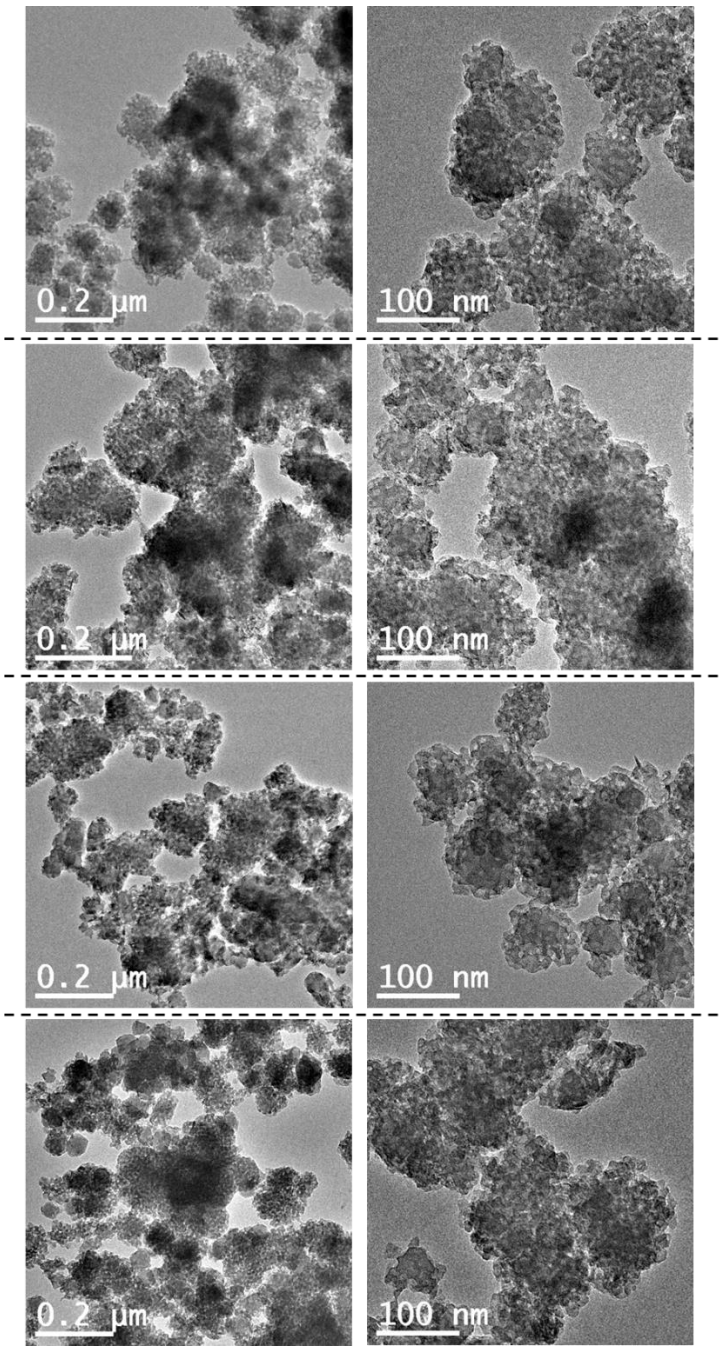

Figure 2.39 TEM images of UiO-66@HM|3$_{rd}$-UiO-66-F$_4$ catalyst after a long storage period (>1 yr) and before the catalysis (top row); and after 1 cycle (2nd row), 2 cycles (3rd row), and 3 cycles (bottom row) of the catalysis.

Chapter 3

Bottom-up synthesis of a 2D cpp UiO-66 structure

by coordination hindrance on Zr_6 clusters

Portions of this chapter will appear in a manuscript: Zhang, F.; Li, Y.; Wang, Y.; Malliakas, C. D.; Si, X.; Luo; L.; Wang, D.; Bao, J.; Tsung, C. K.; Nguyen, S. T., *in preparation*.

3.1 Introduction

In chapter 2, we demonstrated that core-shell HM-UiO-66 materials can be achieved by growing mesopore-containing UiO-66 shell on UiO-66 NP seeds via a template-assisted strategy. In such a process, a low-porosity unknown phase was observed without the presence of the UiO-66 NP seeds. From the similarity of components (Zr-based cluster and terephthalic-acid-type organic linker) and the non-porous characteristics, it was proposed that the material has a 2D structure with sheets stacked together to form particles. In this chapter, we took the opportunity to fully resolve its structure and study the formation mechanism, where we noticed conditions that could restrict linker-node coordination would favor an anisotropic MOF growth and form a 2D network. These findings not only help us better understand how the polymer templates the mesopore during the HM-UiO-66 formation, but also suggest a coordination-hindrance strategy to synthesize 2D MOF materials.

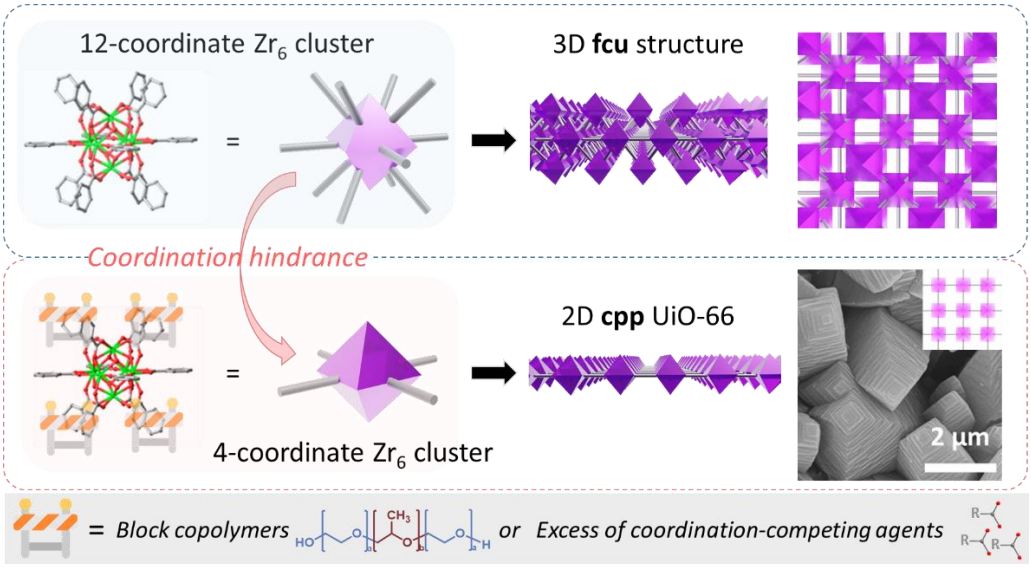

Scheme 3.1 A coordination hindrance on the Zr_6 clusters could result in a lower coordination number, favoring the growth of a 2D MOF network.

3.2 Background and motivation

Two-dimensional (2D) nanomaterials have received much attention in the past decade because of their unique dimension-related properties in separation, catalysis, and energy storage, compared to their bulk counterparts.[129-132] Metal–organic frameworks (MOFs), a class of crystalline porous materials, have emerged as a new member of the 2D-material family, because MOFs combine high diversities of organic linkers with wide choices of metal ions or clusters, which allows a rational design and great tunability of the 2D structure. In the past decade, great progresses have been made on constructing 2D MOFs,[133, 134] a lot of which showed promising utilities in applications such as separation, catalysis, and energy storage.[135-137] Among them, layered Zr-based MOF materials with Zr_6(oxo) as metal clusters are particularly thermally and chemically stable due to strong Zr-O bridging, which make them great candidates for practical applications under harsh conditions.[138] The strong linker-node connection in Zr-based MOFs also tolerates the presence of a decent amount of defects and bring coordination vacancies as active sites for sorption and catalysis.[22, 139] However, the syntheses of 2D Zr-based MOFs are still very challenging as it requires an anisotropic restriction of the crystal growth along the vertical direction without affecting that of the other two lateral directions.[136] Such an anisotropic control of growth is especially difficult in Zr-based MOFs, as the Zr_6 cluster has multiple coordination modes (4-, 6-, 8-, 10-, and 12-coordination), which allows for concurrent formation of multiple 3D topologies even with the same linker.[80, 140]

To form 2D Zr-based MOF structures with Zr_6 clusters, the key is to lower its coordination number (≤ 6), which may allow all linkers on one node to form in-plane coordination bonds (Scheme 3.1 and 3.2). In metal nanoparticle syntheses, polymers (and surfactants) that can preferentially interact with the crystal facets/precursors have been widely used to induce

anisotropic growth.[141, 142] Polymers have also been applied in MOF syntheses to change the morphology of resulted material[88] or to incorporate mesopores into the structure acting as templates.[60] As shown in chapter 2, we have used Pluronic polymers that has affinity to Zr_6 clusters as templates to synthesize hierarchically mesoporous UiO-66 MOFs,[143] a prototypical family of Zr-based MOFs with 12-coordination Zr_6 clusters. Notably, we also noticed an unknown side product induced by the polymer additive, which showed crystallinity but low porosity (see Figure 2.2 and 2.19), resembling characteristics of 2D-layer materials with close packing. The polymer-assisted studies on crystal growths lead us to a hypothesis that the new phase we observed in chapter 2 was a 2D structure with low-coordination Zr_6 clusters caused by coordination hindrance caused by the Pluronic polymers.

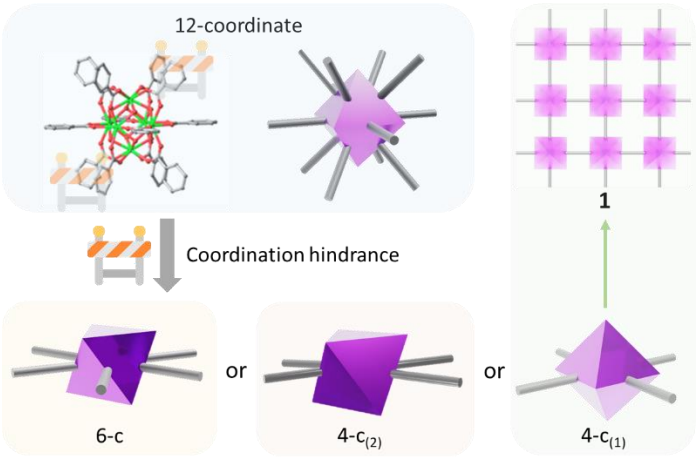

Scheme 3.2 Three possible coordination modes of the Zr_6 cluster that can form 2D networks and the 2D structure (**1**) formed by the tetragonal, 4-coordination cluster.

Herein, we further resolved the structure of this lately discovered material as a new 2D **cpp** UiO-66 structure, based on which we reported a coordination-hindrance strategy to acquire this 2D MOF materials. In this study, diffraction experiments by X-ray (PXRD) and electron (SAED under HRTEM) were carried out to characterize the materials, which suggest a tetragonal network composed of 4-coordination Zr_6 clusters, connected by BDC-F_4 linkers, forming a **cpp** topology.

Resulted from such a 2D network, a flexibility in structure (~7% lattice parameter change) was also observed upon activation. During its formation, Pluronic block-co-polymers were proposed to act as steric barricades to the coordination sites and result in this 2D network (Figure 3.1c). Based on this hypothesis, an excess of monocarboxylate modulators (acetic acid, AcOH) were introduced to the synthesis as the coordination-hindrance agents, which also engendered materials with this 2D structure. As another method to suppress the linker-node coordination, a linker-deficient environment was created by using a hydrophobic porous membrane to separate Zr and BDC-F_4 solutions but allow for a slow diffusion of BDC-F_4 to the other side during the growth. This enabled the growth of this 2D **cpp** UiO-66-F_4 on the Zr-side surface of the membrane and engendered a MOF-membrane hybrid material. By a model UiO-66 MOF, a coordination-hindrance strategy was demonstrated to derive 2D MOF structures from existing 3D MOF materials without looking for new metal nodes or linkers.

3.3 Pluronic-induced formation of the 2D phase

Utilizing the strong affinity between Pluronic polymer and UiO-66, we have successfully used F-127 micelles as templates to grow hierarchically-mesoporous (HM) UiO-66 shell materials on UiO-66 nanoparticle (NP) seeds in an aqueous solution (chapter 2). While the HM-UiO-66 growth was guided by pre-synthesized UiO-66 NP seeds, an unknown phase with little porosity was observed when the seed was absent. Its low porosity and few PXRD diffraction signals at low-2θ region led us to propose that this material is a 2D network rather than a 3D matrix (normally with high porosity and many high-index (2θ) diffraction signals, both resulted from one more spatial dimension). Such a speculation of forming a 2D material with the presence of Pluronic polymers is not unreasonable due to the strong affinity observed between the Pluronics and UiO-

66 MOFs,[88, 143] which could block some coordination sites on the Zr_6 cluster and cause an anisotropic growth.

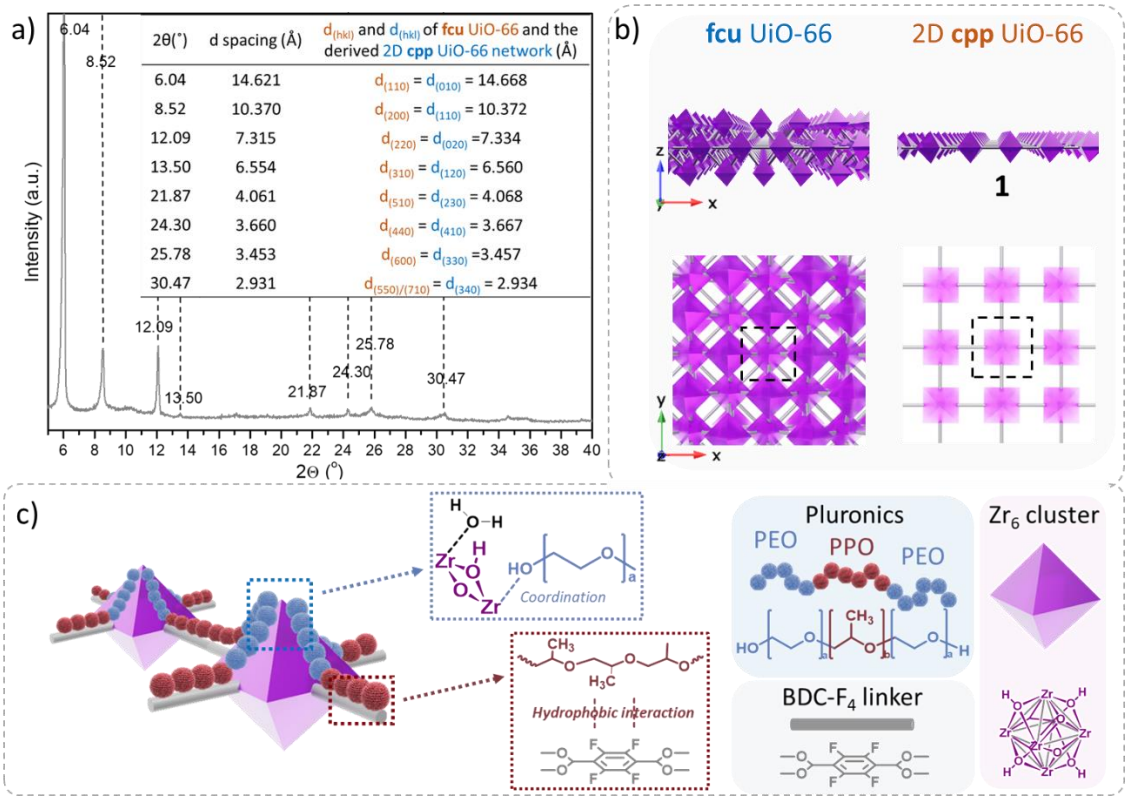

Figure 3.1 a) PXRD profiles of the 2D **cpp** UiO-66|$_{Plu}$ with the 2θ labelled. The inset table lists the d spacing calculated from the experimental 2θ, ideal **fcu** UiO-66 (orange text) and the derived tetragonal 2D **cpp** UiO-66 structure (blue text) with the (*hkl*) plane as subscript. b) Structures of **fcu** UiO-66 and 2D **cpp** UiO-66 viewing from the <010> and <001> direction (unit cells are circled in dashed squares in the images on the bottom). c) A proposed interaction manner between the Pluronic polymers and the 2D-UiO-66-F_4 structure during its growth.

Due to the high temperature growth condition (90 °C, 1 day growth) in previous synthesis (see Section 2.12.2), the weak crystallinity of the unknown side product in the previous work gave only three visible diffraction peaks (6.05, 8.55, 12.16º 2θ; see Figure 2.2). To obtain materials that can provide more structural insights, a slow crystal growth (50 °C, 3 day growth) was employed, which resulted in white-powder products with sharper PXRD signals and the presence of high-index diffractions (see Figure 3.1a and also Figure 3.11, the material was named as 2D **cpp** UiO-66-

$F_4|_{Plu}$). Micron-size particles with a hollow, "coffee-bean" morphology was observed under EM (Figure 3.12).[144] With a close examination on the particle edges, a morphology of stacking layers was also observed. From an attempt of indexing all the detectable diffraction peaks, it was found that they aligned well with the diffractions resulted from (*hk0*) planes of the **fcu** UiO-66 (see inset Table in Figure 3.1a). Notably, the 1st prominent signal is corresponding to (110) diffraction of **fcu** UiO-66, which should not be allowed in the 3D **fcu** structure due to the diffraction extinction of the cubic crystal lattice. All the findings indicate that this new phase partially retains the lattice parameter from the parent **fcu** UiO-66 structure but possibly has a structure losing the long-range order in one direction, which breaks the diffraction extinction rule. According to these reasonings, we thus derived a 2D network from the **fcu** UiO-66 structure as a possible construction of this material (**1**, Scheme 3.2 and Figure 3.1b), which is a network composed with 4-coordination Zr_6 clusters with a C_4 symmetry and **cpp** topology (Figure 3.6). This layered structure could be obtained by slicing the fcu-UiO-66 layer-by-layer at z axis. A simulated PXRD profile resulted from the ideal structure **1** indeed well matches with the experimental data (Figure 3.11).

It was noticed that two other possible 2D networks could be formed by Zr_6 clusters with other coordination modes (4-$c_{(2)}$ or 6-c, Scheme 3.2). According to the simulated structures, the 1st prominent diffractions of the two materials resulted from the (010) plane are corresponding to ~6.75° and 6.87° (2θ) under our diffraction conditions which are in stark contrast with the experimental data (Figure 3.11). In addition, despite its scarcity, we also considered the possibility of Zr_{12} clusters being the metal nodes, which could also form 2D structures, demonstrated by Grey and her co-workers with an **hns** UiO structure built by 12-coordinate Zr_{12} clusters (Figure 3.13).[145] However, due to the orientation of the cluster, it can only form hexagonal networks with a $d_{(010)}$ at ~12.83 Å, corresponding to a diffraction signal at ~6.8˚ (2θ) (Figure 3.13), which is also far away

from the experimental result. Based on the stark contrasts between the experimental PXRD data and predicted profiles of these alternative structures, we further consider that the structure **1** is the most probable construction for this new phase (additional characterization on the structure will be discussed in the later sections in this chapter).

In such a Pluronic-polymer-induced synthesis, it was found that the hydrophobic interaction between the linker (BDC-F_4) and the poly(propylene oxide) (PPO) portion of Pluronic played a critical role to form the 2D **cpp** UiO-66-$F_4|_{Plu}$ material. In a set of syntheses, when Pluronic polymers with low PPO molar ratio were used in the syntheses (i.e., F-127, F-68, F-108), the **fcu** UiO-66's most prominent PXRD signal at ~7.3° (2θ) was observed (Figure 3.14). However, this peak is much less noticeable when L-31 or P-123 was used in the synthesis, which contains ~90 and ~70 mol% PPO in the polymer backbone (Figure 3.14). In addition, we previously tried to grow this 2D **cpp** UiO-$66|_{Plu}$ with F-127 but using four different linkers (BDC-NH_2, BDC-$(OH)_2$, BDC-$(COOH)_2$, and BDC-F_4), where only the growth with BDC-F_4 resulted in the 2D-UiO-66-$F_4|_{Plu}$ material (see Figure 2.20 in chapter 2). The syntheses with the other linkers gave either **fcu** UiO-66 materials (BDC-NH_2 and BDC-$(OH)_2$) or product with little crystallinity (BDC-$(COOH)_2$), suggesting the importance of the F species on the linker to the formation of this 2D network. Together, these data indicate that the growth of the 2D **cpp** UiO-$66|_{Plu}$ material is preferred with a coexistence of BDC-F_4 and PPO-rich Pluronic. Considering a higher hydrophobicity of BDC-F_4 linker compared to that of other linkers,[146] it is proposed that BDC-F_4 interacts with the hydrophobic PPO chain of the Pluronic while the PEO end coordinates with the Zr_6 cluster during the MOF growth (Figure 3.1c). Such an interaction between the Pluronic polymers and the UiO-66-F_4 building blocks could bring a steric coordination hindrance to the

vertical sites on the Zr_6 cluster and thus results in the formation of such a tetragonal 2D network (Figure 3.1c).

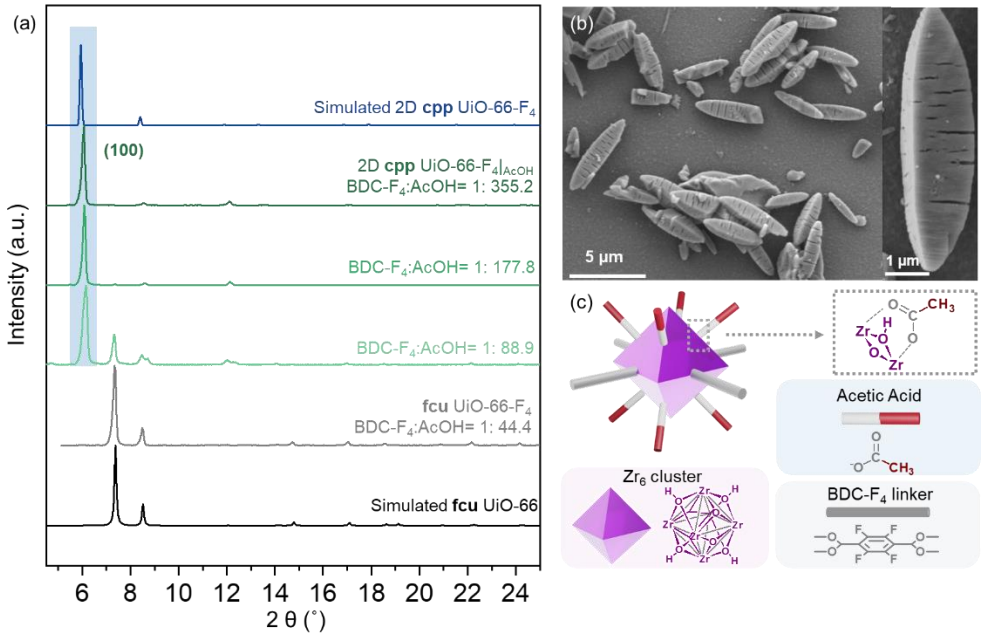

Figure 3.2 a) PXRD profiles of simulated **fcu** UiO-66 (black), products resulted from 2D **cpp** UiO-66-F_4 synthesis with a AcOH : BDC-F_4 ratio of 44.4 (grey), 88.9 (light green), 177.8 (green), and 355.2 (dark green), and the simulated 2D **cpp** UiO-66-F_4 (blue). b) SEM images of the product synthesized with a AcOH : BDC-F_4 ratio of 355.2. c) A cartoon showing the proposed 4-coordinate Zr_6 cluster formed with acetic acid modulators.

3.4 AcOH-induced formation of the 2D cpp UiO-66-F_4 material

Under the same vein, we hypothesized that the introduction of coordination inhibitors (or competing agents) could also restrict the binding of BDC linkers on the Zr_6 node and shift the coordination number on Zr_6 clusters from 12 (that of 3D **fcu** UiO-66) to 4, leading to the same 2D material resulted from the Pluronic-assisted syntheses. Monocarboxylate modulators (such as AcOH), unlike bidentate BDC linkers, could only form coordination bonds with metal nodes/cluster on one end. Therefore, they could compete with BDC linkers and regulate the UiO-66 growth, controlling the particle size and morphology.[147] Also considering its high solubility in the solvent of the synthesis (water) comparing with other organic monocarboxylate modulators,

AcOH is chosen as the coordination competitor. A reported synthesis was first carried out as a control with a regular (moderate) amount of AcOH modulating the crystal growth (BDC-F_4:AcOH = 1:44.4).[99] As expected, the resulted material showed a diffraction pattern resulted from **fcu** UiO-66 (Figure 3.2a) and a cubic morphology (Figure 3.15). As the BDC-F_4-to-AcOH ratio increased to 1:88.9-1:177.8, an intensive peak at ~6.08˚ (2θ) appeared along with other peaks aligning well with that of 2D **cpp** UiO-66-$F_4|_{Plu}$, indicating a formation of the 2D UiO-66-F_4 material. When the amount of AcOH was further elevated (BDC-F_4 : AcOH = 1:355.2), the new peak at ~6.08˚ (2θ) dominated and the peaks belonging to **fcu** UiO-66-F_4 was completely suppressed, giving a PXRD profile the same as that of the 2D cpp UiO-66-$F_4|_{Plu}$ (the resulted material here is noted as 2D **cpp** UiO-66-$F_4|_{AcOH}$). Interestingly, a morphology of rods with stacking layers was observed under SEM (Figure 3.2b), resembling that resulted from screw-dislocation-driven growth of 2D plates with a high growth rate at the dislocation core.[148] These data suggests that the increasing amount of AcOH modulator indeed drives the formation of the proposed 4-coordinate 2D **cpp** UiO-66-F_4 materials rather than the 12-coordinate **fcu** UiO-66-F_4, mimicking the coordination hindrance brought by Pluronics (Figure 3.2c).

3.5 Structural characterizations of the 2D cpp UiO-66-F_4 materials

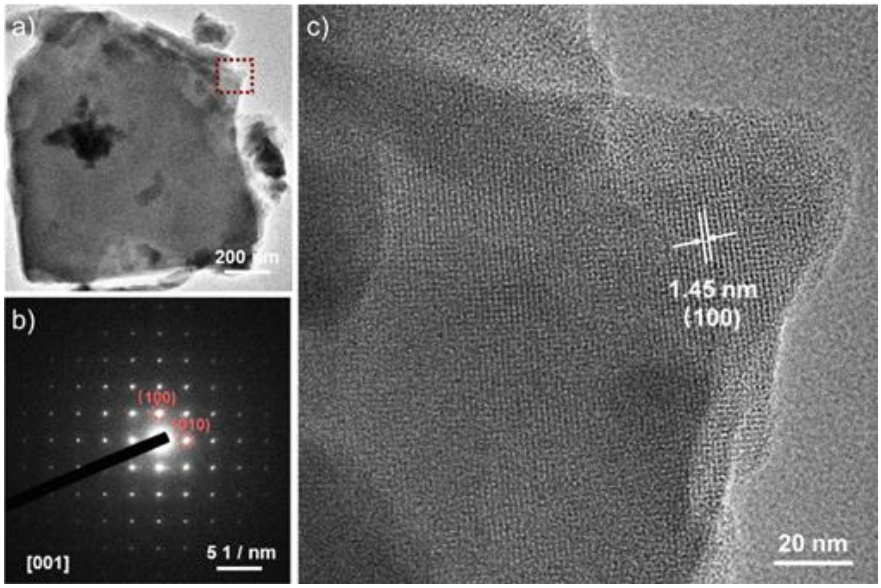

Figure 3.3 a) TEM of a ground 2D **cpp** UiO-66-$F_4|_{AcOH}$ material. b) HRTEM of the area in red box circled in panel a, showing clear crystalline fringes. c) The electron diffraction pattern collected from the corresponding area in panel b.

As a further confirmation of the tetragonal 2D structure, a direct visualization on the crystalline fringes and diffraction pattern were acquired under HRTEM with mildly-ground 2D **cpp** UiO-66-$F_4|_{AcOH}$ material (Figure 3.3).[149] Clear crystal fringes (d = 1.44 nm) were observed under HRTEM (Figure 3b), which matches with the d-spacing of (100) in the proposed structure **1** (14.67 Å). The corresponding selected-area diffraction pattern revealed a pattern with clear C4 symmetry, aligning well with diffractions resulted from {100} and {010} planes of structure **1** along [001] zone axis. Notably, the other potential 2D structures formed by either Zr_6 or Zr_{12} clusters with other coordination modes do not possess a C4 symmetry and thus cannot give such a tetragonal diffraction pattern (see Figure 3.17). These evidences further supported the proposed lamellar structure composed of 4-$c_{(1)}$ Zr_6 clusters, each of which is linked by four in-plane BDC-F_4 linkers with a ~90° angle between the two adjacent ones.

A composition analysis was used to quantify the linker-to-node (L/N) ratio in the 2D **cpp** UiO-66-F_4 materials by carrying out NMR and ICP analysis on digested samples (see Section 3.8.3). A low L/N ratio (~3) was determined for both 2D **cpp** UiO-66-$F_4|_{Plu}$ and 2D **cpp** UiO-66-$F_4|_{AcOH}$, which was much lower that of an ideal **fcu** UiO-66 structure (L/N = 6) or that (L/N = ~5) in an **fcu** UiO-66-F_4 sample (see Table 2.1 in chapter 2). However, it is slightly higher than the L/N ratio of the proposed structure **1** (L/N = 2), which indicates that there could be additional dangling BDC-F_4 linkers with one carboxylate group coordinating on the axial/vertical coordination sites in our materials.

Consistent with the 2D structure composed of low-coordinate Zr_6-clusters, high flexibility in terms of aperture size and structural dimensions was observed upon high-temperature activation, which has also been observed for other 2D MOF materials.[136, 150] When the 2D **cpp** UiO-66-$F_4|_{AcOH}$ sample was activated at three different temperatures to gradually remove solvent molecules from the aperture (120 °C and 150 °C), a gradual shifting of the PXRD pattern toward high 2θ was observed (Figure 3.19). Particularly, the 1st prominent (100) peak shifted from 6.08° (no activation) to 6.52° (after 150 °C activation). (It was noted that the sample has been fully activated at 150 °C, as further shift was not observed when activation temperature was increased to 180 °C.) Such a shifting of PXRD profile was also consistently observed on the 2D **cpp** UiO-66-$F_4|_{Plu}$ material (Table 3.2). This directly reflects an obvious decreasing in lattice parameter on both materials (from 14.52 to 13.55 Å), which is corresponding to a ~28° bending angle between Z-O-C and the ab plane (Figure 3.18), which resembles the twisting observed in other 2D Zr-based MOFs, such as NU-1400 and PCN-700.[151, 152]

3.6 Grow the 2D cpp UiO-66-F_4 on PEEK membrane surface driven by linker deficiency

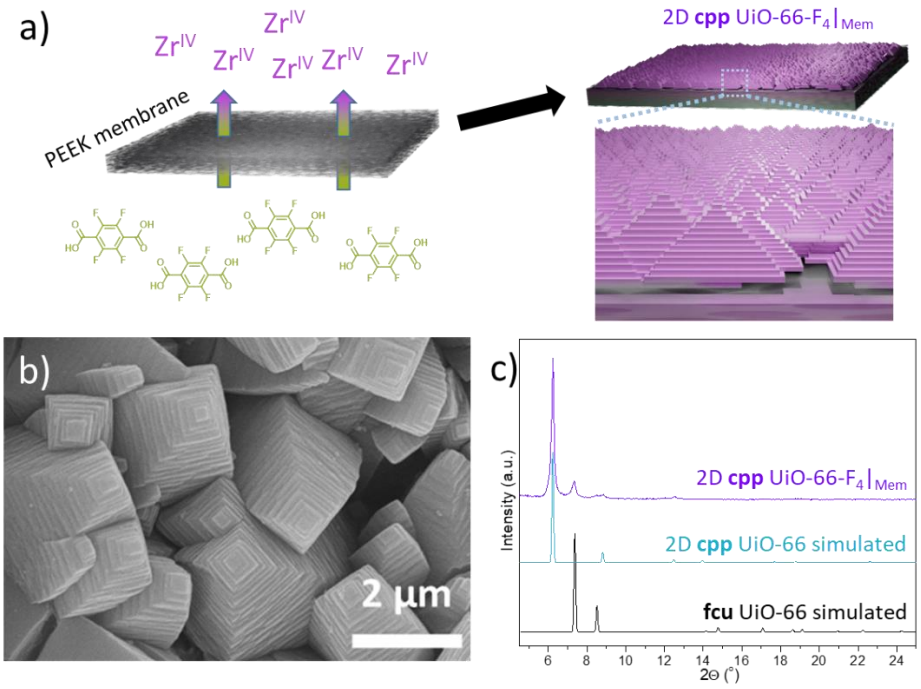

Figure 3.4 a) A PEEK membrane that allows for a slow diffusion of the BDC-F_4 linker to the other side with Zr precurors, which enables the growth of the 2D **cpp** UiO-66-F_4 on the Zr-side surface of the membrane. b) A SEM image (top view) of the Zr-side surface of the 2D **cpp** UiO-66-$F_4|_{Mem}$ product. c) PXRD profiles of simulated **fcu** UiO-66 structure (black), simulated 2D **cpp** UiO-66 structure (cyan), and the 2D **cpp** UiO-66-$F_4|_{Mem}$ (purple).

Given that this 2D **cpp** UiO-66 were synthesized with Pluronic polymers as "coordination barricades" or with an excess of AcOH as "coordination competitors", we recapitulated that the critical factor to induce the 2D growth was a local linker-deficient environment around the Zr_6 cluster which lower the possibility of BDC-and-cluster bonding. To create such a circumstance in a macroscopic scale, we separately placed the Zr precursor and BDC-F_4 (aqueous) solutions in two chambers of a two-compartment cell with a hydrophobic PEEK microfiltration membrane in between (PEEK stands for polyether ether ketone) (Figure 3.7). With the hydrophobic nature of PEEK, the membrane does not allow permeation of water under room temperature (Figure 3.7), while it should allow a diffusion of BDC-F_4 to the Zr-solution chamber under a diffusion-

facilitating condition (Figure 3.4a), for example a moderate heating (~ 60 ºC). After one day, the solution on the Zr side turned cloudy while that on the BDC-F_4 side stayed clear. Rod-like particles with a stacking-layer morphology were observed in the Zr-solution supernatant after the synthesis (Figure 3.20), which resemble that of 2D **cpp** UiO-66-$F_4|_{AcOH}$ (Figure 3.2b). On the Zr-side surface of the resulted membrane (named as 2D **cpp** UiO-66-$F_4|_{Mem}$), a thick crust was observed (Figure 3.21 for cross-section SEM images). Importantly, the PXRD profiles of both the solid products collected from the Zr solution and a strip cut from the 2D **cpp** UiO-66-$F_4|_{Mem}$ showed obvious diffraction signals resulted from the 2D **cpp** UiO-66 structure (Figure 3.4c and see also Figure 3.22). A top view of the crust under SEM shows micron-size spikes with pyramid-like morphologies (Figure 3.4b), which are commonly seen for 2D plates formed by a screw-dislocation driven growth under conditions with a low precursor supersaturation level.[148] These observations clearly suggest that the 2D **cpp** UiO-66-F_4 preferentially formed on the Zr side of the two-compartment cell, where BDC-F_4 linker was deficient, favoring the structure with low-coordinate Zr_6 clusters.

Not surprisingly, the PXRD profile of the 2D **cpp** UiO-66-$F_4|_{Mem}$ also gave noticeable signals resulted from **fcu** UiO-66 (for example, (110) diffraction at 7.3º 2θ, see Figure 3.4c), indicating that some **fcu** UiO-66-F_4 also formed on the surface or/and inside the membrane. To qualitatively determine the spatial distribution of **fcu** UiO-66-F_4 and 2D **cpp** UiO-66-F_4 across the membrane, X-ray diffraction experiments were performed on different areas of the membrane product (with or without the surface crust). Interestingly, a significant decrease of the 2D **cpp** UiO-66-F_4 diffraction signals was observed when the diffraction area did not contain the crust, while the experiment performed on the area with the crust gave suppressed **fcu** UiO-66 signals (Figure 3.23). Also considering a direct diffraction of the crust powder mostly gave 2D **cpp** UiO-66 diffraction

pattern (Figure 3.23), it is concluded that the crust product is attributed to the 2D **cpp** UiO-66-F_4 material and that the **fcu** UiO-66-F_4 is majorly located inside the PEEK porous membrane. Assuming the diffusion of BDC-F_4 was driven by concentration gradient, there would be more BDC-F_4 linker inside the membrane than that on the Zr-side surface of the membrane during the growth, so the 2D **cpp** UiO-66-F_4 growing as a crust layer on the Zr-side surface highlights the importance of a linker-deficiency condition to its formation. Thus, decreasing the amount of linker used in the synthetic condition of the UiO-66-F_4 MOF could also limit the coordination number on the metal node and induce the formation of networks with different topologies.

3.7 Conclusion

In this chapter, we have found a new 2D **cpp** UiO-66-F_4 material and demonstrated a coordination-limiting strategy to shift the growth of a 3D **fcu** UiO-66-F_4 MOF to this 2D network. From PXRD and HRTEM data,[153] we resolved the new structure as a tetragonal network composed of 4-coordinate Zr_6 clusters and BDC-F_4 linkers. From polymer- and modulator-assisted syntheses, we have established that a low linker concentration around the metal cluster is critical to limit its coordination and initiate a 2D anisotropic growth. Guided by this coordination-limiting design, a porous membrane coated with the 2D **cpp** UiO-66-F_4 MOF was synthesized under a linker-deficient, template-free environment. With the conditions we have explored in this work, three synthetic routes are recapped here that could be taken to achieve such a coordination hindrance and drive a 2D-MOF growth: 1) adding "coordination barricades" such as polymers that can interact with building blocks, 2) using an excess amount of "coordination-competing agents", such as monocarboxylate modulators for Zr-based MOFs, and 3) keep a low linker amount in the synthetic solution during the material growth. The rational design and synthesis of this 2D **cpp**

UiO-66-F_4 material shows an untouched route to develop new 2D MOF materials - restricting coordination sites on the secondary building units without trying new linker-node combinations.

3.8 Experimental and supplementary data

3.8.1 Materials and methods

Unless otherwise stated, all reagents were used as received. Zirconium chloride ($ZrCl_4$) was purchased from Strem Chemicals, Inc. (Newburyport, MA, USA). Acetic acid (AcOH), tetrafluoro terephthalic acid (BDC-F_4), Pluronic® F-127, maleic acid, and zirconium ICP standards were purchased from Sigma-Aldrich Co., LLC. (St. Louis, MO, USA) and used as received. Deuterated dimethylsulfoxide (DMSO-d_6, 99%) was purchased from Cambridge Isotope Laboratories, Inc. (Tewksbury, MA, USA). Ultrapure deionized (DI) water (18.2 MΩ•cm resistivity) was obtained from a Millipore Milli-Q Biocel A10 instrument (Millipore Inc., Billerica, MA, USA). Solvents were purchased from either Sigma-Aldrich Co., LLC. (St. Louis, MO, USA) or Fisher Scientific, Inc. (Pittsburg, PA, USA) and used as received.

Powder X-ray diffraction (PXRD) patterns of the materials (except for 2D **cpp** UiO-66-$F_4|_{AcOH}$) were collected on a STOE's STADI-MP powder diffractometer (STOE & Cie. Ltd, Darmstadt, Germany) equipped with an asymmetric curved Germanium monochromator (Cu $K_{\alpha 1}$ radiation, λ = 1.54056 Å), a one-dimensional silicon strip detector (MYTHEN2 1K from Dectris AG, Baden, Switzerland), and a line-focused Cu X-ray tube operated at 40 kV and 40 mA. The as-received powder was sandwiched between two acetate foils (polymer substrate with neither Bragg reflections nor broad peaks above 10 degrees) and measured in transmission geometry in a rotating holder. Prior to the measurement, the instrument was calibrated against a NIST Silicon standard (640d). Measurements were made over the range $5° < 2\theta < 60°$ in 6° steps of the detector and an exposure time of 20 s per step. Powder X-ray diffraction (PXRD) analyses of 2D cpp UiO-

66-$F_4|_{AcOH}$ materials were conducted at Boston College on a Bruker AXS D2 Phaser diffractometer (Cu $K_{\alpha 1}$ radiation, λ= 1.5406 Å) (Bruker Biospin Corp., Billerica, MA, USA). Sodium Chloride or Au powder was mixed with the samples and served as standard.

N_2 adsorption and desorption isotherms were measured on a Micromeritics 3Flex (Micromeritics Instrument Corporation, Norcross, GA, USA) at 77 K. Before each run, samples were activated in a National Appliance Laboratory Bench Vacuum Oven-model M5831 (National Appliance Co., Portland, OR, USA) that was connected to house vacuum (~20 in Hg), and then at 120 °C for 12 h on a Micrometrics Smart VacPrep (Micromeritics Instrument Corporation, Norcross, GA, USA) sample degas station. About 20-50 mg of sample was used in each measurement and the BET area was calculated in the region P/P0 = 0.005-0.01, which is selected to satisfy the first consistency criterion for materials containing micropores, as recommended by Walton and Snurr.[118] The pore-size-distribution functions (PSDFs) of the MOFs were calculated from the adsorption-desorption isotherms by density functional theory (DFT) using the carbon slit-pore N_2-DFT model in the range of $0 < P/P_0 < 1$.

Scanning electron microscopy (SEM) images were obtained at Northwestern University's EPIC/NUANCE facility on an SU8030 FE-SEM microscope (Hitachi High Technologies America, Inc., Dallas, TX, USA) with an acceleration voltage of 10-15 kV or at ShanghaiTech University on a field emission scanning electron microscope (FE-SEM) JEOL JSM-7800F or JEOL-6340F (JEOL Shanghai Semiconductors Ltd., Shanghai, China) with an accelerating voltage of 5-10 kV. Size measurements were obtained from sample populations of >100 particles, which were used to construct the standard normal distribution plots (mean ± 3 standard deviation units) and the histograms.

Transmission electron microscopy (TEM) images were obtained at Shanghai on JEOL JEM-2100 (JEOL Shanghai Semiconductors Ltd., Shanghai, China) plus with an accelerating voltage of 200 kV.

Inductively coupled plasma optical emission spectroscopy (ICP-OES) was conducted on a computer-controlled (QTEGRA software v. 2.2) Thermo iCap 7600 Duo ICP-OES (Thermo Fisher Scientific, Waltham, MA, USA) instrument equipped with a SPRINT valve and a CETAC 520ASX autosampler (Teledyne CETAC, Inc., Omaha, NE, USA).

For obtaining MOF compositions, ^{1}H NMR and ^{19}F NMR spectra were recorded on a Bruker Neo 600 MHz spectrometer (Bruker Biospin Corp., Billerica, MA, USA) equipped with a triple-resonance (HCFN) cold probe w/ Z-gradient and the following manufacturer-reported sensitivities: ^{1}H = 5000, ^{19}F = 7000, and ^{13}C = 800. ^{1}H NMR chemical shifts are referenced in ppm downfield from tetramethylsilane (TMS, δ scale) using the residual solvent resonances as internal standards. ^{19}F NMR chemical shifts are referenced in ppm downfield from trichlorofluoromethane ($CFCl_3$, δ scale). Trifluoroacetic acid (TFA) was used as an internal standard.

A Mettler ToledoTM Micro-Analytical Balance (Mettler-Toledo, LLC., Columbus, OH), located in the IMSERC facility of Northwestern University, was used to weigh samples ≤ 10 mg. To minimize static, samples were weighed into Al sample pans; the weighing apparatus and sample containers were also de-staticized with a Milty Zerostat 3 anti-static gun when necessary.

An IKA-Werke RCT Basic S1 Magnetic Stirrer (IKA Works, Inc., Wilmington, NC, USA) was used to carry out the experiments that requires heating and stirring. The stirring rate was kept at a relatively vigorous rate (~ 800 rpm) to maintain nanoparticle dispersion and favors overgrowth on the seed instead of undesirable self-nucleation. To maintain a consistent temperature

throughout the reaction volume, the reaction vial was immersed in a mineral oil bath in a manner that the top of the reaction volume is below the level of the oil bath.

For the synthesis experiments, centrifugation was carried out in an Eppendorf Centrifuge 5804 R, Model AG 22331 (Eppendorf AG, Hamburg, Germany) equipped with an F34-6-38 rotor. All centrifugations were carried out at 25 ℃ and 8000-11000 rpm (8228-15557 g) for 10-30 minutes.

The drying of MOF samples after synthesis was routinely carried out at 120 ˚C for 24 h in a National Appliance Laboratory Bench Vacuum Oven-model M5831 (National Appliance Co., Portland, OR, USA) that was connected to house vacuum (20 in Hg).

Volume measurements were carried out using mechanical pipets (professionally calibrated every 3 months) for convenience. However, the volume accuracy does not need to be maintain at the ± 0.005 mL level of accuracy that is intrinsic to these instruments.

3.8.2 2D cpp UiO-66 structures and computations

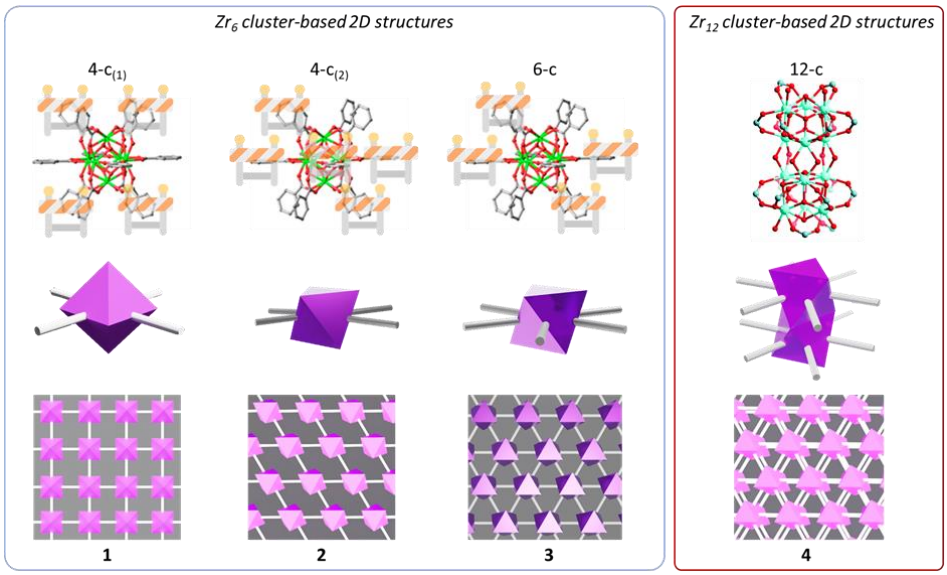

Figure 3.5 Four possible 2D networks could be formed by BDC-F_4 linkers and Zr clusters (Zr_6 or Zr_{12}).

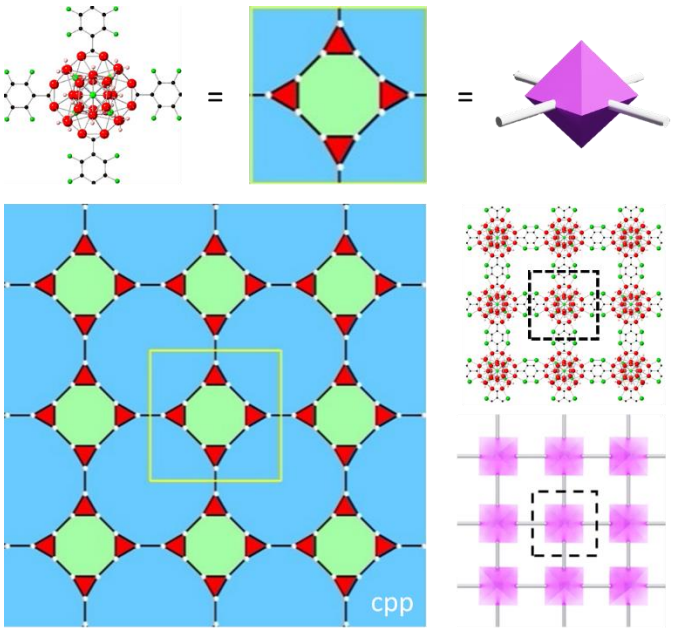

Figure 3.6 Top: The 4-$c_{(1)}$ Zr_6 clusters and its equivalent reticular building block (top). Bottom: A matching between the **cpp** topology[154] and the 2D structure formed by the 4-$c_{(1)}$ Zr_6 clusters (unit cells are circed by black dash lines).

Description on the simulation protocol. To assess the chemical stability of the proposed 2D structures (4-$c_{(1)}$ Zr_6, 4-$c_{(2)}$ Zr_6, 6-c Zr_6, and 12-c Zr_{12}) and predict their corresponding experimental spectra (PXRD, SAED, *etc*.), theoretical models of the structures were constructed (Figure 3.5). For the 4-$c_{(1)}$ Zr_6 structure, a 2D single layer sheet was generated by cutting the conventional unit cell of **fcu** UiO-66-F_4 (20.7 x 20.7 x 20.7 Å) along the z axis.[15] The unit cell of the 2D sheet was then further reduced based on symmetry considerations (14.7 x 14.7 Å). Open metal sites exposed on the surface of the Zr_6 cluster due to removal of linker molecules were capped with hydroxide/water, in a way consistent with the chemical formula of the experimental structure. Similarly, the 4-$c_{(2)}$ Zr_6 and 6-c Zr_6 structures were constructed by cutting the primitive unit cell of **fcu** UiO-66-F_4 (14.8 x 14.8 x 14.8 Å),[155] and also capping exposed open metal sites with hydroxide/water. In the case of 4-$c_{(2)}$ Zr_6, two additional linkers in the plane of the 2D sheet were

removed. Finally, the 12-c Zr_{12} structure was constructed by cutting the conventional unit cell of **hcp** UiO-66-F_4 (14.7 x 14.7 x 37.0 Å) along the [001] axis.[156]

For each generated structure, density functional theory (DFT)-based structure optimization was performed using a plane-wave basis set and the projector augmented wave (PAW) method through the Vienna Ab Initio Simulation Package (VASP version 5.4.4).[157] The Perdew-Burke-Ernzerhof exchange-correlation functional revised for solids (PBEsol) was applied, with dispersion effects accounted for by Grimme's D3 correction with Becke-Johnson damping (D3BJ).[158-160] The cutoff energy was set to 500 eV, and smearing parameter to 0.05 eV to facilitate SCF convergence. Because of the 2D nature of the structures, a 15 Å vacuum layer was used and a dipole correction was applied in the z-direction. From this, the optimized structures of the 2D sheets were obtained. The lattice parameters of the optimized 2D structures did not deviate significantly from their initial values (< 1% change), which are based on the parameters of 3D bulk UiO-66.

To account for the discrepancy in PXRD *d*-spacing values among the activated, inactivated, and 4-$c_{(1)}$ Zr_6 theoretical structures, we hypothesized a decrease in the lattice parameter induced by distortion in the angle between the O_{linker}-Zr-Zr-O_{linker} and O_{linker}-C-O_{linker} planes (Figure 3.18).[152] To test the feasibility of this hypothesis, theoretical structures were constructed in which the planar angle of the 4-$c_{(1)}$ Zr_6 structure is distorted such that its initial lattice parameter is reduced by factors of 0.975, 0.950, 0.925, 0.912, and 0.900. Following optimization of each distorted structure (using the protocol described above), the optimized lattice parameters were found to be 14.61, 14.15, 13.88, 13.62, and 13.42 Å, respectively, with corresponding distortion angles of 11, 21, 25, 28, and 31°. The optimized structure with 11° distortion angle best approximated the inactivated samples with respect to PXRD *d*-spacing, while the structure with

28° distortion angle best approximated the activated samples. Moreover, the electronic energy differences between the undistorted structure and structures with 11 and 28° distortion angles were calculated to be 0.19 and 0.97 kcal/mol per distorted Zr-O_{linker} bond, respectively. These results suggest that Zr-O_{linker} angle distortions are a plausible explanation for the discrepancy in *d*-spacing observed between the unactivated and activated samples.

3.8.3 Synthesis of materials

2D cpp UiO-66-F_4|$_{Plu}$. This material was synthesized by F.Z. with a protocol modified from that of a material in chapter 2 (see section 2.12.2, where the material was named as [Zr+BDC-F_4]*). A BDC-F_4 solution was prepared by dissolving F-127 (3000 mg, 240 μmol) with $AcOH_{aq}$ (100 mL of a 1.75 M aqueous solution), followed by dissolving BDC-F_4 (238 mg, 1 mmol) under sonication (~5 min). Another $ZrCl_4$ solution was prepared by dissolving F-127 (3000 mg, 240 μmol) with $AcOH_{aq}$ (100 mL of a 1.75 M aqueous solution), followed by dissolving $ZrCl_4$ (233 mg, 1 mmol) under sonication (~5 min). For the synthesis, an aliquot (5 mL) of the BDC-F_4 solution was mixed with an aliquot (5 mL) of the $ZrCl_4$ solution in an 8 dram vial, which was then placed into a 50 ºC pre-heated oven for 72 h. For each synthesis, 20 vials were used and they were allowed to cooled down to rt after being taken out from the oven. The resulted solution in all the vials were combined in a 250 mL beaker, which was then evenly dispensed into six 50 mL centrifuge tubes and subjected to centrifugation (10000 rpm, 10 min); the supernatant was removed by decantation to remove unreacted reagents and F-127. MeOH (~25 mL) was added to each centrifuge tube and the tube was sonicated (~10 min) to homogenize the mixture. The resulting MeOH suspension was subjected to centrifugation (10000 rpm, 10 min) and the supernatant was removed by decantation. This MeOH-washing procedure was repeated twice more, after which the product was left to air-dry inside the tube. The dry product was then subjected to Soxhlet

extraction with MeOH. The product was then collected from the Soxhlet thimble, air-dried, and further dried for 12 h inside a 60 ºC oven. Yield = ~165 mg.

2D cpp UiO-66-F_4|$_{Mem}$. This membrane material was obtained by growing 2D **cpp** UiO-66-F_4 material inside and on top of a commercially available PEEK microfiltration membrane (Sterlitech, WA, USA) by using a two-compartment setup (Figure 3.7). The as-received PEEK membrane (10×10 cm^2) was firstly evenly cut into four pieces (5×5 cm^2). Clamp one PEEK membrane (5×5 cm^2) in between the cell with a joint clamp (45/50). A BDC-F_4 solution was prepared by dissolving BDC-F_4 (476 mg, 2 mmol) with $AcOH_{aq}$ (40 mL of a 1.75 M aqueous solution), under sonication (~5 min). Another $ZrCl_4$ solution was prepared by dissolving $ZrCl_4$ (466 mg, 2 mmol) with $AcOH_{aq}$ (40 mL of a 1.75 M aqueous solution) under sonication (~5 min). The two solutions (30 mL each) were simultaneously decanted into the two chambers correspondingly. A rubber stopper poked with a needle was then place on the mouth on each side (the needle was to avoid building pressure in either side which might push the solution to the other side unintentionally during the capping process). Then the cell with one cap (with a needle) on each side was then placed into a 60 ˚C pre-heated oven for ~30 min, after which the needles were removed from the caps and the cell was heated in the oven for another 23.5 h. After the reaction, solid products were observed in the solution of $ZrCl_4$ side, while little was seen on the BDC-F_4 side. Similarly, through the glass, membrane surface on the $ZrCl_4$ side turned rough/powdery, while the surface facing the other side remained smooth. The cell was taken out from the oven and cooled down to rt, after which the joint clamp was removed. Solution from the $ZrCl_4$ side was decanted into a 50 mL centrifuge tube and the solid was collected by centrifugation (10000 rpm, 10 min). The supernatant in the tube was decanted and replaced with fresh MeOH (~25 mL). The tube was subjected to sonication (~5 min) and centrifugation (10000 rpm, 10 min). This washing process of decantation, MeOH

soaking, sonication, and centrifugation was repeated for twice more. Then the palette in the tube was air dried (~1 h), oven dried (60 ºC, overnight), and transferred into a 2-dram vial for later characterizations. The membrane was then transferred into a petri dish containing DI water (~20 mL) and soaked for 1 h. It was then transferred into another petri dish having MeOH (~20 mL) and allowed to be soaked for 1 h. The MeOH was replaced by fresh MeOH (~20 mL) and the membrane was soaked in MeOH for another 1 h. Then the membrane was air dried (for ~1 h) and oven dried (60 ºC, overnight).

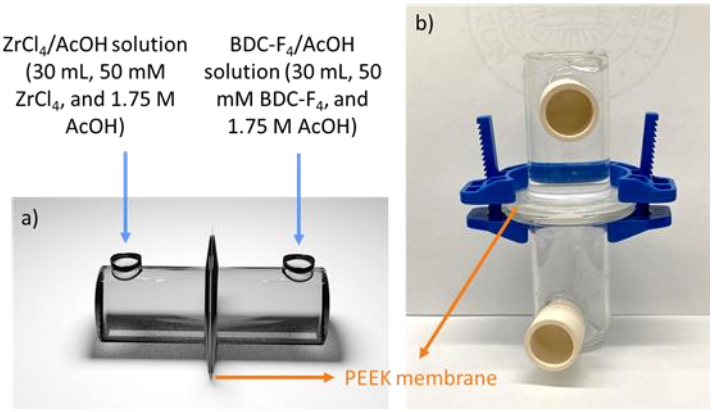

Figure 3.7 a) A 3D-model cartoon showing the two-conpartment cell setup with the PEEK microfiltration membrane clampped in between. The solution components for the 2D **cpp** UiO-66-$F_4|_{Mem}$ synthesis on each side was noted with the arrow. b) The photograph of the two conpartment cell with PEEK membrane, rubber cap, and the joint clamp (the setup was vertical for the ease of taking photo and it was put horizontally flat in a container inside the oven during the reaction (beaker or petri dish)). The upper chamber was filled with water and the bottom chamber was empty (air). The PEEK membrane was clamped in between, which hold the water well overnight without obvious permeation.

fcu UiO-66-F_4. The synthesis of fcu-UiO-66-F_4 was carried out in aqueous phase with acetic acid as limiting agent. Specifically, a BDC-F_4 solution was prepared by dissolving BDC-F_4 (0.183 mmol, 43.5 mg) in an acetic acid aqueous solution (0.5 mL, 8 M) in a 20 mL glass vial, which was heated in an oil bath (50 °C) with stirring until the BDC-F_4 solid fully dissolved. A $ZrOCl_2$ solution was prepared by dissolving $ZrOCl_2 \cdot H_2O$ (0.18 mmol, 58.01 mg) with an acetic acid aqueous

solution (0.5 mL, 8 M) in another 20 mL glass vial. The $ZrOCl_2$ solution was preheated in the oil bath (50 °C) for 5 min before being added to the other vial in the oil bath with the BDC-F_4 solution (in this synthesis, the ratio of BDC-F_4 to AcOH in the mixture was 1:44.4). The mixture was stirred for 1 min and then left undisturbed in the 50 °C oil bath for 24 h. After that, the vial was taken out and cooled down to rt before washing. The supernatant was removed from the resultant product by centrifugation (3000 rpm, 8 min) and decantation. The sample was firstly washed by DMF once and followed by Methanol (3 times). The sample was dried overnight under house vacuum at room temperature, which gave solids in a white powder form.

2D cpp UiO-66-$F_4|_{AcOH}$. The materials were synthesized following the same protocol as that for fcu-UiO-66-F_4 synthesis, but with different BDC-F_4-to-AcOH ratio (1: 88.9 and 177.8). At the ratio of 1: 88.9 (BDC-F_4:AcOH), the BDC-F_4 solution was prepared by adding of BDC-F_4 (0.183 mmol, 43.5 mg) with acetic acid aqueous solution (1 mL, 8 M). While the $ZrOCl_2$ solution was prepared by dissolving of $ZrOCl_2 \cdot H_2O$ (0.18 mmol, 58.01 mg) with acetic acid aqueous solution (1 mL, 8 M). At the ratio of 1: 177.8 (BDC-F_4:AcOH), the same amount of BDC-F_4 and $ZrOCl_2 \cdot H_2O$ was dissolved separately in an additional amount of acetic acid aqueous solution (2 mL, 8 M). Typically for 2D **cpp** UiO-66-$F_4|_{AcOH}$, the BDC-F_4 solution was made by using 4 mL acetic acid aqueous solution (8 M), and the $ZrOCl_2$ solution was also made by using 4 mL acetic acid aqueous solution (8 M). All the other synthetic conditions and workup steps are the same as that of the of **fcu** UiO-66-F_4 synthesis.

Sample Activation. The sample was dispersed in methanol by sonicated for about 5 min and was soaked in methanol for 3 h. Then the solid was collected by centrifugation (3000 rpm, 8 min). Fresh methanol was added to soak the sample for another 3 h. This solvent exchange process was repeated for 8~9 times. The supernatant was removed and the sample was activated at different

temperature under house vacuum (~20 in Hg) for about 48 hours before testing. The activation temperature was 120 °C or 150 °C and the PXRD profiles of the activated products are shown in Figure 3.19.

3.8.4 Compositional analyses of the 2D cpp UiO-66-F_4 materials

The ^{1}H NMR/^{19}F NMR spectra of the digested MOFs can quantitatively reveal the composition of the organic ligands and acetic acid present in each digested sample and the ICP-OES data can yield the weight percentage of Zr composition in the sample. Thus, the linker-to-node (L/N) ratio and chemical formula can be determined for the materials. Data is shown in Table 3.1.

AcOH (^{1}H NMR). In a 2 mL polypropylene centrifuge tube, HF (10 μL) and DMSO-d_6 (90 μL) were added to a small sample (~2 mg) of the material to be analyzed. The resulting mixture was sonicated until the solution became clear (~1 h). Then an aliquot (10 μL, corresponding to ~0.2 mg of the sample) of the resulting solution was transferred to a 2 mL polypropylene centrifuge tube along with an aliquot of maleic acid (MA) solution in DMSO-d_6 (12 mM, 50 μL) and fresh DMSO-d_6 (540 μL). This combined solution was transferred into an NMR tube and then analyzed by ^{1}H NMR spectroscopy with a 90° pulse using a 50 s delay between scans. The amount of each substrate was calculated by comparing the integration against a calibration curve of standards with known concentrations (see Figure 3.8 for calibration curve, and Figure 3.9 for NMR spectra).

BDC-F_4 (^{19}F NMR). In a 2 mL polypropylene centrifuge tube, HF (10 μL) and DMSO-d_6 (90 μL) were added to a small sample (~2 mg) of the material to be analyzed. The resulting mixture was sonicated until the solution became clear (~1 h). Then an aliquot (10 μL, corresponding to ~0.2 mg of the sample) of the resulting solution was transferred to a 2 mL polypropylene centrifuge tube along with an aliquot of 4.0 mM trifluoroacetic acid (TFA) solution in DMSO-d_6 (50 μL), and fresh DMSO-d_6 (540 μL). This combined solution was transferred into an NMR tube and then

analyzed by ^{19}F NMR spectroscopy with a 90° pulse using a 5 s delay between scans, which exceed the T1 relaxation time for BDC-F_4 (435 ms), and TFA (107 ms). The amount of each substrate was calculated by comparing the integration against a calibration curve of standards with known concentrations (see Figure 3.8 for calibration curve, and Figure 3.10 for NMR spectra).

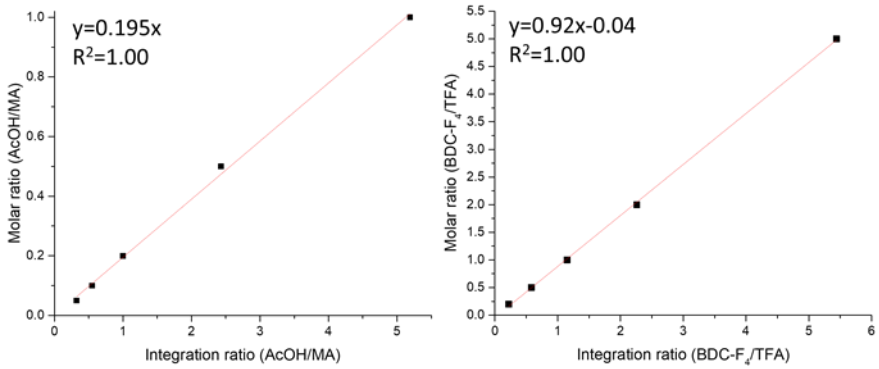

Figure 3.8 NMR (^1H and ^{19}F) calibration curves for AcOH (left), and BDC-F_4 (right) against the internal standards (MA for ^1H; TFA for ^{19}F).

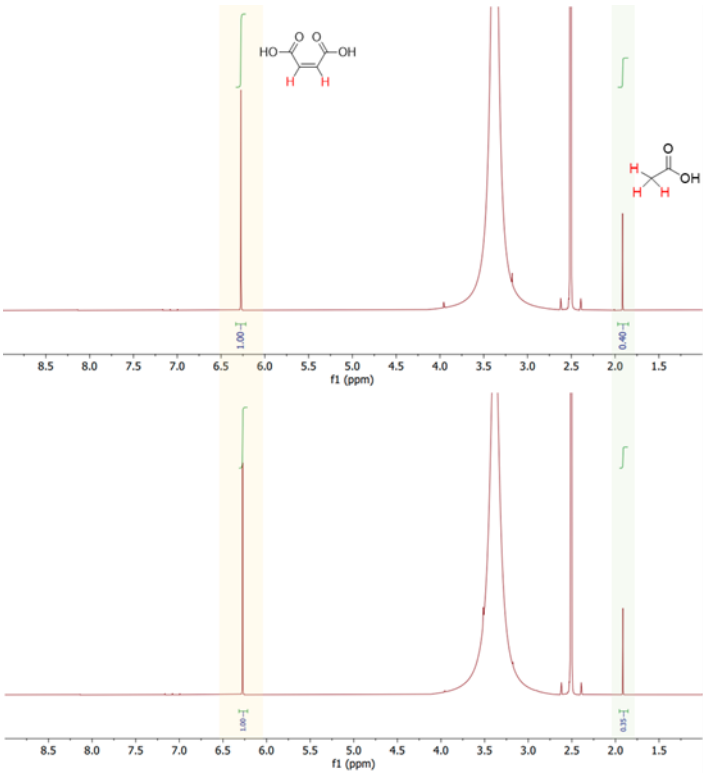

Figure 3.9 ^1H NMR spectrum of the digested 2D **cpp** UiO-66-$F_4|_{Plu}$ (bottom) and 2D **cpp** UiO-66-$F_4|_{AcOH}$ (top) with MA as the internal standard.

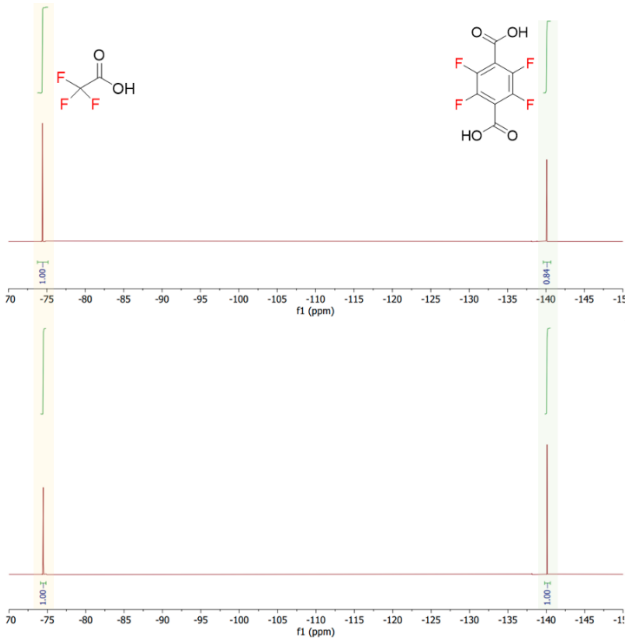

Figure 3.10 ^{19}F NMR spectrum of the digested digested 2D **cpp** UiO-66-$F_4|_{Plu}$ (bottom)and 2D **cpp** UiO-66-$F_4|_{AcOH}$ (top) with TFA as the internal standard.

Table 3.1 Molecular formula of ideal **fcu** UiO-66 and 2D **cpp** UiO-66 materials.

UiO-66 sample	Zr_6-cluster content (μmol/mg of MOF)	BDC-F_4 content (μmol/mg of MOF)	Molecular formula[a]
Ideal **fcu** UiO-66-F_4	-	-	$Zr_6O_4(OH)_4(BDC\text{-}F_4)_6$
2D **cpp** UiO-66-F_4|$_{Plu}$	0.62	1.92	$Zr_6O_4(OH)_4(BDC\text{-}F_4)_{3.1}(CH_3COO)_{0.4}(OH)_{5.4}(H_2O)_{5.4}$
2D **cpp** UiO-66-F_4|$_{AcOH}$	0.62	2.02	$Zr_6O_4(OH)_4(BDC\text{-}F_4)_{3.3}(CH_3COO)_{0.6}(OH)_{4.8}(H_2O)_{4.8}$

[a]The formulas of 2D-UiO-66 MOFs were determined from the ^1H and ^{19}F NMR spectra and ICP-OES data of the digested materials. The open sites were assumed to be terminated by μ_1-OH and μ_1-OH_2.

3.8.5 Characterization data of the 2D cpp UiO-66-F_4 materials

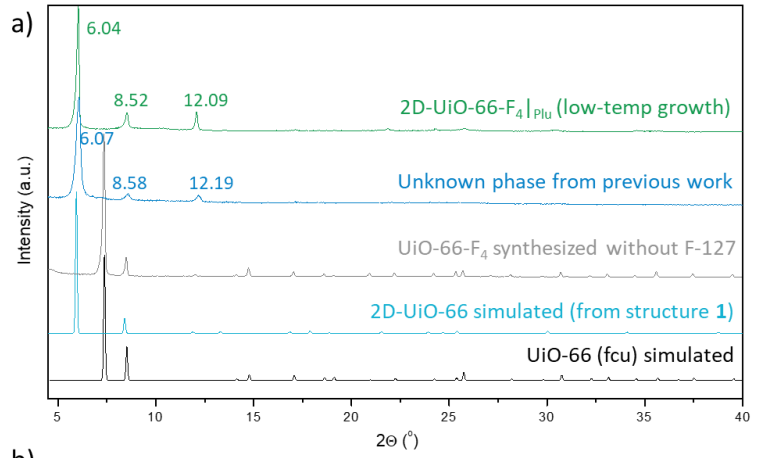

Entry	Coordination modes of the Zr_6 cluster	(010) diffraction signal[a]
1	4-$c_{(1)}$, tetragonal	6.021°
2	4-$c_{(2)}$, hexagonal	6.752°
3	6-c, hexagonal	6.874°

*1st prominent diffraction observed in experimental data: ~6.05°

Figure 3.11 a) PXRD profiles of simulated **fcu** UiO-66 structure (black), simulated 2D **cpp** UiO-66 structure (cyan), UiO-66-F_4 synthesized without Pluronic F-127 (grey), the unknown material reported in chapter 2 (blue), and the 2D **cpp** UiO-66-$F_4|_{Plu}$ (green). b) Zr_6 clusters with three coordination modes that can from 2D networks, along with a table listing the (010) diffraction signals resulted from the possible 2D networks. [a]The diffraction signals of (010) planes resulted from 2D networks constructed by the corresponding Zr_6 clusters (4-$c_{(1)}$, 4-$c_{(2)}$, or 6-c), which were calculated based on Cu K_α source (wavelength 1.5406 Å).

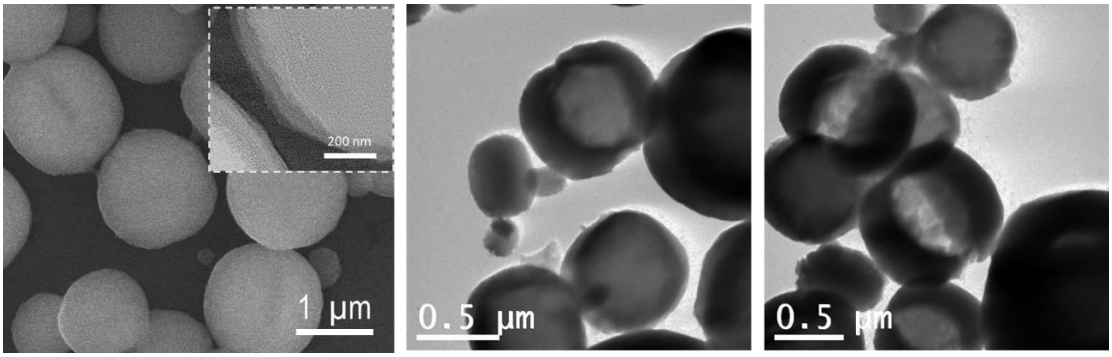

Figure 3.12 SEM images (left) and TEM images (middle and right) of the 2D **cpp** UiO-66-$F_4|_{Plu}$ particles and with a "coffee bean" morphology.

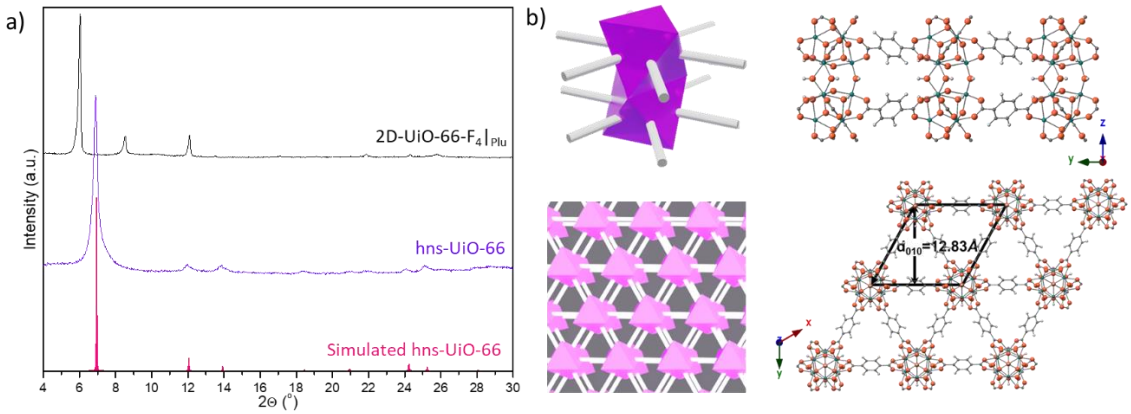

Figure 3.13 a) PXRD profiles of the simulated **hns** UiO-66 (red), **hns** UiO-66 (violet), and 2D **cpp** UiO-66-$F_4|_{Plu}$ (black). The first two were plotted on raw data requested from Firth et al., which were reported previously.[145] b) Left: A polygon demonstration of the 12-coordinate Zr_{12} cluster (top) and the corresponding hns network formed using it as building blocks; Right: Crystalline structure of the hns-UiO-66 viewing from <100> (top) or <001> (bottom).

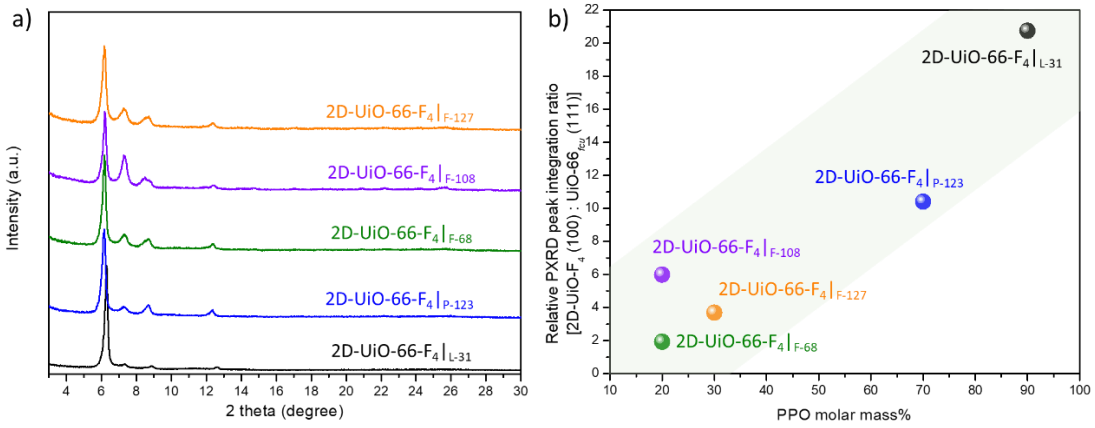

Figure 3.14 a) PXRD profiles of five 2D **cpp** UiO-66-$F_4|_{Plu}$ materials synthesized in a series (on the same day) with different Pluronic: L-31 (black), P-123 (blue), F-68 (green), F-108 (purple), and F-127 (orange). b) Plot of relative PXRD peak integration ratio between 2D **cpp** UiO-66-$F_4|_{Plu}$ (~6.05º 2θ, 100) and **fcu** UiO-66 (~7.30º 2θ, (111)) and the PPO molar mass % in the Pluronic during the synthesis of the 2D **cpp** UiO-66-$F_4|_{Plu}$ material. It shows a positive trend between the PPO molar mass% in the Pluronic and the relative 2D **cpp** UiO-F_4 diffraction intensity, which implies that the hydrophobic chain proportion of the Pluronic facilitates the formation of this 2D-UiO-66-F_4 material during the synthesis.

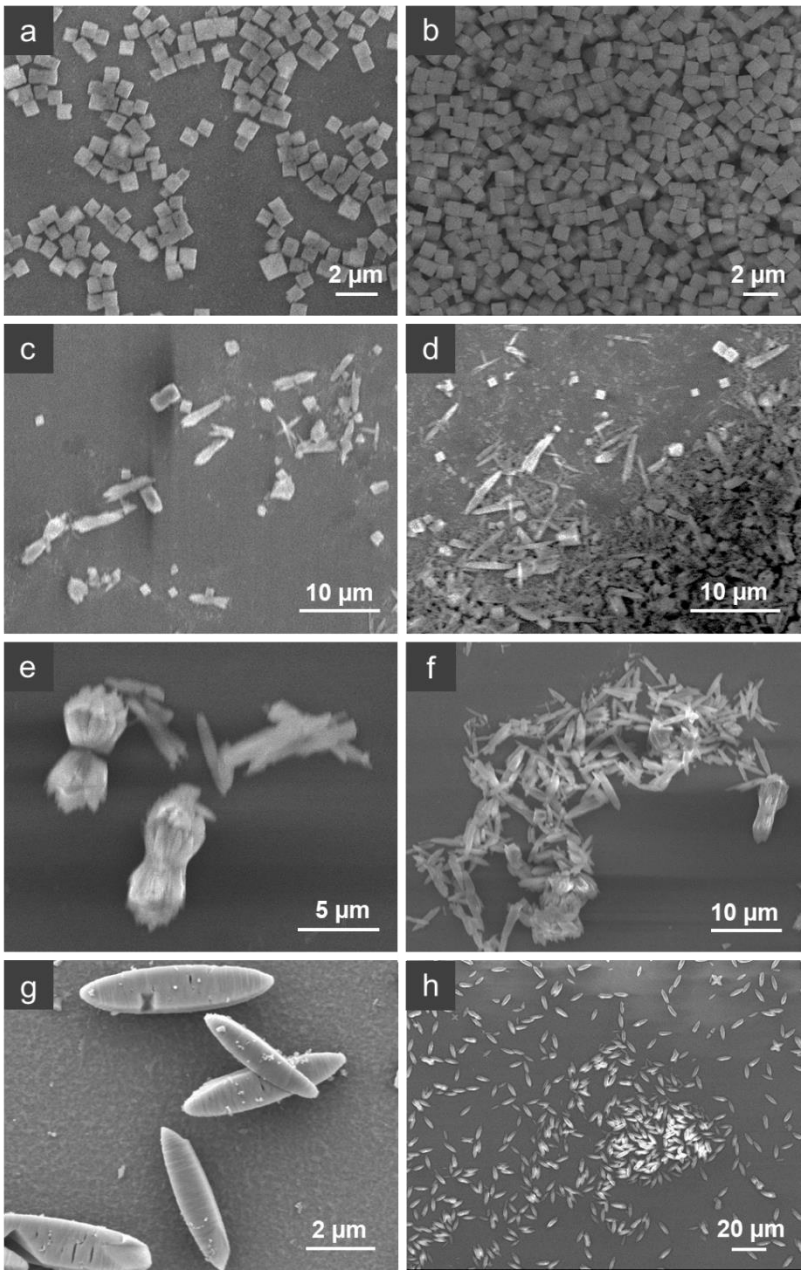

Figure 3.15 SEM images of the products resulted from the 2D **cpp** UiO-66-$F_4|_{AcOH}$ syntheses with different amout of AcOH modulators (see Section 3.8.3 for the detailed protocol). The ratio of BDC-F_4 to AcOH was gradually increased from top to bottom: 1:44.4 (a, b), 1:88.9 (c, d), 1:177.8 (e, f), and 1:355.2 (g, h). A gradual transformation on the particle morphology from cubes to rods with stacking layers was observed, which is consistent with the gradual formtion of the 2D **cpp** UiO-66-F_4 material as the amount of AcOH increases.

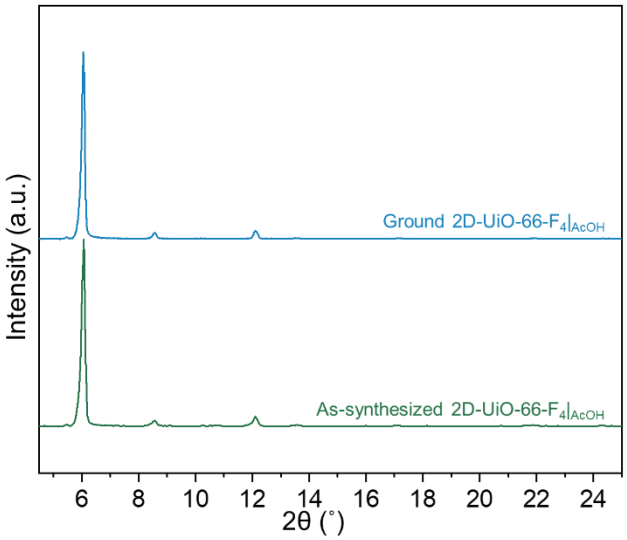

Figure 3.16 PXRD patterns of the 2D **cpp** UiO-66-$F_4|_{AcOH}$ as-synthesized (green) and ground in mortar for 1 min (blue).

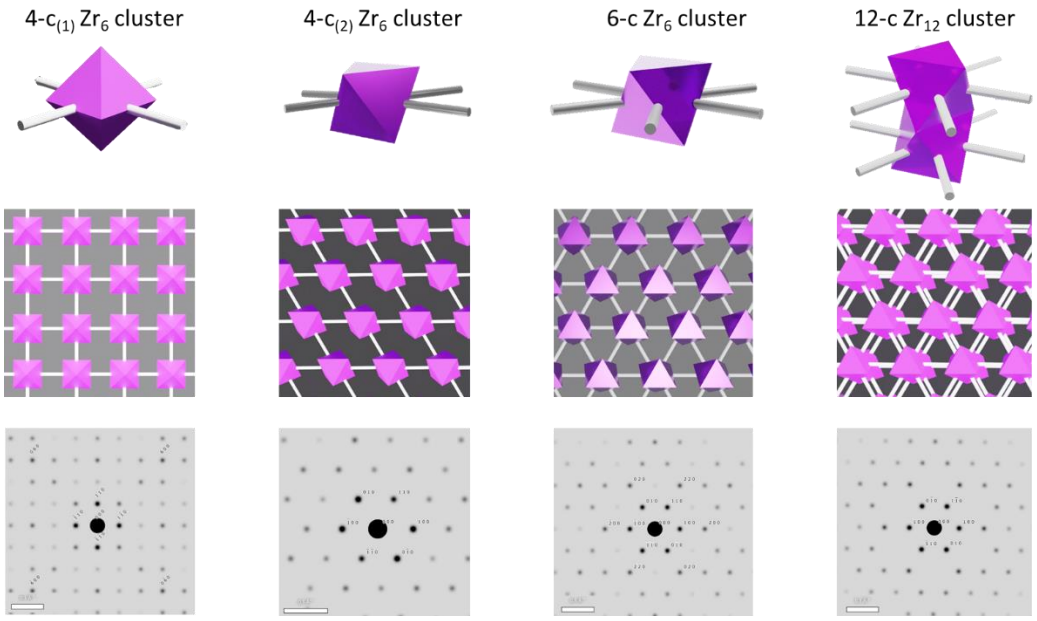

Figure 3.17 $Zr_{(6\ or\ 12)}$ clusters with specific coordination mode (top), the corresponding structure viewing from <001> direction (middle), and the simulated SAED pattern under a <001> zone axis.

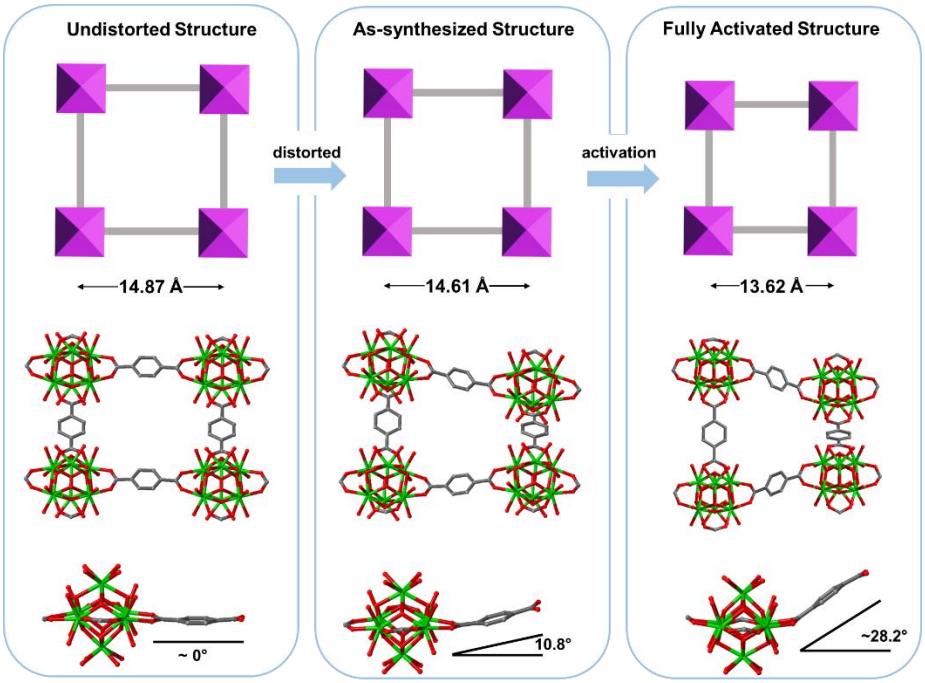

Figure 3.18 Simulated structures without distortion (left), with a tilt angle at ~11˚ (middle) and at 28.2˚ (right). The structure with a 10.8˚ distortion matches gives a lattice parameter with that of our as-synthesized material, while the one with a 28.2˚ distortion alignes well with that of the 150 ˚C activated sample.

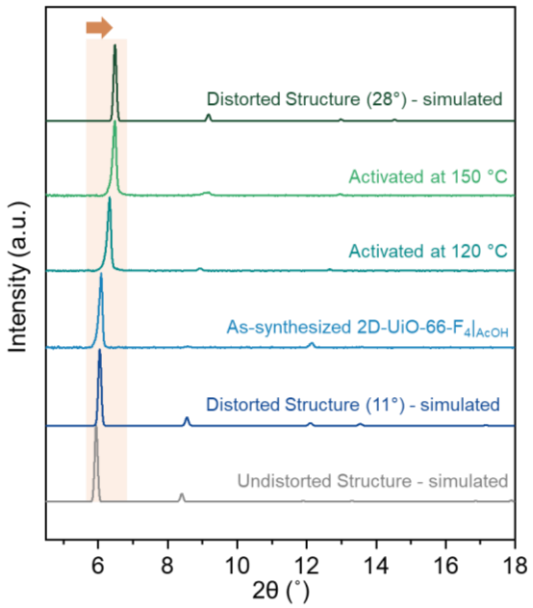

Figure 3.19. From bottom to top: PXRD patterns of simulated 2D **cpp** UiO-66-F_4 structure without distortion, simulated 2D **cpp** UiO-66-F_4 structure with 10.8˚ distortion , as-synthesized 2D **cpp** UiO-66-$F_4|_{AcOH}$, 2D **cpp** UiO-66-$F_4|_{AcOH}$ samples that were activated at 120 °C and 150 °C, and simulated 2D **cpp** UiO-66-F_4 structure with 28.2˚ distortion.

Table 3.2 The peak position in PXRD and d-spacing of (100) planes for as-synthesized 2D **cpp** UiO-66-$F_4|_{AcOH}$, activated 2D **cpp** UiO-66-$F_4|_{AcOH}$, and simulated structures.

Materials or simulated structures	(100) Diffraction (2θ°)	d-spacing of (100)
[a]Simulated structure with distortion at 28.2˚	6.48	13.62
2D **cpp** UiO-66-$F_4|_{AcOH}$ (activated at 150 ˚C)	0.62	13.55
2D **cpp** UiO-66-$F_4|_{AcOH}$ (activated at 120 ˚C)	6.33	13.95
2D **cpp** UiO-66-$F_4|_{Plu}$ (activated at 120 ˚C)	6.35	13.90
As-synthesized 2D **cpp** UiO-66-$F_4|_{AcOH}$	6.08	14.52
As-synthesized 2D **cpp** UiO-66-$F_4|_{Plu}$	6.06	14.57
[a]Simulated structure with distortion at 10.8˚	6.04	14.61
[a]Simulated structure with no distortion	5.94	14.87

[a]The simulated structures were from DFT calculation (see Figure 3.18 for the structure and Secion 3.8.2 for simulation protocols).

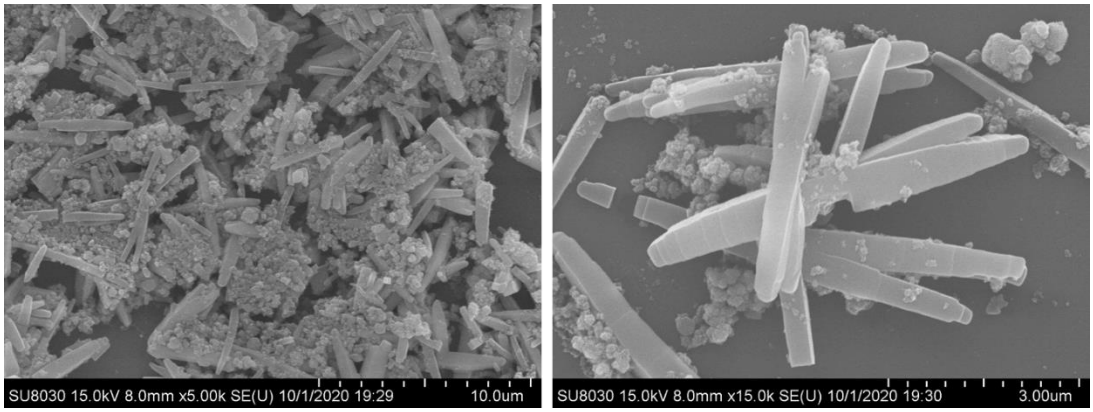

Figure 3.20 SEM images of the product collected from the Zr-side solution in the 2D **cpp** UiO-66-$F_4|_{Mem}$ synthesis.

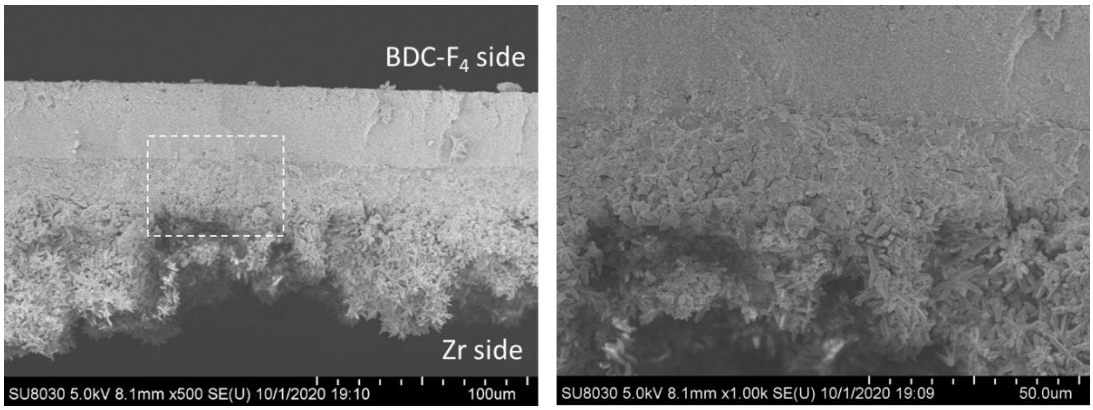

Figure 3.21 Left: Cross-section SEM images of the 2D-UiO-66-$F_4|_{mem}$ membrane with the BDC-F_4 side facing up and the Zr side facing down. Right: A zoom-in SEM image corresponding to the area circled in white dash box in the left panel.

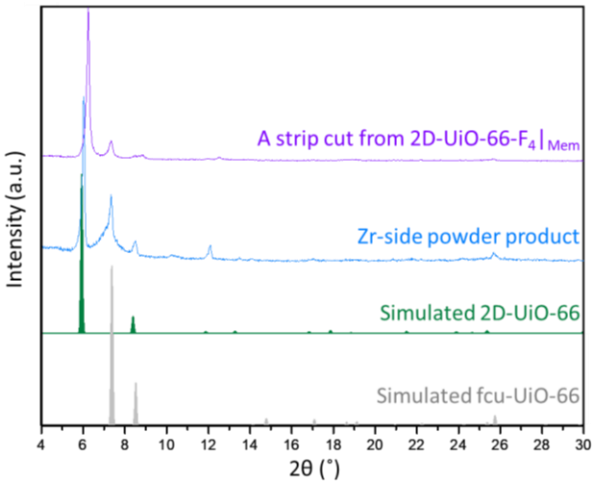

Figure 3.22 PXRD profiles of simulated **fcu** UiO-66 (grey), simulated 2D **cpp** UiO-66 (green), powder product collected from Zr side supernatant after the synthesis of 2D **cpp** UiO-66-$F_4|_{Mem}$ (blue), and a strip sample cut from the 2D **cpp** UiO-66-$F_4|_{Mem}$ (violet). A slight shifting toward high-angle region observed for the 2D **cpp** UiO-66-$F_4|_{Mem}$ strip sample could be resulted from the particle activation after MeOH soaking and overnight drying in an 80 ˚C oven. Please see the Section 3.5 for discussions on how activation could affect the lattice parameter and diffraction profile of the materials.

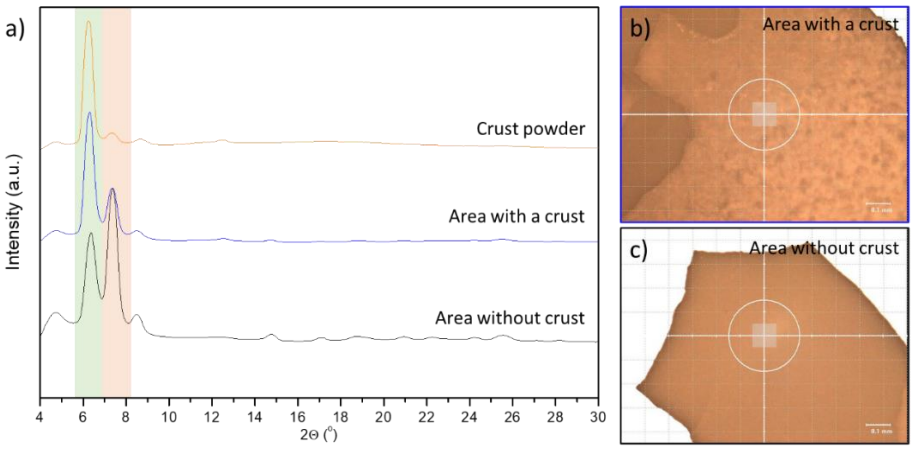

Figure 3.23 a) PXRD profiles collected from a diffractometer (Cu K_α, 1.5406 Å) with the 2D **cpp** UiO-66-$F_4|_{Mem}$ material piece and the crust powder on its surface: the diffraction pattern acquired on an area without crust (black), with obvious crust (blue), and the crust powder scraped from the membrane surface (orange). The green shaded area is corresponding to the 1st prominent diffraction signal (010) from the 2D **cpp** UiO-66-F_4 material, while the organe shaded area highlights the 1st prominent diffraction from the **fcu** UiO-66-F_4 material. b, c) Photographs obtained under an optical microscope in the diffractometer on the corresponding exposure area with and without the crust for the data collection in panel a) (the approximate exposure areas in the experiment are highlighted in semi-transparent squares).

Chapter 4

UiO-66-embeded, macroporous-membranes-enabled, electro-assisted sorption for efficient phosphate remediation

Portions of this chapter will appear in a manuscript: Chaudhury, S.; Zhang, F.; Zhang, E. Y.; Nir, O.; Nguyen, S. T., *in preparation*.

4.1 Introduction

In chapters 2 and 3, we have reported a template-assisted strategy to introduce mesopores into UiO-66 MOFs and constructed hierarchically mesoporous UiO-66 materials, where the growth processes of both HM-UiO-66 and 2D **cpp** UiO-66 have been well studied. While performances of UiO-66 materials in sorption-based applications can be enhanced by mesopores as shown in chapter 2, these materials are in powder form which could cause cumbersome works in regeneration and separation in practical usage. As MOF powder products are formed by an aggregation of numerous particles, which could also limit the accessibility of active sites in the MOF particles that are buried inside the macroscopic bulk when applied in sorption-based applications, such as water purification. Thus, in this chapter we explore the possibility of uniformly growing Zr-based MOFs inside a commercially available microfiltration (macroporous) membrane. Such a hierarchically macro-/microporous membrane not only ease the collection and regeneration process of MOF materials in water purification, but also allows for an electro-assisted sorption technique to be applied to accelerate the adsorption/desorption processes.

4.2 Background and motivation

With the rising demand for potable water and increasing concern from water contamination by nutrients, the removal of both phosphate ($H_{3-n}PO_4^{n-}$, or "P^V") contaminants and toxic arsenates ($H_{3-n}AsO_4^{n-}$, or "As^V") from water becomes critical for clean water supply and environmental protection.[161-165] Among the many adsorbents that have been investigated for selective removal of P^V and As^V from groundwater,[166-171] Zr-based metal-organic frameworks (MOFs), especially UiO-66, is an attractive candidate, as phosphate[34, 172-175] and arsenate[18, 36, 57, 176-178] anions coordinate strongly to the Zr^{IV}-containing nodes of the framework, and very high density of available Zr^{IV}

binding sites due to the massive specific surface areas of these microporous Zr-based MOFs.[33, 179, 180] UiO-66 is also known to have exceptional aqueous stability at varying pH (2-12),[181, 182] high adsorption capacity (up to 415 mg P^V/g[172] and 403 mg As^V/g[18] at pH 7, depending on MOF synthesis conditions), and high selectivity for P^V and As^V over common anions in groundwater.[183-186] However, practical water purification using Zr-based MOFs as sorbents is limited by the slow sorption kinetics due to the intrinsic microporosity of the MOFs and difficulty of regeneration requiring extreme pH (<2 or >12)[177, 178] conditions or multiple washing steps.[172, 187] Our recently developed electro-assisted approach,[188] where the sorption efficiency of the ions to/from a polymer-membrane-based sorbent is enhanced by applying an electric field across the membrane, prompted us to design a UiO-66 based membrane, which can enable efficient and selective removal of P^V and As^V from contaminated water.

Herein, we report an electro-assisted setup utilizing an UiO-66-containing polymer membrane to remove P^V & As^V selectively and efficiently from water under practical groundwater-like conditions (Figure 4.1a). As the sorbent material, UiO-66 nanoparticles were integrated into a commercial ultrafiltration membrane (PEEK) by an *in-situ* growth method. The resulted membrane can remove P^V quickly upon application of an external electric field, with good selectivity over common anions in groundwater. Under high P^V dosages, the UiO-66 component transforms into a porous, stable zirconium phosphate ("ZrP") phase that is selective for P^V and As^V. This ZrP-embedded membrane can not only be quickly regenerated and reused under electro-assisted sorption with minimal loss in P^V removal capability, but also shows an outstanding stability in HCO_3^- solutions, which are very important for practical groundwater purification applications. Overall, this work demonstrates a strategy to apply UiO-66-embedded porous membrane in groundwater purifications (with high-dosage exposure and co-existed anions),

revealing the potential pitfalls/limits and advantages of MOF-containing membranes under realistic conditions.

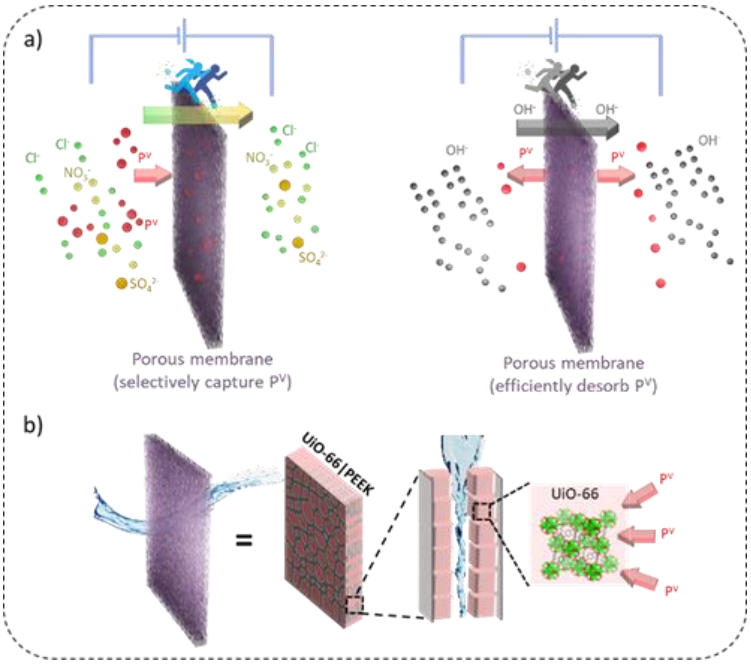

Figure 4.1 a) Scheme showing the electro-assisted sorption process by using a P^V-selective-sorbent porous membrane. b) A scheme showing the UiO-66|PEEK membrane design allowing water to flow across where P^V can be selectively adsorbed by UiO-66.

4.3 Seed-mediated, iterative growth of UiO-66 in PEEK membranes

As UiO-66 MOFs are promising sorbent materials in P^V/As^V-removal water treatment due to their outstanding water stability[189-191] and selectivity (for P^V/As^V [18, 34, 36, 57, 172-178], attempts of incorporating them into membrane forms have been made by *in-situ* growth[192, 193] or into a mixed matrix membrane (MMM) form.[42, 194-196] For applying UiO-66-based membranes to efficiently remove P^V/As^V from water, a design with uniform dispersion of UiO-66 (sorbent) particles inside a macroporous matrix is desired, which allows easier accessible sorption sites for the selective P^V/As^V removal than that in denser membrane designs such as MMMs.[37, 197-199] To achieve this, *in-situ* synthesis of UiO-66 within the pores of a chemically and thermally stable ultrafiltration

membrane (such as PEEK) is proposed. This UiO-66-in-porous-PEEK design also allows an electro-membrane process,[188, 200] which can greatly enhance sorption kinetics and ease the sorbent regenerations.[188, 201]

To facilitate the growth of UiO-66 and uniform distribution the MOF particles throughout the membrane pores, the porous PEEK matrix was "seeded" with pre-formed Zr(oxo)(hydroxo) clusters (presumably $[Zr_6(\mu^3\text{-}O)_4(\mu^3\text{-}OH)_4(OAc)_{12}]$)[91] prior to the MOF growth (see Section 4.9.2). This concept has been used in growing MOFs either in solution[80] or onto substrates.[187, 202-206] The UiO-66 growth inside the pores of PEEK membrane was then initiated with the presence of additional organic BDC linker and Zr precursor under heating. The PXRD pattern (Figure 4.2h) of the composite after one cycle of UiO-66 growth confirmed the presence of crystalline **fcu** UiO-66 particles within the PEEK membrane. Notably, the UiO-66 nanoparticles formed inside the pores after the first growth cycle (Figure 4.2a) can also seed the subsequent iterative growth to increase the UiO-66 mass.[143] By additional growth cycles (each cycle consisting of repeated exposure of the membrane to fresh UiO-66 precursor solution under appropriate growth conditions, Figure 4.2a & 4.2i), the UiO-66 loading in the PEEK membrane can reach up to ~34 wt % (Table 4.1). Interestingly, irrespective of the growth cycle, we observed uniform distribution of the UiO-66 particles within the pores and on the membrane surface (Figure 4.2c & 4.2f) of the resulting UiO-66|PEEK membrane. However, an obvious increase in the MOF particle size (from 156 ± 30 nm to 241 ± 49 nm, Figure 4.2f and 4.2g) and appearance of a prominent surface "crust" (670 ± 110 nm) due to repeated growth cycle is evident (Figure 4.2d). These data show that the iterative, *in-situ* growth method can effectively and uniformly incorporate UiO-66 NPs as sorbent materials inside (and onto) porous PEEK membranes, where the loading, particle size, and surface aggregation of UiO-66 particles can be controlled by changing the number of the growth cycle(s).

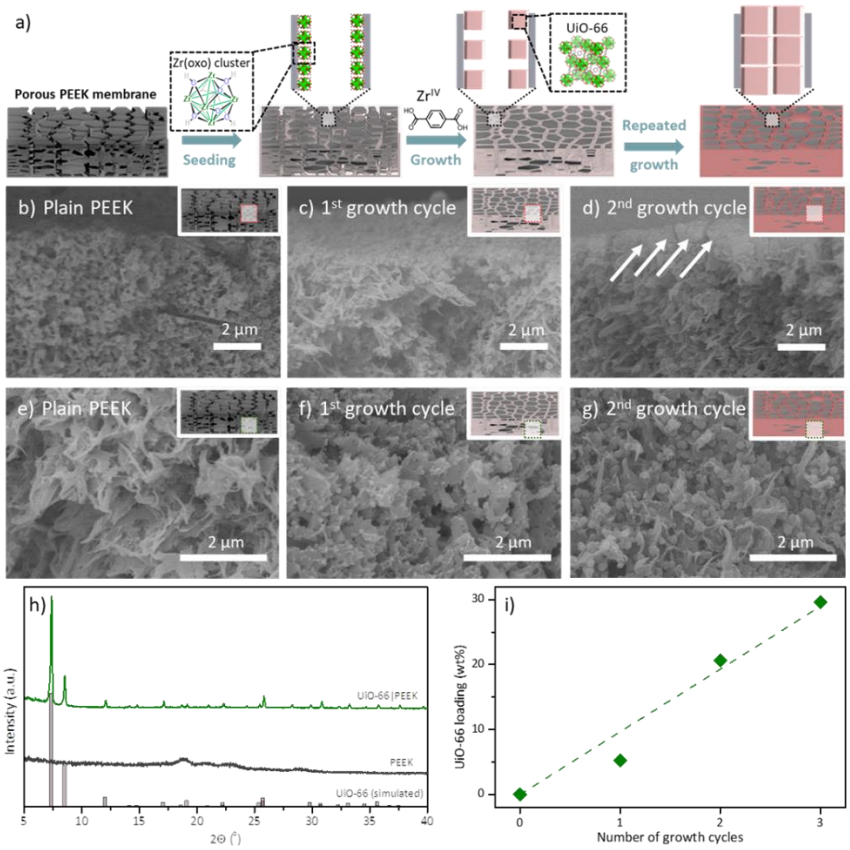

Figure 4.2 a) Schematic of the iterative, seed-mediated growth of UiO-66 nanocrystals inside a porous PEEK membrane. The PEEK membrane is first soaked in a solution of preformed $[Zr_6(\mu^3\text{-}O)_4(\mu^3\text{-}OH)_4(OAc)_{12}]$ clusters,[207] and then immersed in a UiO-66 precursor solution (containing BzOH modulator, BDC linker, and $ZrCl_4$) at 120 °C. b-d) SEM images of the surface portions (as denoted by the box in the insets) of the cross-sections of a UiO-66|PEEK membrane that has been subjected to two cycles of growth. The white arrows indicate the areas that correspond to the surface layer/crust. e-g) SEM images of the inner-membrane portions (as denoted by the box in the insets) of the cross-sections of a UiO-66|PEEK membrane that has been subjected to two cycles of growth. h) PXRD pattern of a typical UiO-66|PEEK membrane after one cycle of growth (green trace) in comparison to that of the amorphous PEEK background (black trace), and that for the simulated defect-free UiO-66 (gray bars). i) A plot of the MOF loadings for another UiO-66|PEEK membrane after three successive growth cycles. The line is included only as a visual guide.

4.4 Selective removal of P^V from solutions of common groundwater anions

Although UiO-66 powder materials have been demonstrated as efficient sorbents for P^V over other anions in lab conditions,[172, 177, 178] selective removal of P^V with the presence of multiple

abundant anions such as in practical groundwater (i.e. Cl^-, NO_3^-, and SO_4^{2-}) has not been demonstrated. Here, we explored this aspect with the fabricated UiO-66|PEEK membranes *i.e.*, the UiO-66 nanoparticles embedded in a porous membrane, by studying the adsorption kinetics of P^V and other competing anions. In a simplified approach, we first studied the adsorption of P^V in the presence of Cl^-,[208] the most abundant anion in groundwater, where the selectivity ($\alpha_x^{P^V}$, calculated from *Eq*. 4.1) reflects the preferential adsorption of P^V over another anion X by the sorbent. The distinctly faster adsorption kinetics of P^V than that of Cl^- (Figure 4.3a), despite the higher concentration of the later (~240 times), clearly indicates selective sorption for P^V by the membrane. As a result, it was possible to quickly remove most of the P^V in the solution (~90% uptake in 60 min), with a high selectivity over Cl^- ($\alpha_{Cl^-}^{P^V} = 4.0$). Similar kinetics experiments (Figure 4.3b), with additional NO_3^- and SO_4^{2-}, also showed preferential adsorption of P^V with high selectivity over the other ions ($\alpha_{Cl^-}^{P^V} = 9.0$, $\alpha_{NO_3^-}^{P^V} = 3.0$, and $\alpha_{SO_4^{2-}}^{P^V} = 2.7$), consistent with the previous observations for UiO-66.[172-174, 177, 209] Notably, the crystallinity (PXRD, Figure 4.21), and particle morphology (SEM images, Figure 4.22) of the UiO-66 were mostly maintained after the P^V uptake. Together, these data suggest that the UiO-66 particles inside a porous PEEK membrane are highly selective to P^V over common anions in groundwater and stable under these conditions.

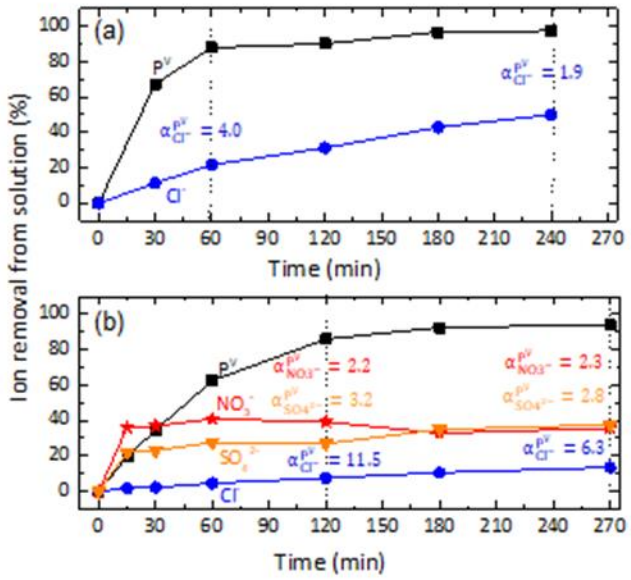

Figure 4.3 The removal rate (in %) of different anions (P^V/Cl^-/NO_3^-/SO_4^{2-}) in UiO-66|PEEK membranes from (a) a solution containing P^V (0.01 mM) + Cl^- (2.4 mM) and (b) a solution containing P^V (0.01 mM) + Cl^- (2.4 mM) + NO_3^- (0.2 mM) and SO_4^{2-} (0.1 mM). The selectivity of P^V over different anions ($\alpha_X^{P^V}$) at different time of solution exposure (marked by the dotted line) are also shown here. Experimental condition for panel a: solution volume = 10 mL, membrane area = 1 cm^2, MOF loading = 26 wt %; experimental conditions for panel b: solution volume = 85 mL, membrane area = 9.1 cm^2, MOF loading = 35 wt %; the % removal of P^V is with respect to the P^V amount present in the initial solution; no external potential applied. The membranes were subjected to pre-wetting treatment (Section 4.9.2) before the adsorption.

It is also interesting to note how the presence of competing anions can influence the P^V adsorption kinetics. The presence of additional NO_3^- and SO_4^{2-} in the solution resulted in slower P^V adsorption (~90% in 180 min, Figure 4.3b) than that in the case, where Cl^- was the only competing anion (Figure 4.3a). In fact, the increased competition due to NO_3^- and SO_4^{2-}, resulted in lower uptake of Cl^- in the sorbent and hence higher (than Figure 4.3a) selectivity over Cl^-. On continued solution exposure even after complete P^V removal, Cl^- sorption to the UiO-66|PEEK membrane continued due to its abundant presence in the solution, which resulted in sharp decrease in the selectivity for P^V over Cl^- (Figure 4.3b). However, due to the low residual amount of NO_3^-

or SO_4^{2-} in the solution, the corresponding selectivity was nearly consistent with no further obvious decrease. These observations suggest that an optimization on the hydraulic residence time should be considered in practical sorption units to take the advantage of a high selectivity during the initial uptake time window.

4.5 Improving P^V uptake by increasing UiO-66 loading in PEEK membranes

In designing the UiO-66|PEEK membranes for P^V removal, we anticipated that increasing UiO-66 loading, such as by the iterative growth described in Section 4.3, would increase the P^V uptake. This was indeed the case: when membranes with higher loadings of UiO-66 were exposed to P^V solution (0.16 mM), higher P^V uptake was observed, with a linear relationship between the mass of UiO-66 and the amount of P^V removed (Figure 4.4). A similar relationship was also observed between Zr content (as measured by XRF) and the amount of P^V removed. These trends suggest that the Zr^{IV} active sites in UiO-66 deposited on the PEEK support are probably fully accessible to the ions in solution and contribute to the P^V removal. We note that, under these static conditions, one of the highest MOF loaded UiO-66|PEEK membrane (34 wt %) could remove ~186 mg P^V per g of UiO-66, which is comparable to the P^V uptake by UiO-66 powder observed by previous literature.[172, 174]

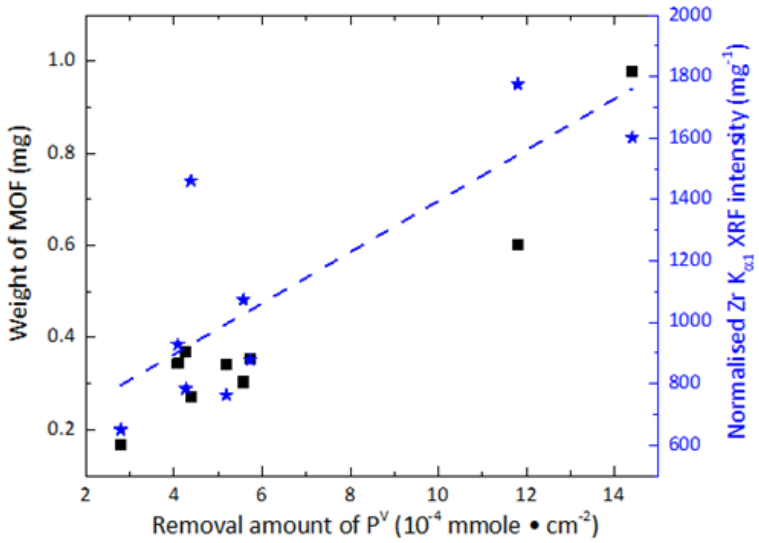

Figure 4.4 The variation of P^V removal amount as a function of initial MOF weight (black points) and Zr intensity (as obtained from XRF measurement, blue points) in the UiO-66|PEEK membranes. The straight lines are the fitted data to the solid experimental points. See Section 4.9.3 for the XRF measurement protocol; See Section 4.9.4 for detailed protocol for the P^V removal experiments.

4.6 Electro-assisted sorption in the synthesized composite membranes

4.6.1 Ion selectivity under an applied electric field

Given that the application of an external electric field across a membrane sorbent can facilitate ion sorption, and that UiO-66|PEEK can selectively remove P^V from anionic mixture solutions, we hypothesized that the UiO-66|PEEK membrane can be applied for continuous, selective removal of P^V anions under an electro-assisted process. As expected, with a 5 V external electric field, we found that the membrane constantly and preferentially removed P^V from a mixed anionic solution (Figure 4.5), which closely mimics the groundwater conditions.[210] Most importantly, in spite of a gradual decrease upon repeated exposure to fresh P/Cl solution (accumulation of Cl^- in the membrane and hence reduced selectivity, see Figure 4.5 caption), the $\alpha_{Cl}^{P^V}$ were constantly higher than 3.5. These promising results demonstrate that under electro-assisted process, the UiO-

66|PEEK membrane can be applied for continuous, selective removal of P^V from a mixed ionic solution, which is critical in practical groundwater decontamination.

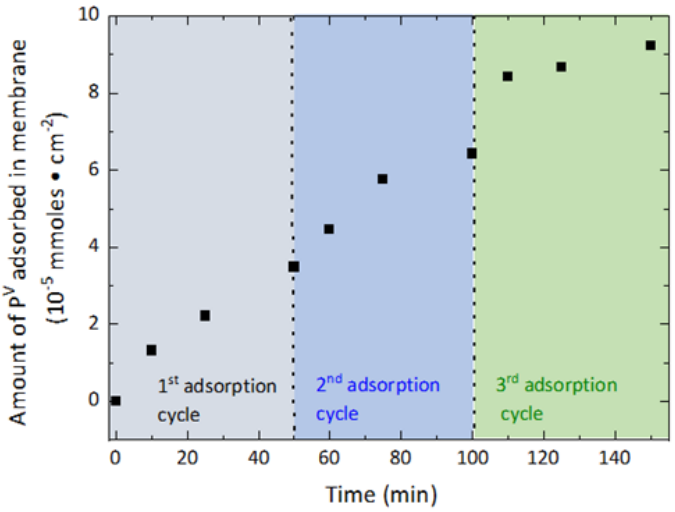

Figure 4.5 Electro-assisted adsorption kinetics of P^V in a 26wt%-UiO-66|PEEK membrane from a solution containing P^V (0.01 mM) + Cl^- (2.4 mM), where the membrane was exposed to three fresh feed solutions, each cycle continuing for 50 minutes. Experimental conditions: feed solution volume = 40 mL, receiver solution contained 40 mL water spiked with H_2SO_4, so that the initial pH became 4.2 ± 0.1, membrane area = 4.16 cm^2, external potential applied = 5 V, experimental setup is similar to that described in Figure 4.14a. The membrane was subjected to pre-wetting treatment (Section 4.9.4) before the electro-assisted adsorption. The measured $\alpha_{Cl^-}^{P^V}$ at the end 1st, 2nd, and 3rd cycle was ~11, 4.2, and 3.5 respectively.

4.6.2 Enhanced adsorption kinetics of P^V by Electro-assisted adsorption

To establish the efficacy of external electric field in obtaining faster adsorption kinetics in the synthesized UiO-66|PEEK membranes, we compared (Figure 4.6a) the electro-assisted (5 V) adsorption kinetics of P^V to that under a static condition (*i.e.*, no electric field – 0 V). For simplicity, instead of a mixed ionic system, here, we chose to work with a solution containing only P^V. At 5 V, due to the additional electromigration ion flux (see Section 4.9.5 for detailed mechanism), a significantly enhanced P^V adsorption kinetics (Figure 4.6a) was observed with a 16wt%-UiO-66|PEEK membrane (see Table 4.3 for current density and pH), comparing to that in the absence of an external electric field (0 V), where the ion transport was driven only by the

concentration gradient (Fickian diffusive flux). Specifically, after ~240 min, the membrane removed 4.3 $\times 10^{-4}$ mmole·cm^{-2} P^V at 5 V, which was twice as much as that under 0 V (2.3 $\times 10^{-4}$ mmole·cm^{-2}). The data here demonstrate that the external electric field facilitates the membrane-based P^V adsorption by accelerating the diffusion of P^V species through the UiO-66|PEEK membrane, where they can bind with the Zr component in the composite membranes.

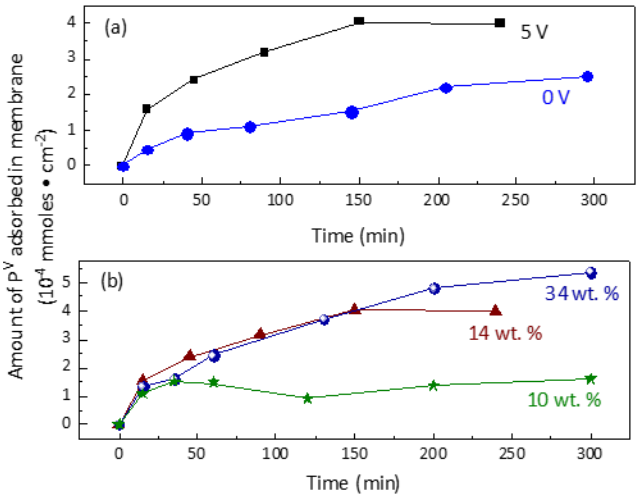

Figure 4.6 (a) Voltage-dependent adsorption and kinetics of P^V to UiO-66|PEEK membrane having ~16 wt % MOF loading and (b) electro-assisted adsorption kinetics of P^V to UiO-66|PEEK membranes differing in initial MOF loading (wt %, calculated with respect to the final composite weight). Two separate freshly synthesized composite membranes of comparable MOF loading (approximate 16 wt %) and thickness were used for the two different voltages in panel a. Experimental setup is as per Figure 4.14a: membrane (active surface area of membrane – 4.16 cm^2) was clamped between a two-compartment cell, with P^V feed solution (40 mL, 0.26 mM) on one side and the receiver solution (40 mL, water spiked with H_2SO_4) on the other (the initial pH was 4.3 ± 0.1). The pH and the current densities are listed in Table 4.3. The membrane was subjected to pre-wetting treatment (Section 4.9.4) before the electro-assisted adsorption.

To explore the possibility of improving the P^V removal amount by controlling the UiO-66 loading, we further applied three UiO-66|PEEK membranes, having different MOF loading (10, 14, and 34 wt %), to electro-assisted adsorption at 5 V. Overall, a continuous increase in P^V removal amount (though not proportionately) was observed with increase in MOF loadings (Figure

4.6b). For instance, the P^V removal amount of the 14 wt % and 34 wt % membrane were 4.5 $\times 10^{-4}$ and 5.5 $\times 10^{-4}$ mmole·cm^{-2} respectively (Figure 4.6b). In the 10 wt % membrane, where most of the spaces within the membrane pores were empty due to the low loading amount, the P^V ions from the feed were electro-driven through the membrane (Figure 4.14a) without being adsorbed, which resulted in significantly lower P^V removal amount (1.6 $\times 10^{-4}$ mmole·cm^{-2}, Figure 4.6b) than that observed in absence of electric field (Figure 4.4). This indicates that, under electro-assisted process, thicker crust on the membrane surface and large size (Figure 4.2) of the NPs, associated with high MOF loading, potentially worked in favor of the adsorption rather than hindering the accessibility of the sorption sites. Thus, to optimize P^V removal by electro-assisted adsorption through UiO-66|PEEK membrane, a high-loading amount is preferred to prevent direct P^V transport across the membrane without adsorption.

4.6.3 Regeneration of the composite membrane by electro-assisted desorption

Based on the enhanced electro-assisted P^V removal kinetics (Figure 4.6a), we contemplated that external electric field should enable easy but effective sorbent regeneration with minimum chemical consumption.[188, 201] To confirm this and also to find out the optimal working pH, we studied the effect of pH (10 – 12.5, Figure 4.7) on the electro-assisted regeneration of a fully P^V saturated UiO-66|PEEK membrane. It was noticed that the sorbents could be regenerated under an external electric field (Figure 4.7; Section 4.9.5 for detailed mechanism). Due to increased competition for the sorption sites by OH^-, the P^V desorption rate and total amount of P^V released gradually increased with an increase in the eluent pH. At pH 12.5, the desorption rate was dramatically higher than the rest, and almost complete (83% of the removal amount i.e., 3.5 $\times 10^{-4}$ mmole·cm^{-2}) sorbent regeneration was achieved within 60 min. However, this was also accompanied by a complete loss of P^V uptake capacity (irreversible sorption properties) of the

sorbent. Thus, from the sorbent reusability perspective, the most efficient eluent was pH 12 KOH under a 5 V electric field, where we obtained significant sorbent regeneration while maintaining high subsequent P^V removal efficiency (1.4×10^{-3} mmole·cm^{-2}).

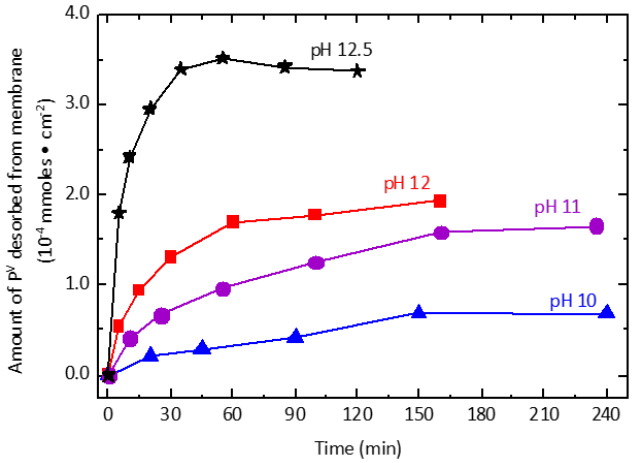

Figure 4.7 pH-dependent electro-assisted (at 5 V) desorption kinetics of P^V from two UiO-66|PEEK membranes (initially started from a 16wt%-UiO-66|PEEK (for pH 10, 11, and 12) and a 15wt%-UiO-66|PEEK(for pH 12.5)). KOH solution (100 mL) of varying pH (10 – 12.5) was used for the desorption. The pre-wetted (see Section 4.9.5) membrane (active surface area – 4.16 cm^2) was exposed (without any external electric field) to 0.26 mM P^V solution (60 mL) for overnight to completely saturate with P^V and then was subjected to an electro-assisted desorption process. Experimental setup is similar to that described in Figure 4.14b. The exact pH and the current densities are in Table 4.3.

On noticing the loss of P^V uptake capacity after desorption with KOH at pH 12.5, We hypothesized that the loss of P^V uptake capacity after desorption with KOH at pH 12.5 is because of materials transformation. We first examined the PXRD and SEM characterizations of the two membranes after electro-assisted desorption at pH 12 and 12.5. The PXRD profiles (Figure 4.15b) showed complete loss of crystallinity of UiO-66 in both cases. After desorption at pH 12, we observed the presence of a mud-like amorphous phase on the surface and a qualitative decrease in particle size inside the membrane (Figure 4.17). However, after pH 12.5 exposure, significantly fewer particles were observed, compared to the one regenerated at pH 12 (Figure 4.17), which

corroborates well with the complete loss of sorption capacity. Combining the discussion in the paragraph above, this indicates that the amorphous materials generated in the membrane after P^V adsorption and pH 12 regeneration can still remove P^V but they are not stable under pH 12.5 (electro-assisted condition).

Further, to identify the step responsible for this transformation of crystalline UiO-66 to the amorphous phase, we performed the same structural and morphological (SEM and PXRD) analysis to the membranes right after the P^V exposure (adsorption under >10 P^V/Zr_6 node) for 24 h. Here, the result was similar to that observed for the membrane after regeneration at pH 12: amorphous material without obvious PXRD pattern (Figure 4.16a) with a particle size decrease inside the membrane (Figure 4.19, middle panel). These observations are in accordance with the literature results, where, an exposure of Zr-based MOFs to high P^V concentration (~35 P^V/Zr_6 node, comparable to our case here) resulted in the formation of amorphous porous ZrP materials 30-50% smaller than the UiO-66 starting materials,[211] which also has been reported to efficiently and preferentially remove P^V.[212] However, in another membrane soaking experiment with lowered P^V dosage (~1 P^V/Zr_6 node), there was no obvious change in peak intensity/width in the PXRD profile even after 24 h P^V exposure (Figure 4.21b). This behavior is in agreement to the retaining of UiO-66 crystallographic structure in low-dosage P^V exposure (~1 P^V/Zr_6 node), as discussed in Section 3.2. With all the observations, we thus concluded that upon high-dosage (>10 P^V/Zr_6 node) P^V exposure, the UiO-66 materials in the PEEK membrane can be transformed into porous ZrP materials (and thus forming ZrP|PEEK membrane), which can still selectively remove P^V.

We also found that the spatial distribution of UiO-66 inside PEEK membrane, where the MOF particles are well separated from each other without agglomeration into large chunk unlike their powdered form, facilitate the contact between the MOF and P^V species and hence the

transformation to ZrP (Figure 4.24). In a powder soaking experiments mimicking the environment of the adsorption conditions, we found that UiO-66 in powder form still partially retained the crystallinity, which contrasts that the UiO-66 particles inside PEEK membrane lost crystallinity after 24 h soaking (Figure 4.16a and 4.24). The results highlight the importance of spatial dispersion of MOF particles in sorption applications, where agglomeration might significantly limit the transportation of sorbates. As ZrP is reported to remove P^V efficiently,[212] we thus explored the possibility to use UiO-66|PEEK membrane as a starting material for continuous selective removal of P^V under an external electric field, even if it gets transformed to the amorphous ZrP form during the process.

4.6.4 Continuous P^V removal by the composite membrane using electro-assisted sorption

To investigate the P^V sorption performances of the formed ZrP materials under electro-assisted process, we carried out a reusability (*i.e.*, repetitive adsorption-desorption) experiment on a 34wt%-UiO-66|PEEK membrane, where a complete high-dosage P^V treatment (transformation) was performed in the 1st cycle in a 3 consecutive electro-assisted sorption cycles (Figure 4.8). At the end of the first adsorption cycle (*i.e.*, at 300 min), 5.4×10^{-4} mmol of P^V was adsorbed per cm^2 of the UiO-66|PEEK membrane. This partially P^V loaded membrane was then soaked in P^V solution overnight (see Figure 4.8 caption), to complete the material transformation from UiO-66 to amorphous ZrP materials, which can reach a P^V removal amount of 1.4×10^{-3} mmole·cm^{-2} (see discussion in Section 3.4.3, and the membrane is noted as ZrP|PEEK after this step). At the end of the 1st desorption step (after 150 min), nearly half of the loaded P^V (amounting to 6.1×10^{-4} mmole·cm^{-2}) could be desorbed from the composite. We observed a constant (~6×10^{-4} mmole·cm^{-2}) P^V adsorption/desorption behavior for the subsequent two consecutive electro-assisted sorption cycles using the same membrane. Thus, this reproducible sorption capability demonstrates that

the formed ZrP material is stable under high P^V exposure (~10 P^V/Zr_6 node) & basic regeneration step (up to pH 12) under an external electric field. This is consistent with the findings by Zhang et al,[212] where the ZrP materials are reported to withstand multiple P^V adsorption/desorption cycles. Overall, it can be conjectured that the UiO-66 MOF itself can be P^V-capturing absorbent or can be used as a Zr source to introduce P^V capturing absorbent (ZrP) into a porous matrix, such as polymer membranes. Also, electro-assisted process in this composite membrane can ensure its facile regeneration at pH 12 and subsequent application in continuous P^V removal.

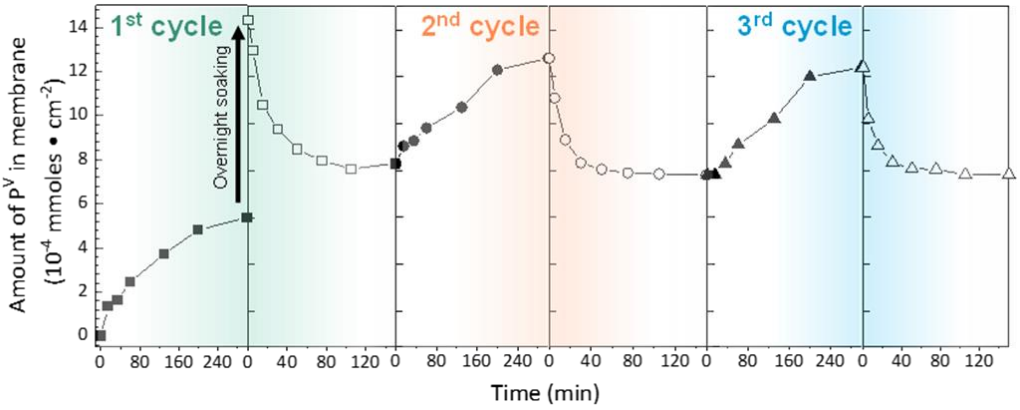

Figure 4.8 Sorption kinetics of P^V to/from a ZrP|PEEK (initially a 34wt%-UiO-66|PEEK) membrane when applied for three consecutive cycles of electro-assisted adsorption at 5 V for 5 h (solid symbols) and electro-assisted desorption at 5 V (pH = 12) for 3 h (empty symbols), indicating the stability/reusability of the membrane. Experimental setup is as per Figure 4.14 (membrane active surface area = 4.16 cm^2). For the electro-assisted adsorption experiment, the feed solution (40 mL) contained exclusively P^V (0.26 mM) and the receiver solution (40 mL) contained water spiked with H_2SO_4, so that the initial pH became 4.3 ± 0.1. The electro-assisted desorption was done using KOH (100 mL, pH = 12). The membrane was subjected to pre-wetting treatment (Section 4.9.4) before the 1st cycle electro-assisted adsorption. At the end of the 1st electro-assisted adsorption stage, the membrane was saturated with P^V by immersing in phosphate solution (0.26 mM, 60 mL) for overnight (without any external electric field). For the next two cycles, it was only electro-assisted adsorption for 300 min, followed by electro-assisted desorption for 150 min, i.e., there was no additional P^V saturation step involved. Here, before the onset of 1st desorption cycle, the P^V removal amount of the membrane is directly from Figure 4.4. This is based on the assumption that the P^V uptake should be the same under (i) overnight soaking (static condition) in 0.26 mM P^V and (2) electro-assisted sorption from 0.26 mM P^V for 300 min, followed by overnight soaking (static condition) in the same solution.

4.7 Selective removal of P^V and As^V from simulated groundwater

Thus far, we have shown that UiO-66|PEEK is a good sorbent for P^V in the presence of Cl^-, NO_3^- and SO_4^{2-}. However, HCO_3^-, the most abundant anion in groundwater, has been shown to digest/corrode UiO-66 MOFs.[213] Hence, for practical applications, the instability of UiO-66 in bicarbonate must be addressed. Considering the transformation of UiO-66 to ZrP in high P^V dosage conditions (Sections 4.6.3-4.6.4), we tested the stability of UiO-66 and two different ZrP materials by agitating the powder in $NaHCO_3$ solution (~200 HCO_3^-/Zr, Table 4.8), and determined the amount of Zr leaching (Section 4.9.8 for protocols and additional discussions). In consistence with the literature,[177] the UiO-66 powder sample underwent significant mass loss (87%) and Zr leaching into supernatant (33.3%) indicating an obvious etching/digestion of Zr-based MOFs. In a stark contrast, the amorphous ZrP materials were extremely stable in this solution with no apparent mass loss of the powder as well as Zr leaching into the solution (see Section 4.9.8 for details). In addition, for both materials, the Zr and P composition (and thus P/Zr ratio) retain the same before and after the $NaHCO_3$ soaking (Table 4.7 and Table 4.9), further confirming the absence of chemical changing during the process. Thus, even though UiO-66 itself is not stable in HCO_3^-, the ZrP materials formed from UiO-66 under the exposure of high dosage (>10 P^V/Zr_6 node) of P^V are very stable in HCO_3^-, which makes them great candidates for practical groundwater removal.

Having addressed the issue of the sorbent stability in bicarbonate, we tested the sorption behavior of the UiO-66|PEEK in a simulated groundwater[210] solution containing P^V, Cl^-, NO_3^-, SO_4^{2-}, HCO_3^-, and As^V. We found that the ZrP|PEEK membranes, irrespective of their initial Zr content, were highly selective ($\alpha_x^{P^V}$ = 2.0 to 2.8) for P^V and As^V over all the other anions, with slightly higher selectivity for P^V than As^V (Figure 4.9, Table 4.5). The strong preference for As^V

adsorption is consistent with previous reports of strong chemisorption of As^V to UiO-66.[18, 36, 57, 176] The slight preference for P^V over As^V can be rationalized using the hard-soft acid-base model, which predicts that the "harder" base P^V should bind more strongly to the "hard" acid Zr^{IV} than the "softer" base As^V. Interestingly, contrary to the expectation of strong competition between P^V and HCO_3^- in UiO-66[172] our starting material, we rather obtain higher $\alpha_{HCO_3^-}^{P^V}$ (~ 3.2 to 4.2) in ZrP|PEEK membranes. This indirectly corroborated the transformation from UiO-66 to a stable ZrP material in groundwater containing ~8 mM HCO_3^-. Furthermore, as expected, the performance of the composite membrane for selective removal of P^V and As^V from simulated groundwater remained equally promising in presence of an external electric field. Here, during the electro-assisted adsorption from the groundwater (Section 4.9.6), a ZrP|PEEK membrane (initially 28 wt % MOF loaded) could preferentially remove almost a quarter fractions of the As^V (5.1×10^{-3} mmole) and P^V (2.2×10^{-3} mmole) present in the initial groundwater within 100 min. Further, when this membrane was subjected to electro-assisted desorption at pH 12, we could desorb 53% and 84% of adsorbed As^V and P^V respectively. This efficient electro-assisted selective sorption behavior for As^V and P^V along with the established sorbent reusability (Section 4.6.4), confirms that the composite membrane, under applied electric field, can be repeatedly used for removing both contaminants from groundwater.

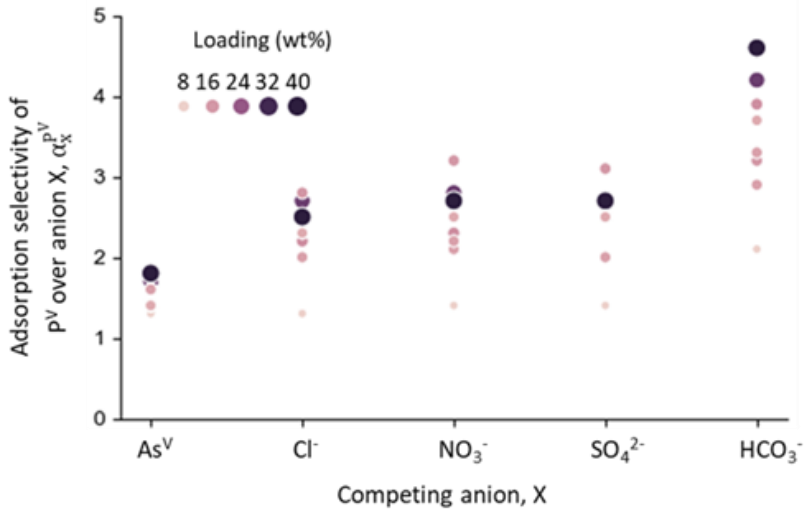

Figure 4.9 Adsorption selectivities of P^V over other anions ($\alpha_x^{P^V}$, *Eq.* 4.1), in ZrP|PEEK membranes differing in initial MOF loading. The performance of the 10 wt % membrane was an outlier than the rest possibly due to the instantaneous accessibility of the competing anions (especially Cl^- and HCO_3^-, which are abundant) to the MOF sorption sites because of low initial UiO-66 loading. For the measurement (see Section 4.9.7 for details), a UiO-66|PEEK pre-wetted membrane (~ 1 cm^2) stirred in simulated groundwater (30 mL, pH = 6.7, composition in Table 4.4) for 24 h, without any external electric field.

As demonstrated above, the incorporation of UiO-66 or UiO-66 derivative (ZrP) into the PEEK microfiltration membrane allows these MOF-loaded membranes to be applied to groundwater treatment. Apart from retaining intrinsic selectivity for P^V and As^V, this membrane design enables application of electro-assisted approach, which can significantly enhance the sorption efficiency, as established by Petrov's[200] and our[188] recent works. Unlike conventional electro-sorption approach (*i.e.*, capacitive deionization[214-216]), where conductive sorbent material is a must, this approach allows the decoupling of conductive electrodes (for applying external electric field) and selective sorbent membrane material (for targeting sorbates). This enables use of any type of non-conductive materials, such as FeO,[188, 200] UiO-66 and ZrP (as established here) in such an electro-assisted process. In this approach, the accelerated ion transport results in improved sorbent (UiO-

66 and ZrP) regeneration using minimal chemical consumption,[188, 201] which often involves harsh chemical conditions (pH < 2 or pH > 12) or repetitive chemical exposure.[35, 172, 211]

Overall, the UiO-66|PEEK membranes can be efficiently used for the selective and simultaneous removal of P^V and As^V, irrespective of groundwater composition (concentrated P^V and/or HCO_3^- present). In case of lower solution concentration of P^V (~1 P^V/Zr_6 node, as in Section 4.4 and 4.6.1) and absence of HCO_3^-, the UiO-66 itself will be the selective sorbent, whilst for a high concentration of HCO_3^- (Section 4.7) and P^V (>10 P^V/Zr_6 node, Section 4.5 and Section 4.6.2 to 4.6.4), the transformed ZrP will play the role. The easy and efficient electro-assisted sorption method, accompanied by the high degree of selectivity of the UiO-66 or the transformed ZrP material, highlight the practical applicability of the synthesized UiO-66|PEEK membranes for groundwater remediation.

4.8 Conclusion

In this chapter, UiO-66|PEEK with a [macropoore + micropore] structure was synthesized by a seed-mediate, iteratively-grown strategy. These membrane materials showed an efficient and selective removal of P^V from groundwater even in the presence of other common anions (Cl^-, NO_3^-, and SO_4^{2-}). The adsorption/desorption processes could further be accelerated by applying an external electric field across the membrane, where a three-cycle, consecutive regeneration and adsorption demonstrated their reusability. A P^V-dosage-dependent (P^V/Zr_6 node ~10) transformation from UiO-66 to a porous ZrP phase was observed in the UiO-66|PEEK membranes and the resultant ZrP showed great stability againt HCO_3^- species (that could easily degrade UiO-66). The outstanding stability of the ZrP phase makes it great candidate in real groundwater applications. This has been demonstrated by applying a UiO-66|PEEK in a high-P^V-dosage, HCO_3^--containing simulated groundwater, which allowed the ZrP-transformation, and an

adsorption with good selectivity toward P^V and As^V was observed. Overall, the works in this chapter has explored a general method to incorporate a microporous MOF in to macroporous substrate, which could be easily extended to other MOF crystals. The resulted [macropore + micropore] material can be further fabricated to engender additional mesopores to give hierarchically porous material with pores in three dimensions ([micropore + mesopore + macropore]; this future direction will be discussed in chapter 5).

4.9 Experimental and supplementary data

4.9.1 Materials and general methods

Unless otherwise stated, all reagents were used as received. Zirconium chloride ($ZrCl_4$) was purchased from Strem Chemicals, Inc. (Newburyport, MA, USA). Acetic acid (AcOH), benzoic acid (BzOH), 1,4-benzenedicarboxylic acid (BDC), and zirconium ICP standards were purchased from Sigma-Aldrich Co., LLC. (St. Louis, MO, USA) and used as received. Deuterated dimethylsulfoxide (DMSO-d_6, 99%) was purchased from Cambridge Isotope Laboratories, Inc. (Tewksbury, MA, USA). Pre-fabricated polyether ether ketone (PEEK) membranes (catalog number 1120935, 0.2 μm, 10 cm × 10 cm) were purchased from Sterlitech Corporation (Kent, WA, USA). Ultrapure deionized (DI) water (18.2 MΩ•cm resistivity) was obtained from a Millipore Milli-Q Biocel A10 instrument (Millipore Inc., Billerica, MA, USA). Solvents and aqueous inorganic acids (HCl, HF, HNO_3) were purchased from either Sigma-Aldrich Co., LLC. (St. Louis, MO, USA) or Fisher Scientific, Inc. (Pittsburg, PA, USA) and used as received.

AR grade sodium chloride (NaCl), potassium chloride (KCl), sodium bicarbonate ($NaHCO_3$), sulfuric acid (H_2SO_4), and potassium hydroxide (KOH) were procured from Bio-Lab Ltd. (Jerusalem, Israel). ACS grade disodium phosphate (Na_2HPO_4) and monosodium phosphate (NaH_2PO_4) were obtained from J. T. Baker, Avantor (Arnhem, Gelderland, The Netherlands).

ACS grade sodium sulphate (Na_2SO_4), sodium nitrate ($NaNO_3$), and inductively coupled plasma-atomic emission spectrometry (ICP-OES) standard grade H_3AsO_4 (in 2-3% HNO_3) were purchased from Merck (Darmstadt, Hesse, Germany). DI water (0.1-0.2 μS/cm, TREITEL Chemical Engineering Ltd., Tel Aviv, Israel) was used for preparing all standard solutions.

The standard P^V solution was prepared using a 1:1 molar ratio of Na_2HPO_4 and NaH_2PO_4. The pH of the resultant solution was within 6.97 ± 0.18. The simulated groundwater sample (500 mL, pH 6.7) was prepared by mixing known amounts of NaCl, $NaNO_3$, Na_2SO_4, Na_2HPO_4, NaH_2PO_4, $NaHCO_3$, and H_3AsO_4 in DI water to reach the desired concentration (Table 4.4).[210] Solutions of mixed anions used in preliminary adsorption selectivity studies were similarly prepared.

For all the manipulations described below, room temperature was 20-25 °C.

A Mettler Toledo™ AB104-S analytical balance (Mettler-Toledo, LLC., Columbus, OH) was used to weigh samples > 10 mg. A Mettler Toledo™ MX5 Micro-Analytical Balance (Mettler-Toledo, LLC., Columbus, OH), located in the IMSERC facility of Northwestern University, was used to weigh samples ≤ 10 mg. To minimize weighing errors due to static electricity, samples were weighed using aluminum weighing pans; the weighing apparatus and sample containers were also de-staticized with a Milty Zerostat 3 anti-static gun when necessary.

Centrifugation was carried out in an Eppendorf Centrifuge 5804 R, Model AG 22331 (Eppendorf AG, Hamburg, Germany) equipped with an F34-6-38 rotor. All centrifugations were carried out at room temperature and 8000-11000 rpm (8228-15557 *g*) for 10-30 minutes.

A Heratherm OMS100 oven (Thermo Fisher Scientific, Waltham, MA, USA) was used for the UiO-66 growth steps in the synthesis of UiO-66|PEEK membranes. Another oven (Shel Lab1325F, Sheldon Manufacturing Inc, Cornelius, OR, USA) was used to oven-dry the UiO-66|PEEK membranes.

Volume measurements were carried out using mechanical pipettes (0.5-5.0 mL, Research Plus single channel pipettes, Eppendorf, Enfield, CT, USA). However, for MOF synthesis, the volume accuracy does not need to be maintained at the ± 0.005 mL level of accuracy that is intrinsic to these instruments.

XRF measurements were carried out on an EDXRF analyzer (model EX-Calibur, Xenemetrix, Migdal Haemek, Israel). XRF sample cups (40 mm double open-ended, catalog #: SC-3340, Premier Lab Supply, Lucie, FL, USA) and Mylar film (catalog #: SKY-135, Premier Lab Supply, Lucie, FL, USA) were used to hold the samples during the XRF spectrum acquisition.

Powder X-ray diffraction (PXRD) patterns were collected on a STOE STADI-MP powder diffractometer (STOE & Cie. Ltd, Darmstadt, Germany) equipped with an asymmetric curved Germanium monochromator (Cu $K_{\alpha 1}$ radiation, $\lambda = 1.54056$ Å), a one-dimensional silicon strip detector (MYTHEN2 1K from Dectris AG, Baden, Switzerland), and a line-focused Cu X-ray tube operated at 40 kV and 40 mA. Powder samples (~ 2 mg) were sandwiched between two pieces of acetate foil (polymer substrate with neither Bragg reflections nor broad peaks for $2\theta < 10°$) and measured in transmission geometry in a rotating holder. Membrane samples (~0.3 cm^2) were folded several times to fit inside a 3 mm mask and similarly sandwiched between two pieces of acetate foil. Prior to the measurement, the instrument was calibrated against a NIST Silicon standard (640d). Measurements were made over the range $5° < 2\theta < 60°$ in 6° steps of the detector and an exposure time of 20 s per step.

Scanning electron microscopy (SEM) images were obtained at Northwestern University's EPIC/NUANCE facility on an SU8030 FE-SEM microscope (Hitachi High Technologies America, Inc., Dallas, TX, USA) with an acceleration voltage of 10-15 kV. Prior to imaging, membrane samples were coated with a film of Au/Pd (~10 nm thickness) using a Denton Desk III

TSC sputter coater (Denton Vacuum, Moorestown, NJ). Size measurements for particles were obtained from sample populations of >100, and these measurements were used to construct standard normal distribution plots (mean ± 3 standard deviation units) and histograms.

Inductively coupled plasma atomic emission spectroscopy (ICP-OES) was conducted on a computer-controlled (QTEGRA software v. 2.2) Thermo iCap 7600 Duo ICP-OES (Thermo Fisher Scientific, Waltham, MA, USA) instrument equipped with a SPRINT valve and a CETAC 520ASX autosampler (Teledyne CETAC, Inc., Omaha, NE, USA).

^{1}H NMR spectra were recorded on a Bruker Neo 600 MHz spectrometer (Bruker Biospin Corp., Billerica, MA, USA) equipped with a triple-resonance (HCFN) cold probe w/ Z-gradient and the following manufacturer-reported sensitivities: ^{1}H = 5000, ^{19}F = 7000, and ^{13}C = 800. ^{1}H NMR chemical shifts are referenced in ppm downfield from tetramethylsilane (TMS, δ scale) using the residual solvent resonances as internal standards.

During the P^{V} removal amount measurement, the membrane samples were weighed using a Mettler Toledo Excellence Plus XP6 microbalance (Tel Aviv, Israel).

For electro-assisted sorption studies, a tailor-made two-compartment Perspex cell (Figure 4.14), a DC power supply (5 A, 0-30 V) and a UNI-T model UT33D digital multimeter (Beersheva, Israel) were used. The two compartments of the cell, each of 40 mL, were separated by the UiO-66|PEEK membrane (active surface area 4.16 cm^2). An electric field (5 V), using the DC power supply, was applied across the membrane by using Pt electrodes positioned ~1.5 cm from the membrane surface on both sides (i.e., in each compartment). The length and the diameter of the Pt wires were 4 cm and 1 mm respectively. A Leadfluid model BQ80S peristaltic pump (Baoding, Heibei, China) was used to mix and recirculate the eluent between the anodic and the cathodic compartments during the electro-assisted desorption process. Notably, due to the difference in the

electrode (wire) and the membrane (circular) geometry, slight non-uniformity in the electric field over the membrane surface can be expected. However, since the diameter of the membrane is small (2.3 cm), the electric field variation over the membrane surface is negligible.

A glass pH electrode attached to a Thermo Scientific Orion Star A211 pH meter (Thermo Fisher Scientific, Waltham, MA, USA) was used to monitor the pH of the solutions.

The concentrations of P^V in solutions not containing As^V were determined using ascorbic acid-based colorimetric assay kits (catalog number MAK030, Sigma-Aldrich Co., LLC., St. Louis, MO, USA). Absorbance at 645 nm was measured using a Tecan Infinite M200 UV plate reader (Neotec, Kefar Sava, Israel). A linear calibration was obtained for the P^V concentration range 0.05 – 5 ppm.

For the experiments involving mixed ionic solutions, the concentrations of As^V and P^V were determined by ICP-OES, using a Spectro-Arcos instrument (AMETEK, Kieve, Germany). The concentration of HCO_3^- was determined by colorimetric titration, using an autotitrator unit (Metrohm, Herisau, Switzerland). The concentrations of Cl^-, NO_3^-, and SO_4^{2-}were determined by ion chromatography, using a Dionex ICS-5000 system (Thermo Fisher Scientific, Waltham, MA, USA). The errors on the data obtained from UV-vis analysis and ICP-OES were within ± 2% and ± 5% respectively.

Zeta potential was measured for the UiO-66|PEEK membrane in an adjustable-gap cell, using an Anton Parr SurPASS electrokinetic analyzer (Graz, Austria).

4.9.2 Fabrication of materials

The fabrication of UiO-66|PEEK membranes required the following three solutions:

Zr_6 oxo cluster ($Zr_6O_4(OH)_4(OAc)_{12}$ solution (solution A). [91] $ZrCl_4$ (1285 mg, 5.5 mmol) was weighed into an Erlenmeyer flask, in which a pre-mixed solution of glacial acetic acid (22 mL, 385 mmol) and DMF (60.5 mL) was then added. The solution was subjected to sonication for ~15

min. Depending on the source of reagent, a small amount of materials may remain undissolved. After sonication, the solution was stored for 1 day at room temperature and then syringe-filtered through a PTFE membrane (Fisher brand catalog 28145-495, 0.2 μm) to remove any undissolved compounds or precipitate.

BDC linker solution (solution B). BzOH (320 mg, 2.62 mmol) was dissolved in DMF (10 mL). BDC (26.4 mg, 0.159 mmol) was added to the solution, and the solution was sonicated (~5 min) to ensure that the solids were completely dissolved.

$ZrCl_4$ precursor solution (solution C). BzOH (320 mg, 2.62 mmol) was dissolved in DMF (10 mL). $ZrCl_4$ (41.2 mg, 0.177 mmol) was added to the solution, and the solution was sonicated (~5 min) to ensure that the solids were completely dissolved.

Fabrication of UiO-66|PEEK membranes. The as-received PEEK membranes were pre-treated as follows: The membranes were cut into 5 cm × 5 cm pieces. Each membrane piece was immersed in methanol (MeOH, ~20 mL) for at least 1 h to remove potential surface impurities. The membrane was then loosely sandwiched between two sheets of filter paper to prevent the membrane from curling up while drying, then allowed to air-dry (~30 min) and oven-dry (60 °C, ~1 h) in a Petri dish. The weight of the pre-treated membrane piece was then measured.

The pre-treated membranes were then "seeded" with the Zr_6-clusters as follows: The membrane was placed in a clean Petri dish (100 mm D × 20 mm H) and immersed in solution A (15 mL) for 24 h. The same drying procedure was repeated and the weight of the Zr_6-cluster seeded membrane was recorded. A reproducible ~2 mg mass increase was observed across tens of trials.

To grow UiO-66 in the Zr_6-cluster seeded PEEK membranes, the membrane was rolled into a tubular shape and placed into an 8 dram vial, into which solution B (10 mL) and solution C (10 mL) were added to achieve complete submersion of the membrane. The capped vial containing

the membrane and precursor solutions was mixed by gentle shaking and then placed in a pre-heated oven (120 °C) for 24 h, after which the vial was taken out and allowed to cool to room temperature. We note that after this heating step, a white powder (UiO-66) was also obtained from the same vial; we characterized this powder to gain indirect insight into the properties of the UiO-66 embedded in the membrane (see Section S10 for stability evaluation by soaking experiments). The membrane piece was taken out from the vial using a pair of stainless-steel tweezers, placed in a clean Petri dish (100 mm D × 20 mm H), and immersed in DMF (~20 mL) for ~2 h. The membrane was removed from the DMF, transferred to another Petri dish, and immersed in MeOH (~20 mL) for ~2 h. This MeOH immersion was repeated once more, and the membrane was air-dried (~30 min), oven-dried (60 °C, ~1 h), and weighed. The weight of the membrane after this first growth cycle is shown in Table 4.1. From the weight data, the MOF loading in weight percentage was calculated by *Eq.* 4.1, where W_1 and W_2 are weights of the membranes before and after MOF growth respectively.

$$\text{MOF loading (wt \%)} = \frac{W_2 - W_1}{W_2} \times 100\% \quad (4.1)$$

For membranes subjected to two or three growth cycles, the same protocols (solvothermal growth, washing, drying, and weighing) protocols were repeated once or twice, respectively. The weight data for all of the syntheses are summarized in Table 4.1. We note that the fabrication protocol as described above is quite reliable and can give membranes with encapsulated UiO-66 of consistent quality, independent of the person who carried out the synthesis (F.Z. or E.Y.Z.).

Variability of PEEK membranes. From weighing and SEM imaging of cross-sections of the as-received PEEK membranes, we found that the thickness and areal density of the PEEK membranes varied by as much as 100% between product batches (see Figure 4.10), and sometimes within the

same product batch. Similar variance in the thickness of prefabricated PEEK membranes has been previously reported.[217] To minimize any effects of membrane variance on the growth of UiO-66 and ion sorption kinetics, we have only made comparisons between UiO-66|PEEK membranes of similar thickness and areal density, as reported in Table 4.1.

Hot MeOH soaking of two UiO-66|PEEK membranes. For two membranes in the studies (entry 8 and 9 in Table 4.1), they were subjected to hot MeOH soaking treatments. Specifically, the as-synthesized UiO-66|PEEK membrane was placed in a clean 8 dram vial, and MeOH (20 mL) was added to immerse the membrane. The vial was capped and placed in a preheated oil bath (80 °C) for 30 min. After the heating, the vial was taken out from the oil bath and the supernatant was decanted. Another aliquot of MeOH (20 mL) was added into the vial containing the membrane, which was subjected to the heating in the same oil bath for another 30 min. After the second round of heating, the membrane was taken out from the MeOH, air- (~30 min) and oven-dried (60 °C, ~1 h).

This hot MeOH soaking was used to further purify the UiO-66 materials inside the membrane, which slightly improve the P^V removal amount (*cf* entry (3, 4, 6, 9) and (7, 8) in Table 4.2). Although noticing that hot MeOH could potentially remove carboxylate ligands from related Zr-based MOFs (like MOF-808),[218] we verified that this MeOH treatment did not change the UiO-66 material by subjecting a UiO-66 powder sample collected from supernatant during the UiO-66|PEEK fabrication (see section 4.9.9 for detailed protocol and powder sample characterization data) to the same soaking treatment. Little change in chemical formula was observed after this hot MeOH soaking (see Table 4.6), we thus conclude that this process probably won't cause chemistry change in the UiO-66 sorbent materials and the slight increasing in P^V removal amount should be attributed to further cleaning by the hot MeOH soaking.

Table 4.1 Weights and thicknesses of the UiO-66|PEEK membranes synthesized and used in the present work.

Entry	Membrane label	Number of UiO-66 growth cycles	Membrane weight[a] (mg)		Membrane thickness[b] (μm) (after UiO-66 growth)
			Before UiO-66 growth	After UiO-66 growth	
1	28wt%-UiO-66	2	26.7	36.9	34.2 ± 0.3
2	10wt%-UiO-66	1	30.0	33.4	31.9 ± 0.4
3	16wt%-UiO-66	1	32.5	38.8	34.3 ± 0.5
4	15wt%-UiO-66	1	36.0	42.6	44.8 ± 1.0
5	34wt%-UiO-66	2	35.0	53.4	40.0 ± 1.2
6	17wt%-UiO-66	1	23.5	28.1	27.2 ± 0.3
7	14wt%-UiO-66	1	35.8	41.4	34.1 ± 0.4
8	15wt%-UiO-66[c]	1	24.9	29.4	30.4 ± 0.6
9	14wt%-UiO-66[c]	1	35.5	41.2	34.1 ± 0.4
10	26wt%-UiO-66	2	34.3	43.6	50.3 ± 0.6
11	35wt%-UiO-66	2	40.8	58.7	50.8 ± 0.4

[a]The weight data were collected by using an analytical balance with a theoretical uncertainty of ± 0.1 mg. [b]The thickness was measured using ImageJ on the cross-section SEM images (Figure 4.10). At least 20 thickness measurements were made across ~100 μm membrane width for each membrane, and these thicknesses are summarized with the mean and standard deviation. [c]The sample was subjected to two additional hot methanol (80 °C) washing cycles (30 min for each cycle), which has been shown to have no effect to the UiO-66 stoichiometry (Table 4.9.6).

UiO-66 powder sample. This material was synthesized as a precursor for ZrP (see Section 4.9.9), using a previously reported literature procedure with minor modifications.[219] In a 1000 mL Erlenmeyer flask equipped with a magnetic stir bar, BzOH (12.926 g, 108 mmol) was dissolved in DMF (412 mL). $ZrCl_4$ (0.848 g, 3.64 mmol) and BDC (0.544 g, 3.28 mmol) were added, and the resulting mixture was stirred until a clear solution was obtained. This solution was then equally partitioned among sixteen 8-dram glass vials by using a 5 mL mechanical pipet (25 mL in each vial). The vials were capped and placed in a preheated oven (120 °C) for 24 h. When the vials were removed from the oven, each vial was observed to contain either a cloudy suspension or a white precipitate. After cooling to room temperature, the contents of the vials were collected by successive centrifugation in six 50 mL centrifuge tubes (to fit the centrifuge rotor configuration). After removing the mother liquor, fresh DMF (~20 mL) was added to the remaining white solid;

the mixture was dispersed by sonication (> 5 min) and then left at room temperature for 14-18 h to dilute out unreacted starting materials. The solid was again pelletized through centrifugation; the supernatant was decanted; fresh DMF (~20 mL) was added; and the mixture was sonicated for 30 minutes before centrifugation again. This sonication-washing process was then repeated once more. After the third DMF washing, the supernatant was decanted, and the remaining wet solid UiO-66 products were suspended in fresh MeOH (~20 mL) and sonicated for 30 minutes before being pelletized out by centrifugation. The MeOH supernatant was then decanted and the solids in all the centrifuge tubes were combined and placed in a laboratory oven (80 °C) to dry before being placed into a microscale cellulose Soxhlet extraction thimble. The UiO-66 was then subjected to Soxhlet extraction (≥ 8 h, > 200 cycles) over MeOH reflux (~50 mL in a 100 mL collection flask) as described at the end of Section S1. After cooling to room temperature, the whole thimble was dried in an oven (80 °C) overnight prior to collection of the UiO-66 (yield ~0.9 g).

4.9.3 Characterization of UiO-66|PEEK membranes

Sample preparation for SEM. For cross-section imaging, the membrane samples were prepared by cutting a small piece (~30 mm^2) from the edge of the membrane, submerging the piece in liquid nitrogen until brittle, then fracturing the cooled membrane between two pairs of stainless-steel tweezers. The sample was mounted on a 90° SEM mount (Ted Pella Inc., Redding, CA, USA) with the fractured edge facing upwards, and then coated with a thin film of Au/Pd as described in Section 4.9.1.

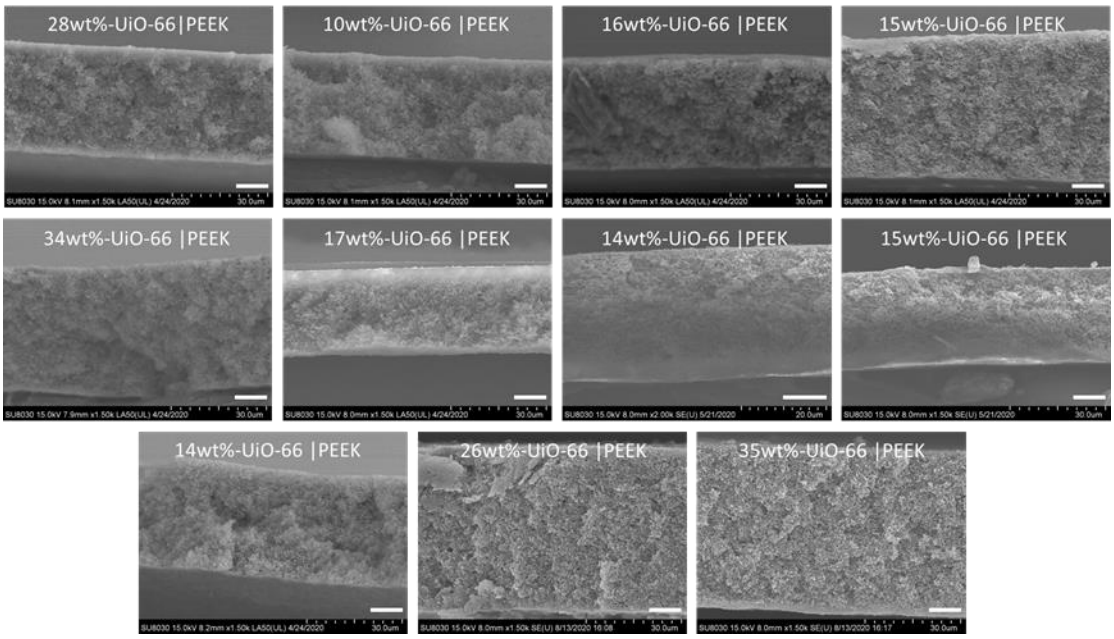

Figure 4.10 SEM images of cross sections of the UiO-66|PEEK membrane samples used in the present work (Table 4.1). Membrane thicknesses were measured using ImageJ at multiple sites spanning ~100 μm of the cross section. The scale bars in the images are 10 μm.

XRF characterization of UiO-66|PEEK membranes. In each measurement, a small piece (~3 mm × 3 mm) was cut from the membrane sample and weighed using a MX5 micro-analytical balance (see Section 4.9.1 for detailed balance information). The membrane sample was placed on a Mylar sheet in a double open ended XRF sample holder. The XRF spectrum was acquired under 150 μA emission current, 25 kV voltage, and 60 s collection time. The Zr $K_{\alpha 1}$ peak (15.28 to 16.16 keV) was integrated to evaluate the amount of Zr in the membrane sample. The weight of UiO-66 in the sample, calculated using the sample weight and the UiO-66 loading, appears to be linearly related to the Zr $K_{\alpha 1}$ peak integration (Figure 4.11). The exact numerical values of the Zr $K_{\alpha 1}$ peak intensities are also given in Table 4.2.

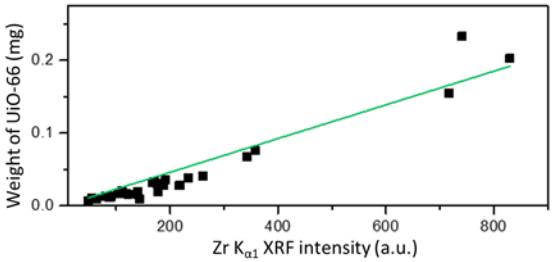

Figure 4.11 A linear relationship between the weight of UiO-66 in the membrane samples and the Zr $K_{\alpha 1}$ peak integration measured with XRF. The green line is obtained from linear regression with a zero intercept. To obtain a good correlation of Zr $K_{\alpha 1}$ signal and MOF loading amount, 17 other membranes were synthesized by the same method (in additional to the 11 membranes in Table 4.1) and used in this XRF experiment.

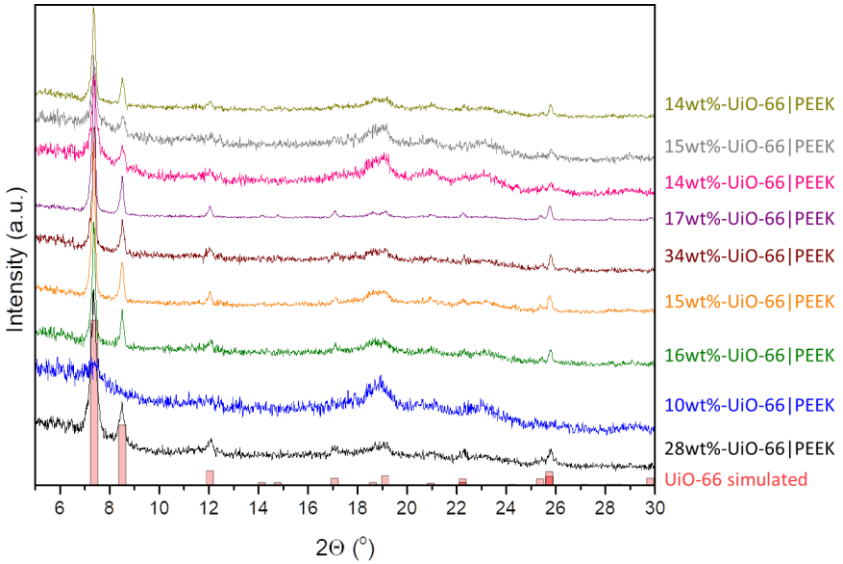

Figure 4.12 PXRD profiles of the UiO-66|PEEK membrane samples (Table 4.1, entry 1-9) prior to soaking in 0.16 mM P^V solution (Section 4.5).

Digestion of UiO-66, ZrP-1, and ZrP-2 powder for quantifying Zr and P content by ICP-OES (see Section 4.9.9 for the syntheses of ZrP-1 and ZrP-2). In a 15 mL polypropylene centrifuge tube, conc. HNO_3 (750 μL), HCl (250 μL), and HF (750 μL) were added to a small amount of sample (~1 mg, weighed using a micro-analytical balance) to be analyzed. The resulting mixture was sonicated until the solid disappeared (~1 h). After the sonication, DI H_2O (3.250 mL) was added into the tube and it was heated in a 70 °C oil bath for ~12 h. After heating, the solution

was clear and no solid was visible. The resulting solution was transferred into a 50 mL polypropylene centrifuge tube and diluted with DI water (45 mL) using adjustable mechanical pipettes. The concentrations of Zr and P in this solution were analyzed by ICP-OES (λ_{Zr} = 343.823, 327.35, 349.621, and 339.198 nm; λ_P = 177.495, 213.618, 185.942, and 178.766 nm) against a calibration curve of standards with known [Zr] and [P].

Quantification of Zr and P content in HCO_3^- supernatant after soaking UiO-66, ZrP-1, and ZrP-2 powder by ICP-OES (see Section 4.9.9 for details of HCO_3^- soaking experiments). In a 50 mL polypropylene centrifuge tube containing the supernatant (25 mL) from the HCO_3^- soaking experiment, conc. HNO_3 (1.5 mL) was added dropwise while swirling. While adding HNO_3, bubbles were generated. After the uncapped tube was left at room temperature for 30 min, conc. HCl (250 μL) and HF (750 μL) were added. The resulting mixture was sonicated for ~1 h. Notably, after the sonication, the solution in one of the three tubes (the supernatant from soaking UiO-66 powder in HCO_3^-) was cloudy and semi-transparent, probably due to insoluble organic species leached during the HCO_3^- soaking, while the other two (corresponding to ZrP) were clear. To fully oxidize potential organic species in the solution, an aliquot of $H_2O_{2(aq)}$ (250 μL, 30 wt %) was added to each tube, then the mixture was heated in a 70 ºC oil bath for ~12 h. After heating, the solution in each tube was clear and no solid was visible. The resulting solution in each tube was then diluted with DI water (22.25 mL) using adjustable mechanical pipettes. The concentrations of Zr and P in these solutions were analyzed by ICP-AES (λ_{Zr} = 343.823, 327.305, 349.621, and 339.198 nm; λ_P = 177.495, 213.618, 185.942, and 178.766 nm) against a calibration curve of standards with known [Zr] and [P].

^{1}H NMR quantitative analyses of UiO-66 powder. The ^{1}H NMR spectra of the digested MOFs can quantitatively reveal the composition of the organic ligands and benzoic acid present in each

digested sample. Together with the ICP-OES determination of Zr, the linker to node ratio and chemical formula can be determined. Chemical compositions are shown in Table 4.6.

In a 2 mL polypropylene centrifuge tube, HF (10 μL) and DMSO-d_6 (90 μL) were added to a small sample (~2 mg, weighed using a micro-analytical balance) of the material to be analyzed. The resulting mixture was sonicated until the solution became clear (~1 h). Then an aliquot (10 μL, corresponding to ~0.2 mg of the sample) of the resulting solution was transferred to a 2 mL polypropylene centrifuge tube along with an aliquot of maleic acid (MA) solution in DMSO-d_6 (12 mM, 50 μL), and fresh DMSO-d_6 (540 μL). This combined solution was transferred into an NMR tube and then analyzed by ^{1}H NMR spectroscopy with a 90° pulse using a 50 s delay between scans. The length of the delay exceeds the T1 relaxation time for BDC (3.7 s) and MA (2.8 s). The amount of each organic ligand was calculated by comparing the integration against a calibration curve of standards with known concentrations, using MA as an internal standard (see Figure 4.28 for the ^{1}H NMR spectra).

^{1}H NMR quantitative analyses of ZrP-1 and ZrP-2 powder (see Section 4.9.9 for the sample syntheses). The sample preparation and analysis were the same as for UiO-66 powder, except that a small amount of Cs_2CO_3 (~1 mg) was added into the HF (10 μL) and DMSO-d_6 (90 μL) solution to facilitate the digestion the ZrP materials. (See Figure 4.27 for the ^{1}H NMR spectra).

4.9.4 Adsorption of P^V in UiO-66|PEEK membranes under static conditions (*i.e.*, no electric field applied)

Preliminary sorption experiments without any prewetting treatment yielded inconsistent results, as the hydrophobicity of PEEK probably caused incomplete wetting. Hence, prior to all sorption experiments with UiO-66|PEEK membranes, the membranes were prewetted according to the following procedure. The membranes were soaked in methanol overnight, and then soaked in

fresh DI water (~25 mL) for 3-4 hours. To ensure complete removal of any methanol bound to the nodes of the MOF (so that it does not affect subsequent ion sorption), the water soaking step was repeated at least 3-4 times. Between the pre-wetting procedure and subsequent sorption experiments, the membranes were stored in DI water.

To measure the P^V removal amount of UiO-66|PEEK, a membrane piece (1 cm^2) was weighed on a microbalance and then stirred (~300 rpm) in P^V solution (0.16 mM, 30 mL, P^V/Zr_6 node ratio ~27; pH 6.97 ± 0.18, no electric field applied) for 24 h. The concentrations of P^V in the solutions before and after the adsorption were determined by UV-vis spectrophotometry using an ascorbic acid-based colorimetric assay kit (see Section 4.9.1). During the experiment, the solution was kept covered using Parafilm, and loss of solution volume due to evaporation was assumed to be negligible. The amount of P^V removed from solution ($n_{p,mem}$ in mmol) was calculated using *Eq*. 4.2 and are given in Table 4.2.

$$n_{P,mem} = V(C_i - C_f) \qquad (4.2)$$

where V is the volume of solution (in L), and C_i and C_f are the P^V solution concentrations before and after the adsorption (in mM).

Table 4.2 Data for plotting Figure 4.4, obtained from nine membrane samples.

Entry	UiO-66 loading (%)	UiO-66 weight in membrane[a] (mg)	P^V uptake (10^{-4} mmol·cm^{-2} of membrane)	Normalized Zr $K_{\alpha 1}$ XRF intensity (mg^{-1})
1	28	0.601	12	1775
2	10	0.168	2.8	649
3	16	0.344	4.1	927
4	15	0.369	4.3	784
5	34	0.979	14	1602
6	17	0.271	4.4	1461
7	14	0.355	5.7	877
8[c]	15	0.303	5.6	1073
9[c]	14	0.341	5.2	763

[a]The UiO-66 weight was calculated by multiplying the UiO-66 loading (%) and the weight of each membrane piece (measured by an ultra-microbalance, see Section 4.9.1 for instrumental detail) used in the XRF experiment. [c]The sample was subjected to two additional hot methanol (80 ºC) washing cycles (30 min for each cycle), which has been shown to have no effect to the UiO-66 stoichiometry (Table 4.9.6).

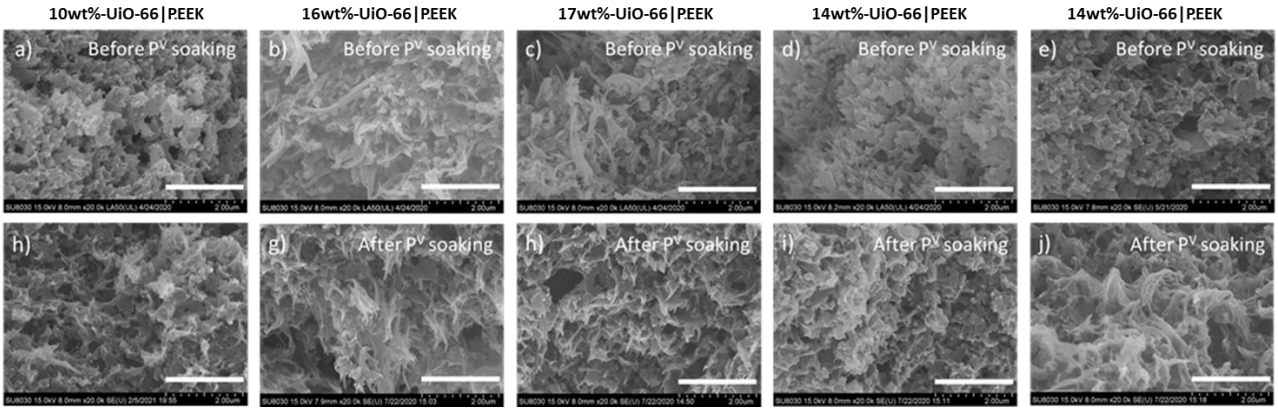

Figure 4.13 SEM images of cross sections of four UiO-66|PEEK membrane samples (10wt%-, 16wt%-, 17wt%-, 14wt%-, and 14wt%-UiO-66|PEEK, entries 2, 3, 6, 7, and 9 in Table 4.1) before (a-e) and after (h-j) soaking in 0.16 mM P^V solution (Section 4.5). Scale bar = 2 μm

4.9.5 Electro-assisted sorption of P^V to/from UiO-66|PEEK

A tailor-made two-compartment cell (Figure 4.14), as described previously in Section 4.9.1, was used for the electro-assisted sorption experiments[188] (at constant voltage mode). An electric field (5 V) was applied across the UiO-66|PEEK membrane by using Pt electrodes positioned ~1.5 cm from the membrane surface on both sides (i.e., in each compartment). A digital multimeter was used to monitor the current flowing through the cell. To avoid film-controlled diffusion at the membrane-electrolyte interface, during the experiments, the solution in both the compartments were stirred at a speed of >300 rpm. For simplicity, the applicability of the electro-assisted sorption method was initially studied for a solution of Na_2HPO_4 and NaH_2PO_4 (Section 4.6.2). In the electro-assisted adsorption step (Figure 4.14a), the cathodic (feed) compartment contained P^V solution (0.26 mM, 40 mL, pH 6.97 ± 0.18) and the anodic (receiver) compartment contained DI water (40 mL). At the beginning, to minimize the solution resistance, the water in the anodic compartment was spiked with H_2SO_4 (~ 0.2 mL), so that its initial pH became 4.3 ± 0.1. The kinetics of P^V adsorption to the UiO-66|PEEK membrane were studied by intermittent sampling (200 μL) from both the compartments and then measuring the P^V concentration of each sample by

UV-vis absorption spectrometry, as described in the previous section. The amount of P^V adsorbed (P_{abs}, in mmoles·cm^{-2}) was calculated as follows (*Eq.* 4.3):

$$P_{ads} = \frac{V\{C_i - (C_{Feed} + C_{receiver})\}}{A} \qquad (4.3)$$

where V is the solution volume in L, C_i (in mM) is the P^V concentration in the initial feed solution before adsorption, C_{Feed} and $C_{Receiver}$ (in mM) are the final P^V concentrations in the feed and the receiver solution, respectively, after electro-assisted adsorption for 5 h, and A is the active area (4.16 cm^2) of the membrane (Figure 4.14).

Mechanistically, [188] during the electro-assisted adsorption stage, an electric field is applied across the membrane (Figure 4.14). OH^- is generated at the cathode in the feed compartment containing contaminated groundwater ($2H_2O + 2e^- \rightarrow 2OH^- + H_2$), and H^+ is generated at the anode in the receiver compartment containing dilute sulfuric acid ($2H_2O \rightarrow O_2 + 4H^+ + 4e^-$). To maintain bulk electroneutrality in both compartments, the anions in the feed compartment migrate towards the receiver compartment. When the anions pass through the UiO-66|PEEK membrane between the compartments, P^V and As^V are selectively adsorbed by the UiO-66 component.

In the electro-assisted desorption step (Figure 4.14b), each of the cathodic and anodic compartments contained 40 mL of KOH solution, while an external glass beaker contained 20 mL of the same solution. To maintain the eluent pH during electro-assisted desorption, the solutions from the anodic and the cathodic compartments were mixed in the external beaker and recirculated (5 mL·min^{-1} flow rate) using an external pump. The kinetics of P^V desorption from the UiO-66|PEEK membrane was studied by intermittent sampling (200 µL) from the beaker and then measuring the P^V concentration by UV visible absorption spectrometry, as described in the previous section. The 16wt%-UiO-66|PEEK membrane was subjected to varying pH (10 – 12.5)

and different voltages (0 V, 5 V). All other membranes were subjected to electro-assisted desorption at pH 12 and a voltage of 5 V.

Mechanistically, we hypothesize that the desorption of P^V is accelerated for two reasons: (1) electromigration of OH^- through the membrane occurs due to H_2 evolution ($2H_2O + 2e^- \rightarrow 2OH^- + H_2$) and O_2 evolution ($4OH^- \rightarrow O_2 + 2H_2O + 4e^-$), thereby increasing the local pH near the sorption sites on UiO-66; (2) desorbed P^V anions electromigrate out of the membrane, decreasing the rate of P^V readsorption due to slow diffusion in the micropores of UiO-66.

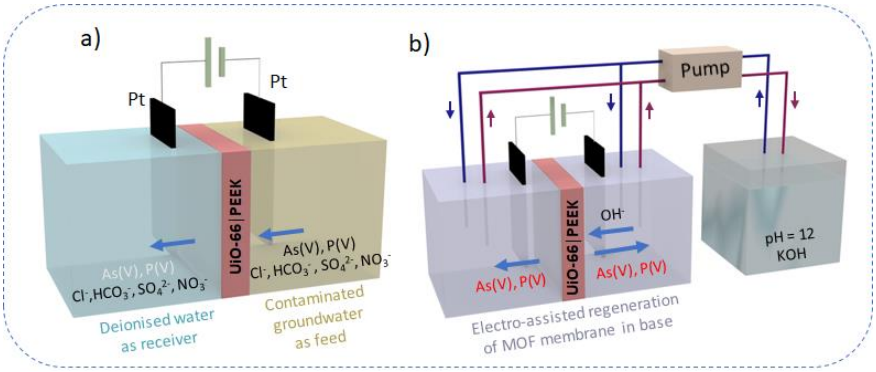

Figure 4.14 Schematic of electro-assisted (a) adsorption and (b) desorption to/from UiO-66|PEEK.

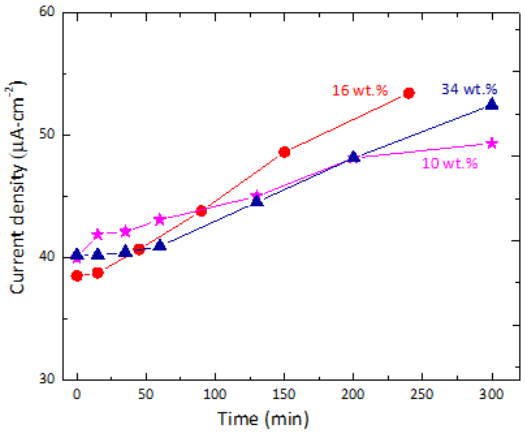

Figure 4.15 The time-dependent current densities during electro-assisted (at 5 V) adsorption of P^V in UiO-66|PEEK membranes with different UiO-66 loading. The measured current was normalized per unit area (4.16 cm^2) of the membrane. The experimental set up is shown in Figure 4.14a. In the electro-assisted adsorption, the a 0.26 mM P^V solution (40 mL) was used as feed and deionized water spiked with H_2SO_4 (40 mL, pH = 4.3 ± 0.1) was used as receiver.

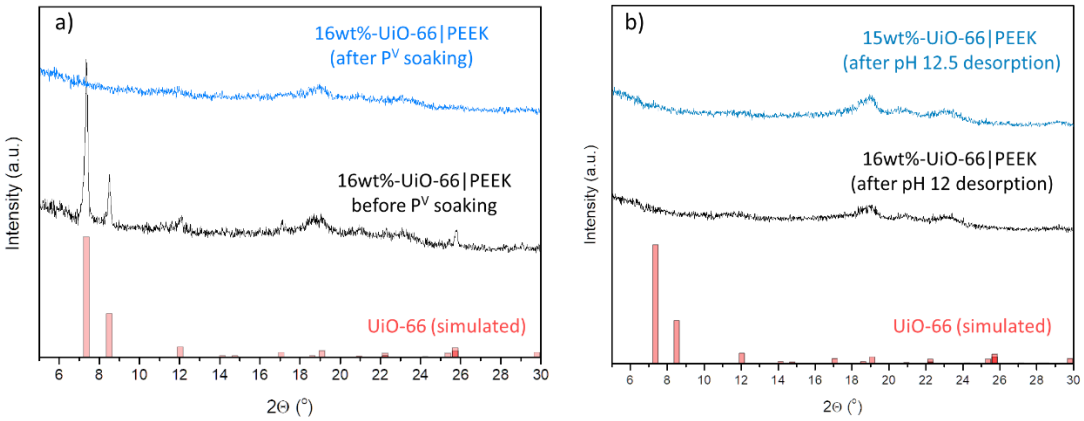

Figure 4.16 a) PXRD profiles of the 16wt%-UiO-66|PEEK membrane sample (Table 4.1, entry 3) before (black) and after (blue) soaking in 0.16 mM P^V solution (Section 4.5). b) PXRD profiles of simulated UiO-66 (red), the 16wt%-UiO-66|PEEK membrane after pH 12 desorption (black), and the 15wt%-UiO-66|PEEK membrane after pH 12.5 desorption (blue).

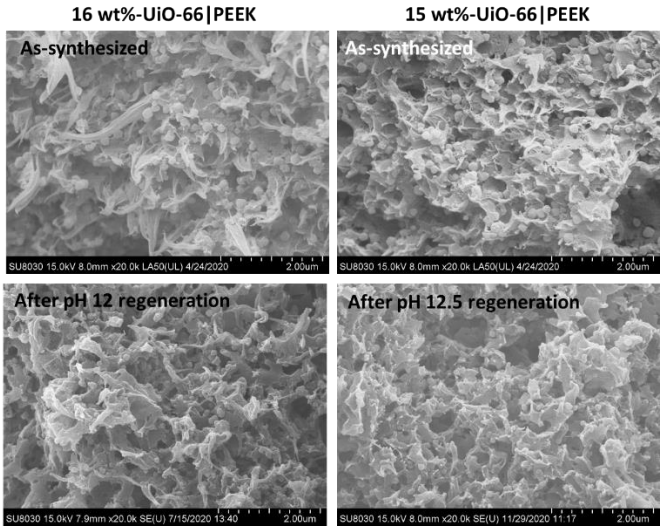

Figure 4.17 SEM images of cross section of 16wt%-UiO-66|PEEK (left panels) and 15wt%-UiO-66|PEEK (right panels) as-synthesized (top) and after regeneration under pH 12 or 12.5 (bottom).

Table 4.3 Physical parameters during electro-assisted sorption experiments.

	electro-assisted adsorption			electro-assisted desorption	
	current density ($\mu A \cdot cm^{-2}$)	pH		current density[b] ($mA \cdot cm^{-2}$)	pH[a]
membrane tags	initial, final	feed (cathode) initial, final	receiver (anode) initial, final		
*28wt%-UiO-66	83, 611	6.70, 9.25	4.19, 3.40	1.75	12
10wt%-UiO-66	40, 50	7.12, 7.85	4.27, 4.07	-	-
16wt%-UiO-66	39, 53	7.12, 8.88	4.26, 3.93	0.025	10.01
	-	-	-	0.29	11.00
	-	-	-	1.63	12.05
	-	-	-	[#]4.46	[#]12.05
15wt%-UiO-66	-	-	-	4.00	12.53
34wt%-UiO-66	40, 53	7.09, 7.80	4.36, 4.07	1.67	12.06
14wt%-UiO-66	31, 46	6.81, 7.45	4.48, 4.18	-	-

For all membranes (except *)- Electro-assisted adsorption (for 300 min)- feed solution (40 mL) contained exclusively 0.26 mM P^V and the receiver solution (40 mL) contained water spiked with H_2SO_4, so that the initial pH became 4.27 ± 0.1. The electro-assisted desorption (for 150 min) was done using 100 mL KOH of respective pH strengths. Membrane active surface area – 4.16 cm^2. The applied potential at Pt electrodes – 5 V
*electro-assisted adsorption- feed solution was 40 mL groundwater, receiver – 40 mL water spiked with H_2SO_4 (initial pH 4.19), membrane active area – 4.16 cm^2. The electro-assisted desorption at 5 V was done using 100 mL KOH of pH 12.05. [a]the variation in pH was within ± 0.05 unit. [b]the variation in current density was within ±3 % of the respective average values quoted here.

The experimental parameters for electro-assisted sorption (current density, pH) for individual membranes are detailed in Table 4.3. As evident from the corresponding plots (Figure 4.15), increased UiO-66 loading within PEEK caused increased cell resistance and hence lower current densities during electro-assisted adsorption.

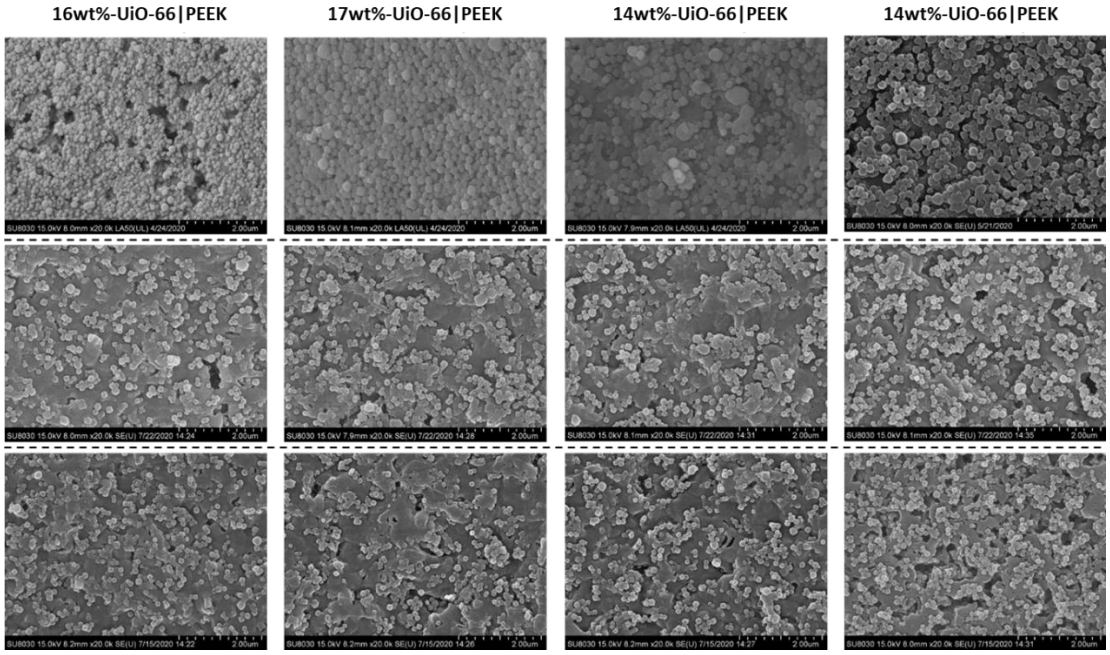

Figure 4.18 Top view SEM images of four membranes before P^V uptake (top panel), after P^V uptake for 24 h (middle panel), and after electro-assisted desorption at pH 12 (bottom panel). From left to right, the membranes are corresponding to entry 3, 6, 7, and 9 in Table 4.1.

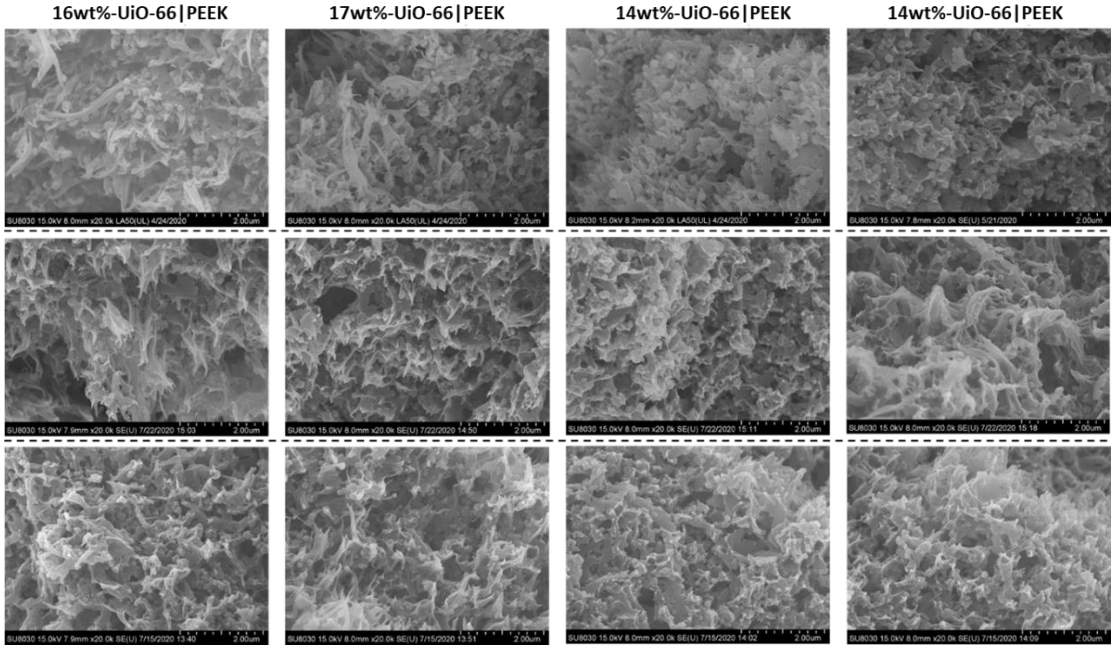

Figure 4.19 Cross-section view SEM images of four membranes samples before P^V uptake (top panel), after P^V uptake for 24 h (middle panel), and after electro-assisted desorption at pH 12 (bottom panel).

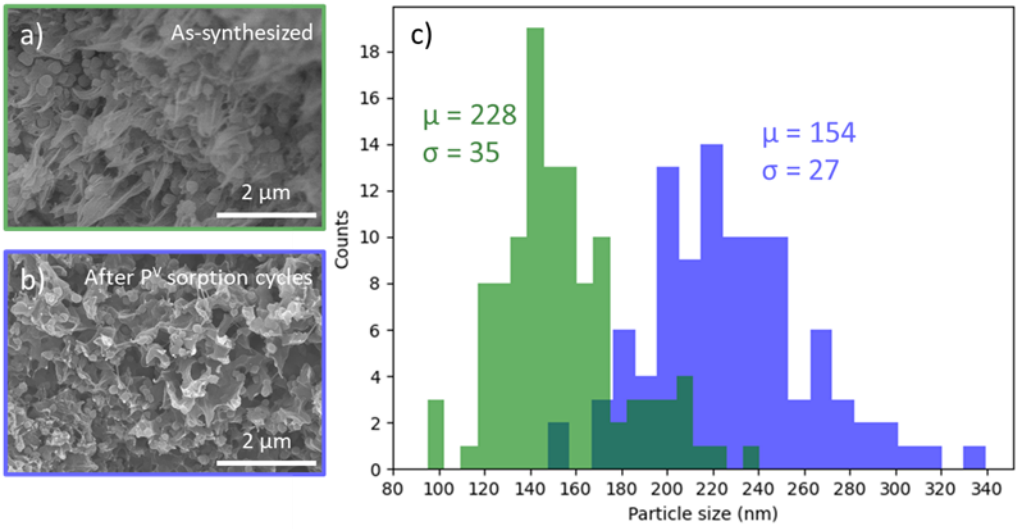

Figure 4.20 SEM images of cross sections of 34wt%-UiO-66|PEEK membrane samples (a) before P^V uptake and (b) after three consecutive cycles of electro-assisted adsorption and desorption. (c) The size distributions of UiO-66 particles observed inside the membrane in the cross section, before (green) and after (blue) three cycles of electro-assisted P^V adsorption and desorption.

4.9.6 Sorption of P^V and As^V from mixed anionic solution/simulated groundwater

To study the influence of competing anions under static conditions (no electric field applied), we studied the adsorption kinetics of P^V and also its selectivity over other anions in UiO-66|PEEK from two different solutions - (a) solution containing 0.01 mM P^V + 2.4 mM Cl^-, and (b) solution containing 0.01 mM P^V + 2.4 mM Cl^- + NO_3^- (0.2 mM) and SO_4^{2-} (0.1 mM). For case "a", 1 cm^2 26wt%-UiO-66|PEEK membrane piece was stirred in 10 mL solution for 4 h. For case "b", 9.1 cm^2 35wt%-UiO-66|PEEK membrane piece was stirred in 85 mL solution for 4.5 h. In both the cases, intermittent solution sampling (200 µL – 1 mL) was done for the ion analyses. We also studied the selectivity of P^V and As^V over other anions (Cl^-, HCO_3^-, NO_3^-, SO_4^{2-}) in a 28wt%-UiO-66|PEEK membrane from a simulated groundwater (Table 4.4). For this a ~1 cm^2membrane piece was stirred in 30 mL simulated groundwater [210] for 24 h, under static condition. The adsorbed amount of the individual ions in the UiO-66|PEEK was calculated from their concentrations in the

initial (before adsorption) and the final (after adsorption) solutions as in *Eq.* 4.2. The adsorption selectivity of P^V over other anions ($\alpha_{Cl}^{P^V}$)were calculated using *Eq.* 4.1, and is shown in Figure 4.8 and Table 4.5.

Table 4.4 Anion concentrations in simulated groundwater used for studying adsorption selectivity of UiO-66|PEEK.

species	ion concentration in simulated groundwater* (mM)
As^V	0.13
P^V	0.06
Cl^-	9.83
NO_3^-	4.55
SO_4^{2-}	0.17
HCO_3^-	8.19

*pH 6.7

Table 4.5 Adsorption selectivity ($\alpha_{Cl}^{P^V}$) of UiO-66|PEEK membranes for P^V over other anions in simulated groundwater.

Membrane	adsorption selectivity of P^V over other anions X ($\alpha_X^{P^V}$)				
	As^V	Cl^-	NO_3^-	SO_4^{2-}	HCO_3^-
28wt%-UiO-66	1.7	2.7	2.8	2.7	4.2
10wt%-UiO-66	1.3	1.3	1.4	1.4	2.1
16wt%-UiO-66	1.6	2.8	3.2	3.1	3.2
15wt%-UiO-66	1.6	2.0	2.1	2.0	2.9
34wt%-UiO-66	1.8	2.5	2.7	2.7	4.6
17wt%-UiO-66	1.4	2.2	2.3	2.5	3.9
14wt%-UiO-66	1.4	2.3	2.5	2.5	3.7
15wt%-UiO-66	1.4	2.0	2.2	2.5	3.3
14wt%-UiO-66	1.4	2.3	2.5	2.5	3.7

In addition to these, we have studied the electro-assisted (5 V) sorption behavior of UiO-66|PEEK from two different solution composition: i) a simple mixed anionic solution (0.01 mM P^V + 2.4 mM Cl^-) containing only two anionic components and ii) a simulated groundwater (Table 4.4) containing P^V, As^V, Cl^-, HCO_3^-, NO_3^-, and SO_4^{2-}.

Here, for the simple mixed anionic solution, a 26wt%-UiO-66|PEEK membrane (4.16 cm^2) was subjected to electro-assisted (5 V) adsorption experiments using a tailor made cell (Figure 4.14a) for three adsorption cycles. Each adsorption cycle consisted of exposure to fresh 40 mL of feed solution for 50 minutes. During adsorption, the receiver solution contained 40 mL water spiked with H_2SO_4, so that the initial pH became 4.2 ± 0.1. Intermittent solution sampling (200 µL – 1 mL) from feed and receiver compartment was done for the ion analyses. The adsorbed amount was calculated using *Eq*. 4.3.

The electro-assisted adsorption from simulated groundwater was done with a 28wt%-UiO-66|PEEK membrane using the same experimental setup (Figure 4.14). Here, we followed the procedure in Section 4.9.5 but replaced the P^V solution in the feed compartment with simulated groundwater. Due to the presence of many electrolytes, the current was significantly higher (initial – 0.3 mA, after 100 min – 2.5 mA) than observed for the P^V-only solution. This caused faster pH changes (Table 4.3) in both the compartments. Hence, to avoid interference from OH^- ions, the adsorption was continued for only 100 min. At this point, the pH of the feed and the receiver compartment were 9.25 and 3.40 respectively. For the electro-assisted (5 V) desorption, the As^V- and P^V-loaded UiO-66|PEEK membrane was exposed to KOH (100 mL, pH 12) for 100 min.

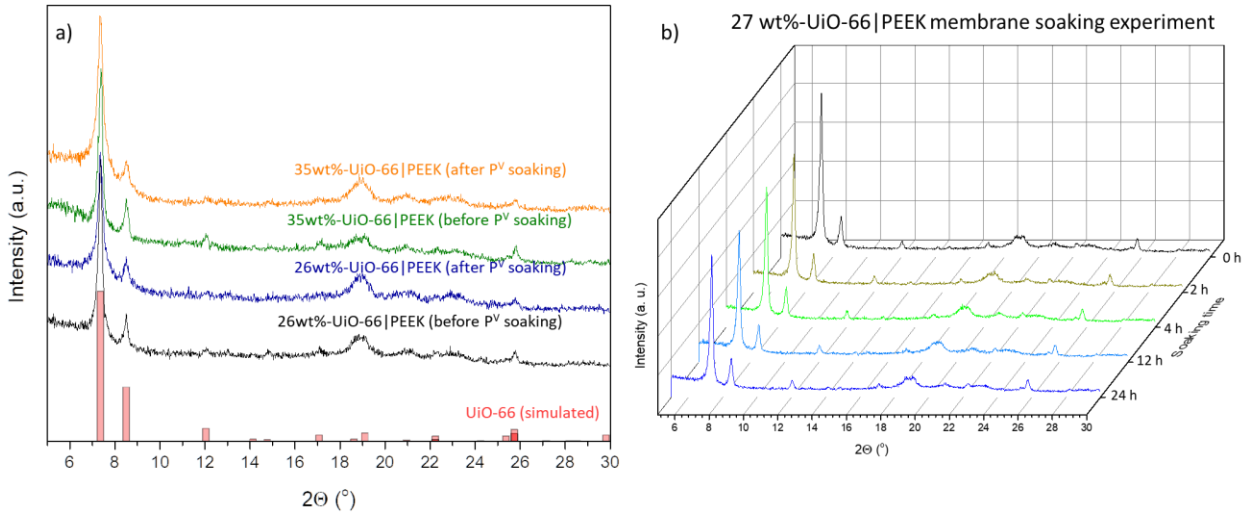

Figure 4.21 a) PXRD profiles of 26wt%- and 35wt%-UiO-66|PEEK membranes before and after soaking in P^V-containing mixed anionic solutions (Section 4.5). The 26wt%-UiO-66|PEEK membrane was soaked in a solution of P^V (0.01 mM) and Cl^- (2.4 mM), while the 35wt%-UiO-66|PEEK membrane was soaked in a solution of P^V (0.01 mM), Cl^- (2.4 mM), NO_3^- (0.2 mM), and SO_4^{2-} (0.1 mM). b) PXRD profiles of membrane strips cut from a 27wt%-UiO-66|PEEK that was subjected to P^V (0.01 mM) and Cl^- (2.4 mM) mixture solution over time (0, 2, 4, 12, and 24 h).

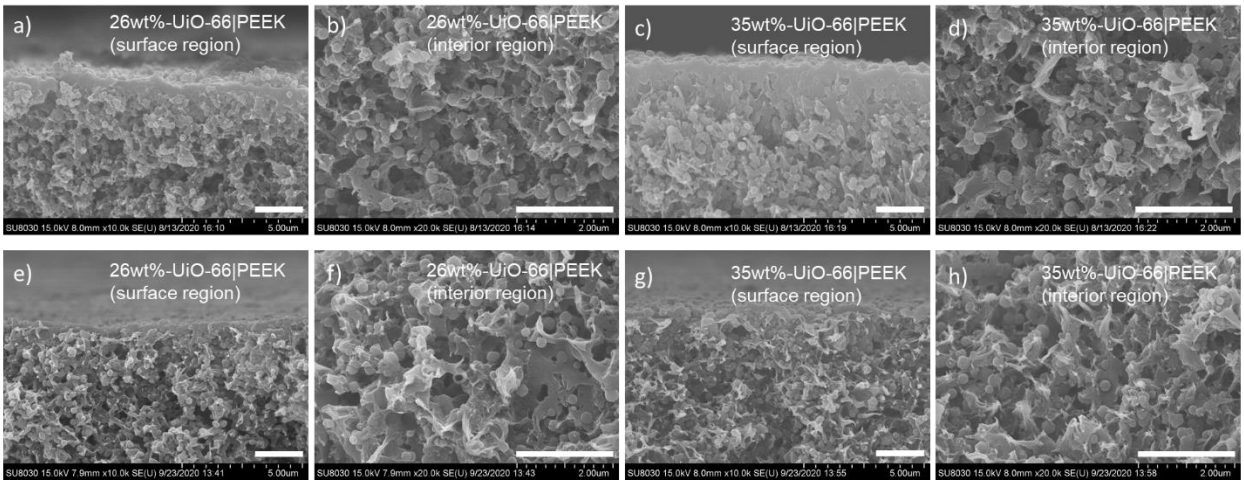

Figure 4.22 SEM images of cross sections of 26wt%- and 35wt%-UiO-66|PEEK membranes before (a-d) and after (e-h) soaking in P^V-containing mixed anionic solutions (Section 4.4). The 26wt%-UiO-66|PEEK membrane was soaked in a solution of P^V (0.01 mM) and Cl^- (2.4 mM), while the 35wt%-UiO-66|PEEK membrane was soaked in a solution of P^V (0.01 mM), Cl^- (2.4 mM), NO_3^- (0.2 mM), and SO_4^{2-} (0.1 mM). The scale bars in the images are 2 μm.

4.9.7 Zeta potential of UiO-66|PEEK membrane

The surface potentials of a 12wt%-UiO-66|PEEK membrane and an unmodified PEEK membrane were probed by measuring the zeta potentials of the membranes within the pH range 3.8 to 12.0 (the pH range of all solutions involved in this work) using KCl (1 mM) electrolyte solution at 23 °C. Both membranes were subjected to pre-wetting treatment before the measurement. As shown in Figure 4.23, the unmodified PEEK had a negative surface charge throughout the scanned pH range. At pH < 6.2, the surface charge of the 12wt%-UiO-66|PEEK membrane was slightly more positive than the unmodified PEEK, while at pH > 6.2, the surface charge of the 12wt%-UiO-66|PEEK membrane was more negative than the unmodified PEEK.

The pH-dependent difference in zeta potentials is consistent with previously reported pH-dependent zeta potentials for UiO-66; the isoelectric point of UiO-66 was reported to be ~6.2.[172].

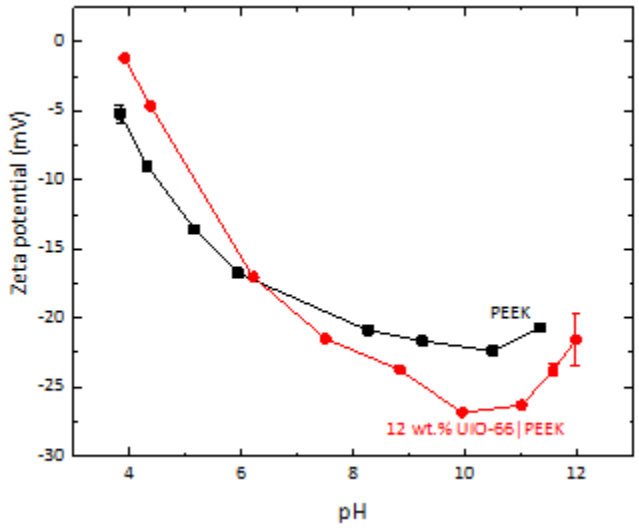

Figure 4.23 The zeta potential of a 12wt%-UiO-66|PEEK membrane and an unmodified PEEK membrane in 1 mM KCl as a function of solution pH. The errors on zeta potential data are directly obtained from the analyzing instrument.

4.9.8 UiO-66 powder and membrane soaking experiments

UiO-66 powder materials collected from supernatant during the UiO-66|PEEK syntheses. As mentioned in Section 4.9.2, during the synthesis of the UiO-66|PEEK membranes, UiO-66 nanoparticles (~200 nm) were concurrently grown in the supernatant. In four syntheses, these unsupported UiO-66 materials were collected by centrifugation, redispersed in MeOH (~25 mL), then subjected to centrifugation. This [redispersion + centrifugation + decantation] process with MeOH was repeated two more times. The pellet obtained from the last centrifugation was air-dried and oven-dried (~60 ºC), resulting in white powder (~25 mg for each batch). These materials were crystalline UiO-66 (PXRD, Figure 4.24a) nanoparticles, about 175 nm in diameter (SEM, Figure 4.24b). A proportion from batch 3 (~5 mg) was collected for composition analysis and hot MeOH soaking experiment (see section 4.9.2). After that, the rest of the batch 3 were combined

with the other three batches, giving a white powder sample (total mass: ~100 mg), as the raw materials for P^V soaking experiments in the next paragraph.

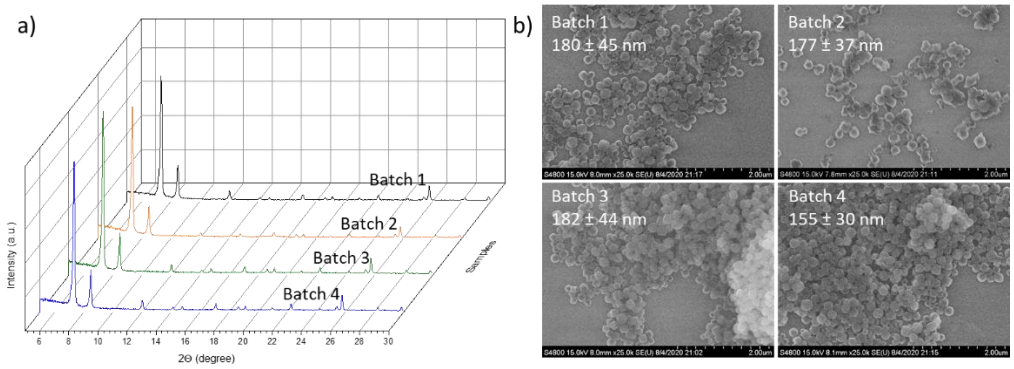

Figure 4.24 (a) PXRD profiles and (b) SEM images of UiO-66 powder materials obtained from the supernatant of four UiO-66|PEEK membrane syntheses.

Table 4.6 The chemical formula of a UiO-66 supernatant powder (batch 3 in Figure 4.24) before and after the hot MeOH soaking (see section 4.9.2 for detailed information of the soaking experiment).

Entry	Before or after the soaking	Proposed formula[a]
1	Before	$Zr_6O_4(OH)_4(BDC)_{4.3}(BzO)_{1.9}(CH_3COO)_{0.3}(H_2O)_{1.2}(OH)_{1.2}$
2	After	$Zr_6O_4(OH)_4(BDC)_{4.6}(BzO)_{1.7}(CH_3COO)_{0.2}(H_2O)_{0.9}(OH)_{0.9}$

[a]The formula of UiO-66 MOFs are determined from ^{1}H NMR spectra and ICP-OES data of digested materials following the same protocol in a reported work,[220] where the open sites were proposed to be terminated by μ_1-OH and μ_1-OH_2.

P^V-soaking experiments with the supernatant UiO-66 powder. A portion of the UiO-66 powder (20 mg) collected from UiO-66|PEEK synthesis (preparation described above) was dispersed in an aliquot (1.0 mL) of P^V solution (0.16 mM) in a 2 dram vial. Then the suspension (1.0 mL) was transferred into a 1 mL dialysis membrane holder (Spectra/Por float-a-lyzer g2, 1000 KD, Spectrum Chemical, New Brunswick, NJ), which was then placed into a 2 L beaker containing a large volume of the P^V solution (0.16 mM, 2 L, P^V/Zr_6 node ~27). The powder was soaked for 24 h at room temperature, while stirring (~300 rpm). The suspension in the dialysis membrane holder was transferred into a 50 mL centrifuge tube, collected by centrifugation and redispersed in

DI water (~10 mL) by sonication (~5 min). This centrifugation-redispersion washing cycle was repeated twice more. The resulting pellet was air-dried and oven-dried (60 °C).

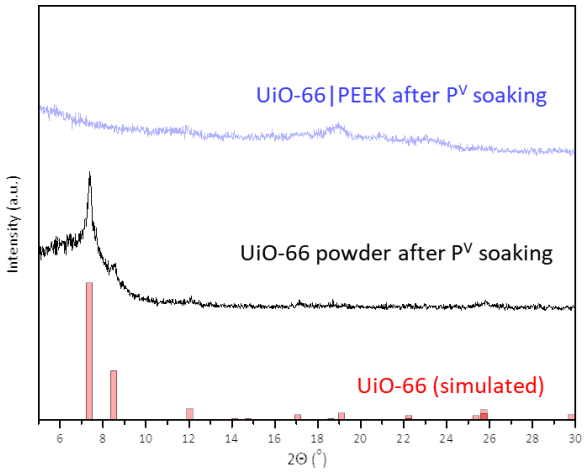

Figure 4.25 PXRD profiles of simulated UiO-66, UiO-66 powder after soaking in P^V solution, and 16wt%-UiO-66|PEEK membrane sample after soaking in P^V (see Section 4.9.4 for experimental details). In both soaking experiments, the P^V dosage was similar (0.16 mM, P^V/Zr_6 node ratio ~25, and soaking time 24 h). The loss in crystallinity after P^V soaking was greater for UiO-66|PEEK. As the loss in crystallinity is due to reactions between Zr component of UiO-66 and P^V species in the solution, the UiO-66 in powder form was less accessible to P^V species than UiO-66 supported on/inside the PEEK membrane.

P^V solution soaking experiment #1 with as-synthesized UiO-66 powder (Synthesis of ZrP-1). The P^V-soaking protocol was adapted from a previous report.[211] UiO-66 powder (50 mg, see the last paragraph in Section 4.9.2 for synthetic protocols) was weighed into a 50 mL centrifuge tube. DI water (5 mL) was added into the tube, which was capped and subjected to sonication (10 min). Na_3PO_4 solution (210 mM, 5 mL) was then added to the tube, which was again capped and subjected to sonication (10 min). The tube was then agitated (300 rpm, room temperature) on a plate shaker for 24 h. The solid products were isolated by centrifugation. To wash the solids, DI water (~10 mL) was added, the mixture was subjected to sonication (10 min), and the solid products were isolated by centrifugation. This washing process was repeated twice. The washed

solid was air-dried and oven-dried (~60 ºC), resulting in some white powder (~37 mg). The solid material here is noted as ZrP-1.

P^V solution soaking experiment #2 with as-synthesized UiO-66 powder. UiO-66 powder (15 mg, see the last paragraph in Section 4.9.2 for synthetic protocols) was dispersed in an aliquot (1.0 mL) of Na_2HPO_4/NaH_2PO_4 solution (0.16 mM P^V) in a 2-dram vial. Then the suspension (1.0 mL) was transferred into a 1 mL dialysis membrane holder (Spectra/Por float-a-lyzer g2, 1000 KD, Spectrum Chemical, New Brunswick, NJ), which was then placed into a 2 L beaker containing the P^V solution (0.16 mM, 1.5 L). The powder was soaked for 24 h at room temperature, while stirring (~300 rpm). The suspension in the dialysis membrane holder was transferred into a 50 mL centrifuge tube, then the solids were collected by centrifugation and redispersed in DI water (~10 mL) by sonication (~5 min). This centrifugation-redispersion washing cycle was repeated twice more. The resulting pellet was air-dried and oven-dried (60 ºC), resulting in some white powder (~10 mg). The solid material here is noted as UiO-66-leftover (see Figure 4.26 for explanation of this nomenclature).

P^V solution soaking experiment #3 with as-synthesized UiO-66 powder (Synthesis of ZrP-2). UiO-66 powder (50 mg, see the last paragraph in Section 4.9.2 for synthetic protocols) was weighed into a 50 mL centrifuge tube. Na_2HPO_4/NaH_2PO_4 solution (80 mM P^V, 10 mL) was then added to the tube, which was capped and subjected to sonication (10 min). The tube was then agitated (300 rpm) on a plate shaker for 24 h. The solid products were isolated by centrifugation. To wash the solids, DI water (~10 mL) was added, the mixture was subjected to sonication (10 min), and the solid products were isolated by centrifugation. This washing process was repeated twice. The washed solid was air-dried and oven-dried (~60 ºC), resulting in some white powder (~42 mg). The solid material here is noted as ZrP-2.

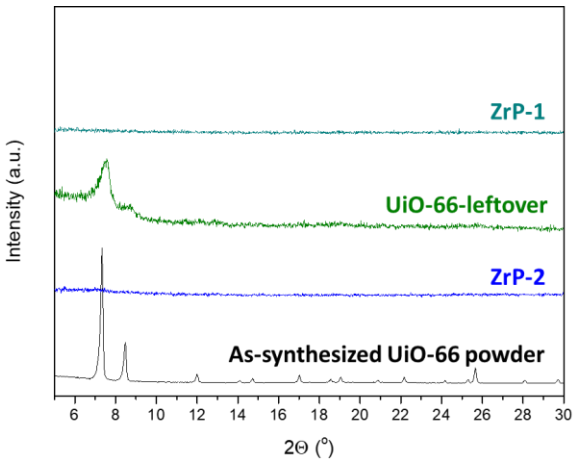

Figure 4.26 PXRD profiles of UiO-66 powder material before soaking and after soaking: ZrP-1 (solid from soaking experiment #1), UiO-66-leftover (solid from soaking experiment #2), and ZrP-2 (solid from soaking experiment #3). For soaking experiments #1 and #3, there was no obvious diffraction peak in the PXRD profile, indicating that the products ZrP-1 and ZrP-2 were amorphous. For the solid obtained from soaking experiment #2, UiO-66 diffraction signals with peak broadening were observed, indicating a decrease in crystalline domain size, indicating partial corrosion of the UiO-66 crystals, and thus the solid was labeled as UiO-66-leftover.

Table 4.7 Zr and P compositions in as-synthesized UiO-66 powder, ZrP-1, and ZrP-2 samples.

Entry	Material	Zr wt %[a]	Zr μmol in 1 mg sample	P wt%[a]	P μmol in 1 mg sample	P/Zr molar ratio
1	ZrP-1	56.9	6.24	9.08	2.93	0.47
2	ZrP-2	61.8	6.78	28.2	9.10	1.34

[a]The weight percentage data was acquired by ICP-OES using procedures described in Section 4.9.3.

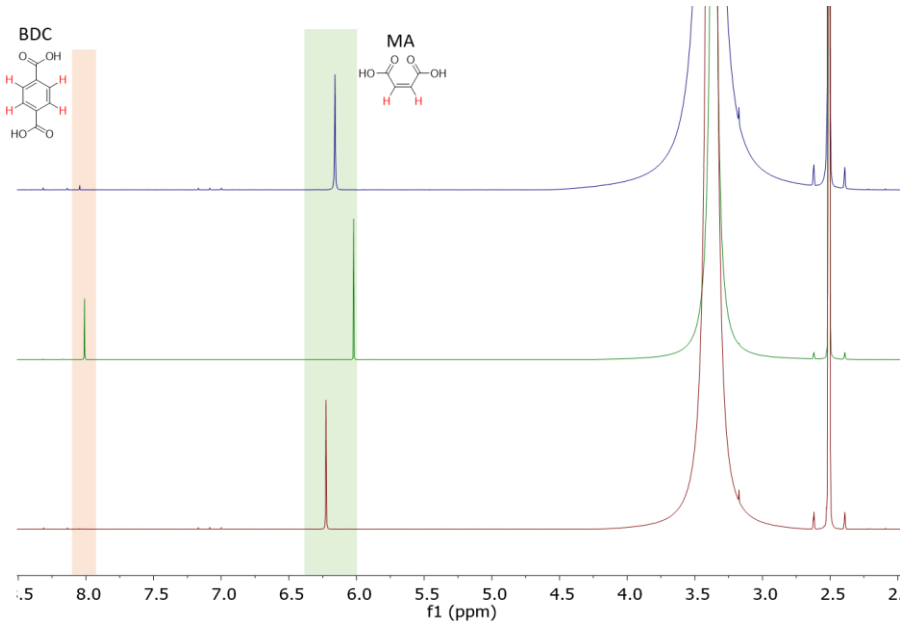

Figure 4.27 The ^{1}H NMR spectra of digested ZrP-1 (blue), UiO-66-leftover (green), and ZrP-2 (red). The products ZrP-1 and ZrP-2 retain almost none of the BDC linkers from the UiO-66 precursor. The presence of some leftover BDC linker in UiO-66-leftover is consistent with the remaining UiO-66 diffraction peaks in Figure 4.26. The shift of the MA signal (6.0-6.5 ppm) is due to the addition of Cs_2CO_3 during the digestion of ZrP solids (see Section 4.9.3 for the digestion protocols).

Soaking UiO-66 and ZrP powder in HCO_3^- solution. A portion (10 mg) of three solid samples (as-synthesized UiO-66 powder, ZrP-1, and ZrP-2) was weighed into a 50 mL centrifuge tube. $NaHCO_3$ solution (1 M) and DI water were added to the tube (see Table 4.7 for the volumes), which was capped and agitated on a thermomixer (room temperature, 300 rpm) for 24 h. After the agitation, the leftover solid was isolated by centrifugation. Half of the supernatant (25 mL) was transferred into a clean 50 mL centrifuge tube for Zr and P quantification by ICP-OES (according to procedures in Section 4.9.3). To wash the leftover solid, DI water (~10 mL) was added, the mixture was subjected to sonication (10 min), and the solids were isolated by centrifugation. This washing process was repeated twice. The washed solid was air-dried and oven-dried (~60 °C) in the tube. The dried solid was weighed (Table 4.7) by an ultra-microbalance (see Section 4.9.1 for model information). The leftover solid samples are labeled as UiO-66|HCO_3^-, ZrP-1|HCO_3^-, and

ZrP-2|HCO_3^-, where "|HCO_3^-" represents the HCO_3^- soaking process) and their compositions determined by ICP-OES are listed in Table 4.8.

Table 4.8 Solution components in the powder soaking experiments in HCO_3^- solution.

Entry	Material	Zr mmol in 10 mg	Volume of 1 M HCO_3^- solution (mL)	Volume of water (mL)	Mass after soaking (mg)
1	As-synthesized UiO-66 powder	0.036	8.27	41.73	1.301
2	ZrP-1	0.063	14.22	35.78	9.651
3	ZrP-2	0.068	15.45	34.55	9.801

Table 4.9 Zr and P compositions in leftover solid after HCO_3^--solution soaking resulted from as-synthesized UiO-66 powder, ZrP-1, and ZrP-2 samples.

Entry	Material	Zr wt %[a]	Zr μmol in 1 mg sample	P wt %[a]	P μmol in 1 mg sample	P/Zr molar ratio
1	UiO-66|HCO_3^-	45.4[d]	4.98	NA[b]	NA[b]	NA[b]
2	ZrP-1|HCO_3^-	54.3	5.95	8.9	2.87	[c]0.48
3	ZrP-2|HCO_3^-	60.2	6.60	27	8.71	[c]1.31

[a]The weight percentage data was acquired by ICP-AES using procedures described in Section 4.9.3. [b]The P signal was close to zero, which was expected as there should not be P in as-synthesized UiO-66. [c]The P/Zr ratios for ZrP-1 and ZrP-2 did not change much after soaking in HCO_3^- solution (see Table 4.6), indicating that there was no change in chemical composition during HCO_3^- soaking. [d]The Zr weight percentage in UiO-66 increased from 33.1 to 45.4 wt %, after the HCO_3^- soaking experiment, indicating the loss of organic species (BDC linkers and BzOH ligands) caused by etching in the presence of HCO_3^- (see Figure 4.28).

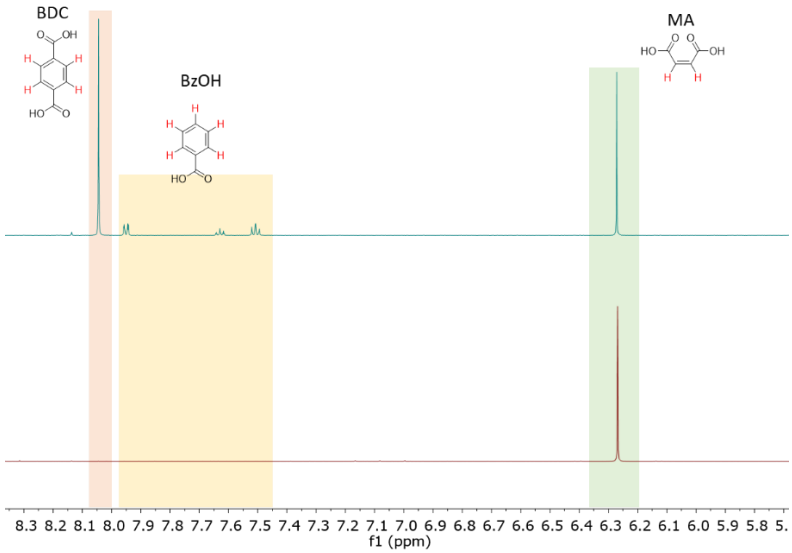

Figure 4.28 The ^{1}H NMR spectra of digested as-synthesized UiO-66 sample (blue) and UiO-66|HCO_3^- sample (red). After the HCO_3^- soaking experiment, BzOH and BDC signals were not observed for UiO-66|HCO_3^-, indicating that these organic species were removed during soaking in the HCO_3^- solution.

Chapter 5

Epilogue

5.1 General conclusions from this thesis work

This thesis demonstrated the use of polymer-assisted strategies in the design and synthesis of hierarchically porous UiO-66 MOF materials with large meso- or macropores, giving rise to materials with enhanced performances in catalysis and environmental applications. To introduce mesopores into the microporous UiO-66, the studies in chapter 2 established a synthetic strategy for using Pluronic block-co-polymers as templates for mesopores, where hierarchically mesoporous (HM) UiO-66-X shell materials (X = F_4, $(OH)_2$, and $(COOH)_2$) could be iteratively grown on top of microporous UiO-66 seeds. Due to additional (meso)pore volume and fast mass transport brought by the hierarchical porosity, a thrice-grown UiO-66@HM|$_{3rd}$-UiO-66-F_4 material exhibited great enhancements (>300%) in both uptake capacity for a dye removal application and reaction rate for a catalytic sulfide oxidation. During the synthesis of this material, we also noticed a new solid phase with porosity and crystalline structure that are completely distinct from that of UiO-66 when the UiO-66 seeds were absent in the reaction media, which implied that the strong affinity of the polymer templates to the UiO-66 components could change the outcome of the MOF synthesis.

The discovery of this intriguing new solid phase prompted us to further study its structure and explore its formation mechanism. As shown in chapter 3, we found through diffraction experiments (X-ray and electron) that this material had a 2D-UiO-66 structure composed of 4-linker-coordinate Zr_6 clusters rather than the 12-linker-coordinate ones in regular UiO-66 materials. Such a decrease in coordination number around the metal nodes was proposed to result from steric hindrance brought by the "coordination" of the Pluronic polymers around the Zr_6 clusters during the synthesis. Consistent with this coordination-hindrance hypothesis, adding an excess amount of the coordination-competing modulator acetic acid to a reaction mixture for UiO-

66 synthesis also induced the formation of this 2D-UiO-66 structure. Guided by these observations, a 2D-UiO-66-on-PEEK membrane material was successfully synthesized by intentionally creating a linker-deficiency condition at the PEEK membrane surface, demonstrating the feasibility for incorporating this new phase onto macroscopic substrate as composite materials.

We next investigated the combination of microporous UiO-66 with macroporous membranes to give [macropore + micropore] composite that can be used in groundwater treatment. In chapter 4, such membranes were fabricated by *in-situ* growing UiO-66 particles inside macropores of commercially available PEEK membranes. The resulted UiO-66|PEEK membranes had UiO-66 particles uniformly distributed inside their porous matrices. With UiO-66 particles being highly selective for phosphate adsorption, the UiO-66|PEEK membranes were shown to be highly efficient for phosphate removal from groundwater. We also placed the membrane inside an electric field and applied an electro-assisted strategy to accelerate ion transport across it and improve the removal kinetics. The chemical stabilities of the UiO-66 particles inside the membrane under different phosphate-dosage exposure were also investigated. While the studies in this thesis focused on strategies for incorporating hierarchical porosity into UiO-66-based materials, the synthetic routes and concepts established here could be combined to design materials with hierarchically connected pores in all three dimensions and be further extended to other Zr-based MOF materials as discussed below.

5.2 Design UiO-66 membrane materials containing micro-, meso-, and macropores for practical utilities

In this thesis, we separately employed polymer templates to incorporate mesopores into UiO-66 (chapter 2 and 3) or combined macroporous membranes with UiO-66 to give composite membrane materials. Considering that mesopores could facilitate molecular transport through the

UiO-66 particles and that the macropores are beneficial for fast liquid flow across the macroscopic bulk, we envision a combination of the two methods to fabricate membrane materials with all three pore dimensions ([micropore + mesopore + macropore], Figure 5.1). This material can be achieved based on the UiO-66|PEEK material established in chapter 4. The initially grown UiO-66 particles in the PEEK membranes could act as seeds for the subsequent growth of HM-UiO-66 materials with the addition of Pluronic templates. Such HM-UiO-66-incorporated based PEEK membrane materials could greatly enhance the kinetic performances of UiO-66 nanoparticles when applied to liquid-phase adsorption or catalysis, and also allow for easy recyclings and implementations of membrane-based devices/techniques.

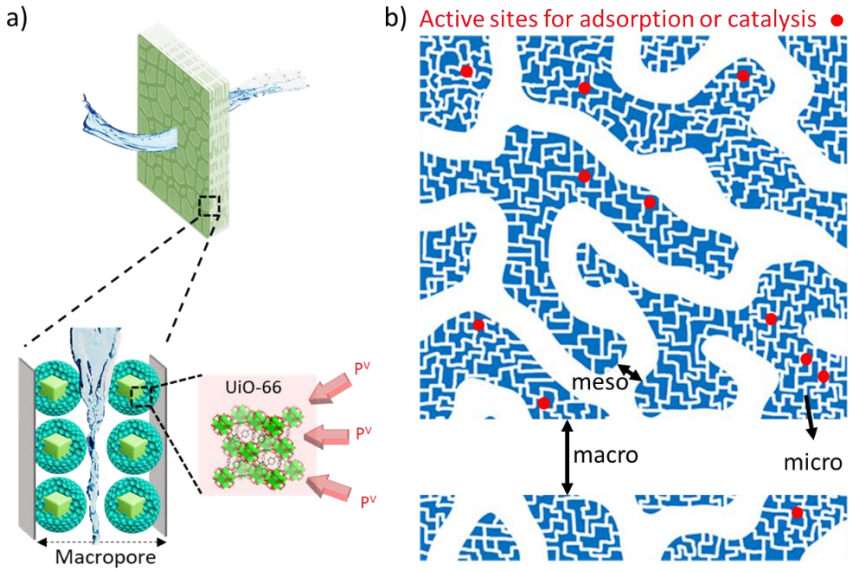

Figure 5.1 a) A proposed HM-UiO-66-corporated PEEK polymer membrane material. b) A hierarchically porous structure having micro-, meso-, and macropores.

5.3 Extend the synthetic strategies to other Zr-based MOF materials

While UiO-66 was used as a model microporous MOF material in this thesis to demonstrate both synthetic strategies (Pluronic-based, template-assisted synthesis and the *in-situ* growth method with PEEK membranes), they can also be applied to other Zr-based MOF materials. For

the Pluronic-templated synthesis, several other Zr-based MOFs share the same Zr(oxo) cluster (Figure 5.2). This should enable similar affinities to Pluronic polymers as that in UiO-66 and thus maintain the templating effects brought by the Pluronic micelles. However, considering that organic solvents (mostly DMF or DEF) are normally used for the syntheses of other Zr-based MOFs, due to low solubilities of the organic linkers, the Pluronic concentration should be elevated correspondingly to meet a higher critical micelle concentration in organic solvents than that in aqueous media. With insufficient Pluronic templates, templating may not occur and morphology change rather than mesopore formation might be observed.[88] Furthermore, depending on the affinity between Pluronic polymers with the Zr-based MOF building blocks, the polymers might induce side-product formation, as the 2D-UiO-66 structure discussed in chapter 3. Under this scenario, seeding with pre-synthesized nanoparticles could help to maintain the purity of the crystalline phase in the product, as demonstrated in the HM-UiO-66 synthesis (chapter 2).

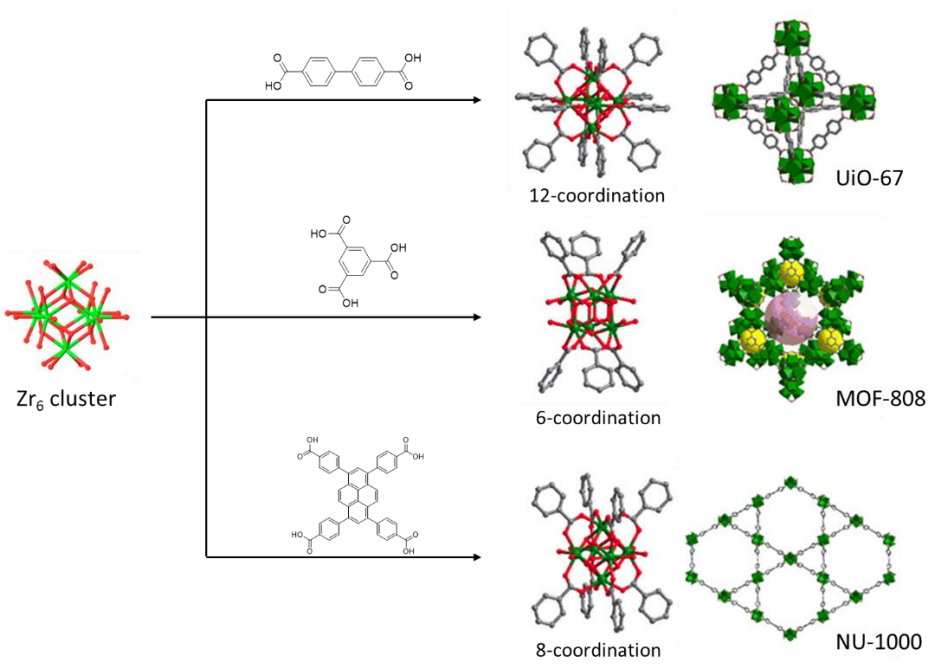

Figure 5.2 Three potential Zr-based MOFs that can be used in the template-assisted strategy or grown into PEEK porous membrane to form hierarchically porous materials.

In addition to UiO-66, the other Zr-based MOFs can also be incorporated into macroporous membranes by using the same Zr_6-cluster seeding pretreatment as that demonstrated in chapter 4 for UiO-66|PEEK synthesis. As many Zr-based MOFs have Zr_6 clusters with lower linker-coordination numbers and thus more coordination open sites (as that in MOF-808 and NU-1000 shown in Figure 5.2), this should lead to higher performances (capacities) in sorption-based applications, such as water purification. However, a careful tuning of the synthetic condition is needed to obtain particles of appropriate sizes that can fit into the porous matrix of the membrane. For example, in our initial attempt to grow MOF-808 into the porous PEEK membrane (see Appendix A), MOF-808 particles scarcely grew inside the resulted membrane due to the large crystal (micrometer scale) formed under the synthetic condition.[221] To solve this problem, synthetic parameters (such as growth temperature, metal precursor and/or linker concentration, and the amount of modulator) could be tuned to achieve MOF-in-PEEK with an uniform particle distribution across the membrane material.[172]

5.4 Last remarks

Beyond Zr-based MOFs, there are a massive number of MOF materials with very different metal nodes and organic linkers. As most of these are microporous materials and currently unexplored as hierarchically porous materials, we hope our works would stimulate interest in designing MOF-based materials with a hierarchy of connected small, medium, and large pores and exploring their utilities in catalysis, adsorption, and other applications. We are confident that more examples of designing hierarchically porous MOF materials will emerge to address challenges in both academia and industry, and we envision that the synthetic strategies demonstrated in this thesis can serve as model references for these future endeavors.

Appendix A

Attempt of growing MOF-808 into PEEK membrane

An initial attempt has been made to grow MOF-808 into porous PEEK membrane. The MOF-808 precursor recipe was taken from a reported solvothermal method used for synthesizing MOF-808 particles in DMF solution.[222] The PEEK membrane pre-treatment, composite synthesis, and product work-up were the same as those for the UiO-66|PEEK membrane (see Section 4.9.2); but the solutions used for the synthesis were different. The BDC solution was replaced with a 1,3,5-benzenetricarboxylic solution (10 mL, 11 mM, DMF/formic acid = 1:1 v/v), while the $ZrCl_4$ solution was substituted by $ZrOCl_2 \cdot 8H_2O$ solution (10 mL, 33 mM, DMF/formic acid = 1:1 v/v). After the synthesis, washing, and drying, a PEEK membrane with ~10% weight gain was obtained.

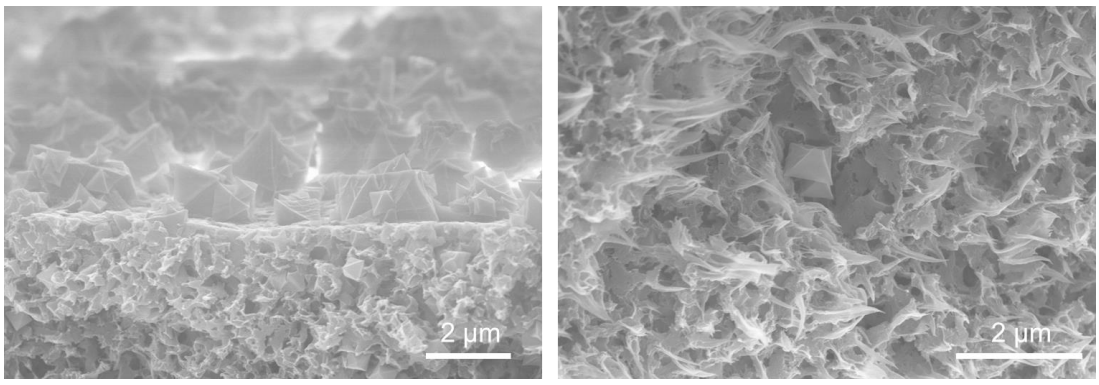

Figure A.1 Cross-section SEM images of the PEEK membrane product resulted from the synthesis described above. MOF-808 particles with an octahedral morphology were observed on the PEEK membrane surface (left panel), while there were few particles seen inside the PEEK membrane. This could be resulted from the large particle size of MOF-808 (~1 μm) resulted from the employed condition, which was reported to be much larger than the PEEK pore size (~100 – 500 nm). To grow MOF-808 uniformly inside the PEEK membrane, the growth condition will need to be carefully tuned. For example, the modulator/linker ratio could be decreased or the growth temperature could be elavated (<1 h) to accelerate the nucleation rate, which should afford MOF-808 particles with smaller sizes.

References and notes

1. Zhou, H. C.; Long, J. R.; Yaghi, O. M., Introduction to metal-organic frameworks. *Chem. Rev.* **2012,** *112*, 673-674.
2. Moosavi, S. M.; Nandy, A.; Jablonka, K. M.; Ongari, D.; Janet, J. P.; Boyd, P. G.; Lee, Y.; Smit, B.; Kulik, H. J., Understanding the diversity of the metal-organic framework ecosystem. *Nat. Commun.* **2020,** *11*, 4068-4078.
3. Kirchon, A.; Feng, L.; Drake, H. F.; Joseph, E. A.; Zhou, H. C., From fundamentals to applications: a toolbox for robust and multifunctional MOF materials. *Chem. Soc. Rev.* **2018,** *47*, 8611-8638.
4. Li, J. R.; Kuppler, R. J.; Zhou, H. C., Selective gas adsorption and separation in metal-organic frameworks. *Chem. Soc. Rev.* **2009,** *38*, 1477-504.
5. Li, J. R.; Sculley, J.; Zhou, H. C., Metal-organic frameworks for separations. *Chem. Rev.* **2012,** *112*, 869-932.
6. Lee, J.; Farha, O. K.; Roberts, J.; Scheidt, K. A.; Nguyen, S. T.; Hupp, J. T., Metal-organic framework materials as catalysts. *Chem. Soc. Rev.* **2009,** *38*, 1450-1459.
7. Rogge, S. M. J.; Bavykina, A.; Hajek, J.; Garcia, H.; Olivos-Suarez, A. I.; Sepúlveda-Escribano, A.; Vimont, A.; Clet, G.; Bazin, P.; Kapteijn, F.; Daturi, M.; Ramos-Fernandez, E. V.; Llabrés i Xamena, F. X.; Van Speybroeck, V.; Gascon, J., Metal–organic and covalent organic frameworks as single-site catalysts. *Chem. Soc. Rev.* **2017,** *46*, 3134-3184.
8. Stassen, I.; Burtch, N.; Talin, A.; Falcaro, P.; Allendorf, M.; Ameloot, R., An updated roadmap for the integration of metal–organic frameworks with electronic devices and chemical sensors. *Chem. Soc. Rev.* **2017,** *46*, 3185-3241.
9. Rouquerol, J.; Avnir, D.; Fairbridge, C. W.; Everett, D. H.; Haynes, J. H.; Pernicone, N.; Ramsay, J. D. F.; Sing, K. S. W.; Unger, K. K., Recommendations for the characterization of porous solids. *Pure Appl. Chem.* **1994,** *66*, 1739-1758.
10. Xuan, W.; Zhu, C.; Liu, Y.; Cui, Y., Mesoporous metal-organic framework materials. *Chem. Soc. Rev.* **2012,** *41*, 1677-1695.
11. Yang, X. Y.; Chen, L. H.; Li, Y.; Rooke, J. C.; Sanchez, C.; Su, B. L., Hierarchically porous materials: synthesis strategies and structure design. *Chem. Soc. Rev.* **2017,** *46*, 481-558.
12. Cychosz, K. A.; Guillet-Nicolas, R.; Garcia-Martinez, J.; Thommes, M., Recent advances in the textural characterization of hierarchically structured nanoporous materials. *Chem. Soc. Rev.* **2017,** *46*, 389-414.
13. Sun, M. H.; Chen, C.; Chen, L. H.; Su, B. L., Hierarchically porous materials: Synthesis strategies and emerging applications. *Front. Chem. Sci. Eng.* **2016,** *10*, 301-347.
14. Bai, Y.; Dou, Y.; Xie, L.-H.; Rutledge, W.; Li, J.-R.; Zhou, H.-C., Zr-based metal–organic frameworks: design, synthesis, structure, and applications. *Chem. Soc. Rev.* **2016,** *45*, 2327-2367.
15. Cavka, J. H.; Jakobsen, S.; Olsbye, U.; Guillou, N.; Lamberti, C.; Bordiga, S.; Lillerud, K. P., A new zirconium inorganic building brick forming metal organic frameworks with exceptional stability. *J. Am. Chem. Soc.* **2008,** *130*, 13850-13851.
16. Taddei, M., When defects turn into virtues: The curious case of zirconium-based metal-organic frameworks. *Coord. Chem. Rev.* **2017,** *343*, 1-24.

17. Li, X.; Zhang, H.; Wang, P.; Hou, J.; Lu, J.; Easton, C. D.; Zhang, X.; Hill, M. R.; Thornton, A. W.; Liu, J. Z.; Freeman, B. D.; Hill, A. J.; Jiang, L.; Wang, H., Fast and selective fluoride ion conduction in sub-1-nanometer metal-organic framework channels. *Nat. Commun.* **2019,** *10*, 2490/1-12.
18. Audu, C. O.; Nguyen, H. G. T.; Chang, C. Y.; Katz, M. J.; Mao, L.; Farha, O. K.; Hupp, J. T.; Nguyen, S. T., The dual capture of As(V) and As(III) by UiO-66 and analogues. *Chem. Sci.* **2016,** *7*, 6492-6498.
19. Limvorapitux, R.; Chen, H. Y.; Mendonca, M. L.; Liu, M. T.; Snurr, R. Q.; Nguyen, S. T., Elucidating the mechanism of the UiO-66-catalyzed sulfide oxidation: activity and selectivity enhancements through changes in the node coordination environment and solvent. *Catal. Sci. Technol.* **2019,** *9*, 327-335.
20. Huang, H.; Li, J. R.; Wang, K.; Han, T.; Tong, M.; Li, L.; Xie, Y.; Yang, Q.; Liu, D.; Zhong, C., An in situ self-assembly template strategy for the preparation of hierarchical-pore metal-organic frameworks. *Nat. Commun.* **2015,** *6*, 8847/1-8.
21. Li, K.; Lin, S.; Li, Y.; Zhuang, Q.; Gu, J., Aqueous-phase synthesis of mesoporous Zr-based MOFs templated by amphoteric surfactants. *Angew. Chem., Int. Ed.* **2018,** *130*, 3497-3501.
22. Fang, Z.; Bueken, B.; De Vos, D. E.; Fischer, R. A., Defect-engineered metal-organic frameworks. *Angew. Chem., Int. Ed.* **2015,** *54*, 7234-7254.
23. Thompson, B. R.; Horozov, T. S.; Stoyanov, S. D.; Paunov, V. N., Hierarchically structured composites and porous materials from soft templates: fabrication and applications. *J. Mater. Chem. A* **2019,** *7*, 8030-8049.
24. Xu, W.; Thapa, K. B.; Ju, Q.; Fang, Z.; Huang, W., Heterogeneous catalysts based on mesoporous metal–organic frameworks. *Coord. Chem. Rev.* **2018,** *373*, 199-232.
25. Eddaoudi, M.; Kim, J.; Rosi, N.; Vodak, D.; Wachter, J.; O'Keeffe, M.; Yaghi, O. M., Systematic design of pore size and functionality in isoreticular MOFs and their application in methane storage. *Science* **2002,** *295*, 469-472.
26. A mutual growth of different networks with spatial crossover between each other, forming a interlinked structure, which usually lead to obvious decreases in porosity.
27. Feng, L.; Yuan, S.; Qin, J.-S.; Wang, Y.; Kirchon, A.; Qiu, D.; Cheng, L.; Madrahimov, S. T.; Zhou, H.-C., Lattice expansion and contraction in metal-organic frameworks by sequential linker reinstallation. *Matter* **2019,** *1*, 156-167.
28. Bueken, B.; Van Velthoven, N.; Krajnc, A.; Smolders, S.; Taulelle, F.; Mellot-Draznieks, C.; Mali, G.; Bennett, T. D.; De Vos, D., Tackling the defect conundrum in UiO-66: a mixed-linker approach to engineering missing linker defects. *Chem. Mater.* **2017,** *29*, 10478-10486.
29. Feng, L.; Yuan, S.; Zhang, L. L.; Tan, K.; Li, J. L.; Kirchon, A.; Liu, L. M.; Zhang, P.; Han, Y.; Chabal, Y. J.; Zhou, H. C., Creating hierarchical pores by controlled linker thermolysis in multivariate metal-organic frameworks. *J. Am. Chem. Soc.* **2018,** *140*, 2363-2372.
30. Guillerm, V.; Xu, H.; Albalad, J.; Imaz, I.; Maspoch, D., Postsynthetic selective ligand cleavage by solid–gas phase ozonolysis fuses micropores into mesopores in metal–organic frameworks. *J. Am. Chem. Soc.* **2018,** *140*, 15022-15030.
31. Kresge, C. T.; Leonowicz, M. E.; Roth, W. J.; Vartuli, J. C.; Beck, J. S., Ordered mesoporous molecular-sieves synthesized by a liquid-crystal template mechanism. *Nature* **1992,** *359*, 710-712.
32. Qiu, L. G.; Xu, T.; Li, Z. Q.; Wang, W.; Wu, Y.; Jiang, X.; Tian, X. Y.; Zhang, L. D., Hierarchically micro- and mesoporous metal-organic frameworks with tunable porosity. *Angew. Chem., Int. Ed.* **2008,** *47*, 9487-9491.

33. Jun, B.-M.; Al-Hamadani, Y. A. J.; Son, A.; Park, C. M.; Jang, M.; Jang, A.; Kim, N. C.; Yoon, Y., Applications of metal-organic framework based membranes in water purification: A review. *Sep. Purif. Technol.* **2020,** *247*, 116947-116966.
34. Lin, K.-Y. A.; Chen, S.-Y.; Jochems, A. P., Zirconium-based metal organic frameworks: Highly selective adsorbents for removal of phosphate from water and urine. *Mater. Chem. Phys.* **2015,** *160*, 168-176.
35. Guan, T.; Li, X.; Fang, W.; Wu, D., Efficient removal of phosphate from acidified urine using UiO-66 metal-organic frameworks with varying functional groups. *Appl. Surf. Sci.* **2020,** *501*, 144074/1-12.
36. Wang, C.; Liu, X.; Chen, J. P.; Li, K., Superior removal of arsenic from water with zirconium metal-organic framework UiO-66. *Sci. Rep.* **2015,** *5*, 16613/1-10.
37. He, Y.; Tang, Y. P.; Ma, D.; Chung, T.-S., UiO-66 incorporated thin-film nanocomposite membranes for efficient selenium and arsenic removal. *J. Membr. Sci.* **2017,** *541*, 262-270.
38. Carboni, M.; Abney, C. W.; Liu, S.; Lin, W., Highly porous and stable metal–organic frameworks for uranium extraction. *Chem. Sci.* **2013,** *4*, 2396-2402.
39. Yee, K.-K.; Reimer, N.; Liu, J.; Cheng, S.-Y.; Yiu, S.-M.; Weber, J.; Stock, N.; Xu, Z., Effective mercury sorption by thiol-laced metal–organic frameworks: in strong acid and the vapor phase. *J. Am. Chem. Soc.* **2013,** *135*, 7795-7798.
40. Wang, B.; Prinsen, P.; Wang, H.; Bai, Z.; Wang, H.; Luque, R.; Xuan, J., Macroporous materials: microfluidic fabrication, functionalization and applications. *Chem. Soc. Rev.* **2017,** *46*, 855-914.
41. Du, L.; Liu, W.; Hu, S.; Wang, Y.; Yang, J., Preparation and photocatalytic properties of macroporous honeycomb alumina ceramics used for water purification. *J. Eur. Ceram. Soc.* **2014,** *34*, 731-738.
42. Liu, X.; Demir, N. K.; Wu, Z.; Li, K., Highly water-stable zirconium metal–organic framework UiO-66 membranes supported on alumina hollow fibers for desalination. *J. Am. Chem. Soc.* **2015,** *137*, 6999-7002.
43. Shangkum, G. Y.; Chammingkwan, P.; Trinh, D. X.; Taniike, T., Design of a semi-continuous selective layer based on deposition of UiO-66 nanoparticles for nanofiltration. *Membranes* **2018,** *8*, 129/1-14.
44. Wang, Y.; Li, X.; Zhao, S.; Fang, Z.; Ng, D.; Xie, C.; Wang, H.; Xie, Z., Thin-film composite membrane with interlayer decorated metal–organic framework UiO-66 toward enhanced forward osmosis performance. *Ind. Eng. Chem. Res.* **2019,** *58*, 195-206.
45. Schneider, D.; Mehlhorn, D.; Zeigermann, P.; Karger, J.; Valiullin, R., Transport properties of hierarchical micro-mesoporous materials. *Chem. Soc. Rev.* **2016,** *45*, 3439-3467.
46. Gao, W. Y.; Cardenal, A. D.; Wang, C. H.; Powers, D. C., In operando analysis of diffusion in porous metal-organic framework catalysts. *Chem. - Eur. J.* **2019,** *25*, 3465-3476.
47. Furukawa, S.; Reboul, J.; Diring, S.; Sumida, K.; Kitagawa, S., Structuring of metal-organic frameworks at the mesoscopic/macroscopic scale. *Chem. Soc. Rev.* **2014,** *43*, 5700-5734.
48. Shen, K.; Zhang, L.; Chen, X.; Liu, L.; Zhang, D.; Han, Y.; Chen, J.; Long, J.; Luque, R.; Li, Y.; Chen, B., Ordered macro-microporous metal-organic framework single crystals. *Science* **2018,** *359*, 206-210.
49. Ma, T.-Y.; Li, H.; Deng, Q.-F.; Liu, L.; Ren, T.-Z.; Yuan, Z.-Y., Ordered mesoporous metal–organic frameworks consisting of metal disulfonates. *Chem. Mater.* **2012,** *24*, 2253-2255.

50. McNamara, N. D.; Hicks, J. C., Chelating agent-free, vapor-assisted crystallization method to synthesize hierarchical microporous/mesoporous MIL-125 (Ti). *ACS Appl. Mater. Interfaces* **2015,** *7*, 5338-5346.
51. Li, J. R.; Kuppler, R. J.; Zhou, H. C., Selective gas adsorption and separation in metal-organic frameworks. *Chem. Soc. Rev.* **2009,** *38*, 1477-1504.
52. Niu, P.; Lu, N.; Liu, J.; Jia, H.; Zhou, F.; Fan, B.; Li, R., Water-induced synthesis of hierarchical Zr-based MOFs with enhanced adsorption capacity and catalytic activity. *Microporous Mesoporous Mater.* **2019,** *281*, 92-100.
53. Zhang, X.; Yang, Y.; Lv, X.; Wang, Y.; Liu, N.; Chen, D.; Cui, L., Adsorption/desorption kinetics and breakthrough of gaseous toluene for modified microporous-mesoporous UiO-66 metal organic framework. *J. Hazard. Mater.* **2019,** *366*, 140-150.
54. Limvorapitux, R.; Chou, L.-Y.; Young, A. P.; Tsung, C.-K.; Nguyen, S. T., Coupling molecular and nanoparticle catalysts on single metal–organic framework microcrystals for the tandem reaction of H_2O_2 generation and selective alkene oxidation. *ACS Catal.* **2017,** *7*, 6691-6698.
55. Nguyen, H. G. T.; Mao, L.; Peters, A. W.; Audu, C. O.; Brown, Z. J.; Farha, O. K.; Hupp, J. T.; Nguyen, S. T., Comparative study of titanium-functionalized UiO-66: support effect on the oxidation of cyclohexene using hydrogen peroxide. *Catal. Sci. Technol.* **2015,** *5*, 4444-4451.
56. Nguyen, H. G. T.; Schweitzer, N. M.; Chang, C. Y.; Drake, T. L.; So, M. C.; Stair, P. C.; Farha, O. K.; Hupp, J. T.; Nguyen, S. T., Vanadium-node-functionalized UiO-66: a thermally stable MOF-supported catalyst for the gas-phase oxidative dehydrogenation of cyclohexene. *ACS Catal.* **2014,** *4*, 2496-2500.
57. Xu, R.; Ji, Q.; Zhao, P.; Jian, M.; Xiang, C.; Hu, C.; Zhang, G.; Tang, C.; Liu, R.; Zhang, X.; Qu, J., Hierarchically porous UiO-66 with tunable mesopores and oxygen vacancies for enhanced arsenic removal. *J. Mater. Chem. A* **2020,** *8*, 7870-7879.
58. Wang, K.-Y.; Feng, L.; Yan, T.-H.; Wu, S.; Joseph, E.; Zhou, H.-C., Rapid generation of hierarchically porous metal–organic frameworks through laser photolysis. *Angew. Chem., Int. Ed.* **2020,** *59*, 11349/1-6.
59. Connolly, B. M.; Aragones-Anglada, M.; Gandara-Loe, J.; Danaf, N. A.; Lamb, D. C.; Mehta, J. P.; Vulpe, D.; Wuttke, S.; Silvestre-Albero, J.; Moghadam, P. Z.; Wheatley, A. E. H.; Fairen-Jimenez, D., Tuning porosity in macroscopic monolithic metal-organic frameworks for exceptional natural gas storage. *Nat. Commun.* **2019,** *10*, 2345/1-11.
60. Bradshaw, D.; El-Hankari, S.; Lupica-Spagnolo, L., Supramolecular templating of hierarchically porous metal-organic frameworks. *Chem. Soc. Rev.* **2014,** *43*, 5431-5443.
61. Zhao, J.; Liu, X.; Wu, Y.; Li, D.-S.; Zhang, Q., Surfactants as promising media in the field of metal-organic frameworks. *Coord. Chem. Rev.* **2019,** *391*, 30-43.
62. Guo, X.; Geng, S.; Zhuo, M.; Chen, Y.; Zaworotko, M. J.; Cheng, P.; Zhang, Z., The utility of the template effect in metal-organic frameworks. *Coord. Chem. Rev.* **2019,** *391*, 44-68.
63. Peng, L.; Zhang, J.; Li, J.; Han, B.; Xue, Z.; Yang, G., Surfactant-directed assembly of mesoporous metal-organic framework nanoplates in ionic liquids. *Chem. Commun.* **2012,** *48*, 8688-8690.
64. Pham, M.-H.; Vuong, G.-T.; Fontaine, F.-G.; Do, T.-O., A route to bimodal micro-mesoporous metal–organic frameworks nanocrystals. *Cryst. Growth Des.* **2011,** *12*, 1008-1013.

65. Sun, L. B.; Li, J. R.; Park, J.; Zhou, H. C., Cooperative template-directed assembly of mesoporous metal-organic frameworks. *J. Am. Chem. Soc.* **2012,** *134*, 126-129.
66. Xue, Z.; Zhang, J.; Peng, L.; Han, B.; Mu, T.; Li, J.; Yang, G., Poly(ethylene glycol) stabilized mesoporous metal-organic framework nanocrystals: efficient and durable catalysts for the oxidation of benzyl alcohol. *ChemPhysChem* **2014,** *15*, 85-89.
67. Sang, X.; Zhang, J.; Peng, L.; Liu, C.; Ma, X.; Han, B.; Yang, G., Assembly of mesoporous metal-organic framework templated by an ionic liquid/ethylene glycol interface. *ChemPhysChem* **2015,** *16*, 2317-2321.
68. Yang, X. L.; Qiao, L. M.; Dai, W. L., One-pot synthesis of a hierarchical microporous-mesoporous phosphotungstic acid-HKUST-1 catalyst and its application in the selective oxidation of cyclopentene to glutaraldehyde. *Chin. J. Catal.* **2015,** *36*, 1875-1885.
69. Sun, Y.; Amsler, M.; Goedecker, S.; Caravella, A.; Yoshida, M.; Kato, M., Surfactant-assisted synthesis of large Cu-BTC MOF single crystals and their potential utilization as photodetectors. *CrystEngComm* **2019,** *21*, 3948-3953.
70. Rani, P.; Srivastava, R., Exploring the dicationic gemini surfactant for the generation of mesopores: a step towards the construction of a hierarchical metal–organic framework. *Inorg. Chem. Front.* **2018,** *5*, 2856-2867.
71. Li, H.; Meng, F.; Zhang, S.; Wang, L.; Li, M.; Ma, L.; Zhang, W.; Zhang, W.; Yang, Z.; Wu, T.; Lee, S.; Huo, F.; Lu, J., Crystal-growth-dominated fabrication of metal–organic frameworks with orderly distributed hierarchical porosity. *Angew. Chem., Int. Ed.* **2020,** *59*, 2457-2464.
72. Zhao, Y.; Zhang, J.; Han, B.; Song, J.; Li, J.; Wang, Q., Metal-organic framework nanospheres with well-ordered mesopores synthesized in an ionic liquid/CO_2/surfactant system. *Angew. Chem., Int. Ed.* **2011,** *50*, 636-639.
73. Huang, X.-X.; Qiu, L.-G.; Zhang, W.; Yuan, Y.-P.; Jiang, X.; Xie, A.-J.; Shen, Y.-H.; Zhu, J.-F., Hierarchically mesostructured MIL-101 metal–organic frameworks: supramolecular template-directed synthesis and accelerated adsorption kinetics for dye removal. *CrystEngComm* **2012,** *14*, 1613-1617.
74. Zhang, X.; Xiong, B.; Li, J.; Qian, L.; Liu, L.; Liu, Z.; Fang, P.; He, C., Dependence of dye molecules adsorption behaviors on pore characteristics of mesostructured MOFs fabricated by surfactant template. *ACS Appl. Mater. Interfaces* **2019,** *11*, 31441-31451.
75. Wu, Y. N.; Zhou, M.; Zhang, B.; Wu, B.; Li, J.; Qiao, J.; Guan, X.; Li, F., Amino acid assisted templating synthesis of hierarchical zeolitic imidazolate framework-8 for efficient arsenate removal. *Nanoscale* **2014,** *6*, 1105-1112.
76. Yi, J.; Li, H.; Jiang, L.; Zhang, K.; Chen, D., Solution-based fabrication of a highly catalytically active 3D network constructed from 1D metal-organic framework-coated polymeric worm-like micelles. *Chem. Commun.* **2015,** *51*, 10162-10165.
77. Do, X. D.; Hoang, V.-T.; Kaliaguine, S., MIL-53(Al) mesostructured metal-organic frameworks. *Microporous Mesoporous Mater.* **2011,** *141*, 135-139.
78. Zhou, M.; Wu, Y.-n.; Qiao, J.; Zhang, J.; McDonald, A.; Li, G.; Li, F., The removal of bisphenol A from aqueous solutions by MIL-53(Al) and mesostructured MIL-53(Al). *J. Colloid Interface Sci.* **2013,** *405*, 157-163.
79. Huang, Y.-B.; Shen, M.; Wang, X.; Shi, P.-C.; Li, H.; Cao, R., Hierarchically micro- and mesoporous metal–organic framework-supported alloy nanocrystals as bifunctional catalysts: Toward cooperative catalysis. *J. Catal.* **2015,** *330*, 452-457.

80. Xu, H. Q.; Wang, K.; Ding, M.; Feng, D.; Jiang, H. L.; Zhou, H. C., Seed-mediated synthesis of metal-organic frameworks. *J. Am. Chem. Soc.* **2016,** *138*, 5316-20.
81. Yot, P. G.; Yang, K.; Ragon, F.; Dmitriev, V.; Devic, T.; Horcajada, P.; Serre, C.; Maurin, G., Exploration of the mechanical behavior of metal organic frameworks UiO-66(Zr) and MIL-125(Ti) and their NH_2 functionalized versions. *Dalton Trans.* **2016,** *45*, 4283-4288.
82. Wu, H.; Yildirim, T.; Zhou, W., Exceptional mechanical stability of highly porous zirconium metal–organic framework UiO-66 and its important implications. *J. Phys. Chem. Lett.* **2013,** *4*, 925-930.
83. Zhuang, J.; Chou, L.-Y.; Sneed, B. T.; Cao, Y.; Hu, P.; Feng, L.; Tsung, C.-K., Surfactant-mediated conformal overgrowth of core-shell metal-organic framework materials with mismatched topologies. *Small* **2015,** *11*, 5551-5555.
84. Ray, A., Solvophobic interactions and micelle formation in structure forming nonaqueous solvents. *Nature* **1971,** *231*, 313-315.
85. He, Z.; Alexandridis, P., Micellization thermodynamics of Pluronic P123 ($EO_{20}PO_{70}EO_{20}$) amphiphilic block copolymer in aqueous ethylammonium nitrate (EAN) solutions. *Polymers* **2017,** *10*, 1-18.
86. Akhter, M. S.; Alawi, S. M., A comparison of micelle formation of ionic surfactants in formamide, in *N*-methylformamide and in *N,N*-dimethylformamide. *Colloids Surf., A* **2003,** *219*, 281-290.
87. Cao, X.; Dai, L.; Wang, L. Y.; Liu, J.; Lei, J. D., A surfactant template-assisted strategy for synthesis of ZIF-8 hollow nanospheres. *Mater. Lett.* **2015,** *161*, 682-685.
88. Luan, Y.; Qi, Y.; Jin, Z.; Peng, X.; Gao, H.; Wang, G., Synthesis of a flower-like Zr-based metal–organic framework and study of its catalytic performance in the Mannich reaction. *Rsc. Adv.* **2015,** *5*, 19273-19278.
89. Ko, Y. S.; Kwon, Y. U., Mesoporous zirconia thin films with three-dimensional pore structures and their application to electrochemical glucose detection. *ACS Appl. Mater. Interfaces* **2013,** *5*, 3599-3606.
90. Alexandridis, P.; Holzwarth, J. F.; Hatton, T. A., Micellization of poly(ethylene oxide)-poly(propylene oxide)-poly(ethylene oxide) triblock copolymers in aqueous-solutions - thermodynamics of copolymer association. *Macromolecules* **1994,** *27*, 2414-2425.
91. Taddei, M.; Dumbgen, K. C.; van Bokhoven, J. A.; Ranocchiari, M., Aging of the reaction mixture as a tool to modulate the crystallite size of UiO-66 into the low nanometer range. *Chem. Commun.* **2016,** *52*, 6411-6414.
92. Tao, Y. S.; Tanaka, H.; Ohkubo, T.; Kanoh, H.; Kaneko, K., Pore structures of ZSM-5 synthesized in the mesopore spaces of a carbon aerogel. *Adsorpt. Sci. Technol.* **2003,** *21*, 199-203.
93. ALOthman, Z. A., A review: fundamental aspects of silicate mesoporous materials. *Materials* **2012,** *5*, 2874-2902.
94. Pabisch, S.; Feichtenschlager, B.; Kickelbick, G.; Peterlik, H., Effect of interparticle interactions on size determination of zirconia and silica based systems – A comparison of SAXS, DLS, BET, XRD and TEM. *Chem. Phys. Lett.* **2012,** *521*, 91-97.
95. Orthaber, A.; Seidel, C.; Belaj, F.; Albering, J. H.; Pietschnig, R.; Ruschewitz, U., Optimized synthesis of tetrafluoroterephthalic acid: a versatile linking ligand for the construction of new coordination polymers and metal-organic frameworks. *Inorg. Chem.* **2010,** *49*, 9350-9357.

96. Chen, Z.; Wang, X.; Noh, H.; Ayoub, G.; Peterson, G. W.; Buru, C. T.; Islamoglu, T.; Farha, O. K., Scalable, room temperature, and water-based synthesis of functionalized zirconium-based metal–organic frameworks for toxic chemical removal. *CrystEngComm* **2019,** *21*, 2409-2415.
97. Takebayashi, Y.; Sue, K.; Yoda, S.; Hakuta, Y.; Furuya, T., Solubility of terephthalic acid in subcritical water. *J. Chem. Eng. Data* **2012,** *57*, 1810-1816.
98. After MeOH rinsing at room temperature, the product still contains a small amount of the F-127 template (~ 2 wt %), which can then be completely removed by Soxhlet extraction in MeOH.
99. Hu, Z.; Peng, Y.; Kang, Z.; Qian, Y.; Zhao, D., A modulated hydrothermal (MHT) approach for the facile synthesis of UiO-66-type MOFs. *Inorg. Chem.* **2015,** *54*, 4862-4868.
100. Thommes, M.; Kaneko, K.; Neimark Alexander, V.; Olivier James, P.; Rodriguez-Reinoso, F.; Rouquerol, J.; Sing Kenneth, S. W., Physisorption of gases, with special reference to the evaluation of surface area and pore size distribution (IUPAC Technical Report). *Pure Appl. Chem.* **2015,** *87*, 1051-1069.
101. Wang, L. F.; Zhang, Z.; Yin, C. Y.; Shan, Z. C.; Xiao, F. S., Hierarchical mesoporous zeolites with controllable mesoporosity templated from cationic polymers. *Microporous Mesoporous Mater.* **2010,** *131*, 58-67.
102. Liu, T.; Liu, Y.; Yao, L.; Yang, W.; Tian, L.; Liu, H.; Liu, D.; Wang, C., Controllable formation of meso- and macropores within metal-organic framework crystals via a citric acid modulator. *Nanoscale* **2018,** *10*, 13194-13201.
103. Katz, M. J.; Brown, Z. J.; Colon, Y. J.; Siu, P. W.; Scheidt, K. A.; Snurr, R. Q.; Hupp, J. T.; Farha, O. K., A facile synthesis of UiO-66, UiO-67 and their derivatives. *Chem. Commun.* **2013,** *49*, 9449-51.
104. The higher value in this range is our data (see Table 2.12.3).
105. Olea, A. F.; Carrasco, H.; Espinoza, L.; Acevedo, B., Solubilization of p-alkylphenols in pluronics F-68 and F-127 micelles: partition coefficients and effect of solute on the aggregate structure. *J. Chil. Chem. Soc.* **2014,** *59*, 2451-2454.
106. Liu, L.; Chen, Z.; Wang, J.; Zhang, D.; Zhu, Y.; Ling, S.; Huang, K.-W.; Belmabkhout, Y.; Adil, K.; Zhang, Y.; Slater, B.; Eddaoudi, M.; Han, Y., Imaging defects and their evolution in a metal–organic framework at sub-unit-cell resolution. *Nat. Chem.* **2019,** *11*, 622-628.
107. This broad interparticle-pore peak was not observed in the UiO-66@HM-UiO-66-F_4 materials.
108. Hu, Z.; Nalaparaju, A.; Peng, Y.; Jiang, J.; Zhao, D., Modulated hydrothermal synthesis of UiO-66(Hf)-type metal-organic frameworks for optimal carbon dioxide separation. *Inorg. Chem.* **2016,** *55*, 1134-1141.
109. Islamoglu, T.; Goswami, S.; Li, Z.; Howarth, A. J.; Farha, O. K.; Hupp, J. T., Postsynthetic tuning of metal–organic frameworks for targeted applications. *Acc. Chem. Res.* **2017,** *50*, 805-813.
110. Wang, Z.; Cohen, S. M., Postsynthetic modification of metal–organic frameworks. *Chem. Soc. Rev.* **2009,** *38*, 1315-1329.
111. While not directly comparable, the kinetic of our materials appears to be similar as that observed by Huang et al. (reference #20) at twice the [DB 86] for a mesoporous UiO-66 material with a similar end-point capacity (250 mg/g). See Figure 2.12.37 in Section 2.12.5.

112. Nemr, A. E.; Abdelwahab, O.; El-Sikaily, A.; Khaled, A., Removal of direct blue-86 from aqueous solution by new activated carbon developed from orange peel. *J. Hazard. Mater.* **2009,** *161*, 102-110.
113. Hussain, C. M., *Nanomaterials in Chromatography: Current Trends in Chromatographic Research Technology and Techniques*. Elsevier: Amsterdam 1043 NX, Netherlands, 2018.
114. Choi, M.; Na, K.; Kim, J.; Sakamoto, Y.; Terasaki, O.; Ryoo, R., Stable single-unit-cell nanosheets of zeolite MFI as active and long-lived catalysts. *Nature* **2009,** *461*, 246-250.
115. Parlett, C. M.; Wilson, K.; Lee, A. F., Hierarchical porous materials: catalytic applications. *Chem. Soc. Rev.* **2013,** *42*, 3876-3893.
116. Sun, Q.; Dai, Z.; Meng, X.; Xiao, F. S., Porous polymer catalysts with hierarchical structures. *Chem. Soc. Rev.* **2015,** *44*, 6018-6034.
117. Zheng, H. Q.; Zeng, Y. N.; Chen, J.; Lin, R. G.; Zhuang, W. E.; Cao, R.; Lin, Z. J., Zr-based metal-organic frameworks with intrinsic peroxidase-like activity for ultradeep oxidative desulfurization: mechanism of H_2O_2 decomposition. *Inorg. Chem.* **2019,** *58*, 6983-6992.
118. Walton, K. S.; Snurr, R. Q., Applicability of the BET method for determining surface areas of microporous metal-organic frameworks. *J. Am. Chem. Soc.* **2007,** *129*, 8552-8556.
119. Lippens, B. C.; de Boer, J. H., Studies on pore systems in catalysts: V. The t method. *J. Catal.* **1965,** *4*, 319-323.
120. Chakraborty, S.; Colón, Y. J.; Snurr, R. Q.; Nguyen, S. T., Hierarchically porous organic polymers: highly enhanced gas uptake and transport through templated synthesis. *Chem. Sci.* **2015,** *6*, 384-389.
121. Marczewski, A. W. ASAP 2405N - N_2 sorption analysis report. http://adsorption.org/awm/ads/meso/RIB-ASAP.htm (accessed 02/05/2018).
122. Liu, Y.; Fu, S.; Lin, L.; Cao, Y.; Xie, X.; Yu, H.; Chen, M.; Li, H., Redox-sensitive Pluronic F127-tocopherol micelles: synthesis, characterization, and cytotoxicity evaluation. *Int. J. Nanomed.* **2017,** *12*, 2635-2644.
123. Parent, L. R.; Denny, M. S.; Patterson, J. P.; Abellan, P.; Ramasse, Q. M.; Paesani, F.; Cohen, S. M.; Gianneschi, N. C., Analytical STEM investigation of the post-synthetic modification (PMS) of metal-organic frameworks (MOFs): metal- and ligand-exchange in UiO-66. *Microsc. Microanal.* **2018,** *24*, 1970-1971.
124. Zhu, L.; Zhang, D.; Xue, M.; Li, H.; Qiu, S., Direct observations of the MOF (UiO-66) structure by transmission electron microscopy. *CrystEngComm* **2013,** *15*, 9356-9359.
125. Tanabe, K. K.; Cohen, S. M., Postsynthetic modification of metal–organic frameworks—a progress report. *Chem. Soc. Rev.* **2011,** *40*, 498-519.
126. Kim, M.; Cahill, J. F.; Fei, H.; Prather, K. A.; Cohen, S. M., Postsynthetic ligand and cation exchange in robust metal–organic frameworks. *J. Am. Chem. Soc.* **2012,** *134*, 18082-18088.
127. Brozek, C. K.; Dincă, M., Cation exchange at the secondary building units of metal–organic frameworks. *Chem. Soc. Rev.* **2014,** *43*, 5456-5467.
128. Huang, Y. H.; Lo, W. S.; Kuo, Y. W.; Chen, W. J.; Lin, C. H.; Shieh, F. K., Green and rapid synthesis of zirconium metal-organic frameworks via mechanochemistry: UiO-66 analog nanocrystals obtained in one hundred seconds. *Chem. Commun.* **2017,** *53*, 5818-5821.
129. Zeng, M.; Xiao, Y.; Liu, J.; Yang, K.; Fu, L., Exploring two-dimensional materials toward the next-generation circuits: from monomer design to assembly control. *Chem. Rev.* **2018,** *118*, 6236-6296.

130. Ma, R.; Sasaki, T., Two-dimensional oxide and hydroxide nanosheets: controllable high-quality exfoliation, molecular assembly, and exploration of functionality. *Acc. Chem. Res.* **2015,** *48*, 136-143.
131. Bolotsky, A.; Butler, D.; Dong, C.; Gerace, K.; Glavin, N. R.; Muratore, C.; Robinson, J. A.; Ebrahimi, A., Two-dimensional materials in biosensing and healthcare: from in vitro diagnostics to optogenetics and beyond. *ACS Nano* **2019,** *13*, 9781-9810.
132. Khan, K.; Tareen, A. K.; Aslam, M.; Wang, R. H.; Zhang, Y. P.; Mahmood, A.; Ouyang, Z. B.; Zhang, H.; Guo, Z. Y., Recent developments in emerging two-dimensional materials and their applications. *J. Mater. Chem. C.* **2020,** *8*, 387-440.
133. Tan, C.; Cao, X.; Wu, X.-J.; He, Q.; Yang, J.; Zhang, X.; Chen, J.; Zhao, W.; Han, S.; Nam, G.-H.; Sindoro, M.; Zhang, H., Recent advances in ultrathin two-dimensional nanomaterials. *Chem. Rev.* **2017,** *117*, 6225-6331.
134. Tan, C.; Liu, G.; Li, H.; Cui, Y.; Liu, Y., Ultrathin two-dimensional metal–organic framework nanosheets—an emerging class of catalytic nanomaterials. *Dalton Trans.* **2020,** *49*, 11073-11084.
135. Zhang, X.; Zhang, P.; Chen, C.; Zhang, J.; Yang, G.; Zheng, L.; Zhang, J.; Han, B., Fabrication of 2D metal–organic framework nanosheets with tailorable thickness using bio-based surfactants and their application in catalysis. *Green Chem.* **2019,** *21*, 54-58.
136. Zhao, M.; Huang, Y.; Peng, Y.; Huang, Z.; Ma, Q.; Zhang, H., Two-dimensional metal–organic framework nanosheets: synthesis and applications. *Chem. Soc. Rev.* **2018,** *47*, 6267-6295.
137. Jiang, Q.; Zhou, C.; Meng, H.; Han, Y.; Shi, X.; Zhan, C.; Zhang, R., Two-dimensional metal–organic framework nanosheets: synthetic methodologies and electrocatalytic applications. *J. Mater. Chem. A* **2020,** *8*, 15271-15301.
138. Ashworth, D. J.; Foster, J. A., Metal–organic framework nanosheets (MONs): a new dimension in materials chemistry. *J. Mater. Chem. A* **2018,** *6*, 16292-16307.
139. Ren, J.; Ledwaba, M.; Musyoka, N. M.; Langmi, H. W.; Mathe, M.; Liao, S.; Pang, W., Structural defects in metal–organic frameworks (MOFs): Formation, detection and control towards practices of interests. *Coord. Chem. Rev.* **2017,** *349*, 169-197.
140. Chen, Z.; Hanna, S. L.; Redfern, L. R.; Alezi, D.; Islamoglu, T.; Farha, O. K., Reticular chemistry in the rational synthesis of functional zirconium cluster-based MOFs. *Coord. Chem. Rev.* **2019,** *386*, 32-49.
141. Tao, A. R.; Habas, S.; Yang, P., Shape control of colloidal metal nanocrystals. *Small* **2008,** *4*, 310-325.
142. Bakshi, M. S., How surfactants control crystal growth of nanomaterials. *Cryst. Growth Des.* **2016,** *16*, 1104-1133.
143. Zhang, F.; Hu, X.; Roth, E. W.; Kim, Y.; Nguyen, S. T., Template-assisted, seed-mediated synthesis of hierarchically mesoporous core–shell UiO-66: enhancing adsorption capacity and catalytic activity through iterative growth. *Chem. Mater.* **2020,** *32*, 4292-4302.
144. This hollow spherical morphology has been observed in other 2D materials. For example, a morphology evolution model has been proposed for the growth of SnS_2 hollow spheres (see: *Phys. Status Solidi RRL* **2019**, *13*, 1900185/1-6.).
145. Firth, F. C. N.; Cliffe, M. J.; Vulpe, D.; Aragones-Anglada, M.; Moghadam, P. Z.; Fairen-Jimenez, D.; Slater, B.; Grey, C. P., Engineering new defective phases of UiO family metal–organic frameworks with water. *J. Mater. Chem. A* **2019,** *7*, 7459-7469.

146. Navarro Amador, R.; Cirre, L.; Carboni, M.; Meyer, D., BTEX removal from aqueous solution with hydrophobic Zr metal organic frameworks. *J. Environ. Manage.* **2018,** *214*, 17-22.
147. Schaate, A.; Roy, P.; Godt, A.; Lippke, J.; Waltz, F.; Wiebcke, M.; Behrens, P., Modulated synthesis of Zr-based metal-organic frameworks: from nano to single crystals. *Chem. - Eur. J.* **2011,** *17*, 6643-51.
148. Meng, F.; Morin, S. A.; Forticaux, A.; Jin, S., Screw dislocation driven growth of nanomaterials. *Acc. Chem. Res.* **2013,** *46*, 1616-1626.
149. Grinding was applied to obtain thin sample and avoid scattering across multiple crystals in bulk materials. The same PXRD patterns of the materials before and after grinding suggest that the grinding did not affect the crystallinity of the material (see Figure 3.16).
150. M. V, V.; Nageswaran, G., Review—2D layered metal organic framework nanosheets as an emerging platform for electrochemical sensing. *J. Electrochem. Soc.* **2020,** *167*, 136502/1-13.
151. Zhang, Y.; Zhang, X.; Lyu, J.; Otake, K. I.; Wang, X.; Redfern, L. R.; Malliakas, C. D.; Li, Z.; Islamoglu, T.; Wang, B.; Farha, O. K., A flexible metal-organic framework with 4-connected Zr_6 nodes. *J. Am. Chem. Soc.* **2018,** *140*, 11179-11183.
152. Yuan, S.; Zou, L. F.; Li, H. X.; Chen, Y. P.; Qin, J. S.; Zhang, Q.; Lu, W. G.; Hall, M. B.; Zhou, H. C., Flexible zirconium metal-organic frameworks as bioinspired switchable catalysts. *Angew. Chem., Int. Ed.* **2016,** *55*, 10776-10780.
153. At the point when the thesis was being written, additional structural characterization was undergoing, which includes synchrotron-based wide-angle X-ray scattering and X-ray total scattering. The data would be coupled with Pawley/Rietveld refinement and pair-distribution function analysis to have additional evidence of the proposed 2D **cpp** structure.
154. The topology information can be found on the RCSR database.
155. Ni, B.; Sun, W.; Kang, J.; Zhang, Y., Understanding the linear and second-order nonlinear optical properties of UiO-66-derived metal–organic frameworks: A comprehensive DFT study. *J. Phys. Chem. C* **2020,** *124*, 11595-11608.
156. Ermer, M.; Mehler, J.; Kriesten, M.; Avadhut, Y. S.; Schulz, P. S.; Hartmann, M., Synthesis of the novel MOF hcp UiO-66 employing ionic liquids as a linker precursor. *Dalton Trans.* **2018,** *47*, 14426-14430.
157. Kresse, G.; Joubert, D., From ultrasoft pseudopotentials to the projector augmented-wave method. *Phys. Rev. B* **1999,** *59*, 1758-1775.
158. Perdew, J. P.; Ruzsinszky, A.; Csonka, G. I.; Vydrov, O. A.; Scuseria, G. E.; Constantin, L. A.; Zhou, X.; Burke, K., Restoring the density-gradient expansion for exchange in solids and surfaces. *Phys. Rev. Lett.* **2008,** *100*, 136406/1-4.
159. Grimme, S.; Antony, J.; Ehrlich, S.; Krieg, H., A consistent and accurate ab initio parametrization of density functional dispersion correction (DFT-D) for the 94 elements H-Pu. *J. Chem. Phys.* **2010,** *132*, 154104/1-20.
160. Grimme, S.; Ehrlich, S.; Goerigk, L., Effect of the damping function in dispersion corrected density functional theory. *J. Comput. Chem.* **2011,** *32*, 1456-1465.
161. Chen, B.; Zhu, Z.; Liu, S.; Hong, J.; Ma, J.; Qiu, Y.; Chen, J., Facile hydrothermal synthesis of nanostructured hollow iron-cerium alkoxides and their superior arsenic adsorption performance. *ACS Appl. Mater. Interfaces* **2014,** *6*, 14016-14025.
162. Hao, L.; Liu, M.; Wang, N.; Li, G., A critical review on arsenic removal from water using iron-based adsorbents. *Rsc. Adv.* **2018,** *8*, 39545-39560.

163. Liu, R.; Chi, L.; Wang, X.; Sui, Y.; Wang, Y.; Arandiyan, H., Review of metal (hydr) oxide and other adsorptive materials for phosphate removal from water. *J. Environ. Chem. Eng.* **2018,** *6*, 5269-5286.
164. Mohan, D.; Pittman Jr, C. U., Arsenic removal from water/wastewater using adsorbents—a critical review. *J. Hazard. Mater.* **2007,** *142*, 1-53.
165. Qiu, H.; Liang, C.; Zhang, X.; Chen, M.; Zhao, Y.; Tao, T.; Xu, Z.; Liu, G., Fabrication of a biomass-based hydrous zirconium oxide nanocomposite for preferable phosphate removal and recovery. *ACS Appl. Mater. Interfaces* **2015,** *7*, 20835-20844.
166. Brockgreitens, J. W.; Heidari, F.; Abbas, A., Versatile process for the preparation of nanocomposite sorbents: phosphorus and arsenic removal. *Environ. Sci. Technol.* **2020,** *54*, 9034-9043.
167. Gupta, A.; Chauhan, V. S.; Sankararamakrishnan, N., Preparation and evaluation of iron–chitosan composites for removal of As(III) and As(V) from arsenic contaminated real life groundwater. *Water Res.* **2009,** *43*, 3862-3870.
168. Liu, B.; Kim, K.-H.; Kumar, V.; Kim, S., A review of functional sorbents for adsorptive removal of arsenic ions in aqueous systems. *J. Hazard. Mater.* **2020,** *388*, 121815/1-18.
169. Abu Samah, N.; Mat Rosli, N. A.; Abdul Manap, A. H.; Abdul Aziz, Y. F.; Mohd Yusoff, M., Synthesis & characterization of ion imprinted polymer for arsenic removal from water: A value addition to the groundwater resources. *Chem. Eng. J.* **2020,** *394*, 124900/1-8.
170. Su, C.; Puls, R. W., In situ remediation of arsenic in simulated groundwater using zerovalent iron: laboratory column tests on combined effects of phosphate and silicate. *Environ. Sci. Technol.* **2003,** *37*, 2582-2587.
171. Zeng, H.; Fisher, B.; Giammar, D. E., Individual and competitive adsorption of arsenate and phosphate to a high-surface-area iron oxide-based sorbent. *Environ. Sci. Technol.* **2008,** *42*, 147-152.
172. Gu, Y.; Xie, D.; Ma, Y.; Qin, W.; Zhang, H.; Wang, G.; Zhang, Y.; Zhao, H., Size modulation of zirconium-based metal organic frameworks for highly efficient phosphate remediation. *ACS Appl. Mater. Interfaces* **2017,** *9*, 32151-32160.
173. Qiu, H.; Yang, L.; Liu, F.; Zhao, Y.; Liu, L.; Zhu, J.; Song, M., Highly selective capture of phosphate ions from water by a water stable metal-organic framework modified with polyethyleneimine. *Environ. Sci. Pollut. Res.* **2017,** *24*, 23694-23703.
174. Qiu, H.; Ye, M.; Zeng, Q.; Li, W.; Fortner, J.; Liu, L.; Yang, L., Fabrication of agricultural waste supported UiO-66 nanoparticles with high utilization in phosphate removal from water. *Chem. Eng. J.* **2019,** *360*, 621-630.
175. Zhu, X.; Li, B.; Yang, J.; Li, Y.; Zhao, W.; Shi, J.; Gu, J., Effective adsorption and enhanced removal of organophosphorus pesticides from aqueous solution by Zr-based MOFs of UiO-67. *ACS Appl. Mater. Interfaces* **2015,** *7*, 223-231.
176. Assaad, N.; Sabeh, G.; Hmadeh, M., Defect control in Zr-based metal–organic framework nanoparticles for arsenic removal from water. *ACS Appl. Nano Mater.* **2020,** *3*, 8997-9008.
177. Wan, P.; Yuan, M.; Yu, X.; Zhang, Z.; Deng, B., Arsenate removal by reactive mixed matrix PVDF hollow fiber membranes with UiO-66 metal organic frameworks. *Chem. Eng. J.* **2020,** *382*, 122921/1-9.
178. Wang, C.; Lee, M.; Liu, X.; Wang, B.; Paul Chen, J.; Li, K., A metal–organic framework/α-alumina composite with a novel geometry for enhanced adsorptive separation. *Chem. Commun.* **2016,** *52*, 8869-8872.

179. Kalaj, M.; Bentz, K. C.; Ayala, S.; Palomba, J. M.; Barcus, K. S.; Katayama, Y.; Cohen, S. M., MOF-polymer hybrid materials: From simple composites to tailored architectures. *Chem. Rev.* **2020,** *120*, 8267-8302.
180. Qian, Q.; Asinger, P. A.; Lee, M. J.; Han, G.; Mizrahi Rodriguez, K.; Lin, S.; Benedetti, F. M.; Wu, A. X.; Chi, W. S.; Smith, Z. P., MOF-based membranes for gas separations. *Chem. Rev.* **2020,** *120*, 8161-8266.
181. Feng, M.; Zhang, P.; Zhou, H. C.; Sharma, V. K., Water-stable metal-organic frameworks for aqueous removal of heavy metals and radionuclides: A review. *Chemosphere* **2018,** *209*, 783-800.
182. Winarta, J.; Shan, B.; McIntyre, S. M.; Ye, L.; Wang, C.; Liu, J.; Mu, B., A decade of UiO-66 research: A historic review of dynamic structure, synthesis mechanisms, and characterization techniques of an archetypal metal–organic framework. *Cryst. Growth Des.* **2020,** *20*, 1347-1362.
183. Kobielska, P. A.; Howarth, A. J.; Farha, O. K.; Nayak, S., Metal–organic frameworks for heavy metal removal from water. *Coord. Chem. Rev.* **2018,** *358*, 92-107.
184. Liu, R.; Chi, L.; Wang, X.; Wang, Y.; Sui, Y.; Xie, T.; Arandiyan, H., Effective and selective adsorption of phosphate from aqueous solution via trivalent-metals-based amino-MIL-101 MOFs. *Chem. Eng. J.* **2019,** *357*, 159-168.
185. Wang, C.; Luan, J.; Wu, C., Metal-organic frameworks for aquatic arsenic removal. *Water Res.* **2019,** *158*, 370-382.
186. Xu, G.-R.; An, Z.-H.; Xu, K.; Liu, Q.; Das, R.; Zhao, H.-L., Metal organic framework (MOF)-based micro/nanoscaled materials for heavy metal ions removal: The cutting-edge study on designs, synthesis, and applications. *Coord. Chem. Rev.* **2021,** *427*, 213554.
187. Wang, X.; Zhai, L.; Wang, Y.; Li, R.; Gu, X.; Yuan, Y. D.; Qian, Y.; Hu, Z.; Zhao, D., Improving water-treatment performance of zirconium metal-organic framework membranes by postsynthetic defect healing. *ACS Appl. Mater. Interfaces* **2017,** *9*, 37848-37855.
188. Chaudhury, S.; Nir, O., Electro-enhanced membrane sorption: a new approach for selective ion separation and its application to phosphate and arsenic removal. *Ind. Eng. Chem. Res.* **2020,** *59*, 10595-10605.
189. Mondloch, J. E.; Katz, M. J.; Planas, N.; Semrouni, D.; Gagliardi, L.; Hupp, J. T.; Farha, O. K., Are Zr_6-based MOFs water stable? Linker hydrolysis vs. capillary-force-driven channel collapse. *Chem. Commun.* **2014,** *50*, 8944-8946.
190. Sumida, K.; Rogow, D. L.; Mason, J. A.; McDonald, T. M.; Bloch, E. D.; Herm, Z. R.; Bae, T.-H.; Long, J. R., Carbon dioxide capture in metal–organic frameworks. *Chem. Rev.* **2012,** *112*, 724-781.
191. Taylor, J. M.; Dawson, K. W.; Shimizu, G. K., A water-stable metal–organic framework with highly acidic pores for proton-conducting applications. *J. Am. Chem. Soc.* **2013,** *135*, 1193-1196.
192. Lu, J.; Zhang, H.; Hu, X.; Qian, B.; Hou, J.; Han, L.; Zhu, Y.; Sun, C.; Jiang, L.; Wang, H., Ultraselective monovalent metal ion conduction in a three-dimensional sub-1 nm nanofluidic device constructed by metal–organic frameworks. *ACS Nano* **2020**.
193. Lee, D. T.; Zhao, J.; Oldham, C. J.; Peterson, G. W.; Parsons, G. N., UiO-66-NH_2 metal–organic framework (MOF) nucleation on TiO_2, ZnO, and Al_2O_3 atomic layer deposition-treated polymer fibers: role of metal oxide on MOF growth and catalytic hydrolysis of chemical warfare agent simulants. *ACS Appl. Mater. Interfaces* **2017,** *9*, 44847-44855.

194. Shen, J.; Liu, G.; Huang, K.; Li, Q.; Guan, K.; Li, Y.; Jin, W., UiO-66-polyether block amide mixed matrix membranes for CO_2 separation. *J. Membr. Sci.* **2016,** *513*, 155-165.
195. Denny Jr., M. S.; Cohen, S. M., In situ modification of metal–organic frameworks in mixed-matrix membranes. *Angew. Chem., Int. Ed.* **2015,** *54*, 9029-9032.
196. Katayama, Y.; Bentz, K. C.; Cohen, S. M., Defect-free MOF-based mixed-matrix membranes obtained by corona cross-linking. *ACS Appl. Mater. Interfaces* **2019,** *11*, 13029-13037.
197. Dechnik, J.; Gascon, J.; Doonan, C. J.; Janiak, C.; Sumby, C. J., Mixed-matrix membranes. *Angew. Chem., Int. Ed.* **2017,** *56*, 9292-9310.
198. Jiang, Y.; Liu, C.; Caro, J.; Huang, A., A new UiO-66-NH_2 based mixed-matrix membranes with high CO_2/CH_4 separation performance. *Microporous Mesoporous Mater.* **2019,** *274*, 203-211.
199. Lin, R.; Hernandez, B. V.; Ge, L.; Zhu, Z., Metal organic framework based mixed matrix membranes: an overview on filler/polymer interfaces. *J. Mater. Chem. A* **2018,** *6*, 293-312.
200. Petrov, K. V.; Paltrinieri, L.; Poltorak, L.; de Smet, L. C.; Sudhölter, E. J., Modified cation-exchange membrane for phosphate recovery in an electrochemically assisted adsorption–desorption process. *Chem. Commun.* **2020,** *56*, 5046-5049.
201. Dong, H.; Wei, L.; Tarpeh, W. A., Electro-assisted regeneration of pH-sensitive ion exchangers for sustainable phosphate removal and recovery. *Water Res.* **2020,** *184*, 116167/1-10.
202. Barankova, E.; Pradeep, N.; Peinemann, K.-V., Zeolite-imidazolate framework (ZIF-8) membrane synthesis on a mixed-matrix substrate. *Chem. Commun.* **2013,** *49*, 9419-9421.
203. Li, W.; Zhang, G.; Zhang, C.; Meng, Q.; Fan, Z.; Gao, C., Synthesis of trinity metal–organic framework membranes for CO_2 capture. *Chem. Commun.* **2014,** *50*, 3214-3216.
204. Liu, J.; Canfield, N.; Liu, W., Preparation and characterization of a hydrophobic metal–organic framework membrane supported on a thin porous metal sheet. *Ind. Eng. Chem. Res.* **2016,** *55*, 3823-3832.
205. Wu, F.; Lin, L.; Liu, H.; Wang, H.; Qiu, J.; Zhang, X., Synthesis of stable UiO-66 membranes for pervaporation separation of methanol/methyl tert-butyl ether mixtures by secondary growth. *J. Membr. Sci.* **2017,** *544*, 342-350.
206. Friebe, S.; Geppert, B.; Steinbach, F.; Caro, J., Metal–organic framework UiO-66 layer: A highly oriented membrane with good selectivity and hydrogen permeance. *ACS Appl. Mater. Interfaces* **2017,** *9*, 12878-12885.
207. The chemical composition of the cluster is proposed based on the components in solution and previous studies. Please see: *Chem. Commun.*, **2016**, *52*, 6411-6414; *Chem. Mater.*, **2020**, *32*, 4292–4302.
208. Here, to replicate the real scenario, the P^V concentration was kept almost comparable to that in the groundwater (please see reference #210 for a comparable groundwater composition).
209. Liu, T.; Zheng, S.; Yang, L., Magnetic zirconium-based metal–organic frameworks for selective phosphate adsorption from water. *J. Colloid Interface Sci.* **2019,** *552*, 134-141.
210. Sahu, P.; Sikdar, P.; Chakraborty, S., Geochemical evolution of groundwater in southern Bengal Basin: The example of Rajarhat and adjoining areas, West Bengal, India. *J. Earth Syst. Sci.* **2016,** *125*, 129-145.
211. Abney, C. W.; Taylor-Pashow, K. M. L.; Russell, S. R.; Chen, Y.; Samantaray, R.; Lockard, J. V.; Lin, W., Topotactic transformations of metal–organic frameworks to highly porous and stable inorganic sorbents for efficient radionuclide sequestration. *Chem. Mater.* **2014,** *26*, 5231-5243.

212. Zhang, Q.; Du, Q.; Jiao, T.; Pan, B.; Zhang, Z.; Sun, Q.; Wang, S.; Wang, T.; Gao, F., Selective removal of phosphate in waters using a novel of cation adsorbent: Zirconium phosphate (ZrP) behavior and mechanism. *Chem. Eng. J.* **2013,** *221*, 315-321.
213. Chu, J.; Ke, F.-S.; Wang, Y.; Feng, X.; Chen, W.; Ai, X.; Yang, H.; Cao, Y., Facile and reversible digestion and regeneration of zirconium-based metal-organic frameworks. *Commun. Chem.* **2020,** *3*, 5/1-7.
214. Biesheuvel, P. M.; van der Wal, A., Membrane capacitive deionization. *J. Membr. Sci.* **2010,** *346*, 256-262.
215. Liu, X.; Wang, J., Electro-assisted adsorption of Cs(I) and Co(II) from aqueous solution by capacitive deionization with activated carbon cloth/graphene oxide composite electrode. *Sci. Total Environ.* **2020,** *749*, 141524.
216. Choi, J.; Dorji, P.; Shon, H. K.; Hong, S., Applications of capacitive deionization: Desalination, softening, selective removal, and energy efficiency. *Desalination* **2019,** *449*, 118-130.
217. Peng, C.; Iqbal, Z.; Sirkar, K. K.; Peterson, G. W., Graphene oxide-based membrane as a protective barrier against toxic vapors and gases. *ACS Appl. Mater. Interfaces* **2020,** *12*, 11094-11103.
218. Jia, N.; Liu, J.; Gao, Y.; Chen, P.; Chen, X.; An, Z.; Li, X.; Chen, Y., Graphene-encapsulated Co_9S_8 nanoparticles on N, S-codoped carbon nanotubes: An efficient bifunctional oxygen electrocatalyst. *ChemSusChem* **2019,** *12*, 3390-3400.
219. Schaate, A.; Roy, P.; Godt, A.; Lippke, J.; Waltz, F.; Wiebcke, M.; Behrens, P., Modulated synthesis of Zr-based metal–organic frameworks: from nano to single crystals. *Chem. - Eur. J.* **2011,** *17*, 6643-6651.
220. Limvorapitux, R.; Chen, H.; Mendonca, M. L.; Liu, M.; Snurr, R. Q.; Nguyen, S. T., Elucidating the mechanism of the UiO-66-catalyzed sulfide oxidation: activity and selectivity enhancements through changes in the node coordination environment and solvent. *Catal. Sci. Technol.* **2019,** *9*, 327-335.
221. The synthetic protocol of this experiment and the SEM images of the resulted membrane are included in appendix A.
222. Jia, C.; Cirujano, F. G.; Bueken, B.; Claes, B.; Jonckheere, D.; Van Geem, K. M.; De Vos, D., Geminal coordinatively unsaturated sites on MOF-808 for the selective uptake of phenolics from a real bio-oil mixture. *ChemSusChem* **2019,** *12*, 1256-1266.

CURRICULUM VITAE

Furui Zhang

Place of Birth: Anhui, China
furuizhangustc@gmail.com

EDUCATION

Ph.D. in Chemistry 2017 - 2021
Northwestern University (NU), Evanston, IL, U.S. (GPA: 3.9/4.0)

M.S. in Chemistry 2015 - 2017
Boston College (BC), Chestnut Hill, MA, U.S. (GPA: 3.8/4.0)

B.S. Material Science & Engineering 2011 - 2015
University of Science and Technology of China (USTC), Hefei, China (GPA: 3.8/4.3)

RESEARCH EXPERIENCE

Graduate Research, Northwestern University, Evanston, IL 2017 - 2021

- Advisor: Dr. SonBinh T. Nguyen
- Developed strategies to construct MOF-based hierarchically porous materials

Graduate Research, Boston College, Chestnut Hill, MA 2016-2017

- Mentor: Dr. Chia-Kuang (Frank) Tsung
- Design one-to-one metal nanoparticle-in-MOF core-shell structures and study how the surfactants at the interface affects metal nanoparticle's catalytic activities

Undergraduate Research, USTC, Hefei, China 2014-2015

- Advisor: Dr. Shu-Hong Yu
- Developed stretchable, wearable fabrics that are sensitive to pressure and deformation by assembling silver nanowires and conductive polymer layers on polyimide fibers

PUBLICATIONS

- Li Y.; Lo, W.; **Zhang, F.**; Si, X.; Chou, L.-Y.; Liu, X.-Y.; Williams, B. P.; Li, Y. H.; Jung, S.-H.; Hsu, Y.-S.; Liao, F. -S.; Shieh, F.-K.; Ismail, M. N.; Huang, W.; Tsung, C.-K., *J. Am. Chem. Soc.*, **2021** (**DOI**: 10.1021/jacs.1c01357) "Creating an aligned interface between nanoparticles and MOFs by concurrent replacement of capping agents". *(1st coauthor and corresponding author)*
- **Zhang**, **F.**; Hu, X.; Roth, E. W.; Kim, Y.; Nguyen, S. T., *Chem. Matter.*, **2020**, *32*, 4292-4302. "Template-assisted, seed-mediated synthesis of hierarchically mesoporous core–shell UiO-66: enhancing adsorption capacity and catalytic activity through iterative growth".

- Liu, X.-Y.; **Zhang, F.**; Goh, T.-W.; Li, Y.; Shao, Y.-C.; Luo, L.; Huang, W.; Long, Y.-T.; Chou, L.-Y.; Tsung, C.-K., *Angew. Chem., Int. Ed.* **2018**, *57*, 2110-2114. "Using a multi-shelled hollow metal–organic framework as a host to switch the guest-to-host and guest-to-guest interactions".
- Ge, J.; Sun, L.; **Zhang, F.**; Zhang, Y.; Shi, L.-A.; Zhao, H.-Y.; Zhu, H.-W.; Jiang, H.-L.; Yu, S.-H., *Adv. Mater.*, **2016**, 28, 722-728. "A stretchable electronic fabric artificial skin with pressure-, lateral strain-, and flexion-sensitive properties".
- **Zhang, F.**; Cai, Y.; Nguyen, S. T., manuscript in preparation. "Post-synthesis engineering of missing linkers into UiO-66: tuning the number of defects through a [modulator + linker] treatment"
- **Zhang, F.**; Li, Y.; Wang, Y.; Malliakas, C. D.; Si, X.; Luo, L.; Wang, D.; Bao, J.; Tsung, C. K.; Nguyen, S. T., manuscript in preparation. "Bottom-up synthesis of a 2D **cpp** UiO-66 structure by coordination hindrance on Zr_6 clusters"

PRESENTATIONS

- "Template-assisted, seed-mediated synthesis of hierarchically mesoporous core-shell UiO-66: enhancing adsorption capacity and catalytic activity through iterative growth", ACS Fall 2020 Virtual Meeting, August 2020, oral presentation (virtual)

AWARDS & HONORS

Grants-in-Aid of Research from Sigma Xi Scientific Research Society 2020
National Scholarship from the Chinese Government 2013 - 2015
Outstanding graduates from USTC 2015

LEADERSHIP

Lab safety officer, Nguyen Group 2018 - 2021
Lab Secretary, Nguyen Group 2018 - 2021

TEACHING

Teaching Volunteer, Science in The Classroom, Northwestern University 2018 - 2019
Graduate Teaching Assistant, BC & NU (8+ courses in chemistry) 2015 - 2019